Imperial College London

Effect of the surfactant on complex multi-phase annular flows

Andrius Patapas

April, 2021

Department of Chemical Engineering

Imperial College London

Submitted in part fulfilment of the requirements for the degree of
Doctor of Chemical Engineering of Imperial College London
and the Diploma of Imperial College London

Declaration of Originality

I hereby certify that the material in this thesis is the result of my own original research. All consulted materials have been properly acknowledged and the literature used referenced.

Copyright Statement

This dissertation is a description of the work carried out by the author in the Department of Chemical Engineering, Imperial College London, under the supervision of Prof. Omar K. Matar, Dr. Karl G. Anderson, Dr. Valeria Garbin and Dr. Ronny Pini. Except where acknowledged, the content is the original work of the author and no portion of it has been submitted in support of an application for a degree at any other university. The copyright of this thesis rests with the author and is made available under a Creative Commons Attribution Non-Commercial No Derivatives licence. Researchers are free to copy, distribute or transmit the thesis on the condition that they attribute it, that they do not use it for commercial purposes and that they do not alter, transform or build upon it. For any reuse or redistribution, researchers must make clear to others the licence terms of this work.

Abstract

In the modern world, the scale of industrial production within all sectors has reached unprecedented levels due to ever-growing demand and consumption of various products. A vast majority of industrial processes exploits the benefits brought by the multiphase flows whose complex dynamics are governed by the concoction of fundamental physics. Probing the details of such flows, experimentally and/or theoretically provides an ability to develop and optimise the needs of industrial applications. Yet, this progression is gradual as it depends on the advancement of measurement technologies that enable the investigation of the complex behaviour and topologies of many different possible combinations of phases utilised in industry. Use of the novel optical diagnostic techniques coupled with bespoke capacitance probes in the present study enables us to explore uncharted territory of two-phase phase gas-liquid annular flows in vertically orientated pipes. In the present study, a recently developed variant of laser-induced fluorescence (LIF) technique, termed structured-planar laser-induced fluorescence (S-PLIF), is used which allows us to eliminate biases commonly encountered during film-thickness measurements of gas-liquid flows due to refraction and reflection of the light at the interface. In parallel, a bespoke capacitance probe is also employed which permits us to conduct film thickness measurements with high temporal resolution along the perimeter of the pipe. Simultaneous application of these two measurement techniques provides an opportunity to study the subtle differences found in thin annular film structures caused not only by the function of liquid and gas flow rates, but also by the surface-active agents which are widely known to cause drastic changes in flow behaviour due to surface tension gradients. The flow characteristics are studied in terms of mean film thickness, roughness, probability density functions, time-scales of the flows, and gas entrainment in the liquid film.

The analysis of the data reveals important changes in the flow characteristics due to the presence of soluble surfactant. Firstly, it is observed that surfactant promotes thinning of annular films at nearly all flow conditions investigated herein, hinting at its influence on the turbulence

within the bulk flow. The behaviour of interfacial waves was also found to be notably altered by the surfactant where the film roughness and the time-scale of the waves increase in gas-sheared film flows with low to moderate turbulence and low gas entrainment. This corresponds to flows not in the 'regular wave' regime. A decrease in both characteristics then follows upon an increase in turbulence to a sufficiently high level of the two phases. The high gas-shear rate not only limits the highest attainable wave amplitude downstream, but also results in high agitation of air and water phases, and thus, high gas and liquid entrainment. Ultimately, this smooths the base film populated with small-amplitude waves and substantially reduces the amplitude of large interfacial waves. Generally, good agreement with relevant literature correlations is found. The estimated time-scales of the wave dynamics and Marangoni flow showed that the surfactant plays an increasingly important role on waves with lower amplitudes. The sizes of the bubbles entrained in the surfactant-free liquid film are found to exhibit log-normal distributions that become flatter with a decrease in the gas Reynolds number, while this distribution is maintained for surfactant-laden flows. On the other hand, wider distributions in the bubble sizes are found for the surfactant-laden flows at the highest gas-shear rate for all liquid Reynolds numbers. The normalised location of the bubbles (quantified as the relative entrainment depth, i.e., distance of the bubble from the local air-water film height in the wall-normal direction divided by the local film thickness) follows a Gaussian distribution where the majority of the bubbles accumulate in the middle of the thin film. Understanding the need for further development of the multiphase flows that involves the use of surfactants, motivated us to develop a method to prepare water-soluble fluorescent surfactant, which is described in the present work. Furthermore, a detailed characterisation of the fluorescent surfactant is also provided, which may encourage further experimental and modelling investigations of the relevant surfactant-laden multiphase dynamics found in small- and large-industrial scale applications.

Acknowledgements

"Nothing in life is to be feared, it is only to be understood. Now is the time to understand more, so that we may fear less."

Maria Skłodowska-Curie

Publications

In chronological order, the work that is the subject of this thesis and results from the experiments have appeared, or are being currently prepared for publication, in:

- The consortium meeting on Transient and complex Multiphase flows and Flow assurance (TMF), Imperial College London, April 2017.

- The consortium meeting on Transient and complex Multiphase flows and Flow assurance (TMF), Imperial College London, September 2017.

- The consortium meeting on Transient and complex Multiphase flows and Flow assurance (TMF), Imperial College London, April 2018.

- The consortium meeting on Transient and complex Multiphase flows and Flow assurance (TMF), Imperial College London, September 2018.

- The consortium meeting on Transient and complex Multiphase flows and Flow assurance (TMF), Imperial College London, April 2019.

- The consortium meeting on Transient and complex Multiphase flows and Flow assurance (TMF), Imperial College London, September 2019.

- 72nd Annual Meeting of the APS Division of Fluid Dynamics, Seattle, WA, November 2019. An experimental investigation of surfactant effects on the wave characteristics of annular flows. A. Patapas, V. Voulgaropoulos, V. Garbin, R. Pini, C. N. Markides, K. G. Anderson, and O. K. Matar.

- The consortium meeting on Transient and complex Multiphase flows and Flow assurance (TMF), Imperial College London, April 2020.

- 73rd Annual Meeting of the APS Division of Fluid Dynamics (Virtual), Chicago, IL, November 2020. An experimental study of the effect of water-soluble fluorescent surfactant on the interfacial wave characteristics of annular flows. A. Patapas, V. Voulgaropoulos, V. Garbin, R. Pini, K. G. Anderson, and O. K. Matar.

- V. Voulgaropoulos, A. Patapas, S. Lecompte, A. Charogiannis, O. K. Matar, M. D. Paepe, and C. N. Markides. Simultaneous laser-induced fluorescence and capacitance probe measurement of downwards annular gas-liquid flows. *International Journal of Multiphase Flow*, 2021.

- A. Patapas, G. F. N. Gonçalves, V. Garbin, R. Pini, K. G. Anderson, R. Rinaldi, and O. K. Matar. Fluorescent surfactant for fluid mechanics applications: Characterisation. *Langmuir*, 2021.

Contents

List of Figures

List of Tables

Nomenclature

All symbols used in this thesis are defined where they first appear. For the reader's convenience, the principal meanings of the commonly used notations are presented in the lists below. Though many of the symbols are specific to the chapter where they are introduced, in certain cases, symbols introduced in previous chapters might be employed with the same meaning in following chapters.

Abbreviations

ACN Acetonitrile

AF 5-aminofluorescein

BBLIF Brightness-based laser induced fluorescence

CAD Computer-aided design

CMC Critical micelle concentration

CP Capacitance probe

DA Dodecanoic acid

DAF 5-dodecanoylaminofluorescein

DAFLOF Downwards Annular Flow Laser Observation Facility

DAQ Data acquisition system

DDABC N-dodecyl-N,N dimethyl amino betaine chlorhydrate

DIC Digital image correlation

EoS Equation of state

FEA Finite element analysis

FEP Fluorinated ethylene propylene

FWHM Full width at half maximum

GC Gas chromatography

HDFL 5-hexadecanoylaminofluorescein

HPLC High-performance liquid chromatography

ID Inner diameter

K-H Kelvin-Helmholtz

LB Langmuir-Blodgett

LIF Laser induced fluorescence

MD Molecular dynamics

MeOH Methanol

NaOH Sodium hydroxide

PDF Probability density function

PLIF Planar laser induced fluorescence

PLIF70 Planar laser induced fluorescence with 70° imaging angle

PLIF90 Planar laser induced fluorescence with 90° imaging angle

PTFE Polytetrafluoroethylene

PVC Polymerising vinyl chloride

R&D Research and development

RMSE Root-mean-square error

SDS Sodium dodecyl sulfate

S-PLIF Structured-planar laser induced fluorescence

S-PLIF70 Structured-planar laser induced fluorescence with 70° imaging angle

S-PLIF90 Structured-planar laser induced fluorescence with 90° imaging angle

UHPLC Ultra-high performance liquid chromatography

UPDI Ultra-pure deionised water

2D Two-dimensional

3D Three-dimensional

Roman letters

A	Internal cross-sectional area of the pipe (m^2)
A_DAF	Molecular area of DAF (Å^2/molecule)
A_droplet	Area of the pendant drop (m^2)
A_eff	Monolayer effective area (m^2)
$C_\mathrm{p,max}$	Maximum capacitance (F)
$C_\mathrm{p,min}$	Minimum capacitance (F)
C_p	Capacitance (F)
C_0	Surfactant bulk concentration (mol m^{-3})
C_apparent	Apparent concentration in pendant drop (mol m^{-3})
$C_\mathrm{corrected}$	Corrected concentration in pendant drop (mol m^{-3})
C_s	Sublayer concentration (mol m^{-3})
D	Internal pipe diameter (m)
D_b	Bulk diffusion coefficient (m^2 s^{-1})
d_eq	Equivalent bubble size (mm)
D_s	Surface diffusion coefficient (m^2 s^{-1})
Δp	Pressure difference (Pa)
E_A	Activation energy for adsorption (J mol^{-1})
E_D	Activation energy for desorption (J mol^{-1})
F_G	Gas flow rate (L min^{-1})
F_L	Liquid flow rate (L min^{-1})
g	Gravitional acceleration ($= 9.81$ m s^{-2})
G	Monolayer at gas phase

$\langle h \rangle$	Time-averaged film thickness (m)
h_{base}	Base film thickness (m)
h_{waves}	Large wave amplitude (m)
$\langle h_{\text{CP,base}} \rangle$	Mean base film thickness acquired using CP (m)
$\langle h_{\text{CP,waves}} \rangle$	Mean wave film thickness acquired using CP (m)
$\langle h_{\text{CP}} \rangle$	Mean film thickness acquired using CP (m)
$\langle h_{\text{SPLIF,base}} \rangle$	Mean base film thickness acquired using S-PLIF (m)
$\langle h_{\text{SPLIF,waves}} \rangle$	Mean wave film thickness acquired using S-PLIF (m)
$\langle h_{\text{SPLIF}} \rangle$	Mean film thickness acquired using S-PLIF (m)
k_{a}	Adsorption rate constant (m s^{-1})
k_{d}	Desorption rate constant (s^{-1})
l_{ib}	Entrainment depth (mm)
LC	Monolayer at liquid-condensed phase
LE	Monolayer at liquid-expanded phase
M_{r}	Molecular weight (g mol^{-1})
Q_{G}	Volumetric gas flow rate ($\text{m}^3 \text{s}^{-1}$)
Q_{L}	Volumetric liquid flow rate ($\text{m}^3 \text{s}^{-1}$)
R_{G}	Gas constant (=8.3145 $\text{J mol}^{-1} \text{K}^{-1}$)
R	Internal pipe radius (m)
R_1	First principal radius of pendant drop curvature
R_2	Second principal radius of pendant drop curvature
T	Temperature (K)
t	Time (s)
u_{iv}	Inception velocity of gas phase (m s^{-1})
$u_{\text{s,G}}$	Gas superficial velocity (m s^{-1})
$u_{\text{s,L}}$	Liquid superficial velocity (m s^{-1})
u_{w}	Wave celerity (m s^{-1})
u_{film}	Liquid film characteristic velocities (m s^{-1})
u_{flow}	Wave characteristic velocities (m s^{-1})
V_{droplet}	Volume of the pendant drop (m^3)

Greek letters

α	Ratio of desorption rate constant and adsorption rate parameter (mol m^{-3})

β_{a}	Adsorption rate parameter ($\mathrm{m^3\,mol^{-1}\,s^{-1}}$)
δ	Film thickness (m)
γ	Surface tension of air-water ($\mathrm{N\,m^{-1}}$)
γ_{c}	Non-contaminated surface tension of air-water ($\mathrm{N\,m^{-1}}$)
γ_{e}	Equilibrium surface tension of air-water ($\mathrm{N\,m^{-1}}$)
Γ	Surface concentration ($\mathrm{mol\,m^{-2}}$)
Γ_{e}	Equilibrium surface concentration ($\mathrm{mol\,m^{-2}}$)
Γ_{ml}	Monolayer surface concentration ($\mathrm{mol\,m^{-2}}$)
Γ_{∞}	Maximum packing concentration ($\mathrm{mol\,m^{-2}}$)
λ	Wavelength (m)
μ_{G}	Gas dynamic viscosity ($\mathrm{kg\,m^{-1}\,s^{-1}}$)
μ_{L}	Liquid dynamic viscosity ($\mathrm{kg\,m^{-1}\,s^{-1}}$)
ν_{G}	Kinematic viscosity of air ($\mathrm{m^2\,s^{-1}}$)
ν_{L}	Kinematic viscosity of water ($\mathrm{m^2\,s^{-1}}$)
Π	Surface pressure ($\mathrm{N\,m^{-1}}$)
ρ_{G}	Gas density ($\mathrm{kg\,m^{-3}}$)
ρ_{L}	Liquid density ($\mathrm{kg\,m^{-3}}$)
σ	Surface tension of air-water ($\mathrm{N\,m^{-1}}$)
$\sigma_{\mathrm{CP,h}}$	Film roughness acquired using CP (m)
σ_{h}	Film roughness (m)
$\sigma_{\mathrm{S-PLIF,h}}$	Film roughness acquired using S-PLIF (m)
σ_{w}	Predicted wave roughness (m)
σ_{lg}	Liquid-gas interfacial tensions ($\mathrm{N\,m^{-1}}$)
σ_{sg}	Solid-gas interfacial tensions ($\mathrm{N\,m^{-1}}$)
σ_{sl}	Solid-liquid interfacial tensions ($\mathrm{N\,m^{-1}}$)
τ	Time-scale for bulk diffusion (s)
τ_{i}	Flow integral time-scale (s)
τ_{int}	Interfacial shear stress ($\mathrm{kg\,m^{-1}\,s^{-2}}$)
τ_{diff}	Diffusion control characteristic time (s)
τ_{kin}	Kinetic control characteristic time (s)
Θ	Contact angle (°)
τ_f	Wave flow time-scale (s)
τ_M	Marangoni flow time-scale (s)

Dimensionless quantities

$\mathcal{A}$	auto-correlation coefficient
b	$\alpha r_{\mathrm{d}}/\Gamma_{\infty}$
C_{s}^{*}	C_{s}/α
C_{w}	Factor that considers the effect of surface tension on the circulation/dissipation flow in the wave
f_{G}	Interfacial gas friction factor
f_{int}	Interfacial friction factor
f_{L}	Interfacial liquid friction factor
f_{W}	Wall friction factor
$f_{\mathrm{CP,waves}}$	Frequency of large waves over the total acquired using CP
$f_{\mathrm{S-PLIF,waves}}$	Frequency of large waves over the total acquired using S-PLIF
f_{waves}	Frequency of large waves over the total
Fr_{G}	Froude number for gas phase
γ^{*}	Non-dimensional surface tension
Gr_{L}	Grashoff number
K	Parameter that accounts for linear variation of the activation energy for desorption on Γ
κ	Ratio of the bulk diffusion time scale to the kinetic scale for desorption
Ku	Kutateladze number
N_{μ}	Viscosity number
Φ	Ratio between diffusion control and kinetic control characteristic times
ψ	Void fraction for capacitance
Re_{G}	Gas Reynolds number
Re_{L}	Liquid Reynolds number
θ	Γ/Γ_{∞}
$\tilde{C}_{\mathrm{p}}$	Normalised capacitance
X	Lockhart-Martinelli number
x^{*}	Gas quality

Subscripts

G	Gas phase

ib	Distance from gas-liquid film height to bubble centre
L	Liquid film

Chapter 1

Introduction

Contents

In this chapter, firstly, a general overview of multiphase flows, and particularly of gas-liquid flows in vertically orientated pipes, the effect of surfactants on these flows, the development works on interfacial phenomena and various measurement techniques is provided. The level of significance that these developments have on a wide scope of industrial applications is also emphasised. Motivation and objectives for this project are also set forth. Lastly, a thesis structure comprised of brief contents for each chapter is presented.

1.1 Background

An incredibly vast variety of fluid dynamics phenomena occurs at every moment in nature and our lives. These complex events can be met at a multitude of scales starting from nanoscopic sizes e.g., nanofluidic circuitry where typical characteristic dimensions are < 0.1 µm, and as big as our planet earth e.g., swirling clouds and the Great Red Spot located on the planet Jupiter where the size of the latter is ~ 16350 km (10159 miles) - large enough to engulf Earth [151]. These are typically comprised of more than one fluid (gas or liquid), hence, the term 'multiphase flows'.

Multiphase flows are encountered in a broad-spectrum of practical applications, where typically two immiscible fluids are used (e.g., gas and liquid) which are separated by an interface. Specifically, pertinent to the present work, simultaneous two-phase air-water flows are typically utilised in pipes that can closely replicate industrial applications such as falling film evaporators, pressurised water reactors or vertical risers, in all of which thin liquid films are flowing across the surface of the wall e.g. pipe, while the core is occupied by the air/vapour phase. The dynamics of such flows in pipes, termed annular flows, are typically characterised in terms of the film thickness, interfacial waves, and entrainment rates, and are determined by a number of physical factors such as the pipe diameter and its orientation, fluid velocities, and the properties of the fluids. Consequently, these will directly influence the inertia, buoyancy, turbulence forces and interfacial tension.

The underpinning work on gas-liquid annular flows was started in the last century by numerous research studies, most notable of which were conducted by Azzopardi [13, 11], Chu and Dukler [39], Hall-Taylor and Nedderman [69], Hewitt and Hall-Taylor [73], Hewitt and Whalley [74], James et al. [81], Woodmansee and Hanratty [177], and many more. These works demonstrate that with progressive advances made in electronic and optical engineering this unveiled capabilities of various experimental methods that allowed one to directly investigate the annular flows for the aforementioned characteristics. The in-depth understanding attained from these and other academic works permitted one to make a significant advancement in relevant industrial processes and technologies that involves the use of gas-liquid annular flows. Owing to an increased controllability of this type of multiphase flows, various unit operations could be designed with an optimal efficiency and productivity, whilst maintaining safety at the highest level.

Furthermore, having an extensive amount of data for various pipe configurations and fluid properties and flows, many predictive tools were developed that further facilitates the design and operation of industrial processes. Specifically for gas-liquid annular flows, the proposed correlations in the literature are able, to some extent, to describe the behaviour of the interfacial flows and predict various characteristics such as wave celerity, frequency and amplitude, droplet entrainment rates, their sizes and velocities, and film thickness. Quantitative details of such models are explored in the reviews by Berna et al. [20, 21]. Despite the substantial progress that was made from the experimental and theoretical perspectives, the highly complex behaviour of annular flows due to the presence of a multitude of phenomena that are discussed in the works of Azzopardi [11] and Hewitt and Hall-Taylor [73], are yet to be fully understood. For

this reason, most of the works mainly focus on two-phase flows using pure fluids i.e., without the addition of contaminants. However, many industrial processes, by design, employ so-called SURFace ACTive AgeNTs (surfactants) such as in the case of falling film reactors [187].

There exists an exhaustive amount of different surfactants, properties of which was demonstrated to have significant effects on gas-liquid systems. For instance, Benjamin Franklin wrote his qualitative observations on application of oil to the sea by the sailors in order reduce and 'calm' the sea waves [19]. Later, more advanced quantitative work was conducted by Agnes Pockels in her application of powders on thin liquid films and the effects of surface tension [131]. Soon thereafter, various scientific fields focusing on surface science and interfacial phenomena started to rapidly evolve due to the broad attention of scientists from many different disciplines towards the inherent versatility of surfactant molecules.

An interface, which is an infinitesimal boundary separating two immiscible fluids e.g., air and water, is formed due to intermolecular interactions. Water molecules located at a surface interact more strongly with the other water molecules located in the interior (due to hydrogen bonds) than with the widely-spaced gas molecules located above the surface. Due to this, water molecules located at the surface have higher potential energies than those in the interior, so work input is required to draw the molecules from the interior to the surface to form an interface [139]. The amount of work required to create this interface equates to a product of surface tension and the area of that created surface. The presence of surface tension acts to minimise surface area while inducing a discontinuity in the pressure field at the interface. Lowering the temperature of the system leads to an increase in the strength of hydrogen bonding in the bulk giving rise to an increased surface tension.

The concept of surface tension was introduced in the famous work of Thomas Young [163]. Following on from this, an equation was derived that describes the interface force balance at the contact line where three phases meet (i.e., gas, liquid, and solid, as shown in Fig. 1.1):

$$\sigma_{lg} \cos \Theta = \sigma_{sg} - \sigma_{sl}, \tag{1.1}$$

where σ_{lg}, σ_{sg}, and σ_{sl} are the liquid-gas, solid-gas, and solid-liquid interfacial tensions, and θ denotes the contact angle. The other significant advance corresponds to the derivation of the Young-Laplace equation which postulates that the pressure discontinuity across a curved interface is expressed as

$$\Delta p = \sigma_{lg} \left(\frac{1}{R_1} + \frac{1}{R_2} \right), \tag{1.2}$$

where Δp is the difference in pressure across either side of the interface and the principal radii of curvature are R_1 and R_2, respectively. The pendant drop tensiometry, shown in Fig. 1.2, offers a simple method to measure the interfacial free energy per unit area which essentially determines the surface tension between the gas and liquid phases (or other immiscible fluid-fluid pairing that forms an interface).
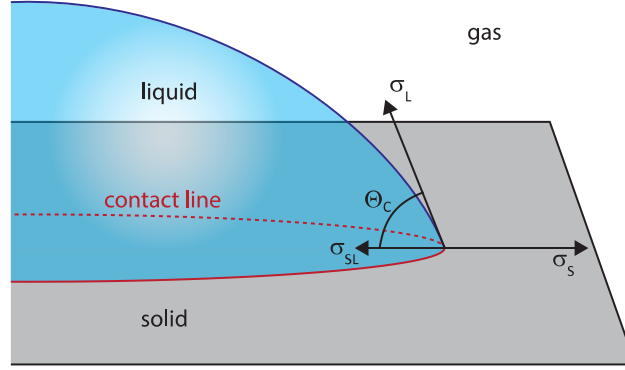
Figure 1.1: Schematic showing the contact angle at a solid-liquid-gas contact line (adapted from [2]).

The structure of the aforementioned water molecules at the surface can be easily broken by the surfactant molecules. Owing to the possession of amphiphilic characteristics by the surfactant allows it to adsorb at the interfaces in an oriented manner i.e., non-polar moiety, termed as the 'tail-group', is water-insoluble (air molecules are also essentially non-polar in nature), whilst polar moiety, termed as the 'head-group', is water-soluble. Upon the adsorption onto the gas-liquid interface at sufficient concentration, surfactant molecules alter the interfacial free energy in a reducing manner (decreasing dissimilarity between the two contacting phases). The distribution of surfactant between the interface and bulk phases depends on the difference in chemical potential and also kinetically on energy barriers for transfer [54]. The representation of the surfactant molecule transport between the bulk and the interface is shown in Figure 1.3.

By increasing surfactant bulk concentration at a fixed temperature, the surface tension is reduced up to a certain value only, after which a plateau is reached. When this point is reached the interface is saturated with a monolayer of surfactant molecules, and no additional area is available for adsorption. This is called the Critical Micelle Concentration (CMC), and the process is depicted in Figure 1.4. This minimum surface tension value (at the CMC) depends on the physico-chemical properties of the surfactant which are dictated by size of the head-group, length and number of the tail-groups, chemical composition [43]. Further increase in bulk concentration does not alter the surface tension significantly, and leads to spontaneous processes of surfactant self-assembly in the bulk phase into various ensemble shapes e.g., micelles,

vesicles, bilayers, etc. Such processes are driven by an increase of entropy when the surfactant hydrophobic groups are removed from the water phase and the ordered structure of the water molecules around these groups is lost.

(a) Pendant drop tensiometer

(b) Pendant drop profile
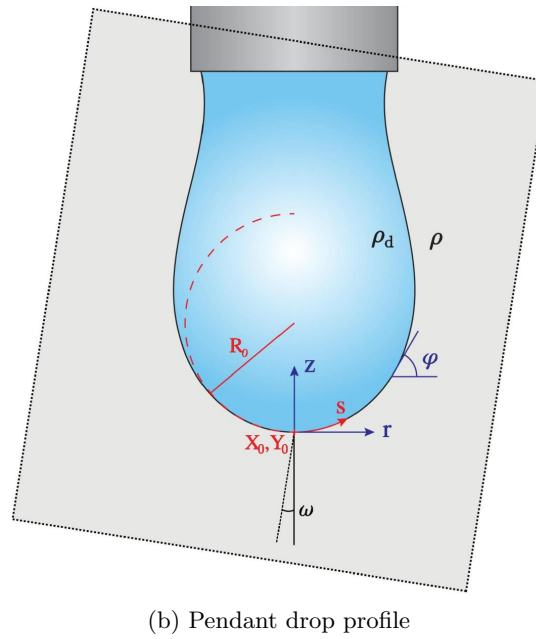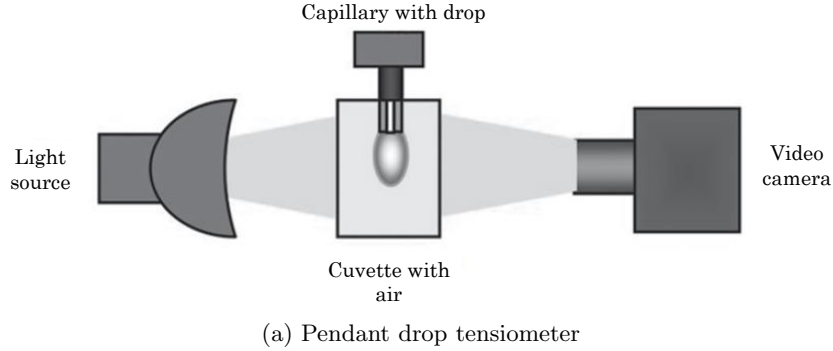
Figure 1.2: Measurement of surface tension using the pendant drop method. (a) Schematic drawing of the pendant drop profile analysis tensiometry, and (b) schematic of a pendant drop profile with the associated variables used to determine the interfacial tension (adapted from [22, 50]).

Relating these phenomena to gas-liquid annular flows, the adsorption of surfactant onto a liquid film may substantially influence the hydrodynamical properties of the surface. This occurs due to continuous change in the shape of the surface by the moving waves, which subsequently stretches and compresses the surfactant film. As a result of this, the surface concentration also changes, varying across the wavy surface, and thus, leading to the existence of surface tension gradients. Areas containing higher surfactant concentration (lower surface tension) will result in surfactant spreading towards regions with lower concentration (higher surface tension), in turn, giving rise to Marangoni stress. This transport of surfactants along the interface is a
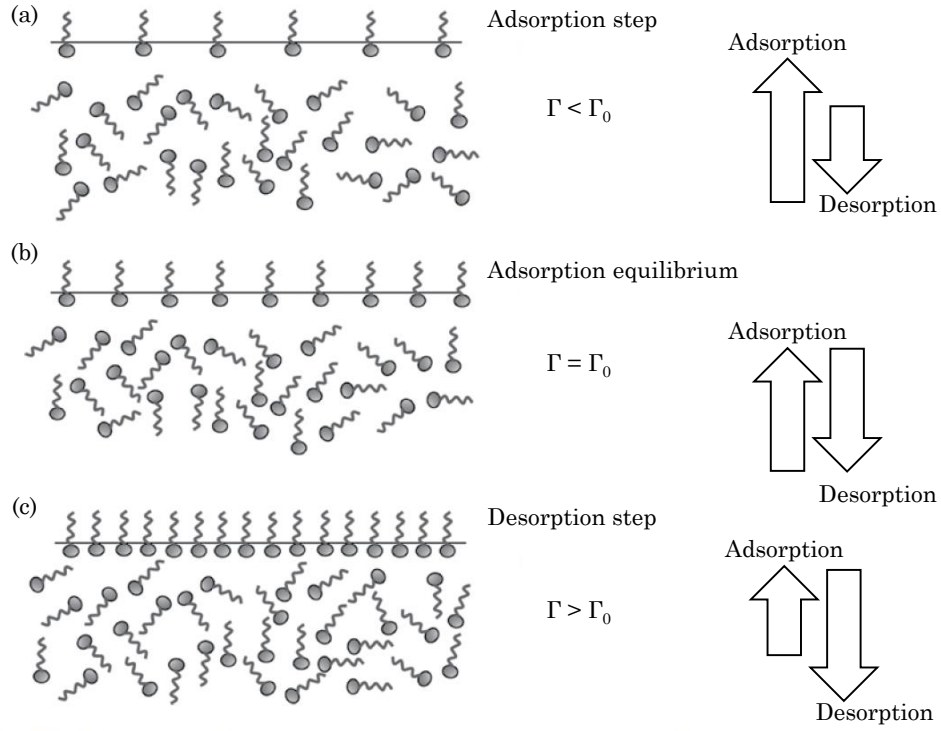
Figure 1.3: Surfactant adsorption and desorption fluxes from the interface, depending on the adsorption state. (a) net adsorption flux to the interface, (b) adsorption and desorption fluxes are equal, (c) net desorption flux from the interface (adapted from [50]).
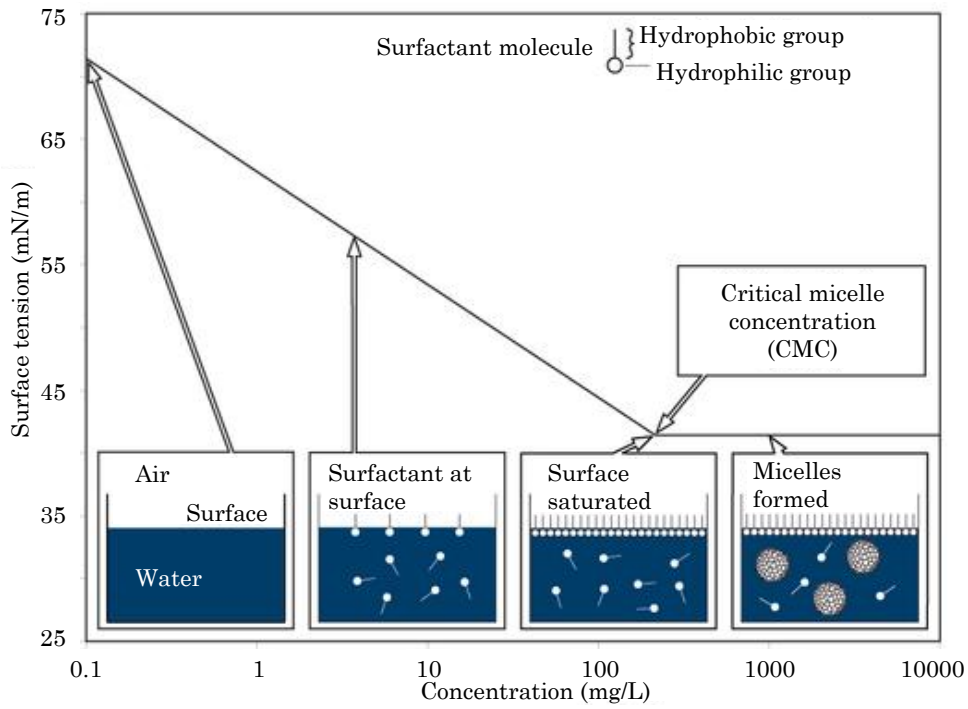
Figure 1.4: The plot represents the change in the surface tension as a function of a surfactant bulk concentration, and schematic drawings of surfactant molecule, its adsorption process, and formation of micelles above the CMC (adapted from [1]).

well-known phenomena called the Marangoni effect [41, 55]. The presence of surfactants in gas-liquid annular flows leads to various observable changes in the flow behaviour, particularly for the flows with high gas and liquid mass flow rates. Numerous works showed that surfactants can alter the morphology of the gas-liquid interface by formation of foam and suppression of interfacial waves. Such flows were also shown to change the complexity of liquid film topology, pressure drop, and entrainment of liquid and gas rates, which consequently influences the flow regime transitions [170, 171]. Yet, majority of the research work was conducted on upwards gas-liquid annular flows due to wider relevance to industrial applications, particularly in oil-and-gas industry, while no studies were found to focus on the effect of the surfactant on downwards gas-liquid annular flows.

As briefly stated above, a variety of measurement tools have been developed for testing and real-time data acquisition in annular flows, which have been investigated actively throughout the last several decades using multiple intrusive and non-intrusive methods including resistive and capacitive impedance, ultrasonic, electromagnetic, and optical methods. At the present time, typical methods employed for evaluation of the effect of the surfactant on gas-liquid annular flows are mainly qualitative (using high-speed imaging) which does not provide reliable quantitative information on the aforementioned flow characteristics. A quantitative study typically utilises non-intrusive methods such as conductance probe, which allows one to acquire the flow characteristics of the annular flows such as the film thickness, wave amplitude and frequency. Even with this, only several works are found in the literature to study surfactant-laden gas-liquid annular flows, one of which was performed recently by Rivera et al. [136] on co-current upwards annular flows with surface tension variation by addition of 1-butanol. More advanced methods that use optical diagnostic techniques such as Planar Laser Induced Fluorescence (PLIF) [186] and Structured-PLIF (S-PLIF) [32] were developed and successfully applied to study downwards air-water annular flows. Due to high accuracy and reliability of these methods, PLIF and S-PLIF allowed one to quantitatively evaluate a wider-scope of flow characteristics that were not accessible before by other foregoing non-intrusive methods. Consequently, this opened up new avenues to study complex gas-liquid annular flows.

1.2   Project motivation and objectives

To date, only a limited number of studies were found on downwards gas-liquid annular flows, all of which focused solely on surfactant-free flows. The unexplored area of surfactant-laden flows offers an opportunity to expand our understanding of the effect of surfactant on complex gas-liquid annular flows. With the simultaneous application of advanced laser-based diagnostic technique, S-PLIF in this case, and capacitance technique it is aimed to identify the differences between surfactant-free and surfactant-laden flows in terms of bulk and interfacial flow dynamics for a wide-range of flow conditions, which may be applicable for industrially relevant processes e.g., falling film reactors. It is well-known that surfactants may lead to considerable effect on phenomenological events such as liquid and gas entrainment, altering mass and energy transfer, which can be explored by direct observation using S-PLIF method. Moreover, a growing interest in understanding the physics of surfactant, especially in the area fluid mechanics, requires detailed characterisation of specific type of fluorescent surfactant e.g., soluble in widely used solvents such as water. Thus, such surfactant needs to be identified and analysed in terms of physico-chemical and optical properties from which its practical usability to study various physical problems can be demonstrated (also potentially applicable to computational modelling). In fact, its behaviour (in terms of bulk and surface concentration) can be measured using various optical techniques such as PLIF. Based on these motivations, the following objectives are set:

1. Identify all molecules containing (1) a single tail-group, and (2) an aromatic head-group with suitable optical properties e.g., that could be probed at 532 nm - the wavelength emitted by Nd:YAG laser available in the laboratory for this project. Upon shortlisting potential surfactant candidates, develop a method using which the selected surfactants can be treated in order to transform them from water-insoluble to water-soluble state.

2. Conduct a series of analytical measurement techniques to characterise the selected fluorescent surfactant (under conditions to be used for large-scale experiments) for its (1) optical properties, (2) molecular stability, (3) surface activity as an insoluble species, (4) surface activity and transport properties as a soluble species.

3. Gather information on key air-water flow characteristics that are required to and can be measured using S-PLIF and capacitance techniques. Concurrently, select the range of gas and liquid flow conditions relevant to the literature data on downwards gas-liquid annular flows, which would be attainable in large-scale experimental facility.

4. Depending on objective (2), modify large-scale Downwards Annular Flow Laser Observation Facility (namely, DAFLOF) such that it would be feasible to conduct the required measurements using S-PLIF and capacitance techniques for the selected range of air-water flow conditions. This includes selection of pipe material and internal diameter, design of the correction box to match refractive indices, independent pumps for liquid and gas phases. For the measurements techniques select the optical filters and lenses for high-speed cameras, data acquisition systems. Additionally, implement the required software and protocols to operate the facility, health and safety and risk assessments. Finally, perform necessary training for operation of laser and high pressure systems.

5. Perform calibration on S-PLIF and capacitance probe instruments for a combination of air and water fluids to ensure accurate and reliable measurements of film thicknesses. Compare preliminary results on mean film thickness measurements with available literature data to ensure the data are within acceptable experimental error bounds.

6. Conduct experimental measurements in DAFLOF using S-PLIF and capacitance techniques firstly for surfactant-free flows followed by surfactant-laden flows for the whole range of selected flow conditions. Perform spatially- and/or time-resolved measurements using at least one technique in order to capture details of important flow characteristics and phenomenological events.

7. Upon successful execution of large-scale experimental campaign, extract all the data acquired using each technique. Develop image processing tools using proprietary software (DaVis) and MATLAB algorithms in order to process all the data that could be transformed into meaningful information and compared with literature data and predicted results from various correlations.

Processed and analysed results within the present work aim to facilitate the operation of industrially relevant processes, and advance our fundamental understanding of vertically downwards gas-liquid annular flows in the presence and absence of surfactants. This includes usage of data in the process of engineering design and optimisation efforts, development of predictive tools in the form of correlations and models, and validation of three-dimensional direct numerical simulations. In addition, the development of a method to prepare water-soluble fluorescent surfactant aims to expand its use in a wide-range of research applications beyond the gas-liquid annular flows.

1.3 Thesis structure

The present thesis mainly focuses on the systematic experimental study of downwards thin film flows in an annular pipe configuration with and without the gas shearing effects. In two sets of large-scale experiments the behaviour of annular air-water flows related to the bulk film, interfacial waves and entrainment characteristics is analysed by performing simultaneous measurements using two independent and non-intrusive methods. One experiment is studied using uncontaminated (clean) air-water system, while the other, corresponds to an air-water system seeded with water-soluble fluorescent surfactant. Both configurations are widely used in various R&D, and industrial sectors, albeit the differences between the two, particularly on the effect of the surfactant on multiphase flow behaviour, are not yet fully explored. The structure of this thesis is organised in the following manner:

- Chapter 2 presents a review of the literature on vertically upwards and downwards gas-liquid annular flows. This comprises quantitative and qualitative results of surfactant-free and surfactant-laden flows using various experimental techniques. A review is also conducted on the functionality of fluorescent surfactants and their application in related gas-liquid systems.

- Chapter 3 describes the details of all the measurement techniques used to characterise the fluorescent surfactant employed for large-scale experimental campaign. This includes the analysis of molecular stability, optical properties and surface activity. The model to describe the surfactant transport is formulated. Following this, a description of the large-scale experimental facility along with the chosen flow conditions is provided. The configuration of optical and capacitance methods are also described in detail.

- Chapter 4 provides details of an in-house developed treatment method to convert insoluble fluorescent surfactant into a water-soluble molecule. With this, the surfactant is characterised for its (i) light absorption and emission properties, (ii) molecular stability post-treatment with alkaline solution, (iii) behaviour and surface activity as a monolayer and soluble species. On the basis of (iii), surfactant transport properties are established.

- Chapter 5 presents measurement details of both surfactant-free and surfactant-laden falling film and gas-sheared film flows from which the effect of surfactant is evaluated based on the qualitative and quantitative differences. The analysis includes the construction of flow pattern maps, and the influence of the surfactant on the behaviour of annular films,

specifically on the film thickness and its roughness.

- Chapter 6 focuses on the effect of surfactant on interfacial waves present in annular films. The underlying differences are explored on the basis of the wave statistics that are processed using various statistical analysis techniques. The influence of the surfactant on the various interfacial waves is also examined by evaluating the time-scales associated with the gravitational, viscous and Marangoni stresses.

- Chapter 7 offers a characterisation of the gas entrainment in the form of bubbles inside the liquid film. The study presents statistics on the bubble sizes as well as the entrainment depth for particular flow conditions that have distinct entrainment rates. Qualitative analysis on the formation of 'foam' close to and at the crests of large waves is also performed.

- Chapter 8 concludes the results of this work and provides suggestions for future work, which includes not only on gas-liquid systems, but also on liquid-liquid.

Chapter 2

Literature review

Contents

An in-depth review of developments up to the present time on the vertical gas-liquid annular flows and the various measurement techniques is presented in this chapter. The review discusses how with the aid of small- and large-scale experimental campaigns conducted through many decades allowed the expansion of our comprehension of the associated flow characteristics found in the surfactant-free and surfactant-laden flows. Using data acquired using various measurement techniques flow pattern maps were constructed and these data were utilised for the elucidation of various mechanisms that describe interfacial flows and entrainment events, and subsequently, to build correlations and models that allow one to predict flow characteristics for a wide-range of gas and liquid flow conditions, fluid properties, and pipe configurations. As a result of these advancements, a significant enhancement in the controllability, efficiency, and productivity of various industrial processes was achieved.

A comprehensive theoretical and practical understanding of the surfactants and their associated phenomena has led to an enormous expansion of practical applications and processes in which surfactants are being employed due to their unique physico-chemical properties. Nonetheless, many theoretical aspects require validation, which can be performed using the fluorescent surfactants whose dynamics and effects can be measured. Thus, a review on the application of

fluorescent surfactant in fluid dynamics problems is conducted and presented herein.

2.1 Vertical gas-liquid annular flows

There exists four main flow regimes in adiabatic and non-reacting gas-liquid flows in a vertically oriented pipes. These can have either counter-current gas-liquid flows (i.e., upwards flows) or co-current gas-liquid flows (i.e., downwards flows). Depending on the individual gas and liquid mass flow rates, properties of selected fluids, and sizes of the fluid domains, typical flow regimes that occur in this type of flow configuration are (1) bubbly flow, (2) slug flow, (3) churn flow, and (4) annular flow, which are illustrated in Fig. 2.1 [16, 168]. Assuming a flow with a sufficiently high and fixed liquid flow rate, flow regimes will transition from bubbly flow to annular flow as the gas flow rate starts to increase. Each of these flow regimes can be described in the following manner:

- Bubbly flow occurs in the continuous liquid phase when the gas flow rate is high enough to form relatively small gas bubbles that experience no slippage [27]. The distribution of bubble sizes is non-uniform as the bubbles can undergo coalescence with one another, which typically increases with gas flow rate. In addition, the motion of gas bubbles are complex, and have a tendency to flow upwards/downwards close to the centre of the pipe.

- Slug flow occurs once the flow rate of the gas phase increases to a sufficiently high value, also in a continuous liquid phase, leading to large amount of small gas bubbles that continuously coalesce forming large 'Taylor' bubbles. These 'Taylor' bubbles occupy cross-sectional areas similar to that of the pipe in which the flow takes a place, and are separated with slugs of liquid that are entrained with smaller bubbles. Taylor bubbles are of short cylindrical shape with a semi-spherical-like front side, while the rear side has a deformed base. An intermittent flow is typically observed at this flow regime due to alternating occurrence of liquid slugs and Taylor bubbles [27, 65].

- Churn flow is characterised by the unstable Taylor bubbles that collapse resulting in a highly turbulent flow pattern with both phases dispersed. Smaller liquid bodies are formed due to disintegration of liquid slugs that decrease in axial length and become highly entrained with small sized bubbles forming froths [27, 65].

- In annular flow, a continuous gas phase flows through the core of the pipe while a thin

liquid film with a wavy surface flows across the pipe wall. Entrainment of gas in the form of bubbles inside the liquid film, and liquid droplets and ligaments into the gas core is often observed at sufficient mass flow rates, especially of the gas phase. Thin liquid films are characterised by the presence of interfacial waves of various amplitudes, frequencies and velocities. Annular flows can be also generated in downwards flows even in the absence of gas flow stream, referred to as falling films [73].
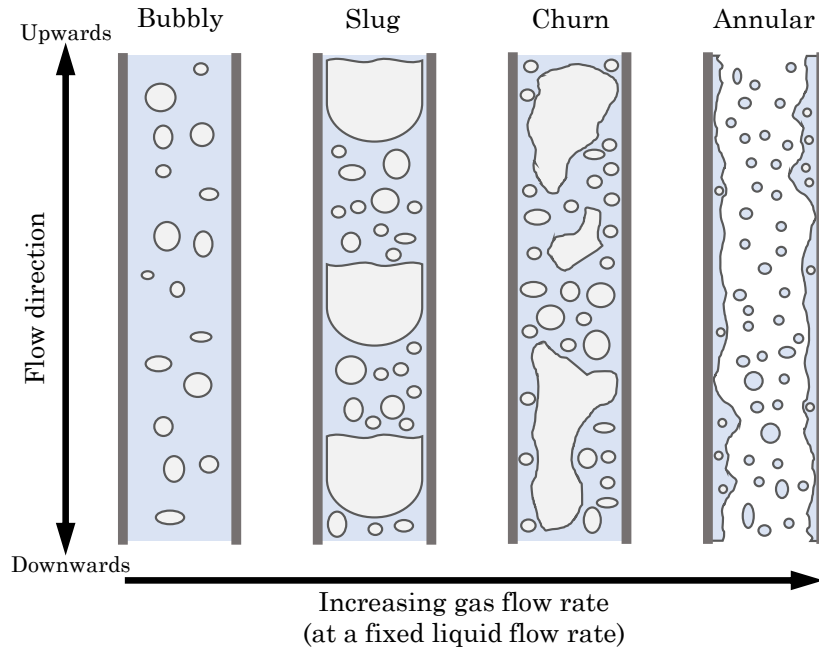
Figure 2.1: Illustration of the well-established flow regimes that occur in vertically orientated pipes of upwards or downwards co-current gas-liquid flows.

Focusing specifically on annular flow regime in vertical pipes, reveals its usage in a diverse range of industrial applications. In oil-and-gas industry upwards annular flows are employed in gas-liquid oil wells, raisers and transfer pipelines. On the other hand, vertically falling films are employed for inspissation purposes in industrial units such as falling-film evaporators or distillation columns. Many of the gas-liquid reactions are also carried out using falling films and annular flows such as chlorination, sulfonation, hydrogenation or ethoxylation [44, 159]. Such a flow configuration offers process benefits in terms of rapid heat removal and minimisation of mass transfer resistance in the liquid phase [187]. Due to high complexity of the associated annular flow characteristics in terms of surface instabilities that appear in the form of interfacial waves and often lead to entrainment events (see illustration in Fig. 2.2). Such physical events were shown to have a significant influence on the mass transfer during the absorption of carbon dioxide by water i.e., increasing by up to 170% [122]. Thus, the continuous development of

15

fundamental understanding of the annular film flow behaviour is key for practical applications at various scales as well as theoretical works (e.g., prediction of mass and heat transfer [113]).
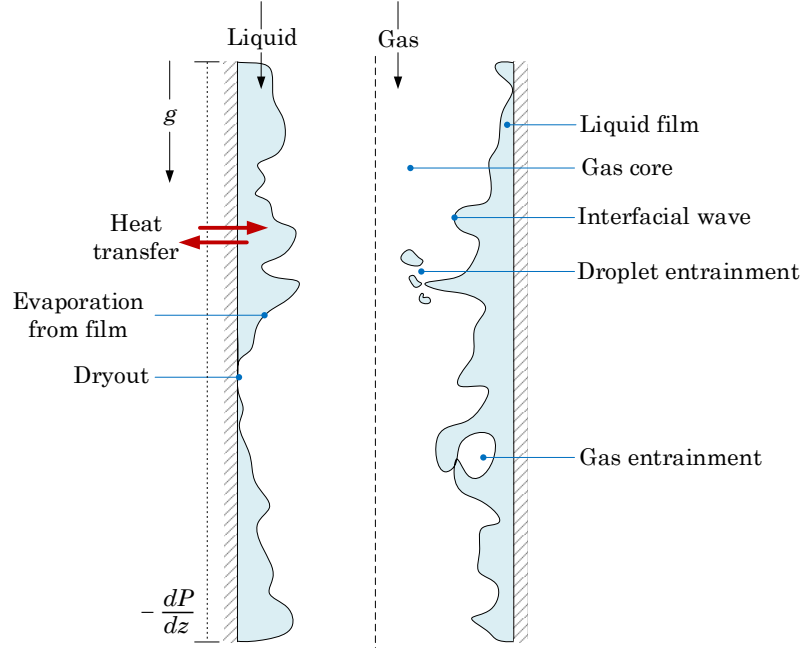
Figure 2.2: Illustration of a typical downwards co-current gas-liquid annular flow and the associated hydrodynamics.

The frictional pressure drop and interfacial waviness, where the latter is often termed as surface roughness and expressed as standard deviation, increases with the growth of the wave amplitude [145]. Once the interfacial waves attain sufficiently large amplitude (at least two times of the mean film thickness) this typically leads to the liquid entrainment events in the form of droplets and ligaments, particularly at high gas Reynolds number [73]. Redeposition of the entrained liquid bodies, particularly those of large size (e.g., ligaments) and high velocity, may promote erosion and corrosion of the inner walls of the process unit [14]. Moreover, in the small- and large-scale processes where heat transfer plays an important role, as in the aforementioned examples, the interface may significantly suffer from the so called 'dryout' areas (see Fig. 2.2) that can form in annular flows where the film is dissipated typically due to high shear rate exerted by the gas stream or evaporation of very thin residual film [82]. As a result of this phenomena, not only the process efficiency can be substantially reduced, but this may also lead to process safety concerns particularly where heat removal is of primary importance.

For all of the above reasons, the lack in understanding of the behaviour of annular flows, especially of turbulent flows, can be improved with the use of advanced experimental measurements techniques that provide both qualitative and quantitative data which could be utilised in

the process optimisation, and validation and further development of predictive tools and models.

The early pioneering works of Chu and Dukler [39, 40], Telles and Dukler [162], and Webb and Hewitt [175], has greatly expanded our knowledge on thin film flows occurring in annular flow regime. Using various advanced experimental measurement methods allowed us to characterise gas-liquid interfacial flows by identifying different types of waves and their corresponding activity. For instance, Webb and Hewitt [175] for the first time described the dynamics of downwards annular flows in terms of flow regimes that vary depending on the gas and liquid flow rates. In their work, four main flow regimes were described: (1) 'ripple wave', (2) 'dual-wave', (3) 'thick ripple', and (4) 'regular wave' regimes. Not until recently, owing to advancements made in optical diagnostic techniques, was the existence of these flow regimes confirmed in the study by Zadrazil et al. [186] who performed Planar Laser Induced Fluorescence (PLIF) measurements for a wide-range of flow conditions in downwards annular flows (except for the 'ripple wave' regime which was limited due to practical reasons). Having a direct non-intrusive capability to visualise thin films using PLIF method, permitted Zadrazil et al. [186] to characterise annular flows more thoroughly in a spatially-resolved manner. This includes not only qualitative evidence of mechanisms by which gas and liquid entrainment occurs, but also quantitative results that characterise thin film flows in terms of various statistical moments, i.e., mean and standard deviation of the film thickness, thickness of the base film, amplitude and frequencies of the waves, and gas entrainment into the liquid film. Coupling their findings with the results of Webb and Hewitt [175], a more accurate flow pattern map was constructed which included an additional flow regime termed 'disturbance wave'. Each flow regime was identified to occur over a particular range of gas and liquid flow rates in terms of Reynolds numbers, Re_{G} and Re_{L}, respectively, and to carry qualitative flow characteristics as per below:

1. 'Ripple wave' regime occurs at $Re_{\mathrm{L}} \leq 121$ and $Re_{\mathrm{G}} \geq 0$, observed to have relatively quiescent liquid films with frequent occurrence of waves with small amplitudes typically referred to as 'ripple waves'.

2. 'Dual-wave' regime occurs at Re_{L} between 306 and 613, and $Re_{\mathrm{G}} \leq 21 \times 10^3$, with relatively quiescent base films characterised by long wavelength and occasional occurrence of waves with large amplitudes (at least several times that of the mean film thickness).

3. 'Thick ripple' regime occurs at Re_{L} between 919 and 1226, and $Re_{\mathrm{G}} \leq 21 \times 10^3$, where the frequency and amplitude of waves increases, while the roughness of the base film increases with waves of small amplitude. Infrequent bubble entrainment is observed.

17

4. 'Disturbance wave' regime occurs at $Re_L \geq 1532$ and $Re_G \leq 21 \times 10^3$, with the formation of irregular waves with larger amplitude and short wavelengths relative to the base film and those observed in 'thick ripple' regime. The presence of waves with small amplitude, most likely ripple waves, are present on the large waves and base films. More frequent gas entrainment in the liquid film is observed, along with liquid entrainment events into the gas core.

5. 'Regular wave' regime occurs at all Re_L values when $Re_G \geq 42 \times 10^3$, where high shear rate exerted by the gas stream results in generation of frequent waves with much smaller amplitudes and short wavelengths than in the previous flow regimes. Significant increase in the bubble entrainment inside the liquid films, and liquid entrainment into the gas core is observed.

To date, many of the research works describe annular flows based on only two types of interfacial waves - ripple waves and disturbance waves. The majority of the research works differ in the way in which these two types of interfacial waves are defined based on their specific characteristics (e.g., amplitude, wavelength, velocity). This is not surprising due to utilisation of various measurement methods where each one provides specific information on annular films, and may carry inherent measurement errors such as spatial-averaging, or simply being an intrusive method which directly disturbs the flow and may provide incomplete picture of the interfacial flow patterns.

Optical diagnostic techniques permitted direct observation of these interfacial waves for a wide-range of flow conditions, which helped to narrow down the defined features of disturbance waves and ripple waves [4, 5, 35, 186]. While in the former case, the waves have distinct large structures which are typically defined in the literature to have an amplitude of at least two mean film thickness, ripple waves, on the other hand, are of much smaller amplitudes which makes it challenging to distinguish them from the base film which continuously varies in thickness. It is worthy of note that the majority of the most advanced non-intrusive methods, as in the case of optical diagnostic techniques discussed in the following section, only provide two-dimensional information on flowing films. However, the film topology can be reconstructed if the technique allows to perform spatio-temporaly resolved measurements with high spatial resolution.

To expand on the present understanding of the ripple and disturbance waves, it is known from the most advanced experimental measurements using optical-diagnostic techniques that ripple waves are typically classified by their velocity. The study of Alekseenko et al. [4, 5]

18

showed the existence of slow- and fast-moving ripple waves that are formed at the rear side of the large amplitude (disturbance) waves (see Fig. 2.3). Slow ripples are found to be generated at the lower end of the disturbance waves (behind the stagnation point of the re-circulation zone within the large wave) trailing at or close to the base film. These waves move at a slower velocity than the 'parent' disturbance waves, thus, starting to lag behind, until the succeeding disturbance wave approaches and absorbs it. On the other hand, fast ripples are found to be formed at the front-slope of the 'parent' disturbance wave (above the stagnation point of the re-circulation zone within the large wave in a reference frame moving with this wave). In this case, ripple waves are moving at a higher velocity than the 'parent' disturbance wave, which results in movement over the top of the large wave until it either decays near the wave-front, or becomes highly unstable induced by the high gas-shear rate which consequently leads to fragmentation into liquid droplets and ligaments (depending on the mechanism) [11, 129, 177].

The understanding of the characteristics and dynamics of the disturbance waves are more broad than of the ripple waves. Although the mechanism responsible for the formation of the disturbance waves is not yet fully understood, it is suggested that these waves occur due to imbalances between inertial, pressure, surface tension and viscous forces that result in the growth of interfacial instabilities [14]. Similarly, the 'birth' of the disturbance waves may occur by the rapid changes in the momentum of the fluid [91]. In near-turbulent and turbulent flows, there are fluid regions that move with lower momentum and higher momentum, where the latter may inflow into the former resulting in a surge of fluid perpendicular to the flow, and thus, forming an unstable flow region with higher liquid volume and momentum which grows with distance. In support of this, an experimental study by Thwaites et al. [164] on the effect of drag reducing agents on falling films has shown that the addition of such agents leads to stabilisation of turbulent flows. This was characterised by a delayed transition of disturbance waves to a higher Reynolds numbers and decrease in the wave frequency. This mechanism was also later confirmed by Martin and Azzopardi [110]. Another observed mechanism on the formation of disturbance waves is built on the basis of experimental and numerical studies [7, 6, 59, 79]. In the case of gas-sheared downwards annular flows, where the liquid film is in laminar flow, at the inlet of the film formation of two-dimensional waves with high frequency is observed. This type of waves is also termed as Kelvin-Helmholtz waves due to their interfacial characteristics. As these two-dimensional waves flow downstream, they become disrupted by the gas-stream resulting in formation of localised solitary three-dimensional waves. Downstream distance at which this disruption occurs decreases with increasing gas flow rate. Moreover, it is found that the frequency of these three-dimensional waves grows with gas superficial velocity. As a matter
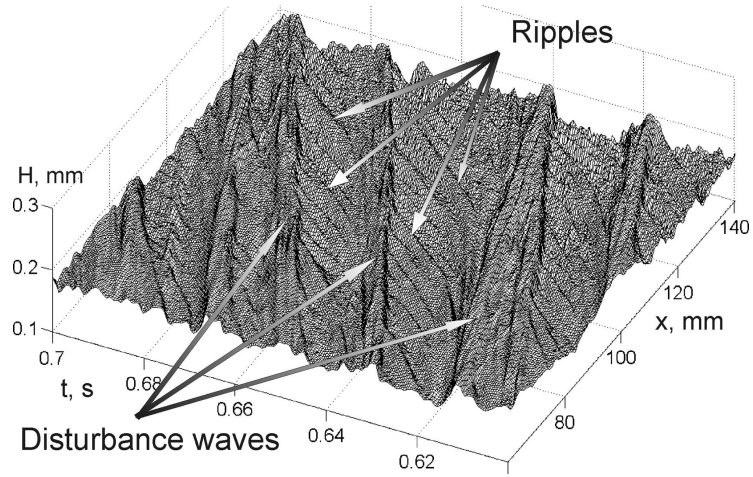
(a) Disturbance and ripple waves
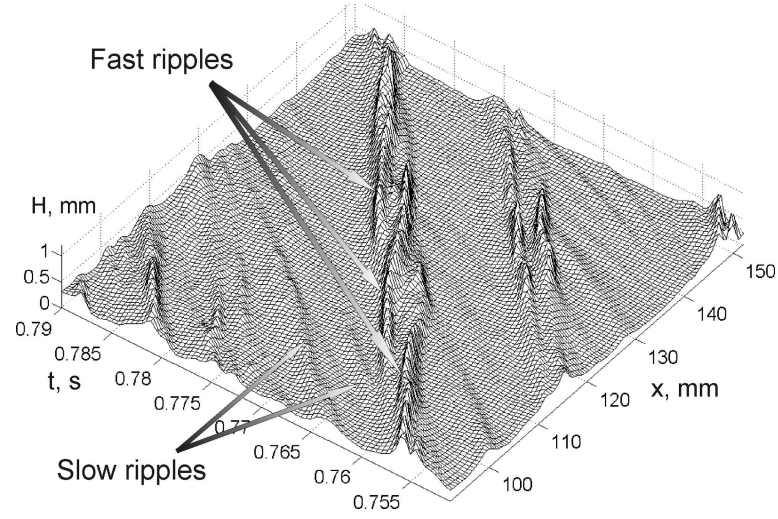
(b) Slow and fast ripples
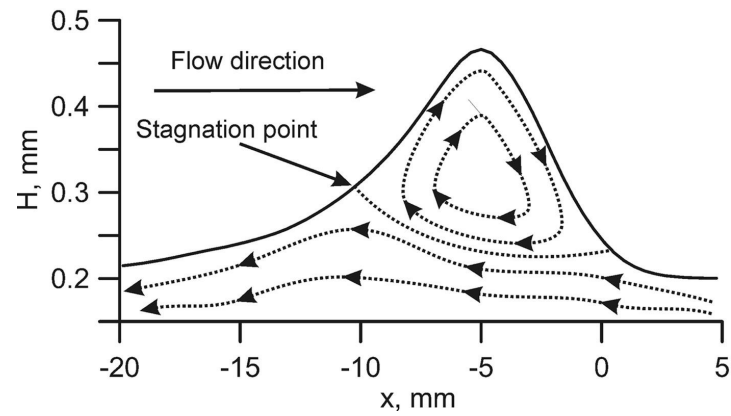
(c) Re-circulation zone

Figure 2.3: Spatio-temporal measurements of film thickness evolution. (a) Film structure in the presence of disturbance and ripple waves, (b) Film structure in the presence of slow and fast ripples on the back slope of disturbance waves, (c) Mean shape of disturbance wave with inception regions for slow and fast ripple waves (adapted from [4]).

20

of fact, for flow with very high gas-shear rate, the two-dimensional waves are disrupted almost immediately after the inlet point. With this, the rate of liquid entrainment also substantially increases.

For both of the aforesaid mechanisms, disturbance waves are found to grow in size and velocity with downstream distance, which are promoted with increasing liquid Reynolds number [39, 40, 86]. It is suggested that this occurs through the coalescence of large amplitude waves that are moving at different velocities. Interestingly, once the coalescence takes a place of two waves where one moves slower than the other, the resultant larger wave will travel at the velocity of the faster wave [68]. Similarly, the frequency of disturbance waves are found to increase with gas and liquid Reynolds numbers, with the former having a greater effect. With further propagation from the inlet, disturbance waves start to attain circumferential coherence which is attributed to the periodic circumferential velocity variations within the liquid film [91, 190]. The amplitudes of these disturbance wave structures are reported to be approximately five times the size of the mean film thickness [186], but not uniform circumferentially due to the presence of other waves, i.e., ripples, which is visible from spatio-temporal field measurements of the film thickness shown in Figure 2.3(a). Once the sufficient amplitude of the disturbance wave is attained (at least three times higher than the base film thickness), the aforementioned re-circulation zone within the bulk of the wave is generated (see Fig. 2.3(c)). The presence of such zones were also confirmed using particle image velocimetry in the study of Zadrazil and Markides [185]. These may be generated due to differences between the interfacial velocity and the wave velocity, where the former being higher [28].

A combination of all the above disturbance wave characteristics is found to be the key driver of liquid entrainment into the gas core [11, 36, 177]. As noted earlier, with downstream propagation of disturbance waves, coalescence events between large amplitude waves occur. Hall Taylor et al. [68] and Wilkes et al. [176] explained that at a moment of such events, liquid entrainment occurs due to imbalance of the resultant mass and momentum of the coalesced waves.

The occurrence of liquid entrainment due to fast-moving ripple waves (touched upon earlier) was shown to be one of the major reasons for high fraction of liquid entrainment in the gas-core due to the high frequency of these waves. The evidence of such events (using high-speed imaging) were demonstrated in the work of Woodmansee and Hanratty [177] for co-current gas-liquid flows in the horizontal rectangular duct. Analogous observations were reported by Pham

et al. [129] for vertical gas-liquid flows. Two entrainment mechanisms that these fast-ripples follow are 'ligament break-up' and 'bag break-up' [11]. In the former case, a liquid jet elongates in front of the disturbance wave until it disintegrates and atomises into droplets. In the latter case, a liquid bag is formed which also expands in front of the disturbance waves until ruptures resulting in formation of droplets that are smaller but faster than those produced via the former mechanism [38].

Ishii and Grolmes [80] expanded our understanding about liquid entrainment by experimentally demonstrating three additional mechanisms by which it takes place: (1) 'bubble burst', (2) 'liquid impingement', and (3) 'wave under-cutting'. These mechanisms were later confirmed using PLIF method applied in the study of downwards gas-liquid annular flows by Zadrazil et al. [186]. Many of the foregoing liquid entrainment mechanism lead to entrainment of gas in the form bubbles inside the liquid film. These are found to be located with higher concentration in the region beneath the disturbance wave than in the base film [71, 174]. The bubble sizes and their volumetric density was also shown to increase with gas and liquid Reynolds numbers [71, 174, 186]. Mostly, the bubbles travel slower than the disturbance waves, lagging into the base film. If the bubble size is small enough, it may travel interchangeably either in the base film or beneath the disturbance wave, potentially undergoing coalescence with other bubbles. If the bubbles are of larger size than the base film, it is likely to burst resulting in generation of fine droplets directed into the gas-core [71].

With increasing gas Reynolds number, the concentration of the entrained droplets was shown to increase, while the size distribution shifts towards larger sizes [12]. In the presence of turbulent gas flows, smaller sized droplets are found to travel at higher velocities than the larger droplets due to greater effect exerted by the high gas-shear rate [11]. The entrained liquid droplets in the gas-core can be redeposited back onto the liquid film via two different mechanisms, 'direct impact' and 'diffusion', which are dictated by the droplet momentum and size [81]. If the droplets are moving at high momentum and are sufficiently large at which their trajectory is not influenced by the gas stream, redeposition will likely undergo the former mechanism. Otherwise, if droplets are small in size and momentum, their motion is observed to be random due turbulent gas stream, and thus, redeposition will follow via the latter mechanism. Interestingly, the redeposition process by 'direct impact' mechanism can generate secondary droplets as it was shown in the experimental measurements by Che and Matar [33].

The complexity of the annular flows is also altered by the inherent presence of various addi-

tives in the bulk fluid that can reduce the surface tension e.g., surfactants. Relevant industrial applications are found in the production of natural gas, where surfactants are utilised as foaming agents that are injected at the bottom of the reservoir, which delays the process of liquid loading permitting the extraction of additional and substantial quantities of gas prior to closing the well [96]. The surfactants affect the gas-liquid flow in the well tubing such that the minimum gas velocity required to lift the liquid to the surface decreases. To date, the effect of surfactant on annular flows, particularly in large-scale applications, has not been thoroughly studied. Only a handful of works are present in the literature that focused their efforts on studying falling film flows and especially annular flows in the presence of soluble surfactant and its effect on hydrodynamics and phenomenological events.

Amongst few works on gas-liquid flows with surfactant, Nimwegen et al. [170, 171] studied the effect of the surfactant on upwards annular flows. Using high-speed imaging, they report that for surfactant-laden flows the morphology of the film becomes more complex relative to the surfactant-free flows due to formation of the foam. In the presence of the foam, the entrainment of large liquid droplets into the gas core is supressed. For flows at low liquid and high gas Reynolds numbers foam is observed to exist only at the crests of small waves (large waves are reported to be absent at these flow conditions). Once the liquid flow rate increases (at high gas Reynolds number), formation of foam across the surface, including on the crests of large waves, and entrainment of bubbles of various sizes within the bulk, especially beneath the large waves, is observed. Similar work was also conducted by Furukawa et al. [61] and Matsuyama et al. [114] which investigated the effect of reduced surface tension (relative to the clean water) on the liquid film structure in vertically upwards gas-liquid annular flows. It was reported that the reduction in surface tension led to a decrease in the frequency of large waves, while the roughness of the base film increased. As a result of higher base film roughness, the interfacial friction force also increased, explaining the observed increase in the mean velocity of the base film, and thus, a reduction in the measured mean film thickness. In contrast, the amplitude of large waves was observed to decrease when the surface tension is reduced, while the mean velocity was affected insignificantly. Moreover, a number entrained bubbles inside the bulk film and liquid droplets into the gas-core increases. Analogous results were also reported in the work by Rivera et al. [136] on upwards gas-liquid annular flows.

The study by Setyawan et al. [147] investigated the effect of surface tension on the wave velocity and wave frequency of gas-liquid annular flows in a horizontal pipe. The work reports a decrease in wave frequency with decreasing surface tension, while the wave velocity decreases

(increases) for low (high) superficial liquid velocity upon reduction in surface tension. At a mild flow conditions and using PLIF method, Bobylev et al. [26] studied the effect of soluble surfactant on gravity-driven water falling films on a vertical plate with liquid Reynolds number below 50 (laminar flow). The study shows that the amplitude of the waves depends on the liquid Reynolds number and the surfactant concentration. Particularly for the latter case, while a stabilising effect by the surfactant is observed at low to moderate concentrations, the opposite (destabilising) effect is observed in the presence of surfactant at large concentrations. Moreover, at high surfactant concentration the absence of initial evolution of two-dimensional waves and immediate development of three-dimensional waves is observed.

2.2   Experimental measurement techniques

Due to the aforementioned reasons in the previous section, accurate measurement of primary flow quantities, such as the film thickness and entrainment rate, can enhance significantly engineering design and optimisation efforts. A variety of measurement tools have been developed for testing and real-time data acquisition in annular flow, which have been investigated actively throughout the last several decades using multiple intrusive and non-intrusive methods including resistive and capacitive impedance, ultrasonic, electromagnetic, and optical methods.

Intrusive methods, such as conductivity-based (i.e., resistive impedance based) wire sensors, measure electrical conductivity of the fluid in contact with the wires, which can be transformed into void fraction information. Early on, Barnea et al. [16] investigated the flow pattern transition of two-phase flows in pipes of 25.5 mm and 51.0 mm inner diameter (ID) and orientations spanning the range from 0° (horizontal) to 90° (downwards) using conductivity probes. Such probes were sufficient to evaluate flow regime transitions and the results were used to generate predictive mathematical models. While easy to use, these sensors are invasive and are also incapable of resolving thin films and small bubble sizes (typically smaller than the wire size). Karapantsios et al. [86] measured the film thickness using a series of parallel-wire conductance probes in a Plexiglass pipe of 50 mm ID. Despite the good agreement reported with previous efforts of e.g., Chu and Dukler [39], Takahama and Kato [157], the authors claimed that the use of thinner wires, which increased the spatial resolution, required greater amplification and introduced errors due to electronic noise. More recently, Andreussi et al. [9] employed an array of conductivity-based wire probes in an effort to increase the spatial resolution of the sensors and performed measurements in near-horizontal pipe configurations of 80 mm ID with films in

the range of 4-20 mm. They reported good agreement with published data for centimetric films, but highlighted uncertainties greater than 20% for thinner films, which were still an order of magnitude thicker than those typical of gas-liquid annular pipe flows.

Non-intrusive methods such as capacitance sensors record void fractions by exploiting the difference in permittivity between the fluid phases. These sensors measure the capacitive impedance which can be correlated back to void fraction and film thickness. Although these methods are capable of high-frequency acquisition ($> 10^4$ Hz), their designs exhibit limitations in spatial resolution, similarly to the conductivity-based sensors mentioned in the previous paragraph, particularly in situations when the gas core moves eccentrically, or fine reconstruction of the interface is required. Webb and Hewitt [175] studied the characteristics of downwards annular two-phase flow in tubes of 31.8 mm and 38.2 mm bore. They used a capacitance probe to measure the film thickness, and produced a flow regime map, which showed good agreement with of Telles [161]. Recently, Belt et al. [18] performed film-thickness measurements in upwards air-water annular flows in a pipe of 50 mm ID and used a series of capacitance probes. The reported time-averaged film-thickness values were only 10% smaller than those predicted by theory.

Optical non-intrusive methods have been developed in more recent years. Laser-induced fluorescence (LIF) techniques for film-thickness measurements are based primarily on measuring the intensity of the fluorescent light emitted by a tracer present in the liquid phase. Zadrazil et al. [186] performed a thorough investigation using planar LIF (PLIF) to generate two-dimensional slices of downwards annular flows. The imaging angle was set at 90° perpendicular to the laser-sheet (PLIF90). Häber et al. [67] performed ray-tracing simulations, and revealed an overestimation in PLIF-derived instantaneous film-thickness measurement of up to 30% (in PLIF90), primarily caused by total internal reflection and refraction effects about the gas-liquid interface. Nevertheless, as discussed in the study by Charogiannis et al. [32], PLIF90 measurements are also prone to a second source of error, associated with the imaging angle used, resulting in underestimation of the film thickness. Interestingly, the two errors were found to be of same order, but with opposite effects, which almost cancelled each other out during the time-averaging process in falling films (resulting in measurements close to theoretical predictions). This behaviour remains unclear for gas-sheared annular flows. Cherdantsev et al. [37] developed a variation of LIF, named brightness-based LIF (BBLIF), which employs the Beer-Lambert law and small imaging angles ($\sim 15°$), to combat such problems. BBLIF was found to be reliable in smooth/flat film regions, but exhibited larger errors in rough and/or thick films.

Correction methods based on ray-tracing simulations for classical PLIF measurements have been since proposed by various researchers e.g., Häber et al. [67], Cherdantsev et al. [37], Xue et al. [183], Xue et al. [182]. These methods, however, are not robust being underpinned by several assumptions, and are validated primarily against 'idealised' smooth falling films, even though downwards gas-liquid annular flows are typically cirumferentially non-uniform, with enhanced wave activity and entrainment. To obviate the need for *a posteriori* corrections, Charogiannis et al. [32] proposed a new experimental method, 'Structured-PLIF' (S-PLIF), which unlike the aforementioned methods, does not depend solely on light intensity but also on the direction of the light path. The light is structured in an alternating dark/bright pattern, which reveals the change in the direction of the light when it hits the gas-liquid interface. The S-PLIF method was demonstrated in falling-film flows in a pipe at two different imaging angles, 70° and 90° to the laser-plane, and a good measurement accuracy was found with the former ($< 10\%$ deviations compared to theoretical predictions).

2.3 Applications of fluorescent surfactants in fluid mechanics

The surface active agents (known as surfactants) possess versatile characteristics that are effectively used in incredibly diverse range of industrial applications spanning from large-scale technological processes such as enhanced and improved oil recovery [42, 154, 160], remediation of contaminated soil [93, 120], pharmaceutical [63, 119, 141] and food industries [95] to development and production of small-scale technologies such as semiconductors [58, 83, 134] and nanomaterials [75, 78, 105, 106].

The unique versatility of surfactants arises from their amphipathic structure that contains both lyophobic and lyophilic groups (weak and strong attractions for the solvent, respectively). These molecules will have higher potential energies at the interface, particularly in the gas-liquid system, relative to a system's interior. Taking a specific example of an air-water system, this allows surfactants to adsorb onto the fluid-fluid interface primarily forming a monolayer with their amphipathic structure orientating accordingly to the property of fluids. Surfactant molecules will start to replace some of the water molecules in the surface where the forces of attraction between water molecules and surfactant are less than the force between water-only molecules, which results in marked reduction of the surface free energy. This brings multiple practical benefits which have been widely recognised specifically in the field of fluid mechanics.

To elaborate further, the work by Kovalchuk et al. [94] has extended our understanding in the spreading performance achieved by a close study on wetting and adsorption kinetics of surfactant solutions on hydrophobic substrates. They experimentally showed that the solution spreading rate is dependent on the surfactant adsorption rate which subsequently determines the rate of Marangoni flow (due to the gradient of surface tension) i.e., the higher the Marangoni flow, the faster the surfactant-enhanced spreading. This was supported by earlier work of Karapetsas et al. [88] who numerically showed that the fast spreading is attained by high Marangoni stresses that are induced close to the droplet edge due to continuous surfactant adsorption from liquid-air to solid-liquid interface. The rate of fast spreading will depend on sorption kinetics that determines the replenishment of surfactant at liquid-air interface and maintaining high Marangoni stresses. Similarly, Aytouna et al. [10] investigated experimentally the effect of surfactant on droplet impact on hydrophobic surfaces. Their measurements have showed that the substantial increase in wetting of surfactant-laden drops relative to the clean water-only drops can significantly reduce the retraction dynamics, thus, preventing droplets partly or even fully bouncing off the surface. Later, Che and Matar [33] explored similar impact of droplets but on liquid films in the presence of surfactants (in drops and/or films) using high-speed imaging. They highlighted several important observations related to the presence of Marangoni stresses and its effect on inertial, gravitational and viscous forces. To name just few, Marangoni flow leads not only to faster propagation of capillary waves (created due to surfactant-laden droplet impact with clean water film) but can also rigidify the film surface promoting droplet bouncing (in surfactant-laden film case) instead of coalescence in the water-water configuration. Within the same field, Liao et al. [99] closely investigated how soluble surfactants affect the deformation and breakup dynamics of stretching liquid bridges. Briefly, with the use of high-speed imaging they found that surfactants not only have a thinning effect on the liquid bridges but also significantly alters the limiting length and the break shapes.

The pronounced effects of surface tension gradients due to the presence of surfactants were also found in more complex air-water flows. Early works, for example, of Temper and Riet [169] and Miles [115] showed from a theoretical perspective that surfactants are capable of damping surface waves. Experimental evidence produced by Davies and Vose [45] confirmed that capillary waves can in fact be damped by different types of surface films. More recently the effect of surfactants on falling film flows was investigated by Karapetsas and Bontozoglou [87]. Performing a linear stability study of a film flowing down a solid substrate in the presence of soluble surfactant has shown that a particular level of solubility, bulk concentration and sorption kinetics of the surfactant can have different stabilising effects due to the presence of varying

Marangoni stresses. Similar findings were also reported by Hu et al. [76] and Katsiavria and Bontozoglou [89]. The above observations were confirmed experimentally by Georgantaki et al. [64] for gravity-driven film flows of aqueous solutions of soluble surfactant. Only recently the group of Bobylev et al. [26] have started to use more advanced experimental techniques that gave a deeper insight about the effect of soluble surfactants on interfacial wave dynamics. Preparing aqueous solutions containing fluorescent rhodamine dye and non-fluorescent surfactant they used laser induced fluorescence (LIF) technique to acquire data of instantaneous film thickness distribution of falling films for a range of different surfactant concentrations. They concluded that damping of waves occurs for low to medium surfactant concentrations, whereas at large concentrations the damping effect is reversed, and the growth of interfacial waves was observed.

While all of the above works have significantly developed our understanding about multiphase flow dynamics in the presence of surfactants, direct experimental evidence of surfactant transport would allow us to make further advancements within this complex field. In fact, attempts of such measurements have already been demonstrated by a number of different groups where surfactant exhibiting fluorescent properties were used allowing to track concentration gradients that are responsible for surfactant effects linked to Marangoni stresses. One of the first ones to perform direct measurements of surfactant concentration simultaneously with small surface disturbances was Fallest et al. [57]. In their experimental setup a laser profilometer and a digital camera was used to conduct spatio-temporal measurements of fluorescent insoluble surfactant (lipid) spreading. Despite having attained concentration gradients along the interface, they found significant discrepancies relative to various well-established models, which may have arisen due to limitations of the optical measurement technique used to obtain quantitative information. Similar measurements using the same fluorescent lipid were done by Strickland et al. [155] who also performed spatio-temporal measurements of dynamic surface concentration and the amplitude of gravity-capillary waves. The progress was made by finding good agreement with some of the numerical results in literature (e.g. Matar et al. [112]), but was noted by authors that further developments are required as the damping factors for waves and surfactant concentration in certain locations of the waves do not agree with literature. Several advancements were also made using liquid-liquid configurations. Chen et al. [34] have synthesised a polyether-based surfactant and used confocal microscope to track surfactant transport by means of fluorescence along the interface of oil-water droplets in a pipe flow as well as liquid-infused surfaces undergoing shear-driven drainage. Subsequently, not only that they conducted direct visualisation of surfactant dynamics along the liquid-liquid and solid-liquid interfaces, but also managed to track surface

concentrations from fluorescence intensity recordings, and hence, couple this with Marangoni stresses due to the presence of concentration gradients. Their findings were reported to be in good agreement with literature. Nonetheless, some limitations, as outlined by the authors, need to be resolved e.g., accuracy of fluorescence intensity quantification, depth of field for confocal microscope and direct measurement of dynamic surface tension. In the work by Dong et al. [49] a LIF technique was used to capture surfactant concentration distribution along the interface of a coalescing aqueous drop with a mixture of organic-aqueous at a flat interface. Using the same fluorescent surfactant as Fallest et al. [57] and Strickland et al. [155] they managed to find very good agreement with literature and verify previously reported numerical predictions of various coalescence dynamics.

All in all, a gradually increasing interest in the use of fluorescent surfactants to study various multiphase flow problems is evident. However, the majority of fluorescent surfactants are not soluble in sustainable and safe solvents such as water and are typically prepared in volatile and/or toxic solvents such as chloroform, methanol, acetonitrile, DMF or DMSO. While this can be sufficient for certain types of experiments, at the same time this creates barriers for certain other experimental setups where, for instance, an alternative solvent is required for direct comparison with theoretical works or use of large quantities of solvent is needed for large-scale experiments making validation a rather difficult task. Hence, specific fluorescent surfactants are required to make further advancements within this field. Recently, such amphiphile molecules have been synthesised by McWilliams et al. [152]. Widely used fluorescent dyes Rhodamine B and Eosin Y were attached (as head-groups) to aliphatic chain of different lengths (6 to 16 carbon atoms). Their respective critical micelle concentration (CMC) and optical properties were measured. As it was shown, these surfactants suffer from rather low surface activity due to small reduction in surface tension ($\sim$62 mN m^{-1} for C12 tail-group), and the corresponding CMC values range between 0.7 mM and 3 mM, depending on the head-group and chain length. Apart from that, these type of amphiphile molecules hold a significant potential as candidates for further research developments due to sufficient solubility in water. It is worth noting that fluorescent surfactants (typically called fluorescent probes) in the reported works above have been previously extensively used in various other fields such as biology, chemistry and medical science (see an example of a review by Xu and Xu [181]).

2.4 Concluding remarks

In-depth literature review has emphasised on the up-to-date progress made by experimental efforts on gas-liquid flowing films. Attention was drawn mostly to the flows in pipes with vertical orientation, with few exceptional works that studied horizontal flows as well as vertical planar flows. Moreover, key differences between surfactant-free and surfactant-laden flows were identified particularly on the the effect of the surfactant on flow characteristics (i.e., film thickness, amplitude, frequency and velocity of interfacial waves, and gas and liquid entrainment). The wide-scope of experimental studies that were performed over several decades, have employed different measurement techniques. The application of these techniques (including advanced optical diagnostics) to study film flows were also reviewed. Lastly, the scope of applications of fluorescent surfactants in relevant fluid dynamics and their potential for advancement is evaluated.

Chapter 3

Methods

Contents

This chapter contains a description of all the materials, experimental details, apparatuses and techniques used to characterise fluorescent surfactant and to study behaviour of thin annular flows. Firstly, methods used for detailed characterisation of the fluorescent surfactant are presented. A theoretical model to describe surfactant transport is also developed. Secondly, a large-scale experimental set-up along with the optical (S-PLIF) and capacitance measurement techniques used to study downwards annular flows over a range of flow conditions at the absence and presence of surfactant are described in detail. A comparison of S-PLIF and capacitance measurements is provided for a range of flow conditions in the absence of surfactant.

3.1 Materials

Anionic SDS surfactant (sodium dodecyl sulfate, $M_r = 288.38$ g mol^{-1}) was purchased from Sigma-Aldrich (GC grade, purity $\geq$99.0 %). DAF surfactant (5-dodecanoylaminofluorescein, $M_r = 529.63$ g mol^{-1}) was purchased from Thermo Fisher Scientific (HPLC grade, purity $\geq$99.0 %). Rhodamine 6G fluorescent dye ($M_r = 479.01$ g mol^{-1}) was purchased from Sigma-Aldrich (dye content $\geq$99 %). NaOH pellets (sodium hydroxide, $M_r = 40.00$ g mol^{-1}) was purchased from Sigma-Aldrich (analytical grade, purity $\geq$99.9 %). AF dye (5-aminofluorescein, $M_r = 347.32$ g mol^{-1}) was purchased from Sigma-Aldrich (HPLC grade, purity $\geq$98.3 %). DA surfactant (dodecanoic acid, $M_r = 200.32$ g mol^{-1}) was purchased from Sigma-Aldrich (GC grade, purity $\geq$99.0 %). MeOH (methanol, $M_r = 32.04$ g mol^{-1}) was purchased from Sigma-Aldrich (HPLC grade, purity $\geq$99.9 %). ACN (acetonitrile, $M_r = 41.05$ g mol^{-1}) was purchased from VWR Chemicals (HiPerSolv HPLC LC-MS grade, purity $\geq$99.9 %). H$_3$PO$_4$ (phosphoric acid, $M_r = 97.99$ g mol^{-1}) was purchased from Sigma-Aldrich (BioUltra grade, $\geq$85 %). All reagents were used as received without further purification. All samples in the experiments were prepared using ultra-pure deionised water (UPDI) with resistivity of 18.2×10^6 Ωcm and pH of 6.6 at 25 °C obtained from Elga Centra R200 water purification system.

3.2 Spectrofluorometer and LIF measurements

Fluorescence measurements were performed using a Horiba FluoroMax-4 spectrofluorometer system. A quartz cuvette of 1 cm pathlength was used and the temperature was at 25 °C. Data acquisition was performed using FluoroEssence v.3.5 software. The slit width was set to 2 nm for both emission and absorption which ensured sufficient signal and prevention of signal saturation. Integration time was set to 0.5 s to attain good signal-to-noise ratio. Three solutions of DAF were prepared at equal concentrations of 18.9 µM but different pH values (= 11, 12 and 13). Samples were weighted using AND BM-252 micro analytical balance. Liquid dispensed using Thermo Scientific Finnpipette F2 single-channel pipettors. Solutions were placed on stirring plates (Heidolph MR Hei-Tec) for continuous mixing using a magnetic bar at 170 rpm and constant temperature of 25 °C for 20 min prior to measurements.

A range of concentrations (4–195 ppm) of DAF solutions at pH 11 placed in a quartz cuvette of 1 cm pathlength at 25 °C were also tested using the LIF method to determine threshold concentration at which the effect of self-quenching occurs. We use a frequency-doubled Litron

Nd:YAG 532 nm laser and form a sheet of 1 mm thickness by connecting LaVision sheet generation optics (optical laser arm, collimator, and 10° divergent lens). A mid-speed camera (LaVision VC-Imager Pro-HS 500) equipped with Sigma 105 mm f/2.8 lens and a 533 nm notch filter (FWHM = 17 nm) was positioned at 90° angle to the wall-normal. Camera recording was performed with a spatial resolution of $64.9\ \text{px}\,\text{mm}^{-1}$ at a frequency of 100 Hz. Recorded images were subsequently processed using a MATLAB algorithm where an area with a short pathlength (20 px) was chosen with a minimal (<1 %) variation in fluorescence intensity across the path length.

3.3 Ultra-high performance liquid chromatography measurements

The stability of DAF molecule under alkaline conditions was evaluated using ultra-high performance liquid chromatography (UHPLC) analysis. An in-house devised procedure has been implemented. A solution of pH 14 was prepared by dissolving 0.63 mg of DAF (weighted using AND BM-252 micro analytical balance) in 16.50 mL of 1 M NaOH (liquid dispensed using Thermo Scientific Finnpipette F2 single-channel pipettors). A sample vial with solution was covered with foil to protect it from light and subsequent photodecomposition. The solution was placed on a stirring plate (Heidolph MR Hei-Tec) for continuous mixing using a magnetic bar at 170 rpm and constant temperature of 25 °C. Samples of 500 µL were taken using 0.45 µm PTFE syringe filter at different reaction times (see Table 3.1) and diluted with 500 µL of mobile phase (ACN:H_3PO_4 (1%)/H_2O, 40:60% v/v). A Nexera XR UHPLC system coupled with a UV-Vis absorption detector was used in all measurements. A Shim-pack XR-ODS column (internal diameter = 3.0 mm, length = 50 mm) was used with a constant temperature of 50 °C. A total flow rate was set to $0.5\ \text{mL}\,\text{min}^{-1}$ and a data acquisition of 10 min at sampling frequency of 12.5 Hz. Absorption data at 225 nm were acquired for all analytes with high signal-to-noise ratio. Instrument control, data acquisition and analysis were performed using LabSolutions software (v. 5.89).

3.4 Langmuir-Blodgett trough measurements

DAF molecule is readily soluble in alcohols, thus, a solution of methanol/DAF at concentration of 4.72×10^{-4} M was prepared by weighing 1 mg of DAF (AND BM-252 micro analytical balance) and dissolving in 4 mL of methanol (liquid dispensed using Thermo Scientific Finnpipette F2

Table 3.1: Sampling time periods for UHPLC analysis.

Time period	Reaction time (min) at pH = 14
t_1	23
t_2	80
t_3	155
t_4	225
t_5	290
t_6	1365

single-channel pipettors). Isotherm measurements at the air-water interface were performed using Langmuir-Blodgett (LB) trough with Teflon edges (MicroTrough X, Kibron). The trough was fixed to a vibration-free optical table. The compression rate of the moving PTFE barriers was controlled through the FilmWare (v.3.62) installed on a computer and set to 8.250 mm min^{-1}. The compression rate was sufficiently slow so as not to produce hysteresis during the re-expansion with surfactant film. Initial effective area was 12272 mm^2. Surface pressure was measured using the Wilhelmy method with a wire rod (1.07 mm diameter and 20 mm length) at sensitivity of 0.01 mN m^{-1}.

Prior to each measurement, the trough and barriers were thoroughly cleaned using methanol followed by ultra-pure de-ionised (UPDI) water repeatedly three times. These were then dried using dry compressed air and placed back into the instrument. The wire rod was also cleaned several times using methanol and UPDI water followed by flaming with a butane welding torch to remove any organic contaminants. Each time the trough was filled with 35.0 mL $\pm$1 mL of UPDI water. The clean wire rod was placed back on the sensor and lowered vertically down until the tip penetrated through the water surface. The tip position was then adjusted to the water level to avoid buoyancy effect. The surface pressure was then calibrated by compressing the clean interface and ensuring that the surface pressure remains constant within 0.1 mN m^{-1} for at least 10 min. For larger surface pressures, the subphase surface was cleaned using a vacuum aspirator, and the barriers were then re-expanded and compressed again. When target surface pressure was attained, the surface pressure was set to zero state. The trough was closed within an acrylic case to avoid any surface contamination (e.g. by dust particles) and to minimise external perturbation of the system during the sample deposition process and data acquisition.

The spreading volume of 50 µL ($\pm$0.5 µL) were applied using microsyringe (Hamilton 84856) through an opening in the acrylic case. A time period of 30 min was given for the methanol to evaporate and for the surface pressure to stabilise (0.01 mN m^{-1}). Compression and surface pressure measurements were then initiated at room temperature of 21.0 °C ($\pm$0.2 °C) and hu-

midity of 36% (±1%). Once the measurements were completed, the acrylic cover was removed, and the liquid subphase was extracted using the aspirator. Cleaning of all instrument components was then repeated as per the above procedure, while the aspirator tip (glass) was replaced by a new one after each cleaning process.

3.5   Pendant drop measurements

Surface tension measurements were performed using the pendant drop method, fitting the Young-Laplace equation to an experimental image through computational routine performed via Krüss ADVANCE software (v.1.11). The experimental setup (Fig. 3.1) was comprised of key components: a camera, light source and a needle attached to a syringe. A Krüss DSA25 instrument integrated with a camera (160 fps at 1200 by 1200 px) and high-power monochromatic LED (470 nm dominant wavelength) was used. The syringe was clamped inside a software-controlled dispensing system. Stainless steel needles (Krüss NE45) of 1.80 mm (±0.01 mm) outer diameter were used. Prior to each measurement, the capillary tip of the needle was positioned vertically (i.e. parallel to gravity) with the help of software edge-detection feature in order to avoid incurring error in the magnification factor. The majority of the needle was placed inside a glass cuvette through a sealable cover (Krüss SC30) fixed to the sample stage below the dispenser. The temperature inside of the jacketed cuvette was controlled by continuous flow of water at 25.0 °C (±0.1 °C) through a combined refrigerated and heating bath circulator (Grant LT ecocool 150). Relative humidity of 44% (±4%) and temperature was measured using digital hygro-thermometer with remote probe (Extech 445715) just outside of the cuvette cell. Data were recorded at 10 fps for the first 10 seconds and at 1 fps afterwards. A droplet for each measurement was generated of consistent volume ≈ 6.6 µL (±0.3 µL), which provides a sufficiently large Bond number (> 0.2) and Worthington number (> 0.2) for accurate and sensitive measurements for the given setup as demonstrated in a detailed study by Berry et al. [22]. The image focus and the brightness of the background illumination have been adjusted accordingly for correct droplet profile recognition (as per manufacturer's calibration procedure).

The measured surface tension of UPDI water at pH of 6.3 using this technique is $71.78 \, \text{mN m}^{-1}$. This agrees well with accurate values presented by Vargaftik et al. [173] at 25 °C. The surface tension of alkaline (NaOH) solution is $71.44 \, \text{mN m}^{-1}$. This is in good agreement with the work by Beattie et al. [17], where they have shown that the surface tension of water is almost independent of pH values between 1 and 13. A marginally lower recorded value is most likely due

to small amount of impurities present in the dissolved NaOH pellets.

To validate the pendant drop method with surfactant, we firstly performed measurements using SDS at pH of 6.3 and compared the acquired data to literature values. The measured equilibrium surface tension values for a range of concentrations (0.2–14 mM) are in excellent agreement with other works such as Casandra et al. [30] and Woolfrey et al. [178] (see Fig. 3.2). The CMC value was found to be ≈ 8.8 mM which also agrees with the aforementioned publications.
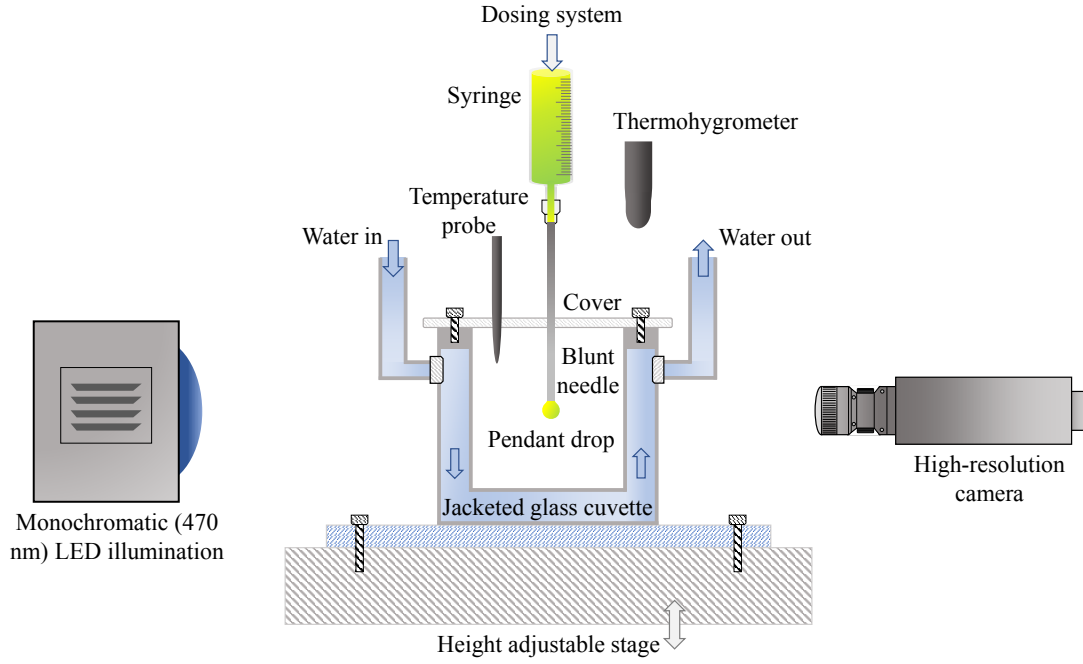
Figure 3.1: Schematic drawing of the pendant drop tensiometer apparatus.

3.6   Model formulation for surfactant transport

The transport of surfactant molecules towards the fluid interface and away from it is determined by the diffusive flux and kinetic flux as shown by Chang and Franses [31]. The former describes surfactant exchange between the fluid bulk phase (far away from the interface) and the sublayer (region close to the interface). The latter describes the exchange between the sublayer and the fluid-fluid interface. These rates of exchange can be determined using Arrhenius framework - the Frumkin equation of state, which is employed in our study:

$$\frac{d\Gamma}{dt} = \beta_{\mathrm{a}}\Gamma_{\infty}C_{\mathrm{s}}(1 - \Gamma/\Gamma_{\infty}) - k_{\mathrm{d}}\Gamma e^{K\Gamma/\Gamma_{\infty}}, \tag{3.1}$$
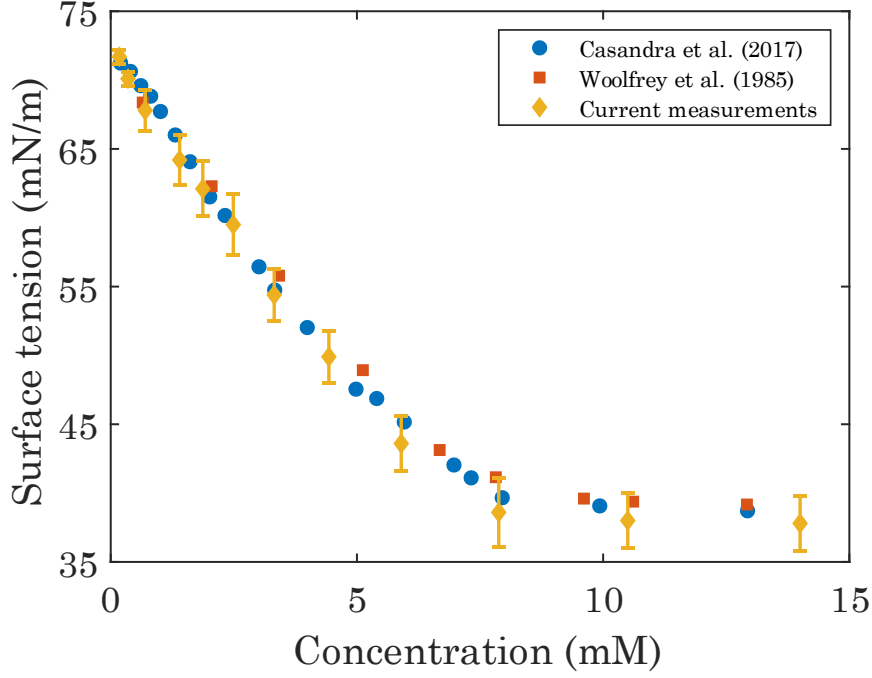
Figure 3.2: Comparison between the measured equilibrium surface tension for air/SDS aqueous solutions and published data.

where Γ is the surface concentration, t is time, β_a is the adsorption rate parameter, Γ_∞ is the maximum packing concentration, C_s is the sublayer concentration, k_d is the desorption rate constant, and K is a parameter that accounts for linear variation of the activation energy for desorption on Γ. The product of β_a and Γ_∞ ($\beta_a\Gamma_\infty$) is defined as the adsorption rate constant, k_a, and is given by:

$$k_a = k_a' \exp\left(\frac{-E_A(0)}{R_G T}\right), \tag{3.2}$$

and k_d is given by:

$$k_d = k_d' \exp\left(\frac{-E_D(0)}{R_G T}\right), \tag{3.3}$$

where k_a' and k_d' are the kinetic coefficients for adsorption and desorption, respectively, and $E_A(0)/R_G T$ and $E_D(0)/R_G T$ are the activation energies for adsorption and desorption (divided by the thermal energy $R_G T$), respectively, both evaluated for a clean interface. One of the ways to determine kinetic rate constants and bulk diffusion coefficients was demonstrated by Pan et al. [128] where they conducted a series of experimental measurements involving clean interface adsorption with soluble surfactant to directly compare with the modelling predictions of surface tension relaxations. For this, the change of surface concentration over time, $\Gamma(t)$, was predicted as a function of the surfactant transport parameters by modelling the kinetic exchange using the above Eq. 3.1, and the bulk diffusive and convective transport with the convective-diffusion equation to obtain the dynamic surface tension, $\gamma(\Gamma)$, from the EoS (see Eq. 4.2 in Section 4 for

further details).

The importance of the effect of surfactant bulk concentration, C_0, on the time scales over which kinetic and diffusion controls dominate the relaxation was also closely investigated by Pan et al. [128] using scaling arguments. Assuming individual maximum rates of adsorption by diffusion control and kinetic control, a ratio of characteristic times (τ_{diff} and τ_{kin}, respectively) to achieve an equilibrium monolayer (when C_0/α is very large) is given by:

$$\Phi^2 = \frac{\tau_{\mathrm{diff}}}{\tau_{\mathrm{kin}}} = \frac{\Gamma_\infty^2 \beta_\mathrm{a}^2}{D_\mathrm{b} k_\mathrm{d} \left[C_0/\alpha\right]}, \tag{3.4}$$

where D_b is the bulk diffusion coefficient and $\alpha = k_\mathrm{d}/\beta_\mathrm{a}$. This shows that the characteristic time scale for diffusion becomes shorter than the time scale for kinetic adsorption as bulk concentration increases. We demonstrate this in Section 4. Such an effect is also evident in different types of surfactants including short chain alcohols (Fainerman and Miller [56]), Triton X-100 (Lin et al. [101, 100]) and bolaform (Bleys and Joos [25]).

We set up the model as per Pan et al. [128] work who studied (polyethoxylated) surfactant exchange at an air-water interface. We assume that the pendant drop is a sphere of radius r_d with bulk farfield concentration C_0. During surfactant adsorption to the clean interface we assume that the surfactant transport is spherically-symmetric with no convective flow. The bulk concentration ($C(r,t)$) is uniform as per C_0, and the surface concentration, ($\Gamma(t)$), is equal to zero at $t=0$. We nondimensionalise kinetic equation 3.1 by scaling the surface concentration, Γ, by Γ_∞ ($\theta = \Gamma/\Gamma_\infty$), the sublayer concentration by the concentration scale α ($C_\mathrm{s}^* = C_\mathrm{s}/\alpha$), and time by the scale for bulk diffusion $(\Gamma_\infty/\alpha)^2/D_\mathrm{b}$ ($\tau = tD_\mathrm{b}(\alpha/\Gamma_\infty)^2$) giving us:

$$\frac{d\theta}{d\tau} = \kappa(C_\mathrm{s}^*(1-\theta) - \theta \exp\left(K\theta\right)), \tag{3.5}$$

where κ is the ratio of the bulk diffusion time scale ($(\Gamma_\infty/\alpha)^2/D_\mathrm{b}$) to the kinetic scale for desorption k_d^{-1}: $\kappa = k_\mathrm{d}((\Gamma_\infty/\alpha)^2/D_\mathrm{b}) = \beta_\mathrm{a}\Gamma_\infty^2/(D_\mathrm{b}\alpha)$. To solve Eq. 3.5 we need to determine the sublayer concentration, C_s^* as a function of τ. For this, we implement the Laplace transformation of the Ward and Tordai equation to express the sublayer concentration as a convolution integral of the change in the surface concentration with time:

$$\begin{aligned} C_\mathrm{s}^*(\tau) = \frac{C_0}{\alpha} &- \frac{2}{\sqrt{\pi}} \int_0^{\sqrt{\tau}} \frac{\mathrm{d}\theta}{\mathrm{d}\tau'} \mathrm{d}\sqrt{\tau-\tau'} \\ &+ \frac{1}{b} \int_0^\tau \frac{\mathrm{d}\theta}{\mathrm{d}\tau'} \exp\left((\tau-\tau')/b^2\right) \mathrm{ercf}\left(\frac{1}{b}\sqrt{\tau-\tau'}\right) \mathrm{d}\tau', \end{aligned} \tag{3.6}$$

where erfc(x) denotes complimentary error function and $b = (\alpha r_{\rm d})/\Gamma_\infty$. The value for b is equal to 0.38 for all simulations, which corresponds to our experimental conditions. The model requires the simultaneous numerical solution of the differential equation Eq. 3.5 and the integral equation Eq. 3.6. To improve the robustness of the algorithm, we opt to split the problem into the solution of two one-dimensional root-finding steps. Given initial values $\theta(\tau_n)$ and $C^*_{\rm s}(\tau_n)$, and a timestep $\Delta\tau_{n+1}$, we proceed as follows: (1) guess a value for $\theta_g(\tau_{n+1})$; (2) guess a value for $C^*_{\rm s,g}(\tau_{n+1})$; (3) calculate $\mathrm{d}\theta/\mathrm{d}\tau_g|_{\tau_{n+1}}$ using Eq. 3.5 and the guesses for the new timestep; (4) calculate $C^*_{\rm s}(\tau_{n+1})$ from the guess of the derivative, using Eq. 3.6; (5) compare $C^*_{\rm s}$ with the initial guess; if the values differ by more than a prescribed tolerance, repeat from (2); (6) calculate $\theta(\tau_{n+1}) = \mathrm{d}\theta/\mathrm{d}\tau|_{\tau_{n+1}}\Delta\tau_{n+1}$; (7) compare $\theta(\tau_{n+1})$ with the guess; if values are different, repeat from (1) with a new guess; (8) using Eq. 4.2, calculate the surface tension at time τ_{n+1}. The guesses are obtained through Brent's method for root-finding, and the value of the integral in Eq. 3.6 is obtained with the trapezoidal rule, with an analytical integration of the timestep close to the singularity $\tau = \tau'$. In order to efficiently cover several orders of magnitude of time-scales, we utilize a timestep growth $\Delta\tau_{n+1} = 1.2\Delta\tau_n$. We nondimensionalise surface tension γ by:

$$\gamma^* = \frac{\gamma(\tau) - \gamma_{\rm e}}{\gamma_{\rm c} - \gamma_{\rm e}}, \tag{3.7}$$

where $\gamma_{\rm e}$ is the equilibrium surface tension for the equilibrium surface coverage $\Gamma_{\rm e}$ (and C_0) as per Eq. 4.1 and Eq. 4.2. The value of γ^* is specified by varying values of κ and C_0/α.

3.7 Large-scale flow facility

The large-scale experiments to study downwards co-current gas-liquid (air-water) annular flows are carried out in an in-house designed and commissioned facility as shown in Fig. 3.3. Previous experimental campaigns in this facility were carried out by others ([186, 32, 37, 185]).

The test-section consists of a vertical $\sim$ 5 m long fluorinated ethylene propylene (FEP) pipe of internal radius, $R = 16.2 \pm 0.2$ mm. The material of the test-section is selected so that it matches the refractive index of the liquid phase and hence enables near-wall optical measurements [179, 77]. Water is circulated using a centrifugal pump (Grundfos CRN5-5), which is connected to a variable autotransformer (Carroll and Meynell). By adjusting the supplied voltage a desired flow rate is achieved and measured using a flow meter (Fluidwell F110) with an accuracy of $\pm 0.5\%$ across the full scale. Annular flows are generated in the test-section by
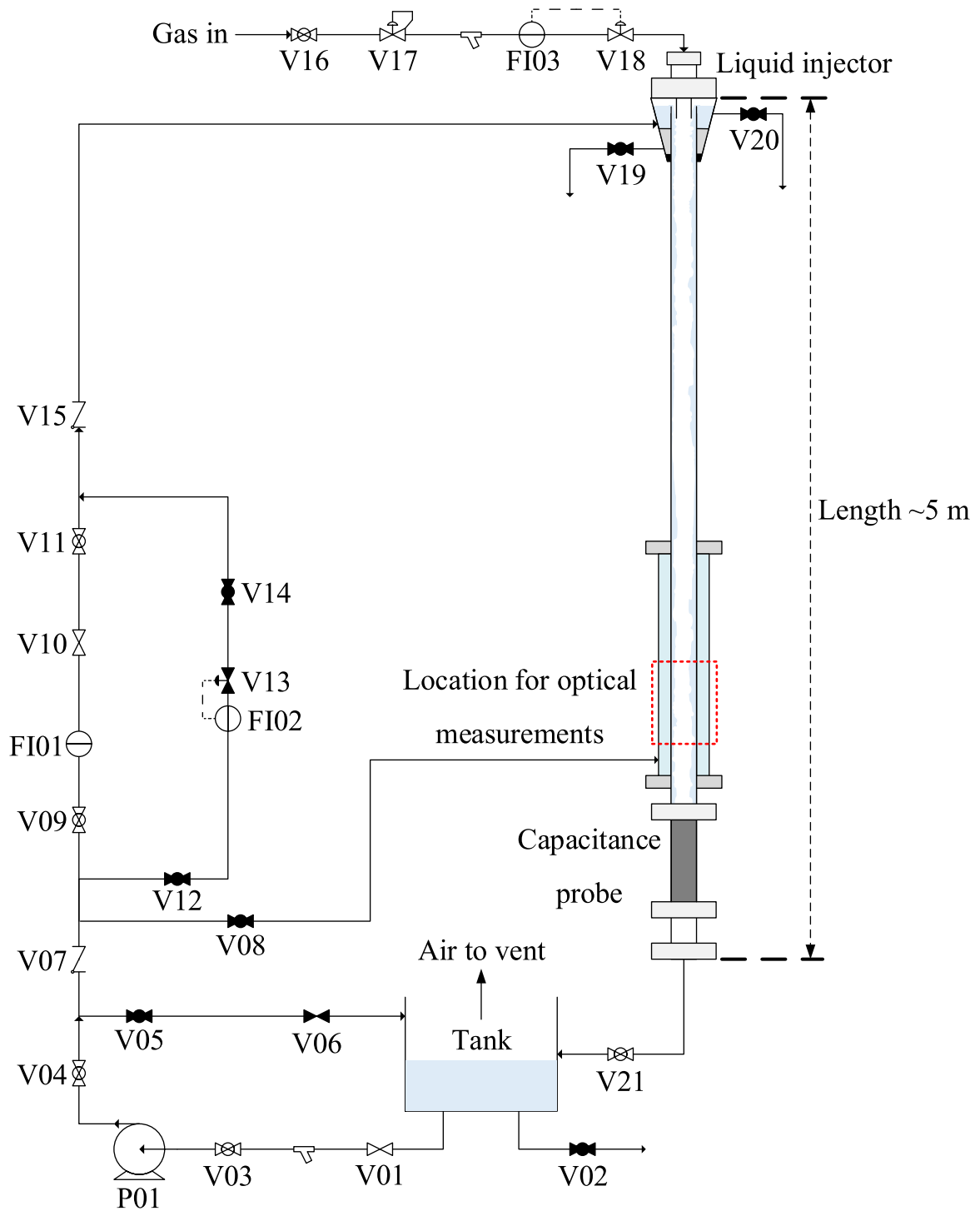
Figure 3.3: Piping and instrumentation diagram of the downwards co-current gas-liquid annular flow facility employed in this work.

supplying water to an in-house manufactured injector; details of its design are provided by [190]. The gas phase is provided from the compressed air central supply at approximately 5.5 ± 0.5 bar. Prior to entering the test-section the air is passed through a filter-regulator (Norgren Olympian), and a mass flow rate controller (Mass-Stream M14) with an accuracy of $\pm 0.2\%$ across the full scale. After the fluids leave the test-section they pass through a open-top gas-liquid separator discharging the air from the system into atmosphere.

The range of the investigated flow conditions (see Table 3.2) is selected so that it allows for comparisons with available literature data. The Reynolds number for the gas phase (air), Re_G, is calculated based on the assumption that the gas occupies the whole internal cross-sectional area of the pipe, $A = \pi R^2$, which can be justified due to the negligible volume occupied by the thin liquid film. The corresponding gas superficial velocity is defined by $u_\mathrm{s,G} = Q_\mathrm{G}/A$, resulting in $Re_\mathrm{G} = 2u_\mathrm{s,G}R/\nu_\mathrm{G}$, where ν_G is the kinematic viscosity of air, which is equal to 1.55×10^{-5} m s^{-2} at 25 °C. The Reynolds number for the liquid phase (water), Re_L, is calculated based on the bulk-averaged film velocity, approximated as $\langle u_\mathrm{s,L} \rangle = Q_\mathrm{L}/(2\pi R \langle h \rangle)$, where $\langle h \rangle$ is the time-averaged film thickness. Thus, $Re_\mathrm{L} = \langle u_\mathrm{s,L} \rangle \langle h \rangle / \nu_\mathrm{L}$, where ν_L is the kinematic viscosity of water, which is equal to 8.94×10^{-5} m s^{-2} at 25 °C. As the film thickness and velocity are not known *a-priori*, Re_L is essentially taken to be four times smaller than the liquid Reynolds number based on the liquid superficial velocity and the pipe diameter in accordance with previous work of our research group [186, 32, 185]. The Re_G is varied between 0 (falling films) and 40000 with increments of ($Re_\mathrm{G} =$) 10000, while Re_L between 500 and 1375 with increments of ($Re_\mathrm{L} =$) 125 (Table 3.2).

3.8 Optical measurements

A novel in-house developed S-PLIF method was used in the present study (as per earlier work of Charogiannis et al. [32]), and the schematic of the optical arrangement is shown in Fig. 3.4. The optical laser-based measurements are performed at $118D$ ($\sim$ 3.8 m) downstream of the annular film formation point to eliminate flow development effects. The development of the flow for a similar range of flow conditions was investigated in the same experimental facility in earlier work, e.g., An et al. [8]. It was demonstrated that the velocity of the disturbance wave reaches a near-constant value as the wave approaches a downstream distance of about 3.5 m. For the non-surfactant case, fluorescent dye Rhodamine 6G was dissolved in the UPDI water at a concentration of 4.2×10^{-4} mM. For the surfactant case, DAF solution at a concentration

Table 3.2: Flow parameters investigated.

F_G L min^{-1}	F_L L min^{-1}	$Q_\mathrm{G} \times 10^{-3}$ m^3 s^{-1}	$Q_\mathrm{L} \times 10^{-3}$ m^3 s^{-1}	$u_\mathrm{s,G}$ m s^{-1}	$u_\mathrm{s,L} \times 10^{-2}$ m s^{-1}	Re_G $\times 10^3$	Re_L
0.00	2.73	0.00	4.55	0.00	5.52	0	500
0.00	3.41	0.00	5.69	0.00	6.90	0	625
0.00	4.09	0.00	6.82	0.00	8.27	0	750
0.00	4.78	0.00	7.96	0.00	9.65	0	875
0.00	5.46	0.00	9.10	0.00	11.03	0	1000
0.00	6.14	0.00	10.23	0.00	12.41	0	1125
0.00	6.82	0.00	11.37	0.00	13.79	0	1250
0.00	7.50	0.00	12.51	0.00	15.17	0	1375
237.3	2.73	3.95	4.55	4.80	5.52	10	500
237.3	3.41	3.95	5.69	4.80	6.90	10	625
237.3	4.09	3.95	6.82	4.80	8.27	10	750
237.3	4.78	3.95	7.96	4.80	9.65	10	875
237.3	5.46	3.95	9.10	4.80	11.03	10	1000
237.3	6.14	3.95	10.23	4.80	12.41	10	1125
237.3	6.82	3.95	11.37	4.80	13.79	10	1250
237.3	7.50	3.95	12.51	4.80	15.17	10	1375
474.6	2.73	7.91	4.55	9.59	5.52	20	500
474.6	3.41	7.91	5.69	9.59	6.90	20	625
474.6	4.09	7.91	6.82	9.59	8.27	20	750
474.6	4.78	7.91	7.96	9.59	9.65	20	875
474.6	5.46	7.91	9.10	9.59	11.03	20	1000
474.6	6.14	7.91	10.23	9.59	12.41	20	1125
474.6	6.82	7.91	11.37	9.59	13.79	20	1250
474.6	7.50	7.91	12.51	9.59	15.17	20	1375
711.8	2.73	11.89	4.55	14.39	5.52	30	500
711.8	3.41	11.89	5.69	14.39	6.90	30	625
711.8	4.09	11.89	6.82	14.39	8.27	30	750
711.8	4.78	11.89	7.96	14.39	9.65	30	875
711.8	5.46	11.89	9.10	14.39	11.03	30	1000
711.8	6.14	11.89	10.23	14.39	12.41	30	1125
711.8	6.82	11.89	11.37	14.39	13.79	30	1250
711.8	7.50	11.89	12.51	14.39	15.17	30	1375
949.1	2.73	15.82	4.55	19.19	5.52	40	500
949.1	3.41	15.82	5.69	19.19	6.90	40	625
949.1	4.09	15.82	6.82	19.19	8.27	40	750
949.1	4.78	15.82	7.96	19.19	9.65	40	875
949.1	5.46	15.82	9.10	19.19	11.03	40	1000
949.1	6.14	15.82	10.23	19.19	12.41	40	1125
949.1	6.82	15.82	11.37	19.19	13.79	40	1250
949.1	7.50	15.82	12.51	19.19	15.17	40	1375

of 0.114 mM and pH of ~ 8 was used. It is worthy of note that the initial pH of NaOH/DAF solution is likely to decrease throughout the experiment forming sodium carbonate, which should not have an effect at the concentration employed for large-scale experiments. To closely match the refractive index of the pipe material and to minimise optical distortion due to its cylindrical shape, an acrylic optical correction box is installed on the periphery of the FEP pipe and filled with UPDI water. We employ a frequency-doubled Litron Nd:YAG 532 nm and LaVision sheet generation optics (10 ° divergent lens, collimator and optical laser arm) to form a sheet of approximately 1 mm thickness. The laser-sheet is positioned at a 30° angle ($\pm$ 1°) to the streamwise (flow) direction and is passed through a Ronchi ruling of 10 cycles/mm that is attached to the outside wall of the correction box resulting in formation of required structured light pattern, as shown in Fig. 3.4(b).

(a) y-z view

(b) x-y view
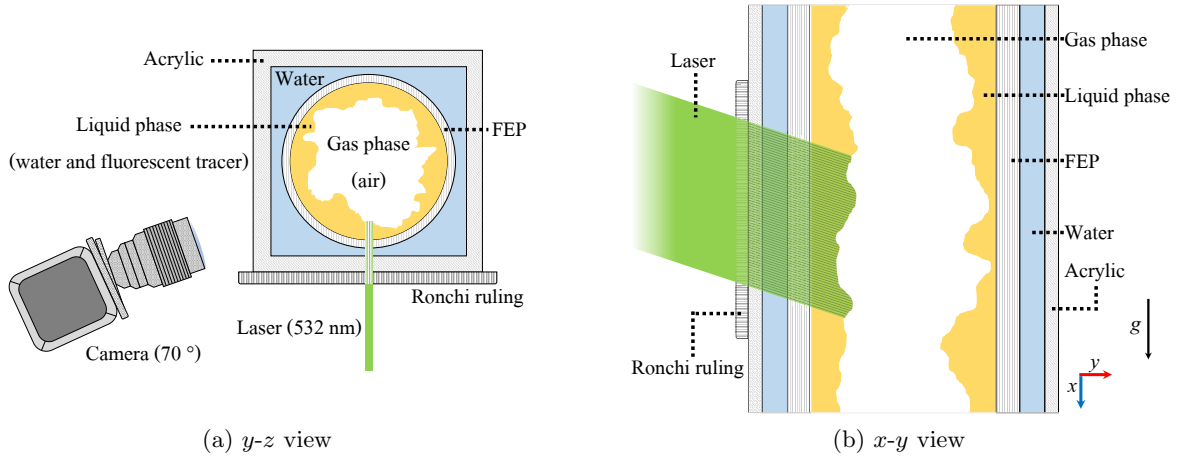
Figure 3.4: Schematic illustration of the optical arrangement used in the large-scale experiments.

We use an 8-bit mid-speed camera (LaVision VC-Imager Pro-HS 500) equipped with a Sigma 105 mm f/2.8 lens, and either a 540 nm long-pass filter or a 533 nm notch filter (FWHM = 17 nm) for the dye-only or surfactant case, respectively. The camera is positioned at a 70 ° angle to the wall-normal, as shown in Fig. 3.4(a). The imaging angle has been selected based on the past findings by our research group on falling films [32], which details how PLIF-based measurements of circumferentially non-uniform ('rough') films performed typically at 90° suffer from underestimation of the actual film thickness, as the wavy film obscures the measurement region of interest (referenced as 'Type-II' errors by [32]). The camera recording frequency is set at 100 Hz. Each experimental flow condition is recorded for 20 s.

The image analysis procedure steps followed to obtain spatially resolved film-thickness information with the S-PLIF method are shown in Fig. 3.5 and are detailed below:

- Image correction (distortion effects due to the imaging angle) and calibration is performed by recording reference images with a custom made graticule target located inside a water-flooded pipe (see example image in Fig. 3.5(a)). The spatial correction algorithm of DaVis v.10.0 (LaVision) is used (Fig. 3.5(b)). The spatial resolution is 15.4 µm/pixel, the total field of view spans 1295×961 pixels^2 or 20×14.8 mm^2, and the standard deviation of fit for the camera is equal to 0.77 pixels.

- The images are eroded over 15×15 pixel^2 areas to artificially enhance the laser-light modulation and increase the signal-to-noise ratio, as shown in Fig. 3.5(c). The filter achieved a significant increase in the intensity ratios between the bright and dark areas of the film from about 1.5 to 5.

- In each recorded image a considerable change in the direction of the incident laser light at the air-water interface is observed. The location of all such occurrences is tracked in each image by obtaining a reference image (with the pipe fully flooded with water and dissolved fluorescent tracer) and by using a digital image correlation (DIC) algorithm of DaVis to correlate (in the frequency domain; similarly to particle image velocimetry algorithms) between the reference and test images over 8×8 pixel^2 windows with 75% overlap. The resulting tracking resolution is 2 pixels or approximately 31 µm.

- The resulting displacement fields (Fig. 3.5(d)) are segmented with a global thresholding algorithm, binarising areas with a higher than 0.9 correlation values derived from the DIC algorithm (Fig. 3.5(e)). The boundaries of the binarised image are then captured, as shown in Fig. 3.5(f).
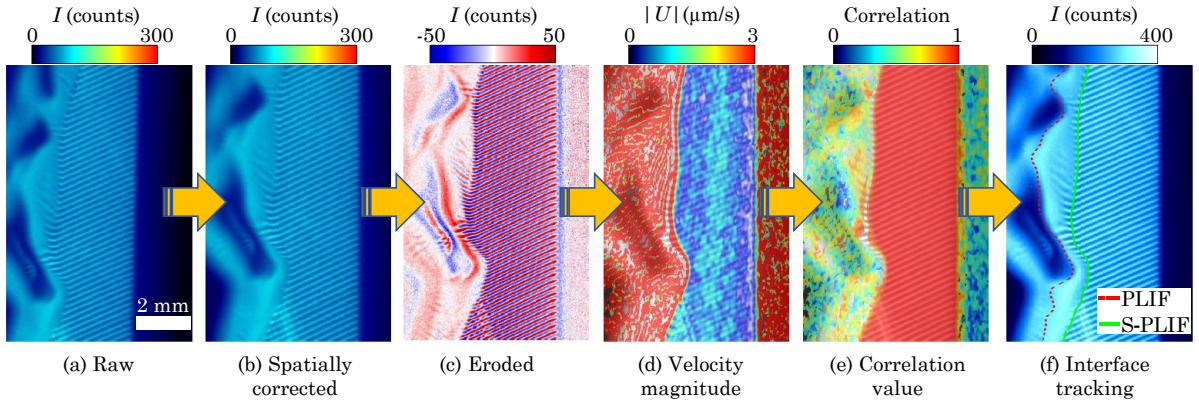
Figure 3.5: An illustration of the image analysis procedure followed to obtain spatially resolved film-thickness measurements with the S-PLIF method. The images are cropped here to focus on the area of interest. The flow direction is from top to bottom.

For each flow condition we select 20 film-thickness data points per image pair for the whole recording period consisting of 2000 images. Data points are selected at random and without re-placement, and results in standard errors of less than 1% (typical statistical convergence tests are shown in Appendix A). The calculated errors (by DaVis) in the correlation of the DIC algorithm based on the method proposed by [146] and are found to be negligible (approximately 2% of the velocity magnitude). We find the last subroutine of the image analysis procedure (Fig. 3.5(e) to (f)) is the most 'sensitive' part of the film-thickness measurement as the segmentation of the correlation fields requires a selection of a correlation value. The effect of the selection of different correlation values during the segmentation stage of a film-thickness measurement for a typical image is shown in Figure 3.6. We examine a range of correlation values (from 0.6 to 0.95) for all flow conditions and ~ 300 images, and find that values of 0.9 ± 0.025 provide the most accurate tracking of the interface. Based on this analysis, the worst-case relative error is estimated in the substrate film ($\langle h_{\mathrm{SPLIF,base}} \rangle$) $\sim 16\%$, in the mean film thickness ($\langle h_{\mathrm{SPLIF}} \rangle$) at $\sim 14\%$, and in the wave amplitude ($\langle h_{\mathrm{SPLIF,waves}} \rangle$) $< 6\%$. Larger errors may occur due to gas entrainment inside the liquid film particularly where air bubbles are located at the interface as shown in Fig. 3.7 for the larger bubble. Such events are neglected during the processing as they exhibit low correlation values, as demonstrated in Fig. 3.7(b). Areas with smaller bubbles entrained deeper in the bulk of the film, as for the small bubble in Fig. 3.7, are included in the processing as in such case it does not affect the correlation close to the gas-liquid interface.

(a) Image overlay

(b) Region of interest
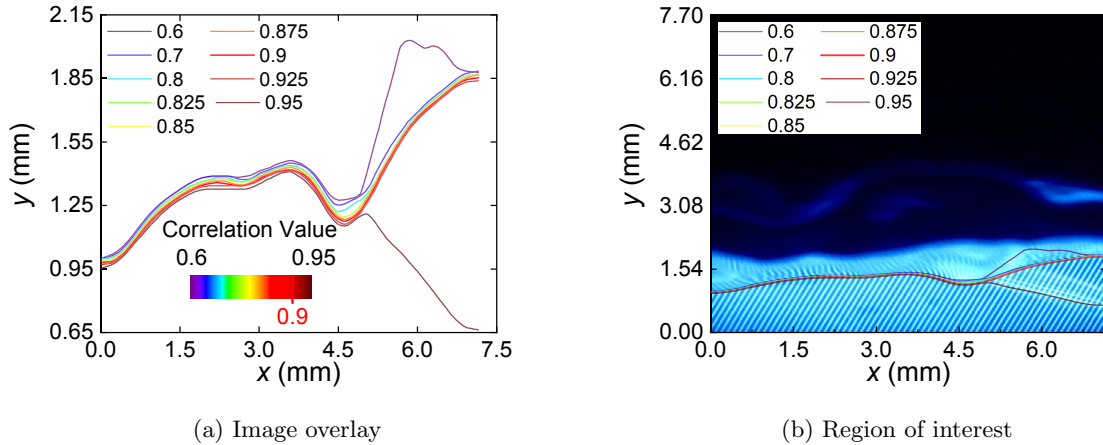
Figure 3.6: Sensitivity analysis performed for the S-PLIF film-thickness measurements and shown for different correlation values used in the segmentation subroutine. The flow direction is from left to right.

At the same time, we can use the images to obtain spatially resolved information of the film-thickness using the traditional PLIF method. The spatially corrected images are segmented with an adaptive image binarisation algorithm, which is based on local first order statistics. The

resulting PLIF-derived film-thickness information is shown for a typical image in Fig. 3.5(f). Similar methods have been developed for film-thickness measurements via PLIF [186, 32, 185]. Evidently, uncorrected instantaneous PLIF measurements overestimate the film-thickness due to reflection and refraction effects about the interface (Type-I errors referenced by [32]), which cause the fluorescent light to extend further inside the gas core. For this reason, the PLIF measurements are only shown here to illustrate the need for structured-light measurements and for holistic purposes (demonstrate the aforementioned Type-I error in such flows).
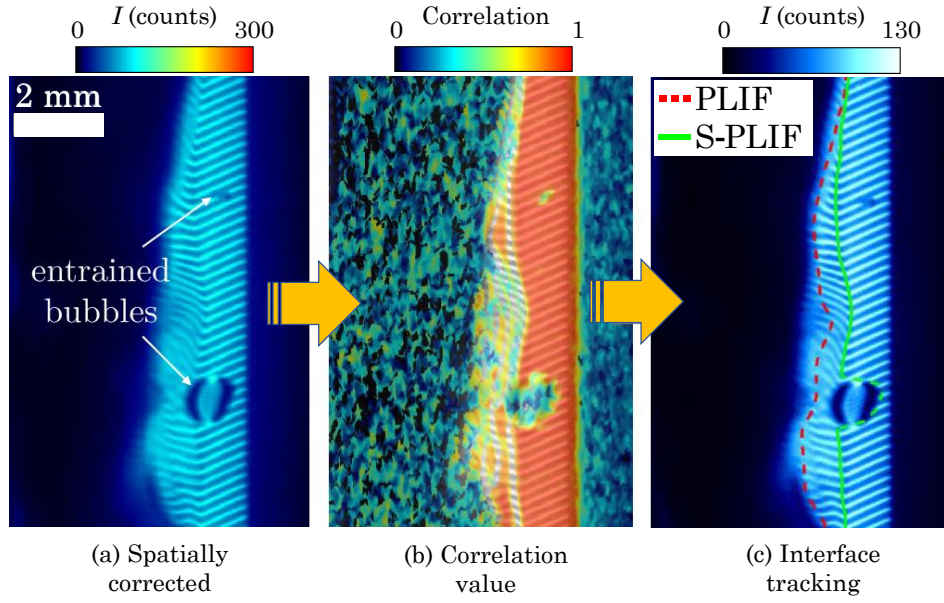
Figure 3.7: Interface tracking for liquid films with bubbles present at the interface and inside the film. The dotted green line denotes the 'false' interface around the bottom/downstream bubble (artifact). The flow direction is from top to bottom.

3.9 Capacitance measurements

The capacitance probe measurements are performed at $133D$ (~ 4.3 m) downstream of the water injection point. The capacitance probe consists of two 16 mm long electrodes where both are placed with an angle of 100° on opposite sides of the probe (see Fig. 3.8). Each electrode has a length in the circumferential direction of 2.78 cm and is located between two 'guard' electrodes (cf. Fig. 3.8) to achieve a more uniform electric field [135]. Flexible circuit material (R/Flex 3000 from Rogers Corporation) is used to form the inner tube wall of the sensor. The electrodes are etched out of the copper cladding on this circuit material. The thickness of the dielectric layer is 50 µm ($\pm 12.5\%$), with an electrical resistance of 10^{12} MΩ cm^{-1} and a relative permittivity of ~ 2.9 at 25 °C. After the electrodes are etched on the circuit material they are glued in

polymerising vinyl chloride (PVC) parts, which provide structural strength. These PVC parts are then placed into a stainless steel cylindrical casing, and the annular gap between the PVC and the casing are filled with an epoxy resin. Note that the casing is not shown in Fig. 3.8(a).

(a) Computer-aided design (CAD) of the capacitance probe construction.

(b) Close-up of the electrode arrangement with dimensions.
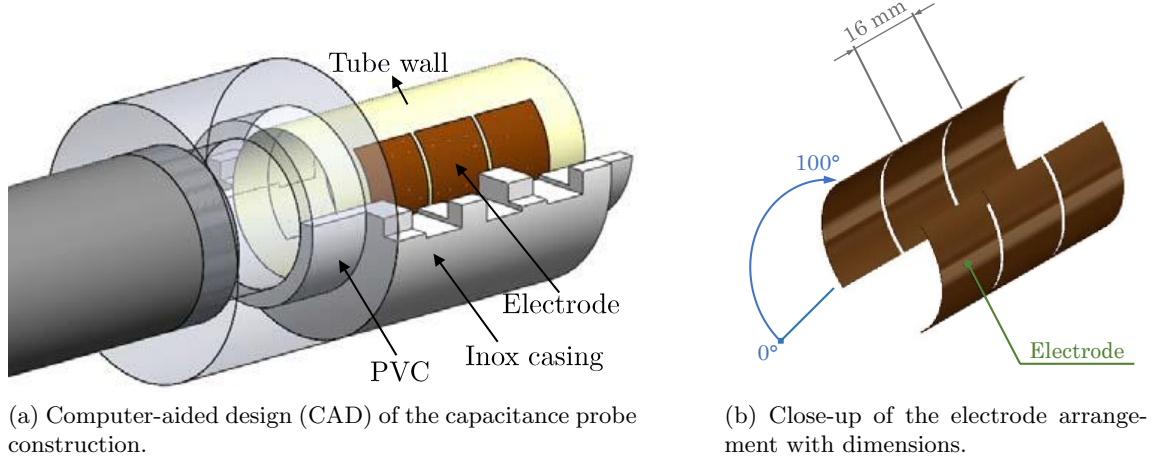
Figure 3.8: Schematic drawings of the capacitance probe and its key components.

The capacitance between the electrodes is measured using an in-house made transducer. The transducer design is based on the one proposed by Yang and Yang [184]. The output of the transducer is a voltage between 0 and 10 V, while its sensitivity is 1.16 $V\,pF^{-1}$ and the output accuracy is 4 mV. The voltage is logged with a data acquisition (DAQ) system. For measurement of each flow condition the capacitance time-trace is acquired for 20 s (identical to optical measurements) at a frequency of 10 kHz. A calibration procedure is followed to relate the capacitance measured to the film thickness. It has been found that the measured capacitance does not necessarily vary linearly with the void fraction [46], which can be attributed to the geometry (curvature) of the electrodes. This curvature imposes a non-homogeneous electric field. The capacitance will also change based on the spatial distribution of the gas and liquid phases.

Two approaches are conventionally used to calibrate the probe. The first one uses inserts to mimic the gas-liquid interfacial structure. The drawback of this approach is that the inserts are severely limited by their shapes and size, and they need to have similar dielectric constants as the fluid phases. The second technique uses finite element analysis simulations to determine the void fraction-capacitance relation. For each flow regime a simplified gas-liquid interfacial structure is assumed and subsequently simulated. Due to limitation of the former case, the latter approach, based on finite elements analysis, is followed. Technical details about the calibration

procedure can be found in the work by De Kerpel et al. [47] and Lecompte et al. [97], but a brief outline of the procedure followed is offered here for completeness:

- The flow structure of the annular films is simplified by assuming that the liquid flows between two concentric circles (i.e., as a smooth and circumferentially uniform film). Note that this void fraction thus defines a three-dimensional volume-averaged value.

- The dielectric constant for air is set to unity and for the liquid phase (UPDI water-only and NaOH/DAF solution to 80 [60, 116], while the dielectric constant for the FEP is set to 3.5 [127] and of the PVC to 2.1 [52].

- The resulting electric potential distribution for a typical annular flow with a film thickness of 1.62 mm is illustrated in Fig. 3.9(a), which shows that the gradient of the electric potential in-between the electrodes is very consistent. This consistency is achieved by the choice of the electrode-placement at 100°, which promotes the homogeneity of the electric field. As a result, the void fraction and the capacitance approaches a desired linear relation.

The FEA simulation is repeated for 20 evenly distributed steps between void fractions, ψ, of 0 and 1. The result of this calculation can be found in Fig. 3.9(a). The capacitance, C_p is normalised with its minimum ($C_{\mathrm{p,min}}$ for $\psi = 0$) and maximum value (C_max for $\psi = 1$). The normalised capacitance is taken as $\tilde{C}_\mathrm{p} = (C - C_\mathrm{min}) / (C_\mathrm{max} - C_\mathrm{min})$, and is determined by defining the calibration voltage (which in turn depends linearly on the capacitance) for C_min and C_max, i.e., $\psi = 0$ and 1, respectively. The relation between the void fraction and normalised capacitance is quasi-linear, as shown in Fig. 3.9(b). This calibration curve can effectively be used to determine a volume-averaged void fraction, and hence film thickness, h_CP, from the measured capacitance.

3.10 Comparison of optical and capacitance measurements

In order to better understand the capabilities of each measurement method applied in the large-scale experimental study (as explained above) and to evaluate differences between the two, film-thickness measurements were performed for a wide-range of flow conditions for the non-surfactant (clean) case. In addition to the flow rates outlined in Table 3.2, additional 24 flow conditions were added i.e., $Re_\mathrm{G} = 15 \times 10^3$, 25×10^3 and 35×10^3 for all 8 liquid flow rates. For
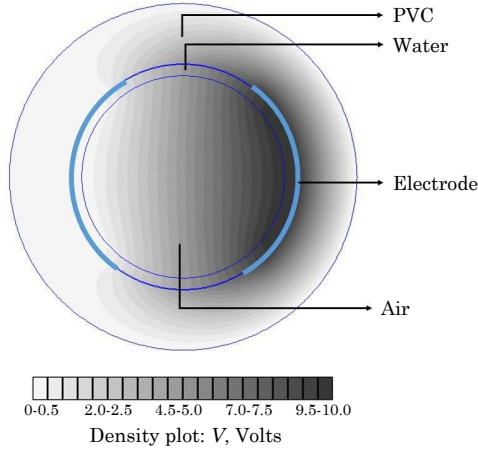
(a) FEA density plot of the voltage-field in the probe.
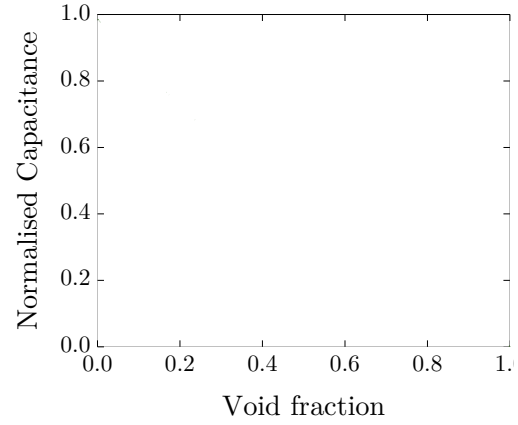
(b) Relation between the void fraction and the capacitance.

Figure 3.9: Capacitance probe calibration procedure.

comparative purpose, contour plots of the joint probability distributions of the film thickness, standard deviation, relative film roughness, base film thickness, wave amplitude and frequency of waves have been generated and are shown in Figures 3.10(a)-(f), respectively. Figure 3.10(a) shows a direct juxtaposition of the time-averaged film thickness (normalised with R) measured with S-PLIF and the capacitance probe. For $\langle h \rangle < 0.045R$, the S-PLIF measurements are approximately 10% higher than the capacitance probe, while the behaviour reverses at higher film thickness ($\langle h \rangle > 0.045R$), with the capacitance probe recording about 20% higher values than S-PLIF.

The comparison between the film roughness measured with each method portrays a clear pattern, shown in Figure 3.10(b). The S-PLIF-derived film roughness is consistently higher than that of the capacitance probe. This trend can be explained by the spatial-averaging effects inherent to the measurement principle of the probe (discussed in Section 3.9), which in turn inhibit large variations in the measured film thickness. The $\sigma_{\mathrm{rms}} = 0.0065R$ or 105 µm with a mean relative deviation measured for all data at 17% (with a maximum of 33 %). Figure 3.10(c) shows the overall capability of the two methods in measuring the mean and standard deviation of the film thickness, by illustrating the differences in the relative film roughness ($\sigma/\langle h \rangle$). The relative film roughness is measured higher by the S-PLIF method for all cases, for the aforementioned reasons, resulting in a 0.162 rms value (with a maximum of 0.369).

Figures 3.10(d) and (e) show comparisons of the base film thickness and the amplitude of the waves, respectively. The former is defined as $h_{\mathrm{base}} \leq 2 \times \langle h \rangle$, while the latter as $h_{\mathrm{wave}} = h > 2 \times \langle h \rangle$. The factor of 2 was selected after careful consideration of the data, and according to

previous experimental studies [186]. The comparisons of h_{base} and h_{wave} follow similar trends as those of $\langle h_{\text{base}} \rangle$ and σ_{h}. The frequency of the waves, f_{waves} is defined as the number of samples with $h > 2\times$ over the total. The joint probability distributions of it are shown in Fig. 3.10(f), does not a exhibit a clear trend. Both the probe and the optical methods are able to capture the higher frequency of waves present in the strongly gas-sheared films. Interestingly, the deviations between the capacitance probe and the S-PLIF measurements are found primarily at lower Re_{G}, i.e., not in the 'regular wave' regime. This may be due to the same spatial-averaging measurement effects inherent in the capacitance probe, which will become more apparent in Chapter 5 when the normalised film roughness measurements are compared.

Implementation and use of two methods simultaneously provides not only a comparison between the two, but also it stands as a compliment to each other by providing access to crucial data on the annular and interfacial film behaviour. For instance, whilst one method carries limitations in terms of inherent spatial-averaging effects (as in the case of CP), which may conceal fine details of the differences between surfactant-free and surfactant-laden flows, the other (S-PLIF) method provides local film thickness data that are highly accurate for all given flow conditions as demonstrated earlier in Section 3.8. That said, CP allows to obtain highly temporally-resolved measurements of the film thickness that permits to determine time-scale of interfacial wave activity in turbulent flows, as the ones used herein, while the S-PLIF system used for this study is not able to offer the acquisition of such data due to camera's technical limitations. Nevertheless, on the basis of reliable and statistically significant data that is collected using S-PLIF (owing to large amount of data points), it permits to elucidate the fine differences between surfactant-free and surfactant-laden flows using key flow characteristics that are most relevant to industrial practical applications, and to explain key fundamentals of gas-liquid annular flows, in agreement with literature, forming the basis of the present work.
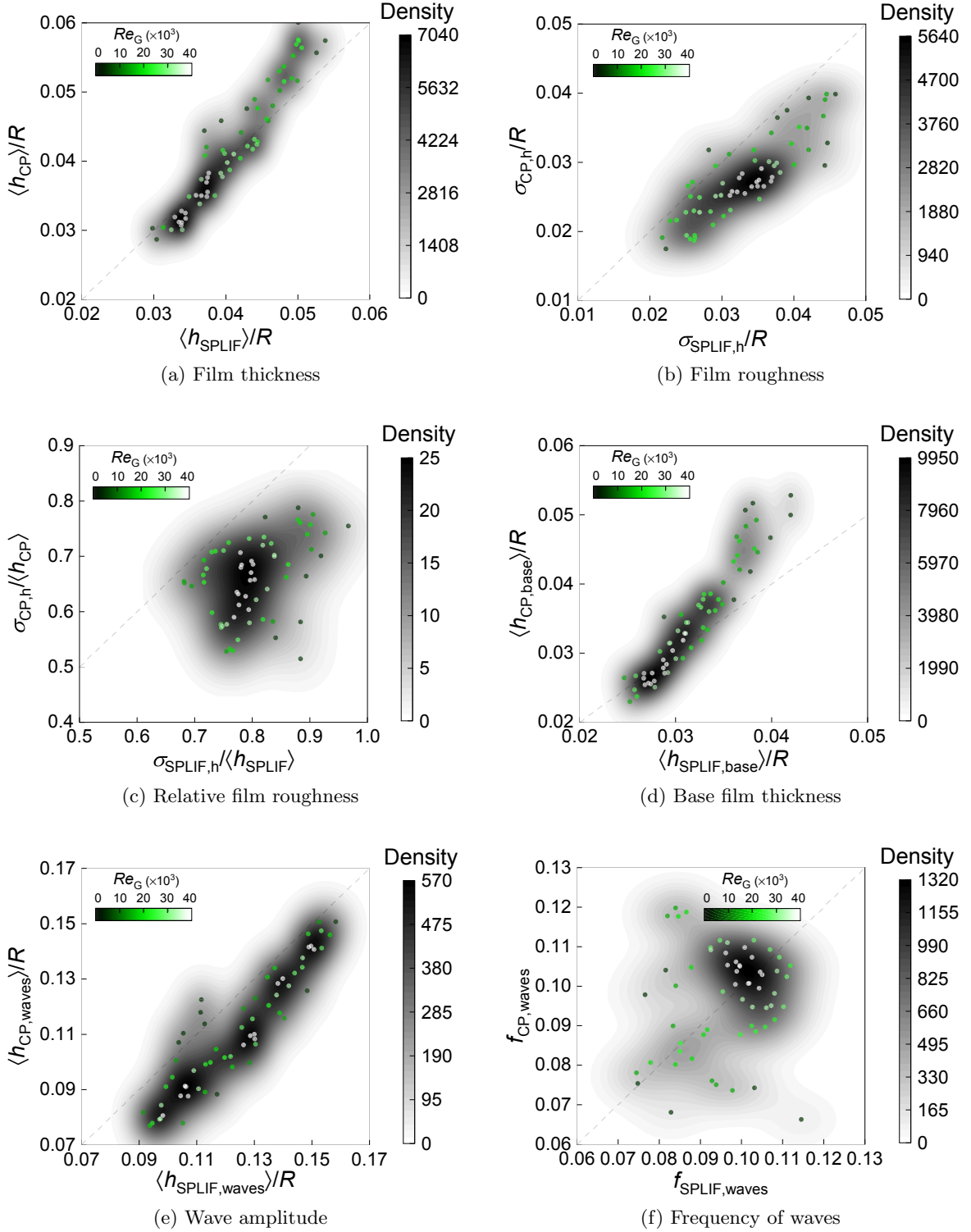
Figure 3.10: Contour plots of the joint probability distributions of the film-thickness measurements recovered with S-PLIF and the capacitance probe. The effect of the gas Reynolds number is shown by the data point fill color. Two 'outlier' data points have been removed from each figure.

Chapter 4

Surfactant characterisation

Contents

As discussed in the Literature review Chapter, pronounced effect of surface tension gradients due to the presence of surfactant were found in a wide-range of air-liquid and liquid-liquid systems. This was demonstrated in small-scale experiments (e.g. [33]), large-scale experiments (e.g. [26]) and from a theoretical perspective (e.g. [87]). Only several works in recent years have practically demonstrated that the actual surface tension gradients can be evaluated from direct optical measurements of surfactant concentration distribution along the fluid-fluid interface (e.g. [34, 49, 57, 155]). Tracking molecular concentration became feasible by exciting fluorescent lipids using a laser and recording its subsequent fluorescence with a camera. The obtained results have already helped to verify some numerical predictions and explain effects caused by Marangoni stresses ([34], [49]). However, all the fluorescent surfactants used to date in fluid dynamics applications have proven to be insoluble in safe and sustainable solvents such as water essentially limiting its usability. A vast range of aforementioned theoretical works as well as small- and large-scale experiments found in the literature have particularly focused on the study of air-water systems. Moreover, what is missing is the detailed characterisation of such fluorescent surfactants

(e.g. optical and transport properties) which would allow to better describe surfactant behaviour in various gas-liquid systems from a quantitative perspective and expand its usability. In order to fulfil these crucial areas, the previously mentioned DAF fluorescent surfactant (structure shown in Fig. 4.1) is analysed for its optical properties, molecular stability under alkaline conditions, behaviour as an insoluble monolayer, and its surface activity at an air-water interface as a water-soluble surfactant. A combination of different transport models are investigated in order to identify the type of control responsible for surface relaxation, and thus, the resultant surfactant transport rate constants are determined.
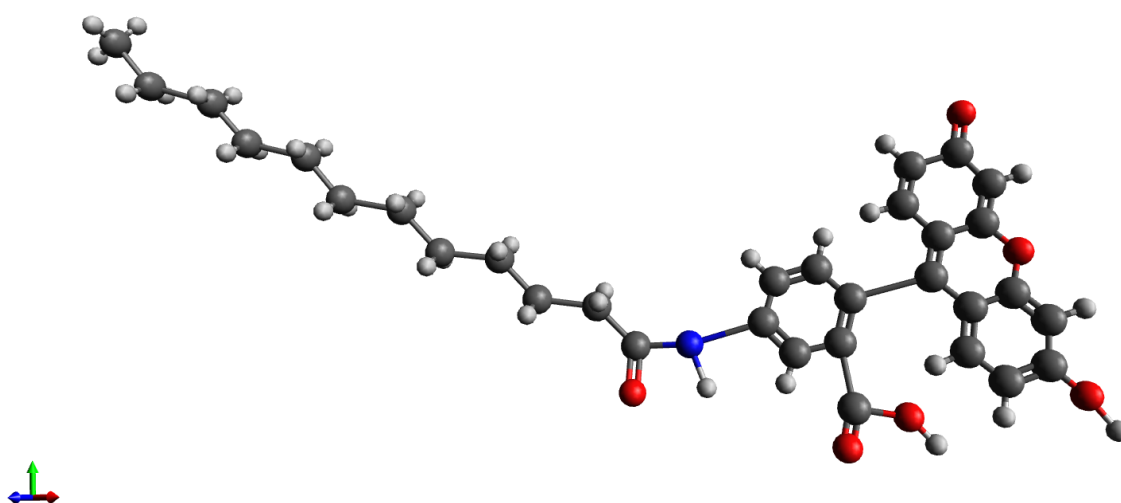
Figure 4.1: Visualisation of a model molecular structure of 5-dodecanoylaminofluorescein (DAF), where circles of different colours represent a particular atom (light grey = hydrogen; dark grey = carbon; red = oxygen; blue = nitrogen) and the lines connecting atoms represent single bonds (one line) and double bonds (double line). Displayed interatomic distances and angles are not strictly correct.

4.1 Optical properties of DAF

In this section, the light absorption and emission spectra of DAF molecule are analysed under various alkaline conditions using spectrofluorometer. DAF fluorescence is also measured as a function of its concentration using LIF method. This is required to determine the threshold concentration of self-quenching. The results will permit to design the optical measurement arrangement for the large-scale experiments.

Measurements show (Fig. 4.2) that individual peaks have remained constant at 467 nm and

517 nm for absorption and emission, respectively. Reducing the pH value from 13 to 11 increases the total intensity of absorption from a normalised value of ~ 55 to ~ 69. Similarly, the total intensity of emission also increases from ~ 36 to ~ 46, which is in agreement with literature [137, 104, 111]. At a fixed dye concentration (18.9 µM) this is a direct indication of self-quenching mechanism, where with an increase in pH the emission intensity first plateaus and then follows a gradual reduction past a certain threshold in pH value [121]. This can be due to the fact that structure of fluorescein (head-group) in aqueous solution can hold different prototropic forms i.e., neutral, cationic, anionic and dianionic [111, 137]. These forms are directly affected by the presence of ions in the solution (e.g., basic or acidic) which alters its light absorption and emission properties.

It is worth noting that for non-surfactant fluorescein dye as the pH of the solution decreases from basic to acidic the absorption intensity decreases, and the peak is blue-shifted. Likewise, emission spectrum starts to broaden towards infrared while the peak maintains constant [111, 137]. Due to high pH value for the current measurements, weak, yet similar behaviour is observed in Fig. 4.2, particularly between pH value of 13 and 11.
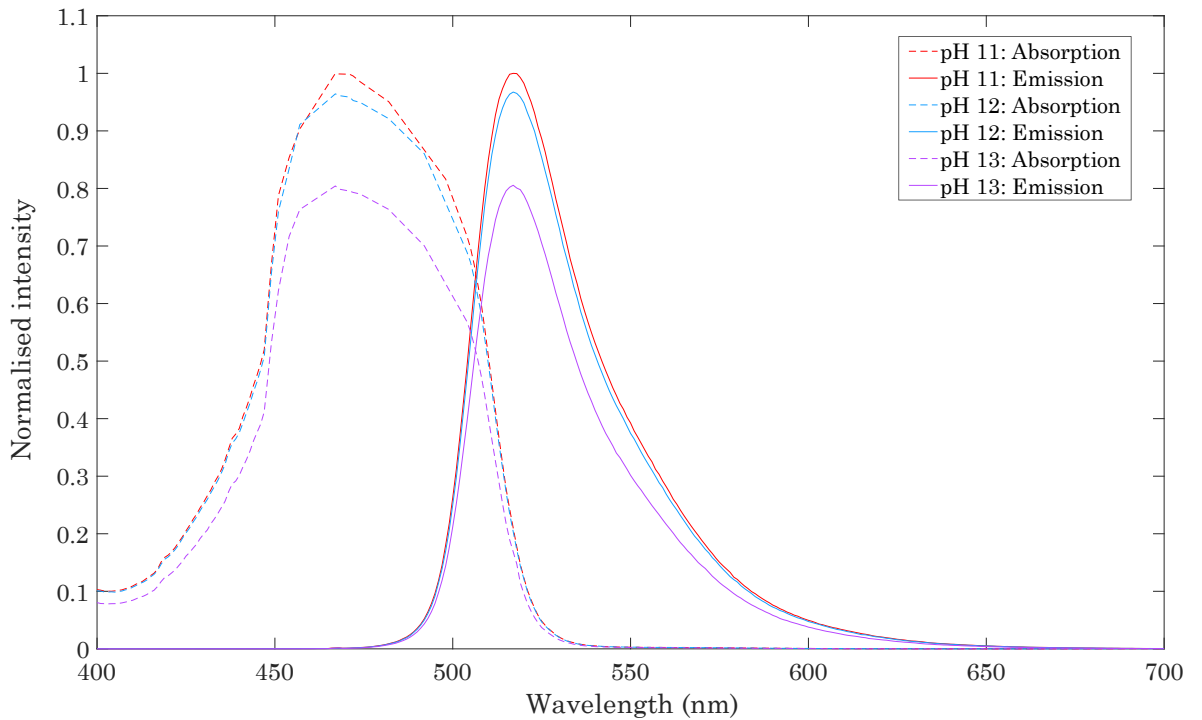
Figure 4.2: Measurements of absorption and emission of DAF at fixed concentration of 18.9 µM for three different pH values (11 = red; 12 = blue; 13 = purple).

Additional measurements of DAF solutions as a function concentration at a constant pH value of 11 were carried out in order to determine the threshold of self-quenching. These measurements

have been performed using high-speed camera equipped with a notch filter that allows to filter out excitation light (532 nm) simultaneously capturing DAF fluorescence light at all wavelengths below 524 nm and above 541 nm. The corresponding measurement data, shown in Fig. 4.3 (image noise = ±5 counts), indicate that the self-quenching occurs at approximately 50 ppm (∼0.09 mM). This is in good agreement with Doughty [51] who used sodium fluorescein dye in basic solutions to find critical concentration at which self-quenching occurs.

Given sufficient amount of fluorescence light is still attained by means of using an alternative laser of shorter excitation light wavelength (i.e., Argon-ion or Copper vapour), more sensitive cameras (high quantum efficiency) or image intensifier, higher surfactant concentrations can be used for broader analysis particularly with LIF methods. Alternatively, DAF can be dissolved in polar solvents such as ethanol which will result in red shift of both absorption and emission spectra allowing to use either Nd:YLF or Nd:YAG [188]. Excitation with Nd:YAG laser light was found to generate sufficient amount of fluorescence light at the full laser power (photodegradation is negligible due to short exposure times).
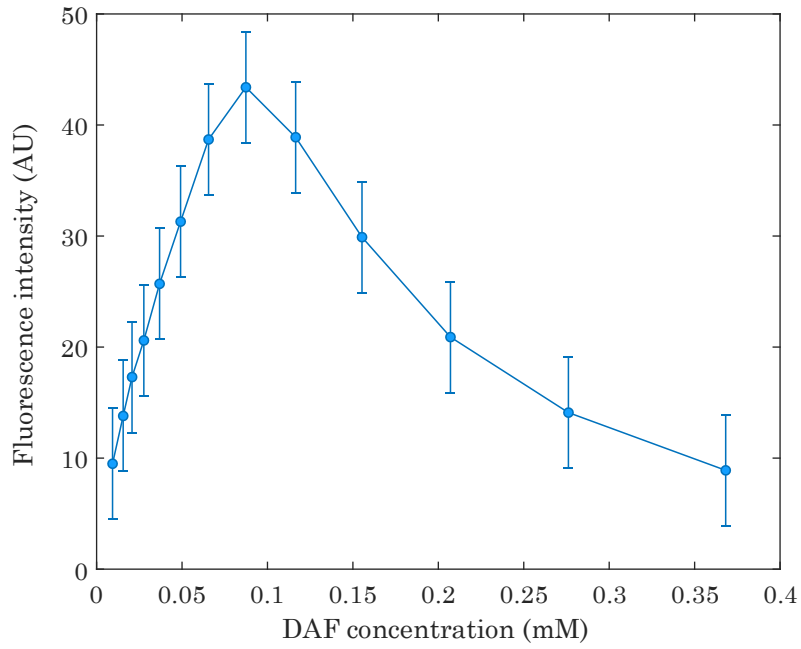
Figure 4.3: Measured data of DAF fluorescence as a function of concentration (pH = 11) using LIF method.

4.2 DAF molecular stability

The generic hydrolysis reaction mechanism of amides follows a nucleophilic hydroxide ion addition to the carbonyl carbon to form a tetrahedral intermediate (shown Fig. 4.4a). The nitrogen is then removed as the free amine in the presence of water and a carboxylic acid is formed. Similar decomposition would be expected for DAF molecule where dodecanoic acid (DA) and aminofluorescein (AF) would be formed. The molar ratio in the present hydrolysis reaction of DAF (as shown in Fig. 4.4b) is equal, thus, an increase in the absorption signal for one of the decomposition products would appear and the signal for DAF would subsequently reduce.
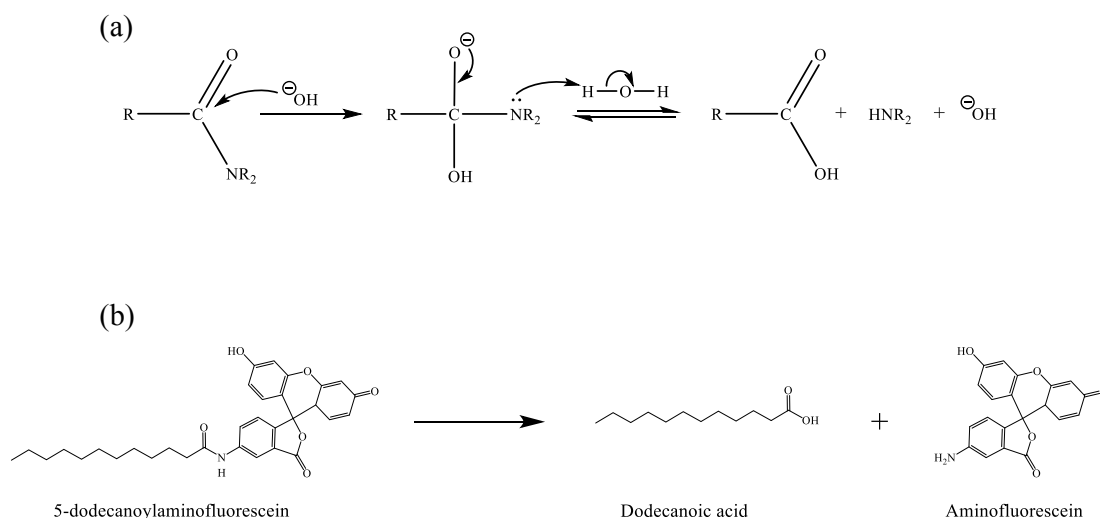
Figure 4.4: (a) Mechanism of the base catalysed hydrolysis of amides; (b) Hydrolysis reaction of DAF and resultant products.

In the present case, it was found that DA is not sensitive to absorption of light at the given spectra, but AF produced a strong signal with a peak at approximately 1.73 min (see Fig. 4.5). Signal for DAF is detected at approximately 5.60 min, which provides a very distinctive separation (retention time) between the two components. Insets in Fig. 4.5 show other signals detected at $1.1 - 1.4$ min and $8.2 - 9.6$ min that correspond to signals of pure sodium hydroxide solution. The latter signal appears most likely due to the formation of a salt. Evidently, there are more salt groups present in dissolved DAF molecule than AF or Na^+ alone, hence, a much stronger signal.

The measured absorption data for the whole reaction cycle (see Fig. 4.6) was found to

have consistent signals in terms of retention time and intensity. This shows that the molecular stability of DAF is high under basic conditions (pH = 14). The recorded absorption signal was identified to stay within the measured error bounds (see Fig. 4.6b). It was shown previously that the secondary amides have resistance to hydrolysis by hydroxide groups [29, 124].
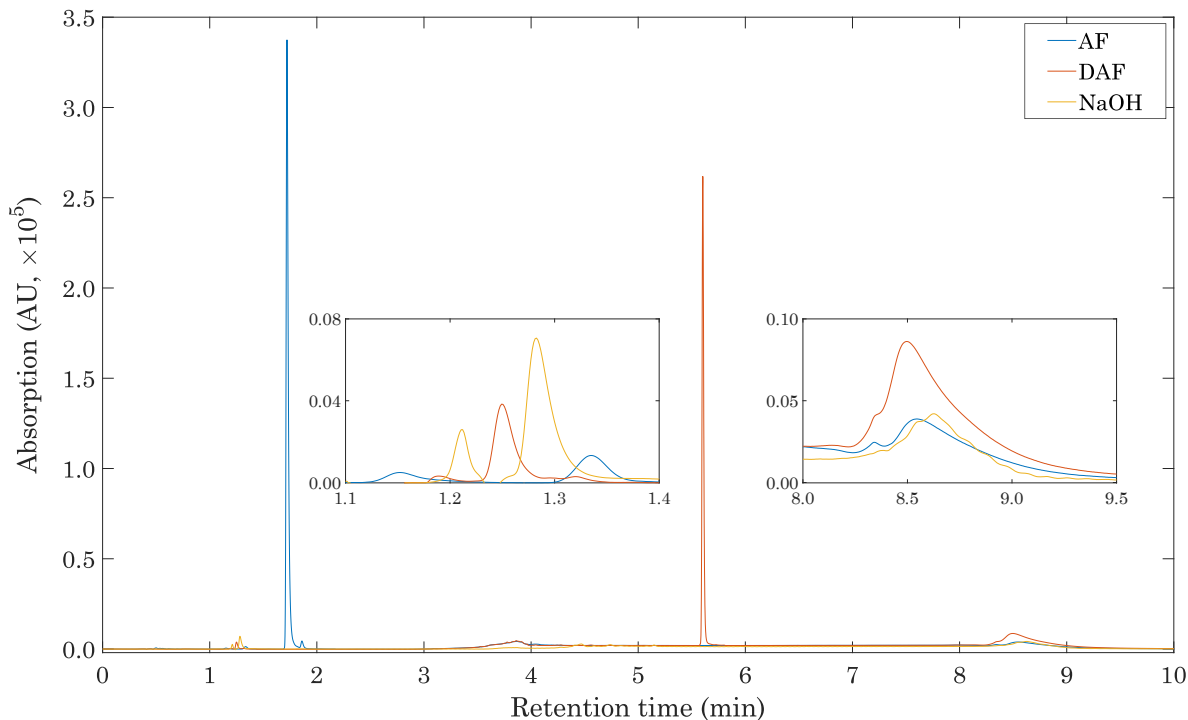
Figure 4.5: Combined data of individual analysis of AF, DAF and NaOH solutions. Insets show overlapping signals of individual components which are excluded from further analysis.

A more effective cleavage of C-N bond would require elevated temperatures (~ 100 °C) and presence of metal ions to catalyse the reaction [142]. Moreover, from the analysed solutions we have not observed any evident signal at ~ 1.7 min which would correspond to signs of AF molecule. Other noticeable signals could appear due to various impurities that are present in individual chemicals, but the peaks do not change in their respective areas over time and are well-aligned with signals of pure NaOH solution. Thus, we conclude that DAF surfactant does not undergo hydrolysis reaction in alkaline solution at high pH during continuous mixing for almost 23 hours at temperature of 25 °C.
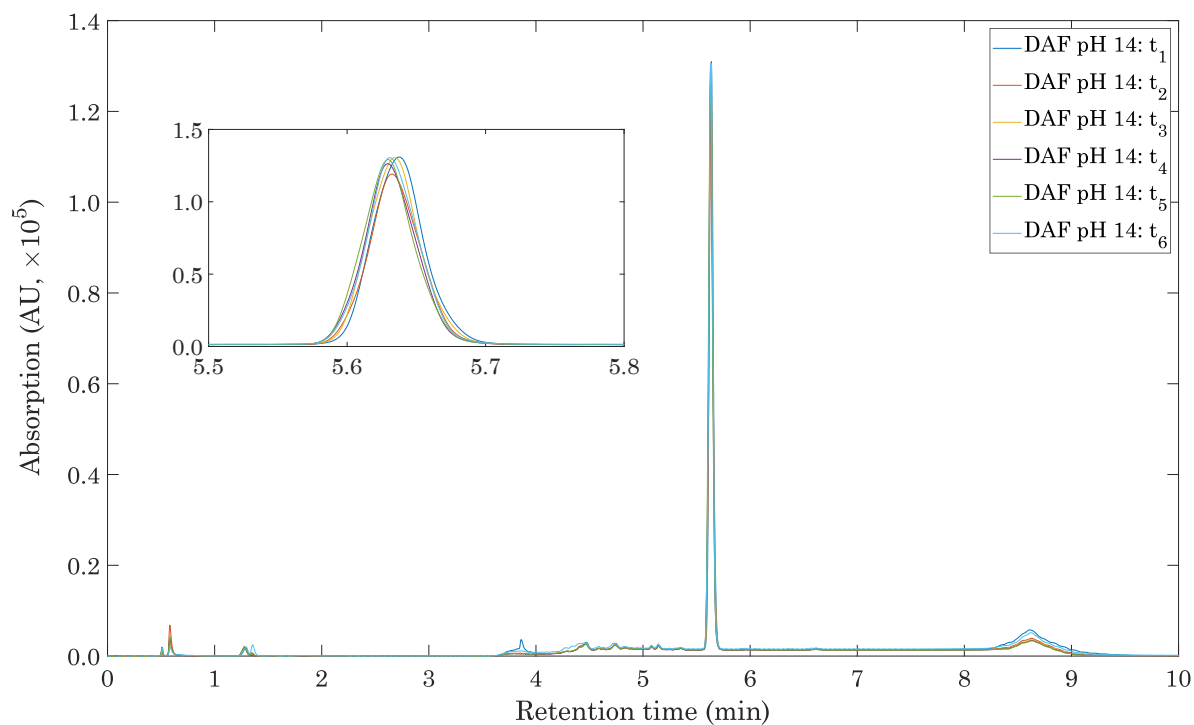
(a) UHPLC chromatogram
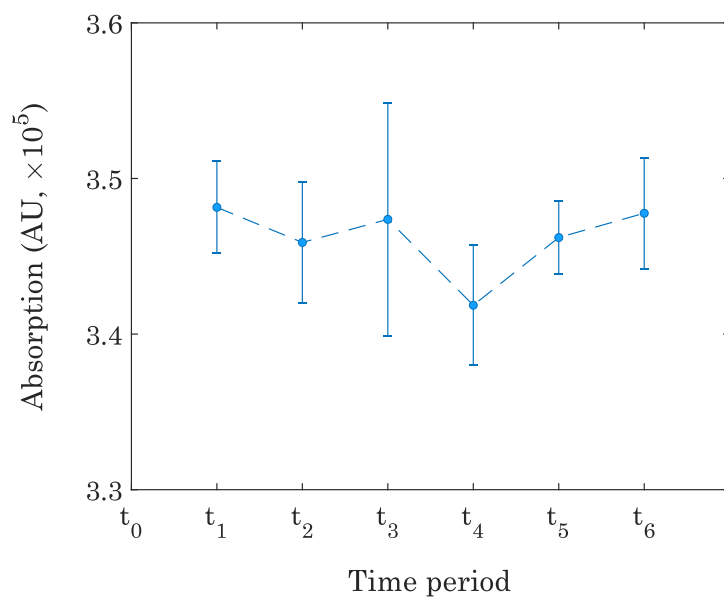
(b) Absorption intensity

Figure 4.6: DAF hydrolysis reaction results measured using UHPLC. (a) Chromatogram of DAF samples at pH = 14 taken at six different time points during the reaction process, inset: a magnification of signals (corresponding to DAF retention time); (b) Measured absorption intensity of DAF samples at different time points.

4.3 Surface pressure-Area isotherms

In this section, the behaviour of DAF surfactant as an insoluble monolayer is investigated by conducting Langmuir-Blodgett trough measurements. Determining the existence of various monolayer phases at particular surface pressures with respect to surface concentration permits for direct comparison with the results obtained for the soluble case discussed in further sections.

The measurements of surface pressure (Π) against molecular area (A_{DAF}) isotherms for 50 µL spreading volume of DAF at concentration 4.72×10^{-4} M was performed and the corresponding data is shown in Figure 4.7. Measurements have been repeated three times resulting in good reproducibility. The isotherm has shown the existence of several phases. At flat region of up to 68 $\text{\AA}^2$/molecule (~ 0.13 µg/cm^2) corresponds to a gas (G) phase. At this range of surface pressures the hydrophobic tail-groups of DAF makes little contact with each other but a significant contact with the water surface [62]. It is clearly visible from Fig. 4.7 that surfactant molecules do very little in reducing the surface tension, hence, close to zero surface pressure.

As the film continues to be compressed beyond 68 $\text{\AA}^2$/molecule, the molecules start to reorientate resulting in transitioning from G state to liquid-expanded (LE) state. An increasing number of hydrophobic tail-groups of DAF molecules begin to point outwards from the water surface making less contact with it. This growth continues up to approximately 50 $\text{\AA}^2$/molecule (0.18 µg/cm^2) where the monolayer is fully in LE state. With further increase in surface density a phase transition from LE to liquid-condensed (LC) state is observed, and continues up to 41 $\text{\AA}^2$/molecule (0.21 µg/cm^2). After this point an abrupt increase in surface pressure with nearly constant slope corresponds to a transition phase from LC to a solid condensed state. This is in good agreement with measurements performed by Gutiérrez et al. [66] who used similar surfactant to DAF, 5-hexadecanoylaminofluorescein (HDFL), at the air-water interface by spreading 60 µL of HDFL at 1.00×10^{-4} M dissolved in ethanol-chloroform mixture. Our results also agree with those of Dutta and Salesse [53] who used HDFL at the air-water interface by spreading 100 µL of 2.00×10^{-3} M solution. They used fluorescence microscopy to confirm the phase change of the monolayer during the film compression, which supports our results. Interestingly, it was shown that during the evolution (compression) of LE film random segments of the film produced bright fluorescent areas with patches of dark domains which was likely caused due to the formation of agglomerates. Beyond a certain surface pressure (13 mN m^{-1} in their case) the concentration of these agglomerates increased so much such that a complete fluorescence quenching occurred by the efficient (fluorescence) energy transfer from the active

60
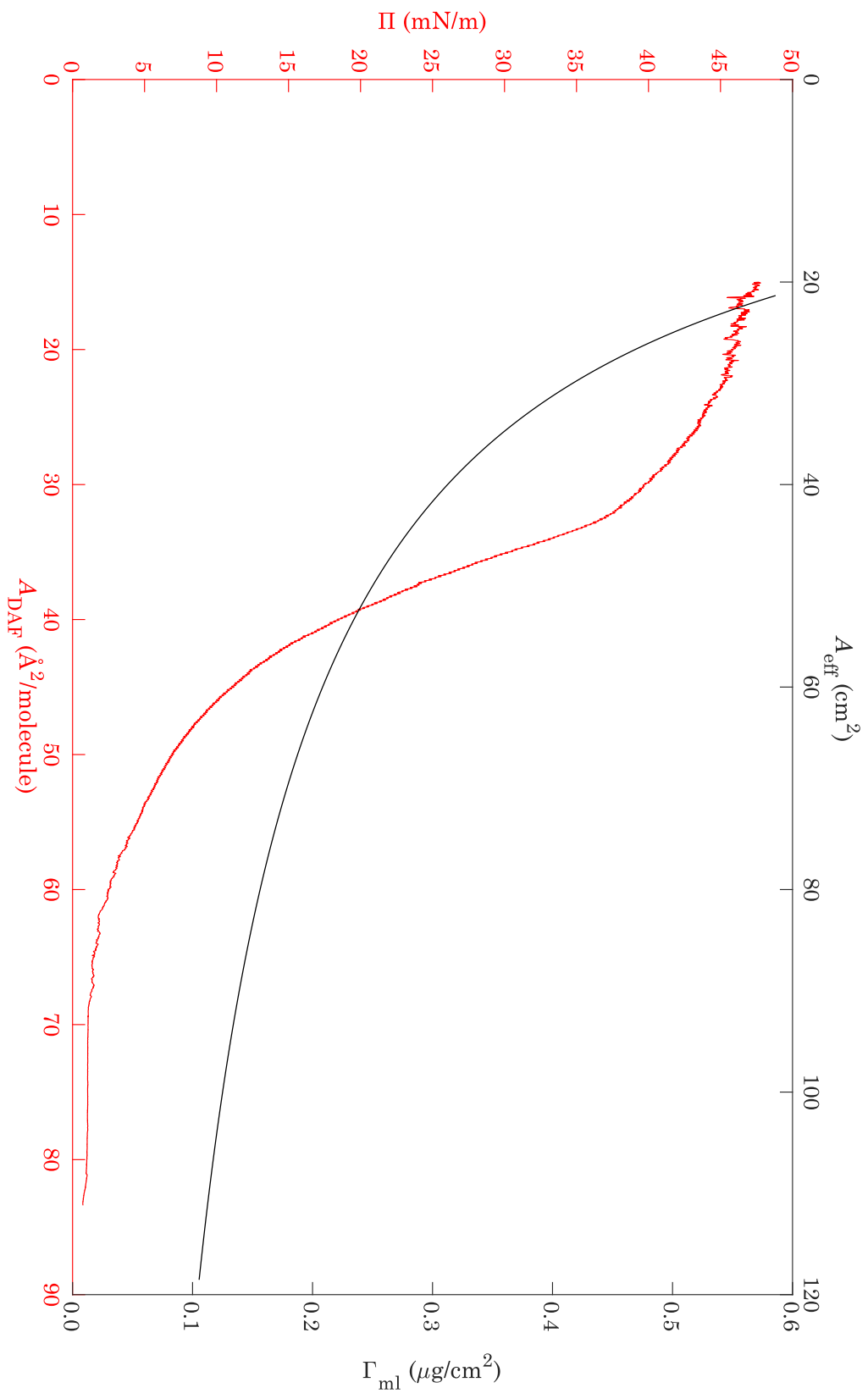
Figure 4.7: Surface pressure-area per molecule isotherm and effective spreading area-monolayer density of DAF obtained by spreading 50 μL of DAF/methanol solution of 4.72×10^{-4} M concentration.

monomers to these aggregates. During film decompression the fluorescence re-occurred with much higher intensity relative to initially non-compressed films at all surface pressures. From the micrographs it is evident that agglomerates are still present even at low surface pressure (~ 3 mN m^{-1}).

Returning to our case, as the compression continued below 23 Å^2/molecule no significant increase in surface pressure was observed. Such behaviour can be explained by the fact that the monolayer has reached its compression limit and its 2D nature starts to destabilise, hence, the increased noise. Very similar dynamics are observed by Gutiérrez et al. [66] for HDFL. Consequently, monolayer collapses yielding a structure in the third dimension by means of fracturing, ejection to the subphase or formation of aggregates [98]. The minimum surface tension of DAF monolayer at this point is approximately 27 mN m^{-1}.

A hypothetical area per DAF molecule occupied at an uncompressed close-packed layer can be extrapolated by taking the second linear portion of the isotherm corresponding to the solid phase transition and an intercept with x-axis at zero surface pressure [66]. The resultant limiting molecular area is 48 Å^2/molecule. It is important to note that this value is strongly dependent on the spreading solvent as found by Orbulescu et al. [126], thus, the measured isotherms for the same molecule need to be compared adequately as they may differ substantially.

4.4   Equilibrium adsorption and equation of state measurements

In this section, we show the results acquired from the pendant drop measurements, and subsequent output from calculations used to construct a graph of equilibrium surface tension as a function of concentration. A comparison of the two isotherms (soluble and insoluble cases) is provided and key differences are analysed.

We have established a CMC value at 0.32 mM which corresponds to the surface tension γ_{cmc} of 26.6 mN m^{-1} (± 0.5 mN m^{-1}). This is in good agreement with the work by Pinazo et al. [130] who used N-dodecyl-N,N dimethyl amino betaine chlorhydrate (DDABC) surfactant (molecular structure partially similar to DAF) to perform dynamic surface tension measurements using spinning bubble tensiometry. To the best of our knowledge, as mentioned at the beginning, there was only one other work carried out with similar water-soluble fluorescent surfactants by McWilliams et al. [152] which focused more on the synthesis of such molecules rather than their

in-depth characterisation. Yet, the work provides results of equilibrium surface tension as a function of concentration for only one fluorescent surfactant which is capable of reducing surface tension to only ~ 63 mN m^{-1} at $\geq$CMC making it rather ineffective as a surfactant. The CMC values of other surfactants were also provided. The most similar surfactant to DAF contains Rhodamine head-group with twelve carbon atoms tail-group whose CMC = 0.75 mM, which is more than double relative to DAF. Moreover, the CMC of all other studied surfactants are higher by at least a factor of two even those with longer hydrophobic tail-groups (e.g. C16).

From the work presented in the previous chapter, the Frumkin equation (Eq. 3.1), we can define the adsorption isotherm as

$$\frac{\Gamma_\mathrm{e}}{\Gamma_\infty} = \frac{1}{1 + (k_\mathrm{d}/(\beta_\mathrm{a}C_0))\mathrm{e}^{K\Gamma/\Gamma_\infty}}, \tag{4.1}$$

and equation of state (EoS) as:

$$\gamma(\Gamma) = \gamma_c + RT\Gamma_\infty \left(\ln\left(1 - \frac{\Gamma}{\Gamma_\infty}\right) - \frac{K}{2}\left(\frac{\Gamma}{\Gamma_\infty}\right)^2 \right), \tag{4.2}$$

where γ_c is the surface tension of the uncontaminated air-water interface (= 71.44 mN m^{-1}). For a range of DAF concentrations we have measured corresponding equilibrium surface tensions and using the last two Frumkin equations (Eq. 4.1 and Eq. 4.2) we generate a fit of least squares method (see Fig. 4.8). During the adsorption process there is a possibility of significant depletion of surfactant concentration in the bulk of the pendant drop which can result in a lower bulk concentration than the apparent solution concentration. To account for this, we make a correction for each data point:

$$C_\mathrm{corrected} = C_\mathrm{apparent} - \Gamma_e \left(\frac{A_\mathrm{droplet}}{V_\mathrm{droplet}} \right), \tag{4.3}$$

where A_droplet and V_droplet is the area and volume of the measured pendant drop, respectively. Performing this correction provides a good fit of the corrected equilibrium data to the Frumkin EoS. The resultant output values for $\alpha = k_\mathrm{d}/\beta_\mathrm{a} = 1.66 \times 10^{-3}$ mol/m^3, $K = 3.75$, and Γ_∞ = 4.78×10^{-6} mol/m^2. The obtained value of K is positive which signifies that the repulsion forces between DAF head-groups are higher than the cohesive van der Waals forces between the tail-groups in the monolayer. Hence, such marked reduction of surface tension at $\geq$CMC. Also, this interaction is particularly evident for higher concentrations where a good match is found, whereas at lower concentrations (i.e., 0.045 mM) the model underpredicts due to significance of the cohesion forces, hence, the higher surface tension. These forces can also determine formation

of different monolayer phases as the surface concentration increases. Such evidence was gathered by Gutiérrez et al. [66] for HDFL (as discussed above). They have shown experimentally how the molecular orientation relative to the interface is changing as the monolayer becomes compressed (surface concentration increases).
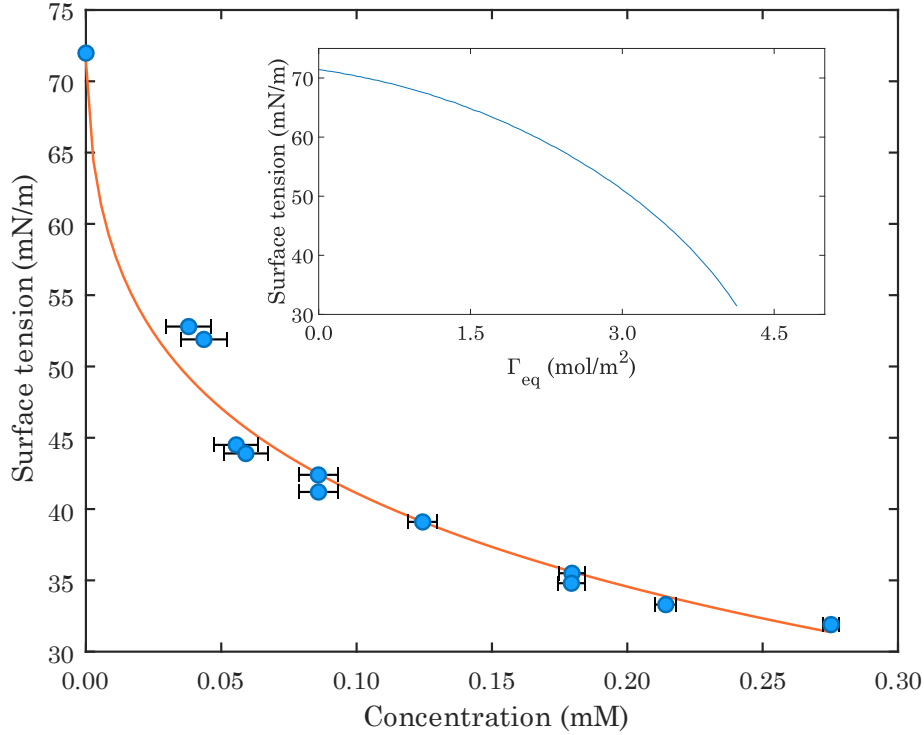
Figure 4.8: (a) The equilibrium surface tension as a function of concentration for air/DAF aqueous solutions and the Frumkin model fit (solid line); (b) The inset shows the equilibrium surface tension as a function of equilibrium surface concentration.

By performing a comparison between the surface concentration at equilibrium obtained from Equations 4.1 and 4.2 and the measured Γ_{ml} values from the Π-A_{DAF} isotherm we find interesting results (see Fig. 4.9). Evidently, a higher surface concentration at any given surface pressure of the insoluble monolayer relative to the soluble surfactant is observed. What is more, even before the surface tension starts to rapidly decrease in the insoluble surfactant case, the surface tension of $\sim$56 mN m^{-1} was already reached in the soluble surfactant case. Once the same surface tension is reached in the insoluble surfactant case, the corresponding Γ_{ml} exceeds Γ_e by $\sim 1.5 \times 10^{-6}$ mol/m^2. Interestingly, the maximum surface concentration of Γ_{ml} also exceeds Γ_∞ (maximum packing) by 2.77×10^{-6} mol/m^2.

Such behaviour can be caused by a difference in phase transitions and intermolecular interactions. It is evident that the surface pressure at which transition of the same phase takes a place for soluble and insoluble monolayers is different. For instance, while an abrupt increase in
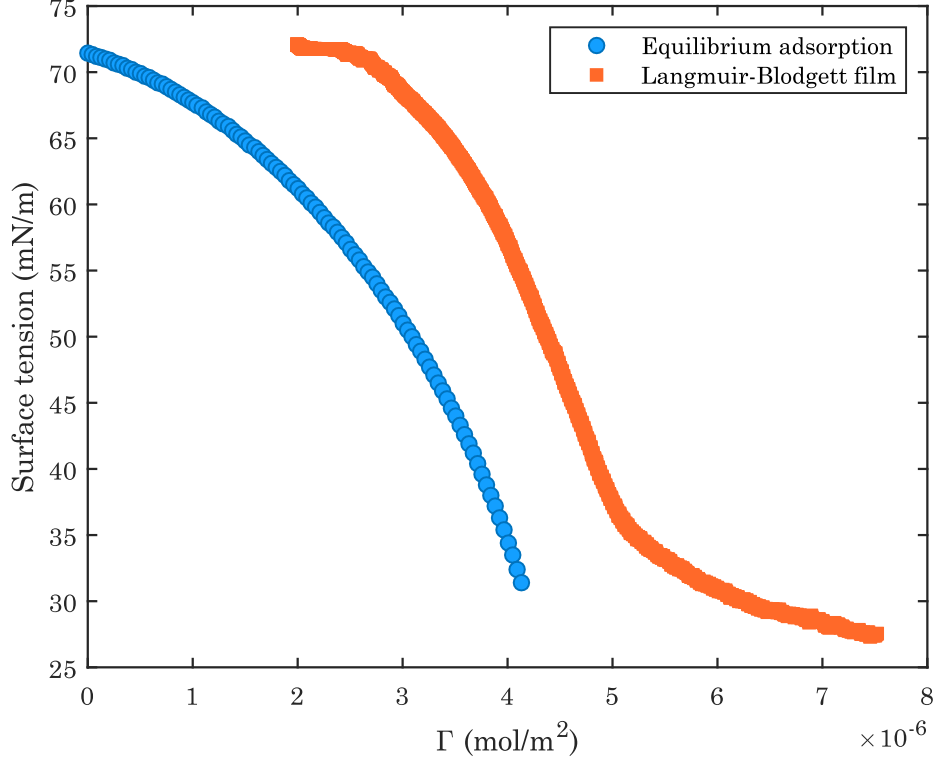
Figure 4.9: Comparison between modelled equilibrium surface tension as a function of surface concentration (blue circles) and Langmuir-Blodgett film measurements (orange circles).

surface pressure is observed at very low concentrations for soluble case due to early formation of LE state, in the insoluble case the formation of the full LE state occurs at $\Pi = 7 \text{ mN m}^{-1}$. The clustering of surfactant molecules in each case during the phase transition is probably different due to dissimilar molecular attraction. While the hydrophobic tails are flexible in both cases, soluble surfactant molecules, due to increased affinity, may have a weaker ordering dictated by balance of forces at the interface hinting that tails can also be in partial contact with the solvent (yet still pointing into the air) together with the ionised head-group. Large size of DAF head-group and its high hydrophilicity suggests that it is, most probably, located below the air-water interface but are sterically hindered preventing from close contact with other neighbouring DAF molecules [53]. Such probable molecular arrangement was previously demonstrated by Tomas-sone et al. [165] who carried out a systematic Molecular Dynamics (MD) study of the phase behaviour of soluble and insoluble surfactants on a liquid-vapour interface. Due to stronger hydrogen bond formation between polar groups and water molecules on the surfaces of soluble surfactants it may lead to a higher mean tilt angle of the molecular dipole with the interface normal than in the insoluble case. Similar measurements for the insoluble monolayer were per-formed previously by Gutiérrez et al. [66] using optical second harmonic generation technique coupled with Π-A_{DAF} isotherms (as mentioned earlier). Consequently, soluble molecules should

occupy a larger area resulting in a more effective surface tension reduction, hence, a lower surface concentration at the same surface pressure. To support this, our calculated minimum molecular area at the highest surface pressure for soluble case was found to be ~ 44 Å^2/molecule, which is similar to the extrapolated value of 48 Å^2/molecule occupied at an uncompressed close-packed layer, and is higher than the insoluble monolayer (~ 22 Å^2/molecule) at the same Π.

4.5 Numerical results

Three plots (Fig. 4.10, 4.11, 4.12) have been generated of nondimensional dynamic tension γ^* as a function of the nondimensional time τ from which the effect of different κ values (0.5 – 500) for fixed values of C_0/α (11.36, 113.61 and 567.58) is investigated (see Chapter 3 for definition). The diffusion control dynamics are plotted with $\kappa \to \infty$. The selected C_0/α values correspond to our investigated concentration range in the experimental measurements. As explained earlier, κ and τ are independent of C_0, thus, surface tension relaxation can be studied from a physical perspective at different bulk concentrations and fixed kinetic parameters. Values of the parameter Φ^2 (see Chapter 3 for definition) ranges from 8.8×10^{-4} to 43.9 for the corresponding κ values which shows the relative importance of kinetics to bulk diffusion.

The first observation we can make from these plots is the relationship between the bulk concentration and diffusion. We see that the diffusion limited relaxation becomes more rapid with increasing bulk concentration. This occurs due to fast kinetics that essentially drain the sublayer concentration to zero of newly created clean interface resulting in surfactant transport by bulk diffusion where the rate is proportional to the bulk concentration (i.e., the higher the concentration the faster is the surfactant transport). Similarly, we can clearly see that for any fixed value of κ and with increasing bulk concentration the finite kinetic curve moves away from the diffusion limited curve meaning that the relaxation is largely controlled by the kinetic effects. If for any fixed C_0/α value the κ is increased, this results in faster kinetic rates (k_d and β_a) while their ratio, α, is held constant over the same time scale. As a result of faster kinetic exchange, the mixed diffusive-kinetic control starts to approach diffusion control. The parameter Φ^2 ($= \kappa/(C_0/\alpha)$) also provides a good indication about the type control for surfactant adsorption process. In all cases we see that as Φ^2 decreases the curves shift away from the diffusion limited curve towards kinetically controlled relaxation (i.e., $\Phi^2 < 44$).
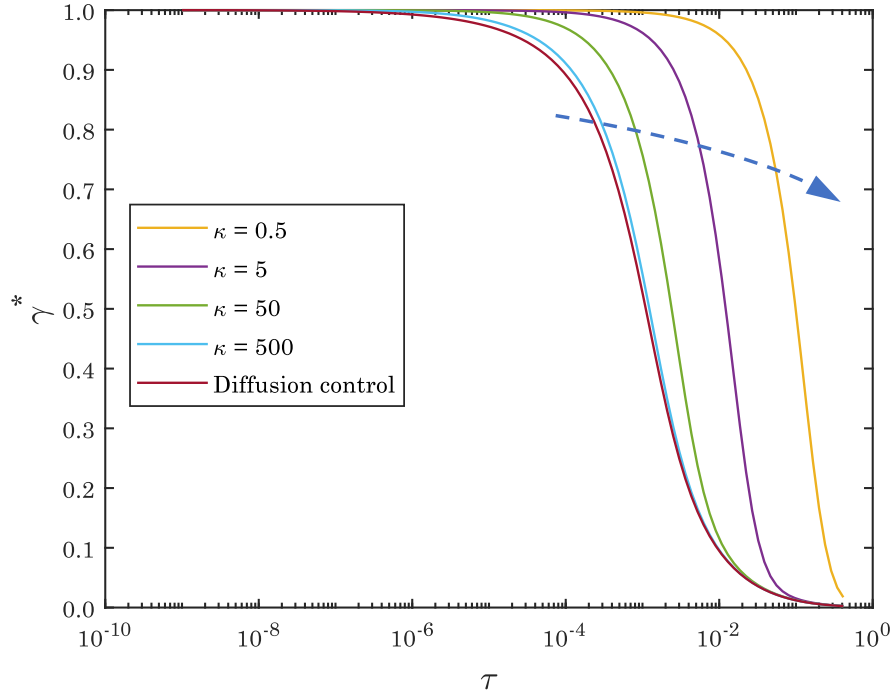
Figure 4.10: The comparison of the diffusive control and mixed diffusive-kinetic control surface tension relaxations as a function of nondimensional time, for $C_0/\alpha = 11.36$ and decreasing κ from left to right. The corresponding Φ^2 for each κ also decreases from 43.92 to 0.043 (left to right).
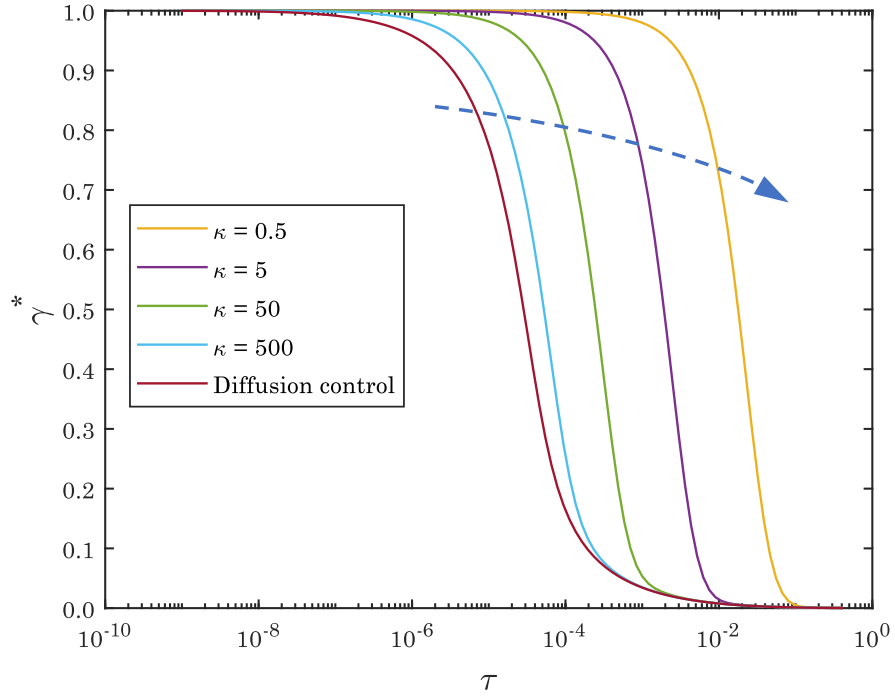
Figure 4.11: The comparison of the diffusive control and mixed diffusive-kinetic control surface tension relaxations as a function of nondimensional time, for $C_0/\alpha = 113.61$ and decreasing κ from left to right. The corresponding Φ^2 for each κ also decreases by a factor of 10 from 4.39 to 0.0044 (left to right).
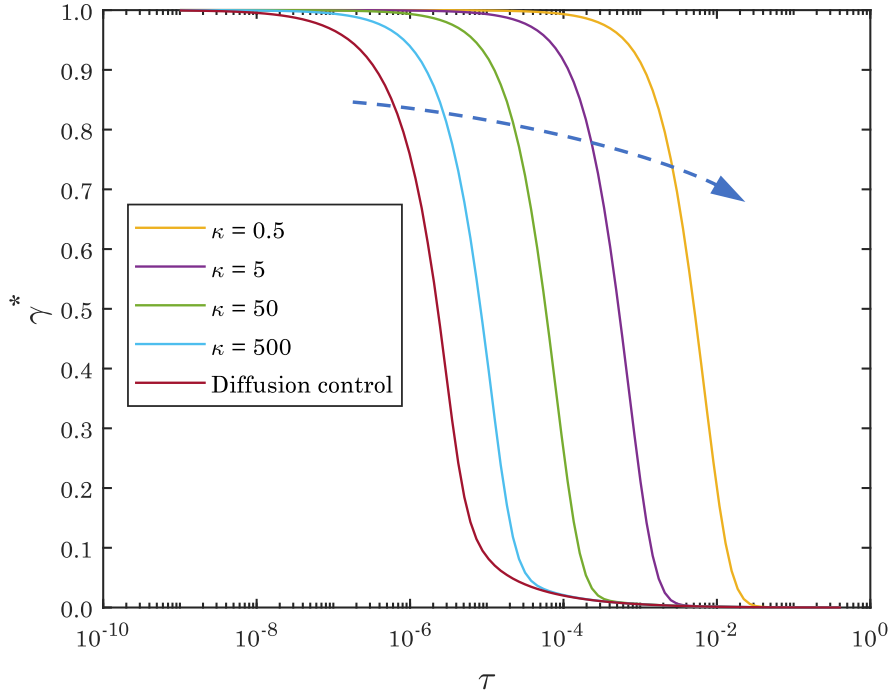
Figure 4.12: The comparison of the diffusive control and mixed diffusive-kinetic control surface tension relaxations as a function of nondimensional time, for $C_0/\alpha = 567.58$ and decreasing κ from left to right. The corresponding Φ^2 for each κ also decreases by a factor of 10 from 0.88 to 0.00088 (left to right).

4.6   Clean interface adsorption experiments

Using kinetic-diffusive transport model we have generated individual fits for dynamic surface tension measurements at three different concentrations (0.053 mM, 0.094 mM and 0.189 mM) applying a single kinetic parameter β_a and diffusion coefficient D_b (see Fig. 4.13). From this, we have estimated that the β_a value $= 0.02038$ m^3/mol/s and $D_b = 5.6 \times 10^{-10}$ m^2/s. Subsequently, we calculate the $\beta_a \times \Gamma_\infty = k_a = 9.73 \times 10^{-8}$ m s^{-1} and $k_d = 3.39 \times 10^{-5}$ s^{-1}. The corresponding Φ^2 values are 0.0044, 0.0087 and 0.0156 for highest to lowest concentrations, respectively. As noted previously, since $\Phi^2 < 44$ for all three cases, relaxations follow mixed diffusive-kinetic control. In order to avoid overcrowding in the plot, we avoid displaying all the dynamic surface tension runs. Pinazo et al. [130] have also found that a mixed kinetic-diffusive control model better describes the dynamic surface tension behaviour of the DDABC surfactant. Moreover, their obtained diffusivity and adsorption rate constants also agree well with our calculated rate constants.

Having a very good fitting of the chosen model, we observe several marginal differences for two concentrations (0.094 mM and 0.189 mM). The overpredictions and underpredictions are
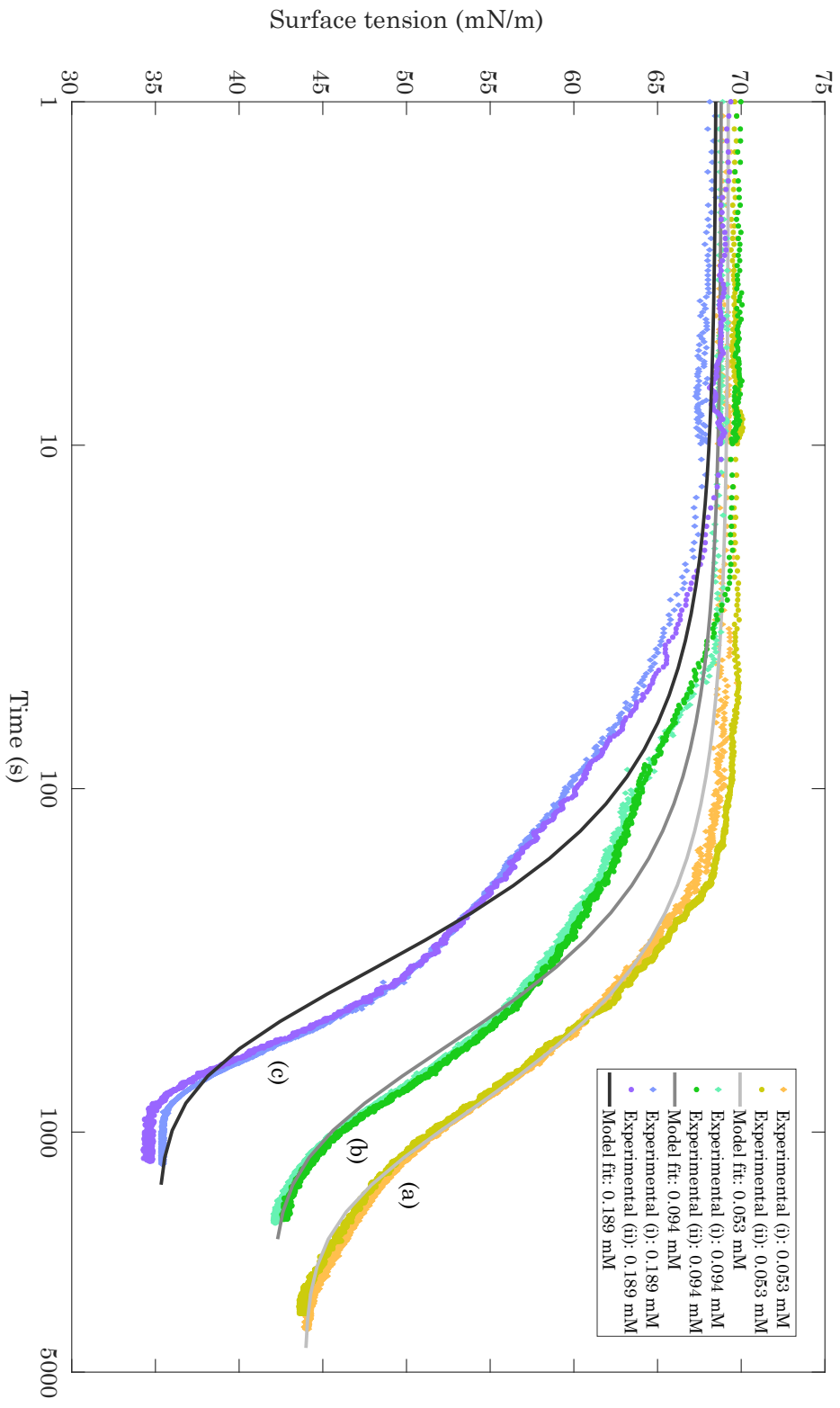
Figure 4.13: Dynamic surface tensions in DAF aqueous solution and mixed diffusive-kinetic control theoretical fit with $D = 5.6 \times 10^{-10}$ m^2/s and $\beta_a = 0.02038$ m^3/mol/s for three concentrations: (a) 0.053 mM; (b) 0.094 mM; (c) 0.189 mM.

associated with the presence of phase transitions that occur at different time periods. As a new clean interface is created an induction period exists at which the surface tension remains close to that of the clean interface until a decrease in γ is observed. During this period the surfactant initially starts to adsorb into the gaseous state reducing the surface tension marginally followed by a plateau, which we have observed when starting data recording after $\sim$1 s from the drop formation. As the adsorption continues with time, liquid-expanded state appears and coexists with the gaseous state. As the former state grows at the expense of gaseous state, a negligible change in the surface tension continues until the surface is fully occupied by surfactant at the liquid-expanded state. After this point, the induction period ends, and a sudden decrease in the surface tension occurs. This induction period shortens as the bulk concentration increases due to larger diffusive flux. For the DAF surfactant the observed induction period is below 2 s for concentrations above 0.28 mM.

Since the Frumkin model does not account for the phase transition, hence a slight misalignment of the model fit, a transport model that would account for this is required. This was well-demonstrated both experimentally and theoretically by Subramanyam and Maldarelli [156]. For the surfactant adsorption into a gaseous state the group has used Arrhenius rate law by considering a critical surface concentration in this phase as a function of time. Once this critical concentration is attained, a second regime is introduced with additional adsorption whilst being in thermodynamic equilibrium (i.e., coexistence of gaseous and liquid-expanded phases). Once the surface is completely covered with liquid-expanded state, a third regime of adsorption into the liquid-expanded state is initiated. Although they found a good agreement with no adjustable constants, their model fits for all concentration (and particularly for higher values) also marginally misalign as the equilibrium values are approached (at approximately second elbow).

4.7 Concluding remarks

In this chapter, we presented a commercially available fluorescent surfactant (DAF) and a novel method to prepare an aqueous DAF solution along with detailed characterisation of DAF surfactant that proves suitability for a wide-range of applications in the field of fluid dynamics. By performing quantitative measurements we obtained detailed information about optical properties, molecular stability, and surfactant monolayer and transport properties. This allowed to prove the usability of DAF in sustainable and safe solvents (i.e. water) with addition of sodium hydroxide which can be neutralised by using a buffer. Such configuration opens opportunities

for new experimental work where the use of surfactants hold an interest in practical solutions as well as validation of modelling results. This was already shown by numerous researchers where, for instance, interfacial concentration gradients lead to Marangoni stresses that markedly affect fluid behaviour. We have provided light absorption and emission spectra as a function of pH from spectrofluorometer measurements. In agreement with literature, we found that intensity of spectra decrease as the pH increases above 11. We have also applied LIF technique for the purpose of not only to identify a critical concentration for self-quenching but also to demonstrate the usability of DAF solution for multi-scale experimental investigations. The self-quenching was found to occur at about 0.09 mM at pH = 11.

Since the preparation of DAF aqueous solution involves using a strong base (NaOH at pH ≥ 13), we carried out an analysis of potential hydrolysis reaction using UHPLC. By dissolving DAF in basic solution (pH = 14 at 25 °C) and continuously mixing for almost 23 hours, we have analysed samples at different periods of time in order to verify the extent of DAF decomposition into its subsequent tail-group and head-group. Interestingly, not only that we did not find any new signals that could be linked to the reaction products, but we also observed that the signal intensity corresponding to DAF was stable and varied within the measured error bounds. These observations suggest that DAF does not undergo hydrolysis reaction under the chosen conditions.

In order to understand the ability of DAF to reduce the air-water surface tension and its behaviour as a monolayer, we conducted Langmuir-Blodgett trough measurements and obtained surface pressure-area isotherms. Compression of an insoluble DAF monolayer have shown the presence of several different phases and their subsequent transition with increasing surface pressure. It was established that up to 68 Å^2/molecule the monolayer is in the gas phase. Further compression leads to transition from gas to liquid-expanded phases until the latter is fully formed at 50 Å^2/molecule. Further increase in surface pressure results in transition towards formation of liquid-condensed state at 41 Å^2/molecule. After this point additional compression creates an abrupt increase in surface pressure indicating transition from liquid-condensed to solid-condensed phases up to about 23 Å^2/molecule. Beyond this, no significant reduction in surface tension is observed. These have been found in excellent agreement with literature data for very similar fluorescent surfactants.

We also conducted pendant drop measurements from which we obtained dynamic and equilibrium surface tension plots for different concentrations. We determined the CMC = 0.32 mM.

By finding a good fit of the Frumkin model to the measured equilibrium plot we obtained necessary fitting parameters. With these, we used kinetic-diffusive transport model to generate fits for the dynamic surface tension plots for three different concentrations which resulted in very good agreement. Consequently, the calculated adsorption and desorption rate constants are 9.73×10^{-8} $\mathrm{m\,s^{-1}}$ and 3.39×10^{-5} $\mathrm{s^{-1}}$, respectively, and the diffusivity constant is 5.6×10^{-10} $\mathrm{m^2/s}$. The maximum packing concentration was found to be 4.78×10^{-6} $\mathrm{mol/m^2}$. Our numerical results on the comparative analysis of surface relaxation by diffusive control and mixed diffusive-kinetic control has clearly shown that the latter control is in place for the range of concentrations used in our experiments. This has been widely demonstrated in literature also for other types of surfactants. A markedly different behaviour in the phase transition is observed between the compression of an insoluble film and the monolayer at equilibrium of increasing surface concentration formed by adsorption of soluble surfactant. Primarily, a higher surface concentration at any given surface pressure is observed for the former case. Also, the maximum obtained surface concentration for insoluble monolayer (highest surface pressure) exceeds the maximum packing of a soluble surfactant by 2.77×10^{-6} $\mathrm{mol/m^2}$. We propose that such dynamics can be caused due to differences in the intermolecular interactions between the two cases, hinting at the fact that surfactant molecules can have different orientation relative to the water surface. Such findings are in good agreement with previous experimental and modelling results found in literature.

Chapter 5

The effect of surfactant on annular films

Contents

The behaviour of annular films varies depending on the given flow conditions of both the liquid and gas phases. Such variations have already been widely studied (e.g., Chu and Dukler [39, 40], Karapantsios et al. [86], Liu et al. [103], Morgan et al. [117], Schubring et al. [144], Webb and Hewitt [175], Zadrazil et al. [186]) which demonstrated the presence of distinct flow characteristics that occur through and lead to various physical mechanisms. The most commonly measured annular flow properties are the change in the film thickness, the film roughness (i.e., 'waviness'), and the entrainment of gas and liquid phases into one another. Qualitative and quantitative analyses of these data expanded our understanding of annular flows by e.g., categorising certain flow patterns into specific types of flow regimes and flow regime maps were constructed by several works (see refs. [175, 186] and references therein). Substantial differences, however, are still found in the proposed flow regime maps which mainly differ due to the type(s) of measurement method(s) used. Depending on the particular method, the acquired data will correspond to either spatially-averaged or local film thickness information (e.g., heights of the film and waves). In the former case, typically performed using capacitance probes (CPs),

the classification of flow regimes is limited due to smoothing of film thickness measurements and absence of other vital characteristic information such as gas and/or liquid entrainment. In the latter case, often done using optical methods, the classification can be characterised by additional data of the flow properties that are more distinctive such as local measurements of thickness and wavelengths of substrate films and interfacial waves, and gas entrainment, allowing for a more reliable assessment. As discussed in Chapter 2, such measurements have already been performed using the PLIF method, which, however, was proven to incur significant errors in identifying the film thickness and its interfacial structure due to total internal reflection and refraction associated with the gas-liquid interface [32, 67]. To overcome these limitations, a newly-developed measurement technique, S-PLIF [32], was used in the present study.

In this chapter, measurements of film thickness in adiabatic downwards annular flows for a wide range of flow conditions (see Table 3.2) and flow regimes are presented, covering not only the falling films, but also, for the first time, gas-sheared annular film flows. Simultaneous measurements by S-PLIF and CP allows the identification of the complementarity and the limitations present in the two measurement methods by analysing the flow characteristics. Moreover, no such measurements were previously conducted by optical diagnostic techniques on downwards annular flows in the presence of (fluorescent) surfactant. A flow regime map for surfactant-laden flows (at a concentration of 0.114 mM, see Chapter 3) is also constructed for the first time. The effect of the surfactant on annular film flows are identified and compared closely with literature data, including predicted values from various correlations, in parallel, discussing the potential causes for the observed complex gas-liquid flow phenomena.

5.1 Phenomenology and flow regimes

The range of flow conditions investigated in this work (see Table 3.2) gives a rise to a variety of flow patterns that are characterised by distinct flow properties such as the interfacial wave activity, base film flow behaviour, and entrainment of gas (bubbles) into the liquid film. Both the wave activity and the base film behaviour are underpinned by a distinct range of amplitudes, frequencies and wavelengths, with the base film typically exhibiting longer wavelengths compared to large interfacial waves (e.g., quiescent flows are observed to occur in the laminar flow at $Re_L < 540$). The presence or absence of entrained gas bubbles inside the liquid film is also controlled by several interfacial mechanisms, some of which are detailed in works by Hann et al. [71], Rodríguez and Shedd [138], and Tran et al. [166], and discussed further below. All

of these dynamics can be established using optical methods. Therefore, a flow regime can be classified in a qualitative manner by direct visualisation of the images of the flow. This approach was taken by Webb and Hewitt [175] from which they identified four key flow regimes present in annular films, namely: 'ripple wave', 'dual-wave', 'thick ripple', and 'regular wave' regimes. Later, Zadrazil et al. [186] explored downwards annular flows at even higher liquid Reynolds numbers, and using the PLIF method, confirmed the four flow regimes mentioned above and identified an additional one, the 'disturbance wave' regime.

In this study, we use S-PLIF and instantaneous images of wave fronts and base films to construct flow regime maps for the flow conditions shown in Table 3.2. It is worthy of note that the flow regime 'ripple wave' occurs at liquid Reynolds numbers that are below those used in the present study. The presence of the defined characteristics of the film were also checked from the time-traces obtained using the CP method. From the analysis of the combined data obtained using two independent methods, the resulting flow regime maps for annular flows with and without DAF surfactant are shown in Fig. 5.1(a). A summary of observations for each flow regime follows:

- The 'dual-wave' regime is generated at low Re_{L} (approximately 500-800) and Re_{G} (approximately 0-25 $\times 10^3$). The base film is characterised by long wavelengths with , with an occasional appearance of waves with amplitudes (h_{waves}) 3-16 times higher than the thickness of the base film (h_{base}) (see Figs. 5.1(b) and (f)), depending on the flow conditions. Gas entrainment is rarely observed for the surfactant-free flows, while it is more frequent for surfactant-laden flows.

- The 'thick ripple' regime is encountered at similar Re_{G} (approximately 0-25 $\times 10^3$), but at higher Re_{L} (ranging from 850 to about 1250). The frequency and amplitude of interfacial waves appear to increase compared to the 'dual-wave' regime (see Figs. 5.1(f)), which lies primarily in the similarity of these waves to the structure of quiescent base films of higher thickness. Ripple-like waves of small amplitude and short wavelength also appear at the base film. Rare gas entrainment in the bulk film is observed in the front of the travelling waves (Figs. 5.1(b)) for surfactant-free flows, while more frequent and larger bubbles are found in surfactant-laden flows.

- The 'disturbance wave' regime occurs at similar Re_{G} as the aforementioned regimes, but at the highest Re_{L} explored (1125-1375 and 1250-1375 for surfactant-laden and surfactant-free flows, respectively) in this work (Table 3.2). The range of this flow regime is spec-

ulated to extend to even higher Re_L and is characterised by the appearance of irregular large amplitude waves of shorter wavelength than those of the base film, carrying small amplitude waves (Figs. 5.1(d) and (f)) [186]. Disruption of these disturbance waves by the co-current gas stream leads to the creation of droplets that are then entrained into the gas core [11, 73, 80], and to the entrapment of gas by the liquid film in the form of bubbles [71]. Details of these events are discussed further below.

- The 'regular wave' regime appears at all tested Re_L, but only once the Re_G is increased above 25×10^3. The enhanced gas shear has a prevailing effect on the film flow, generating waves of short wavelength and increased amplitude (Fig. 5.1(e)) in a regular (repetitive) manner – clearly seen in the film thickness time-trace of Fig. 5.1(f). The frequency of interfacial waves increases with Re_G. This trend is even more pronounced as the gas shear increases for the film flows at 'regular wave' regime. A significant increase in gas entrainment is observed across the whole film bulk, which can be attributed to a marked increase of interfacial disturbances.

The a wide-range of flow conditions explored herein, allows for a more detailed identification of the flow regime boundaries compared to previously reported flow regime maps in downwards annular flows. The resultant boundaries for surfactant-free flows were found to be in good agreement with the results and observations made by Webb and Hewitt [175], and Zadrazil et al. [186], where in the latter study the same pipe material and internal diameter was used as in the present work.

By analysing the characteristics of each flow regime from S-PLIF images and CP time-traces for every flow condition, it was found that flow regimes for two flow conditions have changed for the surfactant-laden flows (Fig. 5.1(a)). At $Re_L = 500$ and $Re_G = 30 \times 10^3$ it was identified that the flow regime shifted from 'dual-wave' to 'regular wave' relative to the surfactant-free flows (see Fig. 5.1(a)). The first evident characteristics observed from instantaneous S-PLIF images and film time-traces (for the latter see Fig. 5.2(a) and (b)) of this shift are the increase in the frequency of large waves (defined as the number of samples with $h > 2\times$ over the total) by $\sim 22\%$, and decrease in their mean height (i.e., waves with $h > 2 \times \langle h \rangle$) by $\sim 26\%$. For the surfactant-free flows (qualitatively visible from the film time-traces shown in Fig. 5.2(c) and (d)), the frequency and the mean amplitude of large waves increase by $\sim 8\%$ and $\sim 38\%$, respectively. As a result of a stronger coupling between gas and liquid phases due to increased gas flow rate, the peaks of the waves with sufficiently high amplitude are sheared by high gas flow
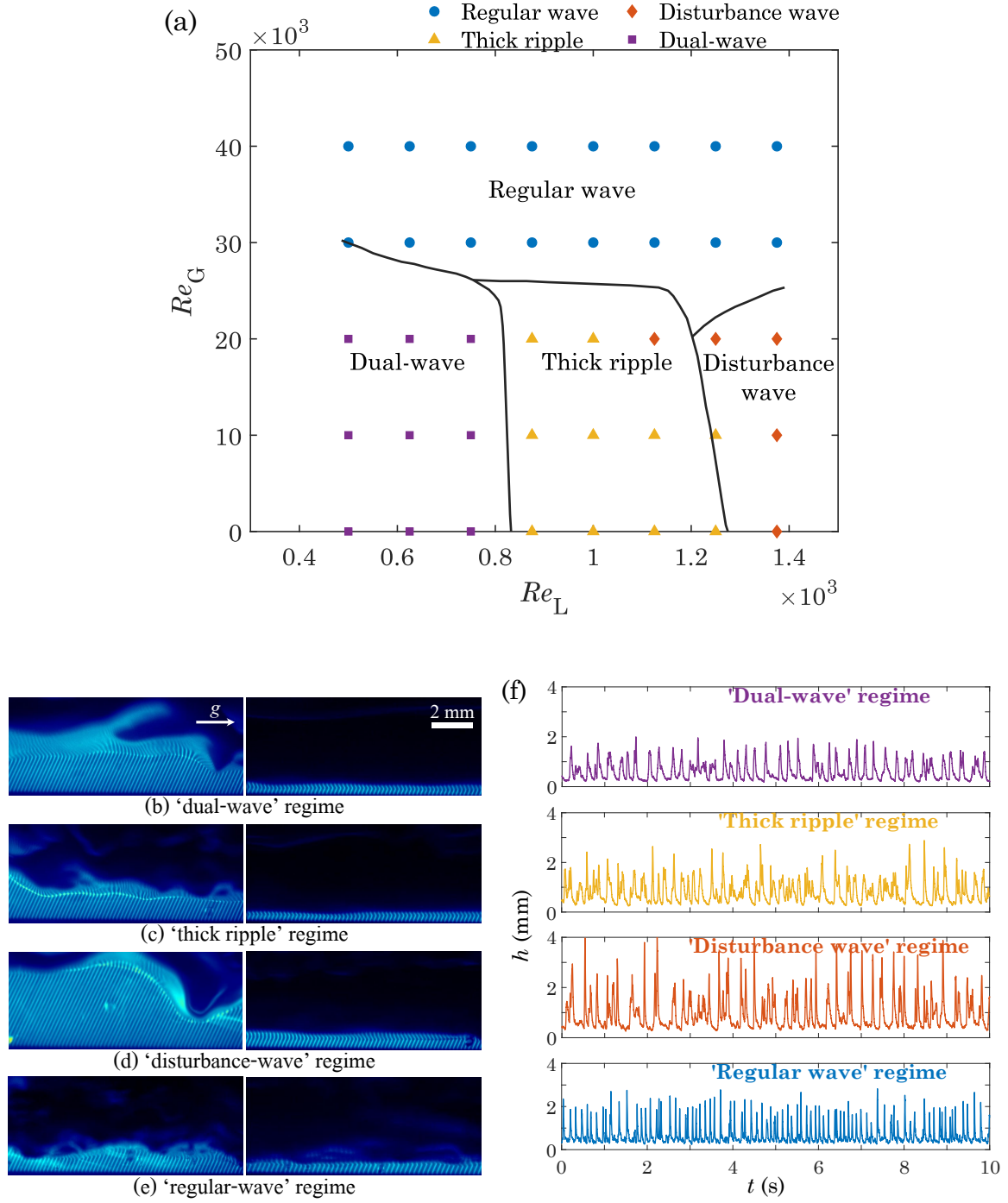
Figure 5.1: Flow regime classification. (a) Flow regime map produced from a series of S-PLIF images and instantaneous images of wave fronts and base films for the flow conditions listed in Table 3.2. The continuous lines represent the boundaries obtained for the surfactant-free cases, while filled shapes represent surfactant-laden cases; (b)-(e) typical instantaneous S-PLIF images (clean case) for each flow regime encountered (left: wave front; right: base film); (b) $Re_L = 625$ and $Re_G = 0$; (c) $Re_L = 1000$ and $Re_G = 0$; (d) $Re_L = 1375$ and $Re_G = 20 \times 10^3$; (e) $Re_L = 1250$ and $Re_G = 40 \times 10^3$. The scale bar has a length of 2 mm. The flow direction aligns with the direction of the acceleration of gravity, which is depicted by the symbol g; (f) time-traces obtained using the capacitance probe method, corresponding to the flow conditions of (b)-(e).

stream limiting the highest attainable wave amplitude, forming droplets and ligaments that are entrained into the gas core [11, 129]. The presence of surfactant reduces the interfacial tension which, in turn, lowers the required shear force exerted by the gas on the interface to give rise to entrainment events via various physical mechanisms such as, for instance, 'wave-undercut' [186]. As a result of this, it was shown previously by Alamu and Azzopardi [3], and James et al. [81] that these mechanisms lead to an increase in droplet entrainment and subsequent droplet deposition on the film as well as entrainment of gas pockets by wave breakage [186]. Additionally, a steep reduction in the film roughness (normalised to mean film thickness) by $\sim 28\%$ is observed for surfactant-laden flows, while it increases by $\sim 6\%$ for surfactant-free flows when Re_{G} is increased from 20×10^3 to 30×10^3 at $Re_{\mathrm{L}} = 500$. This change is delayed in the surfactant-free case to Re_{G} value of 40×10^3 (see Fig. 5.2(e)) at which the normalised film roughness also follows a rapid reduction by $\sim 29\%$. Another typical feature of a 'regular wave' regime is high gas entrainment (see Chapter 7), which was also qualitatively confirmed for the flow condition of $Re_{\mathrm{L}} = 500$, $Re_{\mathrm{G}} = 30 \times 10^3$ in the presence of DAF surfactant, while no marked entrainment is observed for the same flow condition without the surfactant (see Fig. 5.3).

For $Re_{\mathrm{L}} = 1125$, and following an increase of Re_{G} from $Re_{\mathrm{G}} = 10 \times 10^3$ to $Re_{\mathrm{G}} = 20 \times 10^3$, it was found that the flow regime changes from 'thick ripple' to 'disturbance wave' for the surfactant-laden flows. It was observed that the frequency of large waves with amplitudes above 1.5 mm increases by approximately a factor of 4 (see corresponding time-traces in Fig. 5.4(a) and (b)). It is also evident that the structure of interfacial waves changes, where the frequency of waves with longer wavelengths has decreased and, instead, waves with higher amplitude and shorter wavelengths are created. This indicates that the mean wave amplitude increases while the mean base film thickness (i.e., film with $h \leq 2 \times \langle h \rangle$) decreases. In fact, it is observed that the former increases by $\sim 7\%$, and the latter decreases by $\sim 4\%$. For surfactant-free flows both characteristics are observed to decrease by $\sim 7\%$ and $\sim 10\%$, respectively. Moreover, the film roughness (normalised to internal pipe radius R) is also found to increase by $\sim 12\%$ for surfactant-laden flows, supporting the observed change in flow regime. The normalised film roughness for the same flow conditions is observed to increase by only $\sim 2\%$ for surfactant-free flows. In addition, from qualitative analysis of instantaneous S-PLIF images it was found that a trail of small-amplitude waves on the rear side of the large waves appeared more often, which agrees with the results of Rivera et al. [136] who studied upwards annular flows in the presence of soluble surfactant. Moreover, as is typical for this type of flow regime, a higher proportion of air bubbles are found to be entrained in the liquid film for surfactant-laden flows (see Chapter 7 for a more detailed qualitative and quantitative analysis). This is often a result
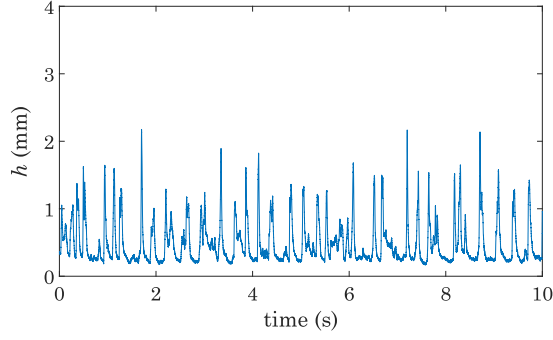
(a) $Re_L = 500$, $Re_G = 20 \times 10^3$ (surfactant case)
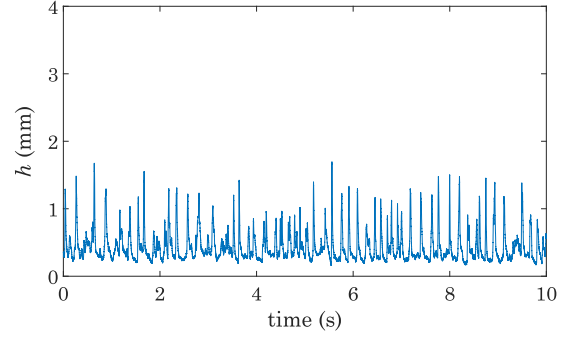
(b) $Re_L = 500$, $Re_G = 30 \times 10^3$ (surfactant case)
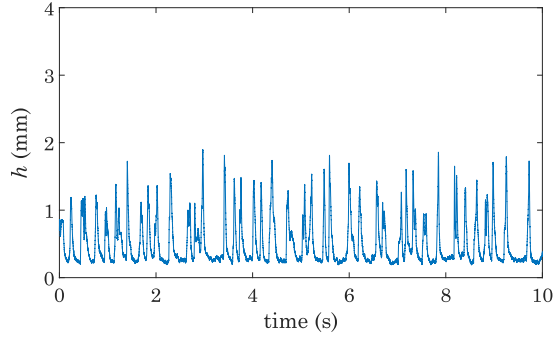
(c) $Re_L = 500$, $Re_G = 20 \times 10^3$ (clean case)
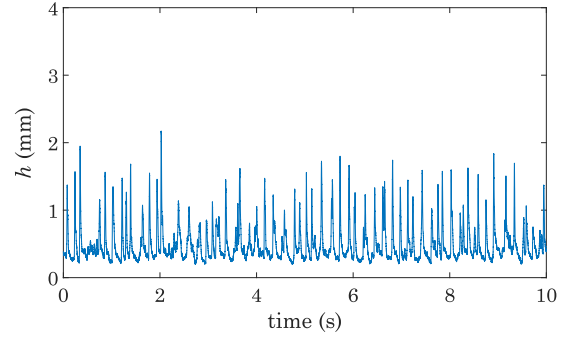
(d) $Re_L = 500$, $Re_G = 30 \times 10^3$ (clean case)
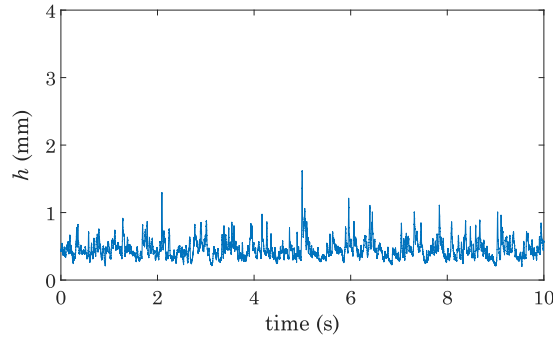
(e) $Re_L = 500$, $Re_G = 40 \times 10^3$ (clean case)

Figure 5.2: Time-traces obtained with the capacitance probe showing a change in the film behaviour during flow regime transition from 'dual-wave', (a) and (c), to 'regular wave', (b) and (e), as a function of Re_G at $Re_L = 500$ in the presence and absence of surfactants as shown in panels (a) and (b), and (c), (d), and (e), respectively.

(a) Base film (surfactant case) (b) Large wave (surfactant case)

(c) Base film (clean case) (d) Large wave (clean case)
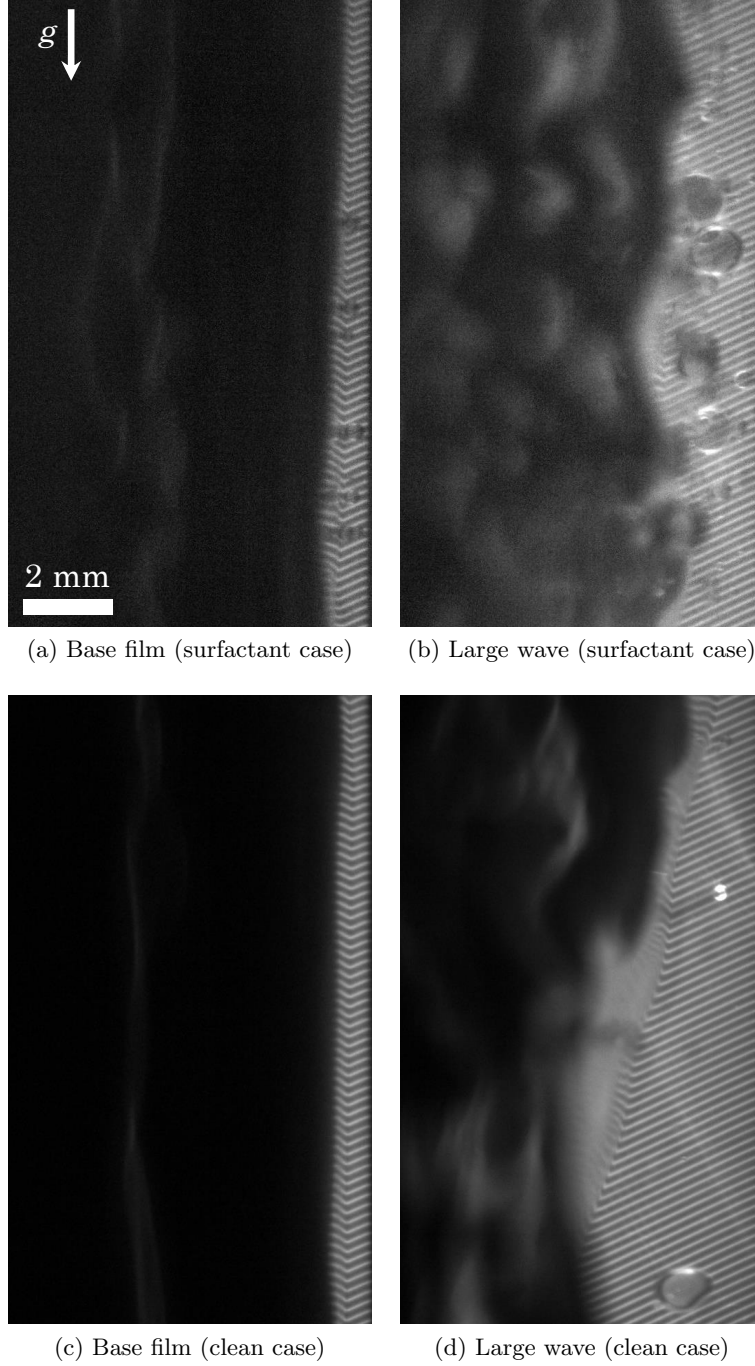
Figure 5.3: Typical instantaneous S-PLIF images of surfactant-laden ((a)-(b)) and surfactant-free ((c)-(d)) flows at $Re_L = 500$ and $Re_G = 30 \times 10^3$.

of increased interaction between the two fluid phases that induces the formation and disintegration of interfacial waves via mechanisms that are found to be responsible for gas and liquid entrainment [170, 177]. One type of such waves are small-amplitude waves (e.g., ripple waves) found at the rear of large waves that are responsible for significant liquid entrainment rate [4]. In comparison with the surfactant-free case for the same flow conditions, it is evident not only from the qualitative assessment (i.e., rare gas entrainment), but also from the absence of the aforementioned features seen on the corresponding time-traces (shown in Fig. 5.4(c) and (d)).

(a) $Re_\text{L} = 1125$, $Re_\text{G} = 10 \times 10^3$ (surfactant case)   (b) $Re_\text{L} = 1125$, $Re_\text{G} = 20 \times 10^3$ (surfactant case)

(c) $Re_\text{L} = 1125$, $Re_\text{G} = 10 \times 10^3$ (clean case)   (d) $Re_\text{L} = 1125$, $Re_\text{G} = 20 \times 10^3$ (clean case)
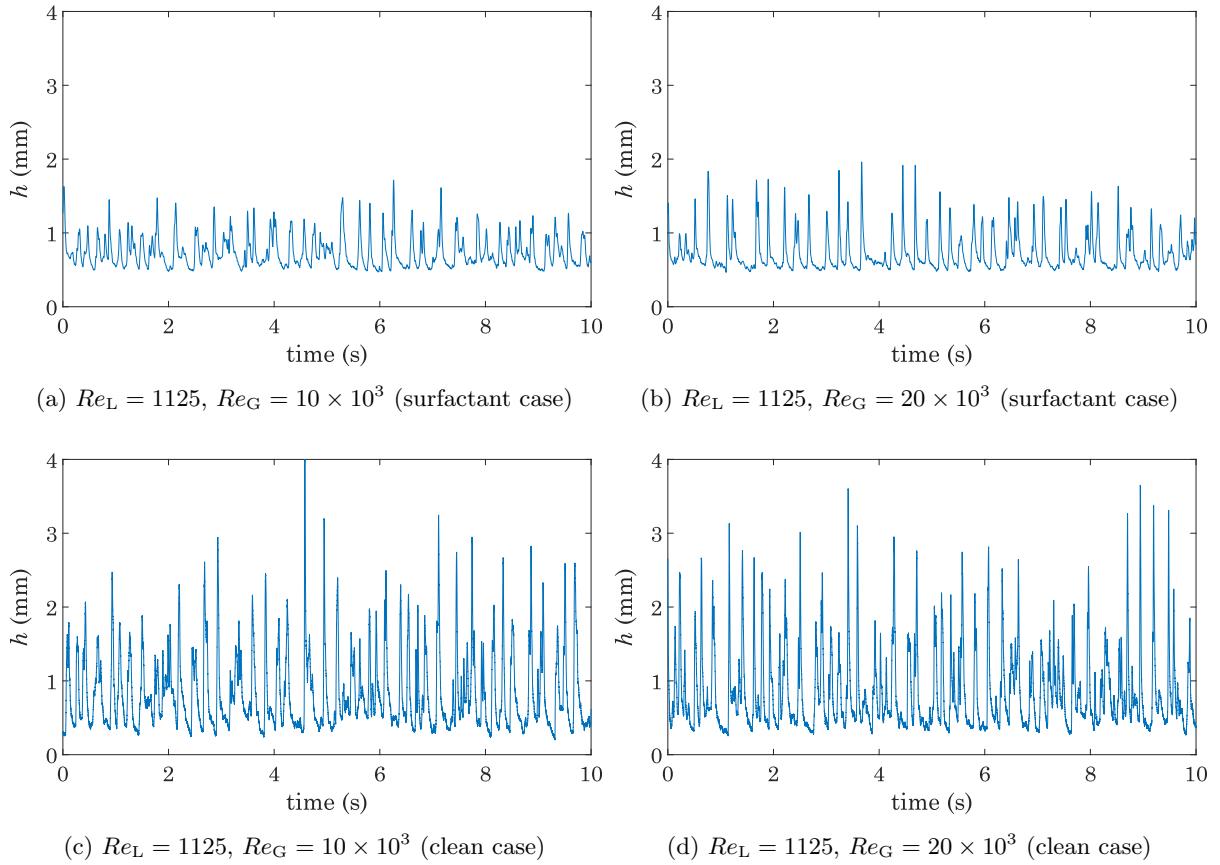
Figure 5.4: Time-traces obtained with the capacitance probe showing a change in the film behaviour during flow regime transition from 'thick ripple' to 'disturbance wave' for surfactant-laden flows (a) and (b) as a function of Re_G at $Re_\text{L} = 1125$, while 'thick ripple' regime is maintained for surfactant-free case at the same flow conditions (c) and (d).

5.2 Mean film thickness measurements

In order to further understand the behaviour of annular flows as a function of Re_L and Re_G (as per Table 3.2), data obtained using both S-PLIF and CP are analysed and presented below. The results for surfactant-free case are compared with surfactant-laden flows, and the resultant differences are examined. Figure 5.5 offers a comprehensive comparison between time-averaged film

thickness ($\langle h \rangle$) data of falling films ($Re_{\mathrm{G}} = 0$) obtained from the present study of surfactant-free and surfactant-laden flows, and for surfactant-free flows obtained from the available literature, from literature correlations, and from theoretical predictions. Three optical methods (variations of laser-induced fluorescence) have been previously employed for the same large-scale experimental facility (DAFLOF, described in Chapter 3), including PLIF and S-PLIF (both deployed at two different imaging angles, namely 70° and 90°) [32, 186], as well as BB-LIF [37]. Additionaly, this includes the experimental results obtained by Karapantsios et al. [85, 86] using a parallel-wire electrical conductance probe, Webb and Hewitt [175] using a conductance probe, as well as the results of Takahama and Kato [157] obtained with the needle contact and electric capacity methods. The Nusselt solution [123], developed for surfactant-free laminar falling films, as well as the correlation developed by Mudawwar and El-Masri [118] for surfactant-free turbulent falling films is also shown. According to Fig. 5.5, it was found that the time-averaged film thickness measurements of the optical method (S-PLIF70) and the capacitance probe are in good agreement with each other and with literature data for the range of conditions explored (Re_{L} values between 500 and 1375).

Evidently, the obtained results herein are in good agreement with the literature data. Data points from the present study and literature for low liquid Reynolds number ($Re_{\mathrm{L}} = 500$) is well-described by the Nusselt flow predictions. Experimentally measured film is found to be relatively flat at low Re_{L}, which meets the assumption of the Nusselt flow (i.e., absence of interfacial instabilities and a parabolic velocity profile), and hence, provides good agreement. But as the Re_{L} increases the theory begins to underpredict the mean film thickness due modified velocity profile and appearance of various interfacial instabilities in the form of waves that varies in amplitude. The present results for the surfactant-free flows show not only a very good agreement with the previously published experimental work, but also with the theoretical prediction for turbulent falling films.

Comparison between the surfactant-free film thickness measurements of Zadrazil et al. [186] (with PLIF90) and those conducted in the present work (with S-PLIF70 and the capacitance probe) show good agreement for falling films (Fig. 5.5), resulting in relative deviations < 8%. However, this percentage increases for gas-sheared films. Specifically, it is found that relative deviation between the PLIF90 film thickness measurements of Zadrazil et al. [186] and the S-PLIF70 is equal to approximately -11%, while the deviation between PLIF90 and the capacitance probe is equal to about -18%. The underestimation of the film thickness by PLIF90 can be attributed to the presence of stronger 'Type-II' errors [32] in gas-sheared flows, i.e., errors

due to refraction or total internal reflection of the light at the interface of a circumferentially non-uniform film. No statistically significant increase between the relative deviation and Re_G was found.

For the first time, such comparison is also performed for downwards annular falling films in the presence of water-soluble (fluorescent) surfactant. The measured data of time-averaged film thickness was found to be consistently lower for all Re_L relative to surfactant-free flows. Additional set of measurements for both S-PLIF and CP unveiled that the highest mean relative difference is less than 2.3% between two independent runs. Thus, the errors bars in all subsequent figures are omitted being smaller than the symbol size (applicable for Chapters 5 and 6). Moreover, the analysis of the effect of the number of samples per each image on the calculated values of the mean and standard deviation of the film thickness has showed that selection of 20 samples per image pair for every flow condition results in good statistical convergence and statistical independence between the samples (see Appendix A). The total uncertainty in the measurement of the instantaneous and local film thickness was 3 pixels, which corresponds to ± 0.05 mm (error bars omitted in Fig. 5.5 for the purpose of visual clarity).

In order to further develop our understanding of surfactant-induced effects on the behaviour of annular films, the effect of the gas shear (i.e., $Re_\mathrm{G} > 0$) on the time-averaged film thickness and its standard deviation is also investigated. Figures 5.6(a) and (b) provide the time-averaged film thickness measurements (normalised on the internal pipe radius, R) for the clean and surfactant cases, respectively, acquired using the S-PLIF method. Similarly, Figures 5.6(c) and (d) show the data acquired using the capacitance probe method for the clean and surfactant cases, respectively. In accordance with the literature [186], a quasi-linear increase (decrease) of the film thickness with Re_L (Re_G) is expected for the range of conditions investigated. Both measurement methods capture this trend for the surfactant-free and surfactant-laden flows.

A minor difference ($< 4\%$) is observed in the relative film thickness for nearly every Re_L value when increasing Re_G from $Re_\mathrm{G} = 0$ to $Re_\mathrm{G} = 20 \times 10^3$ for each individual case in the presence and absence of surfactant. Only for some flow conditions, this difference is above 4% with the highest being at 7.5% for the S-PLIF, and 9% for the CP data. It is also observed that the percentage difference is narrower for the surfactant-laden flows than for the surfactant-free flows. Referring back to the flow pattern map shown in Fig. 5.1, the annular flows within this range of flow conditions behave as one of the three flow regimes (i.e., 'dual-wave', 'thick ripple' or 'disturbance wave'), which differ more by the activity of interfacial waves rather than by
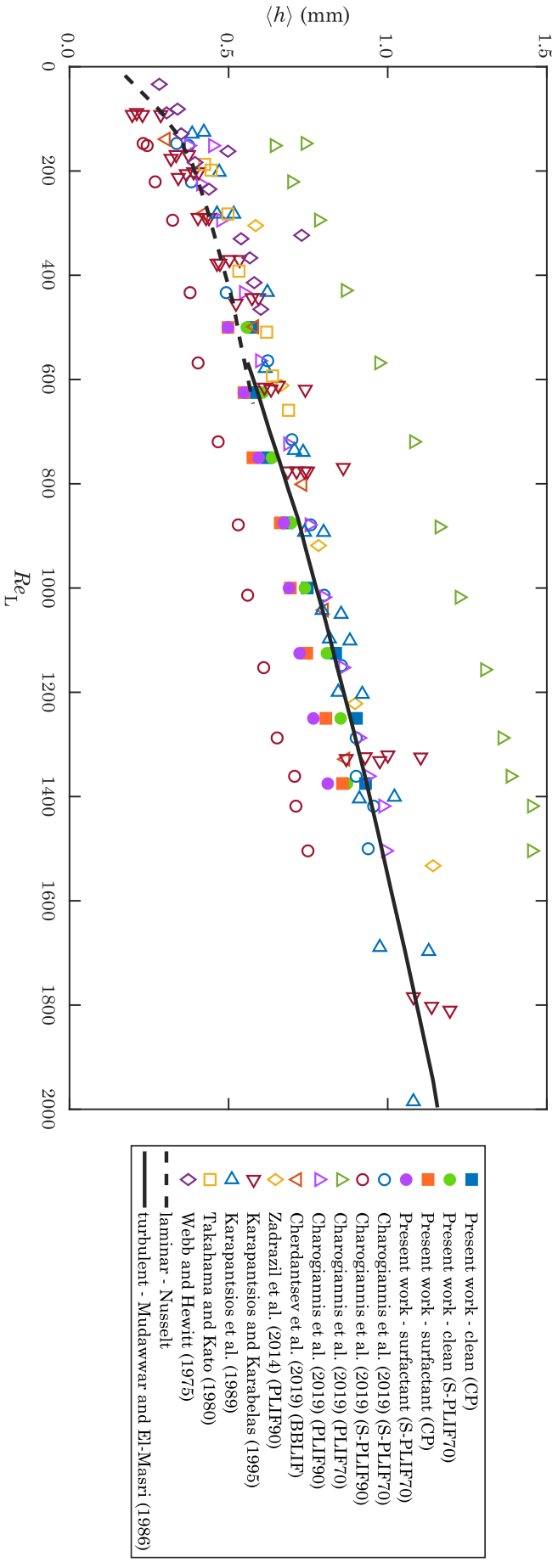
Figure 5.5: Time-averaged film thickness measurements obtained for falling films ($Re_G = 0$) with S-PLIF and the capacitance probe as a function of the liquid Reynolds numbers. The results are compared to measurements from other investigators.
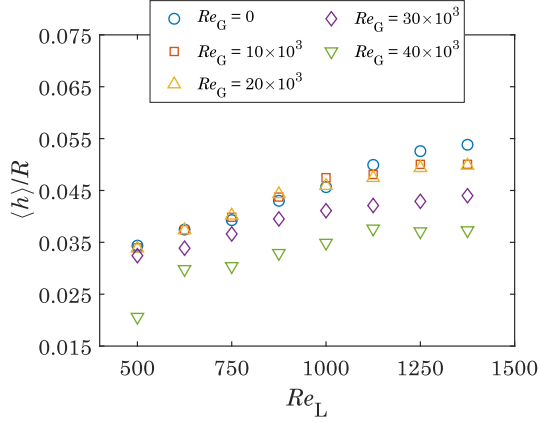
(a) S-PLIF (clean case) (b) S-PLIF (surfactant case)
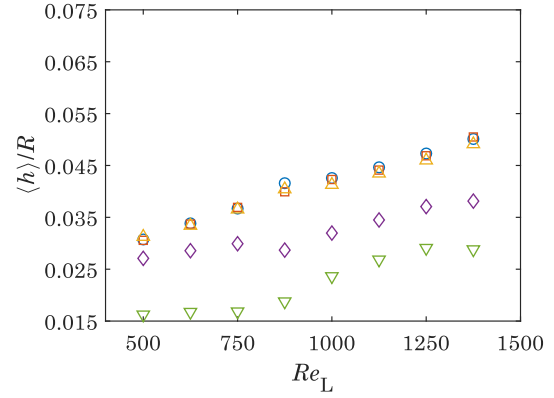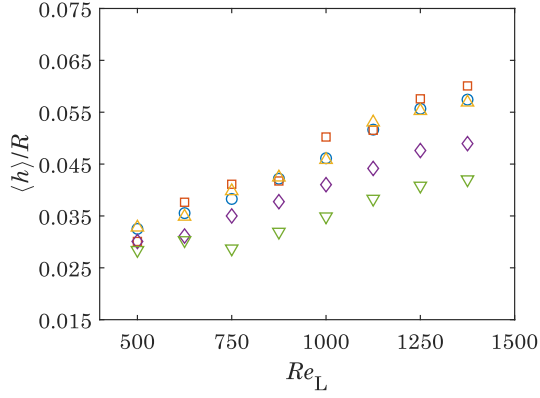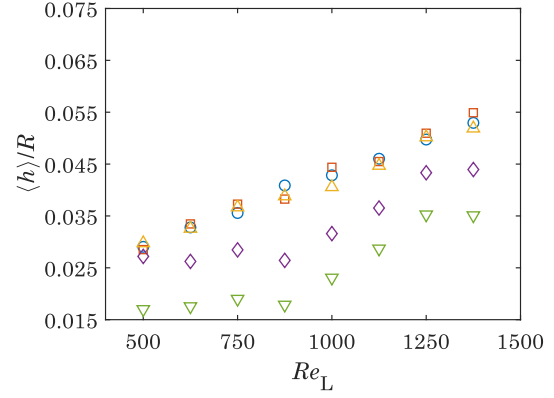
(c) Capacitance probe (clean case) (d) Capacitance probe (surfactant case)

Figure 5.6: Time-averaged film-thickness measurements, normalised by the pipe radius R, as a function of the liquid Reynolds number, Re_L, with Re_G varying parametrically.

the reduction in the film height (discussed further below). Only as the Re_G is set to a value of 30×10^3 does film thinning become sufficiently pronounced. The high shear stress exerted by the gas stream increases not only the velocities of the waves and the bulk film, but also leads to a substantial change in the interfacial topology that may accelerate liquid and gas entrainment events that were shown to occur through various mechanisms particularly at these flow conditions [11, 80, 186]. This is one of the main characteristics of the 'regular wave' regime described in the previous section.

One of the striking difference between the surfactant-free and surfactant-laden flows is observed in the relative film thickness, where it is found to decrease in the presence of surfactant for nearly all applied flow conditions measured with both S-PLIF and CP methods. The root-mean-square error (RMSE) between the two cases for the S-PLIF and CP measurements are 0.074 mm and 0.077 mm, respectively. The only values for relative film thickness with insignif-

icant difference between the two cases are found for S-PLIF at $Re_\mathrm{L} = 1375$ and Re_G between 10×10^3 and 20×10^3 where $\langle h \rangle / R \approx 0.05$. This may be due to the high thickness of the film and wave amplitudes that are less affected by the surfactant (discussed further in Chapter 6). The extent of the film thinning for the surfactant-laden flows is found to be greater under flow conditions with high gas shear ($Re_\mathrm{G} \geq 30 \times 10^3$), evident from the individual data sets obtained using S-PLIF and CP methods. This can potentially occur due several reasons. Firstly, DAF surfactant can have similar effects on the film flow dynamics as drag-reducing agents, particularly in thinner films and high gas shear rate, which were shown to increase the wave velocity [150, 164]. Interfacial waves are known to carry the highest amount of energy in the shape of the liquid film interface (this will be discussed more closely in Chapter 6) [186]. The fast-moving small amplitude waves (defined in Chapter 2) were shown to be the key drivers of liquid entrainment into the gas core in the form of small droplets [4, 5, 15]. Thus, upon a potential increase of the wave velocity for surfactant-laden flows, the observed film thinning may also occur due to the greater disintegration of the small waves that may also result in the higher entrainment rate and formation of initially larger droplets [153]. What is more, a sufficiently high gas flow strongly interacts (by shearing stress) with the crests of the large waves potentially resulting in the formation of small droplets that become entrained into the gas core, and the gas entrainment into the liquid film. The latter was found to occur particularly at the crests and beneath of the large waves in surfactant-laden flows (discussed further in Chapter 7). This is in agreement with the extensive work by Nimwegen et al. [170] which has experimentally demonstrated that the presence of surfactant in upwards annular flows leads not only to an increase of gas entrainment rate in the bulk film, but also the respective size of the gas bubbles, which also promotes liquid entrainment through 'bubble burst' mechanism [73]. Additional details on the mechanisms of the above phenomena, and further reasoning for the observed film thinning must be analysed together with the film roughness data which is discussed in the following section.

To date, many experimental campaigns were performed with an aim to use the obtained data to construct different correlations that could predict flow characteristics for various flow conditions, flow configurations and fluid properties. Particularly for an air-water system, one of such studies was performed by Ishii and Grolmes [80] who developed a correlation that predicts film thickness in vertical annular flows. Herein, this correlations is employed to estimate and compare the corresponding values with the results of the present work (as per Fig. 5.6). To estimate liquid film thickness a following correlation was proposed:

$$h = 0.347 Re_\mathrm{L}^{2/3} \left(\frac{\rho_\mathrm{L}}{\tau_\mathrm{int}} \right)^{0.5} \frac{\mu_\mathrm{L}}{\rho_\mathrm{L}} \tag{5.1}$$

where τ_{int} is the interfacial shear stress defined as

$$\tau_{\text{int}} = \frac{1}{2} f_{\text{int}} \rho_{\text{G}} \left(u_{\text{s,G}} - u_{\text{s,L}} \right)^2 \tag{5.2}$$

where f_{int} is the interfacial friction factor, which can be calculated using Wallis correlation,

$$f_{\text{int}} = f_{\text{G}} \left(1 + 300 \frac{\langle h \rangle}{D} \right) \tag{5.3}$$

where $\langle h \rangle$ is the experimentally measured mean film thickness, and f_{G} is the single-phase gas friction factor, typically defined as

$$f_{\text{G}} = \frac{0.079}{Re_{\text{G}}^{0.25}} \tag{5.4}$$

The predictions of the film thickness h (normalised by the internal pipe radius R) using correlation expressed in Eq. 5.1 for the corresponding air-water flow conditions as per Table 3.2 (except for $Re_{\text{G}} = 0$) are shown in Fig. 5.7. For the surfactant-free and surfactant-laden flows, the correlation increases in an approximately linear manner in agreement with the experimental data, but it appears to over-predict the film thickness for all Re_{L} values at $Re_{\text{G}} = 10 \times 10^3$ by $\sim 30\%$ to $\sim 50\%$. Once the Re_{G} increases to 20×10^3, the correlation results are under-predicted relative to the present experimental data, but with better agreement than for the previous low gas-shear rate i.e., difference was found to range between $\sim 7\%$ and $\sim 30\%$. This shows the sensitivity of the correlation to the shearing effects on the liquid film exerted by the high gas flow rate. The difference between the predicted and experimental values for surfactant-free flows at $Re_{\text{G}} \geq 30 \times 10^3$ increases and ranges between $\sim 20\%$ and $\sim 55\%$. On the other hand, for the surfactant-laden flows, the predicted values are in better agreement with a difference reaching as low as $\sim 1\%$ and a maximum of $\sim 35\%$, whilst the majority of the data points are within a 20% difference. It is worthy of note that no reliable correlations were found in the literature for vertical annular flows that account for the effect of surfactant in terms of surface tension reduction. Evidently from the aforementioned results, surfactant has a marked difference on the film thickness, and alters the liquid film flow behaviour, particularly at high gas shear rates. Possible corrections to the present model are discussed further in Chapter 8.
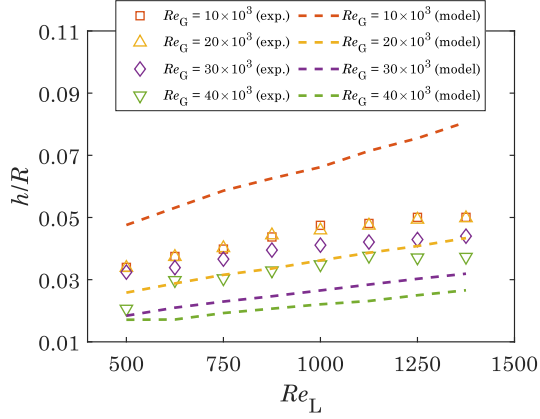
(a) S-PLIF (clean case)
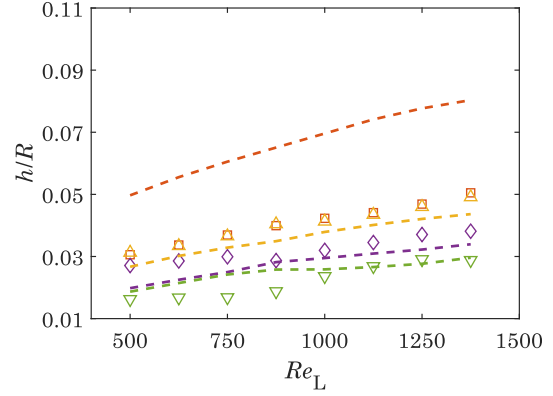
(b) S-PLIF (surfactant case)
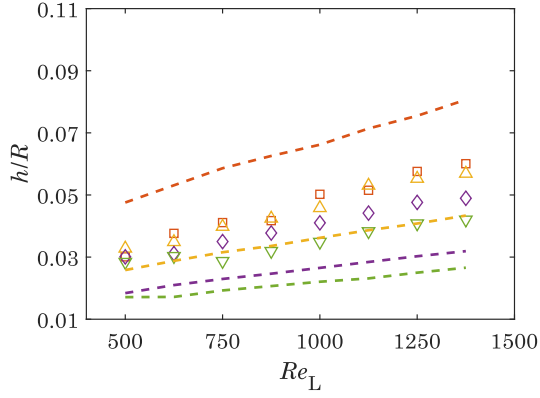
(c) Capacitance probe (clean case)
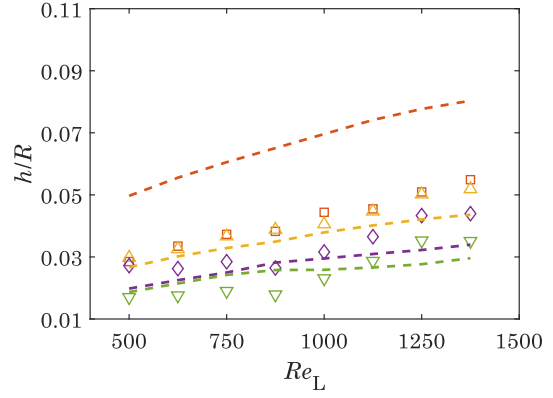
(d) Capacitance probe (surfactant case)

Figure 5.7: Results of film thickness normalised to internal pipe radius R obtained from the present experiments (hollow shapes) and correlation using Equations 5.1–5.4 (dashed lines) displayed as a function of the liquid Reynolds number.

5.3   Annular film roughness

The variation over time of the film thickness for the investigated flow conditions (Table 3.2) in the absence/presence of DAF surfactant was also measured by both S-PLIF and CP methods as outlined in Chapter 3. By taking the square root of the second moment (i.e., variance), the standard deviation of the recorded film thickness is obtained, and is termed here as the film 'roughness'. Since it provides an indication of how closely the values are spread about the mean, it is normalised here either with internal pipe radius R or the mean film thickness h, where the latter value corresponding to each individual flow condition is used. These two datasets have revealed several interesting trends outlined further below.

By firstly investigating the film roughness normalised to R (shown in Figure 5.8), it was
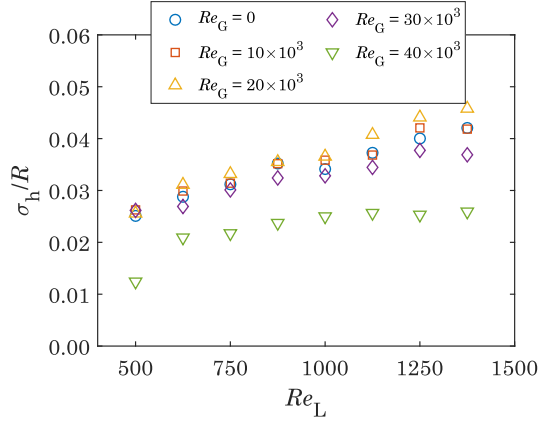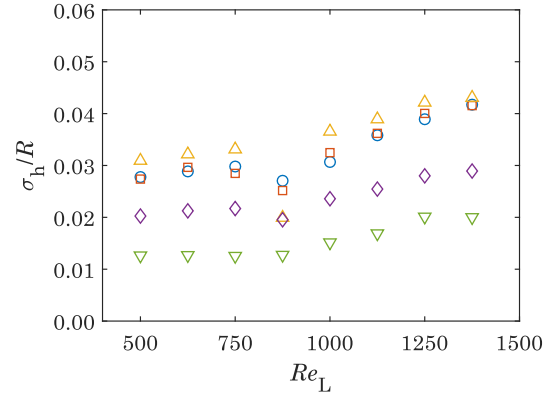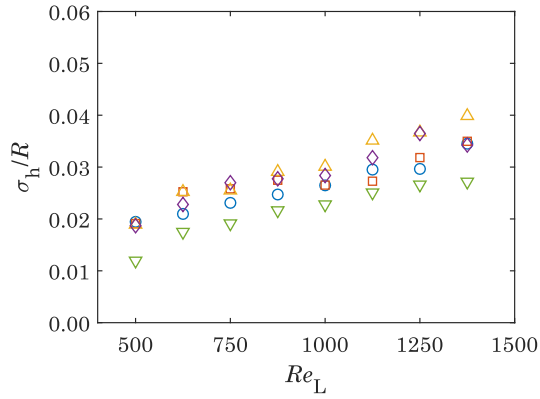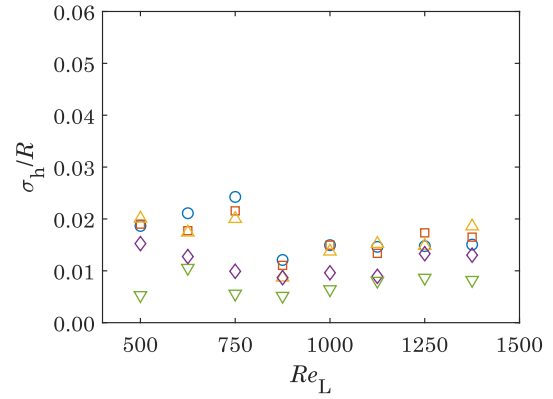
Figure 5.8: Measurements of film roughness normalised to internal pipe radius R displayed as a function of the liquid Reynolds number.

found that it follows a pattern of increasing value with Re_L in agreement with experimental literature data for the surfactant-free case (downwards flows [186]) and for the surfactant-laden flows (upwards flows [136]). In contrast, the pattern is observed to vary when gas Reynolds number increases. For surfactant-free and surfactant-laden flows, the σ_h/R for all Re_L values is practically unaffected by an increase in Re_G from 0 to 10×10^3. This may be due to insufficient shear force exerted by the gas stream to interact with the liquid film and generate higher interfacial disturbances, particularly when the film is thin (i.e., at low Re_L values). Only as the Re_G is set to 20×10^3, does σ_h/R increase above that associated with the previous two gas flow conditions (see Fig.5.8(a)-(c)). Although the mean film thickness remains very similar at these flow conditions (as shown earlier in Fig. 5.6), a higher gas shear rate potentially interacts more with the flowing film not only at the inlet which induces additional interfacial disturbances in the form of Kelvin-Helmholtz (K-H) waves, but also along the whole flow pathway resulting in greater film destabilisation and formation of solitary three-dimensional waves [7, 6]. As a

89

result of this, it may increase the probability of gas and liquid entrainment events [11]. In fact, such behaviour can be linked to the flow regime transition from 'dual-wave' to 'thick ripple' or 'disturbance wave'. Since the mean film thickness is observed to vary very little, it can be deduced that the mean film velocity grows with Re_{G} [185]. Increasing Re_{G} further to 30×10^{3} and 40×10^{3} begins to lower the σ_{h}/R for the surfactant-free and surfactant-laden flows (except in the former case at $Re_{G} = 30 \times 10^{3}$ measured using CP, which remains close to the values obtained at $Re_{G} = 20 \times 10^{3}$, see Fig. 5.8(c)). At these flow conditions, the film enters 'regular wave' flow regime at which the gas shearing is sufficiently high which limits the maximum attainable amplitude by the waves and the base film. Moreover, the slope for increasing Re_{L} decreases, which is particularly visible at the highest Re_{G} value (i.e., $= 40 \times 10^{3}$). For flows in the presence of DAF surfactant, the extent of the reduction of the σ_{h}/R at two highest gas Reynolds numbers is greater relative to these flow conditions for flows in the absence of surfactant. This may occur due to an observed increase in the gas entrainment and foam wetness, which, as a result, protects thin annular film from direct shearing effects exerted by the high gas flow stream and dampens interfacial waves, particularly large waves [170]. The evidence of gas entrainment events are discussed further in Chapter 7.

Mixed patterns in σ_{h}/R were recorded using capacitance probe for flows in the presence of DAF surfactant (see Fig. 5.8(d)). Firstly, a sudden decrease in σ_{h}/R at $Re_{L} = 875$ for Re_{G} values ranging between 0 and 20×10^{3} has been recorded, which agrees with the trend obtained using S-PLIF method, although the recovery of the values is not as rapid with Re_{L}. With further increase of Re_{L} above 875, the σ_{h}/R increases between approximately 20% to 37% (with Re_{G}), and maintains a relatively stable σ_{h}/R values ranging between ≈ 0.013 and 0.019 for all flow conditions at $Re_{G} = 0$ to 20×10^{3}. A similar pattern is also observed for $Re_{L} \leq 875$ at Re_{G} values of 30×10^{3} and 40×10^{3} at which σ_{h}/R first decreases and then follows a gradual increase as Re_{L} exceeds a value of 875. As explained earlier, this may be due to the fact that in the presence of surfactant the thickness of the base film increases while the height of the waves decreases (this is investigated further below with σ_{h} normalised to $\langle h \rangle$). The mean relative difference of σ_{h}/R between the cases with and without DAF surfactant is measured at 13.5% and 48.9% for data acquired using S-PLIF and CP methods, respectively. Since it was found that the normalised film thickness ($\langle h \rangle/R$) is affected mainly in a decreasing manner due to the presence of DAF surfactant (see Fig. 5.6 in the previous section), the normalisation of the film roughness to the corresponding mean film thickness for each flow condition would describe the observed pattern more accurately.
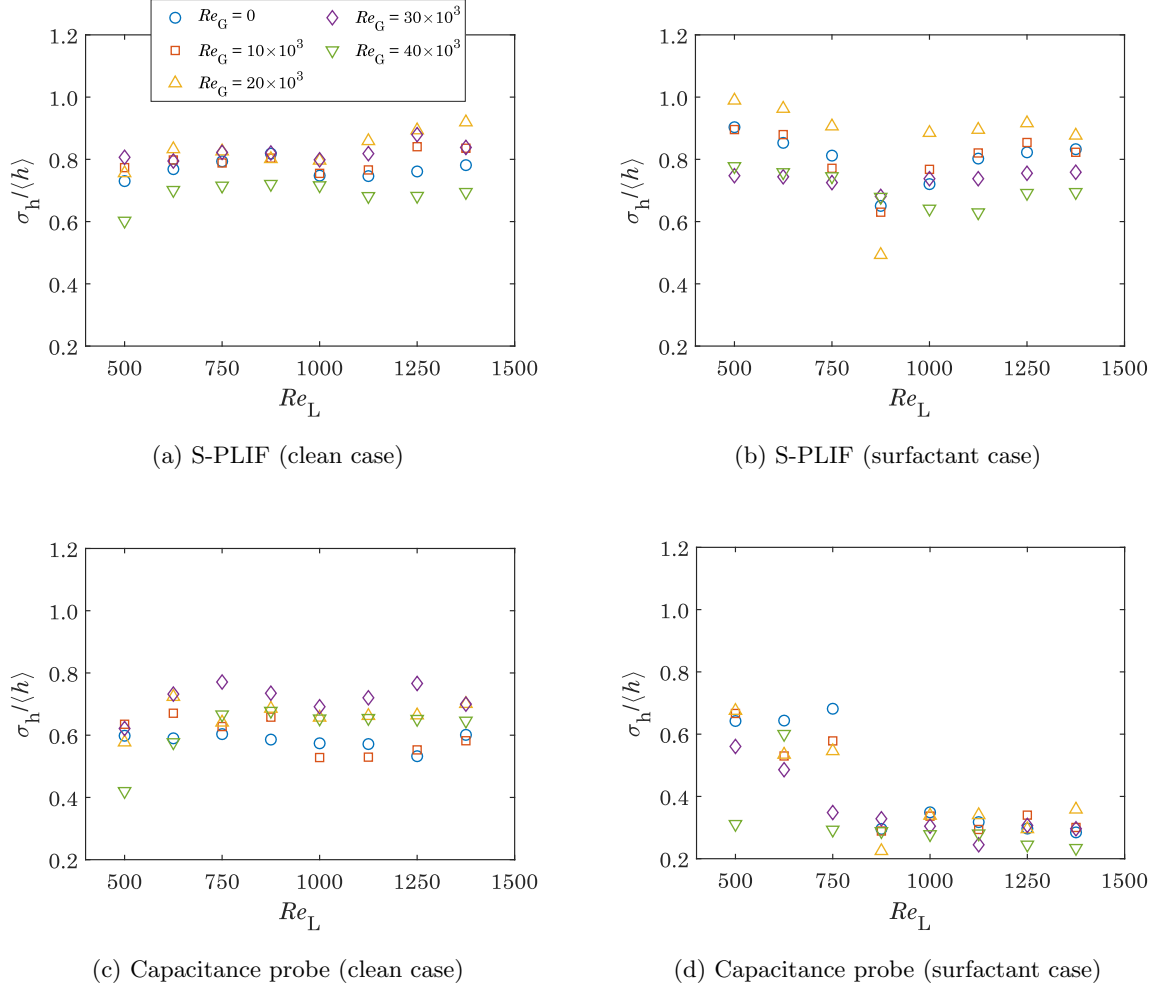
Figure 5.9: Measurements of film roughness normalised to individual mean film thickness h displayed as a function of the liquid Reynolds number.

From the Fig. 5.9, it can be deduced that generally a decreasing pattern of $\sigma_\mathrm{h}/\langle h \rangle$ with both Re_L and Re_G is observed for surfactant-laden flows, whilst for surfactant-free flows Re_L has nearly no effect, while Re_G also has a decreasing pattern (see Fig. 5.9). In the surfactant case, it is evident that Re_G has a more pronounced effect on $\sigma_\mathrm{h}/\langle h \rangle$ than Re_L. As a matter of fact, increasing liquid Reynolds number results in the higher probability of wave coalescence, which subsequently leads to formation and increase in the frequency of large waves rather than small waves, and thus, thickening of the base film [6]. This is also directly linked to the change of flow regimes discussed in the previous section, and will be further evidenced in Chapter 6 by exploring these effects on thickness of the base film and large waves, and the frequency of interfacial waves.

Increasing the gas shear rate (up to Re_G values of 20×10^3 and 30×10^3 for flows with DAF and without it, respectively), initially has an increasing pattern, as observed from the

S-PLIF data, followed by a rapid decrease above this gas flow rate (observed by both S-PLIF and CP methods). The influence of Re_G on $\sigma_h/\langle h \rangle$ is substantially higher for surfactant-laden flows than for surfactant-free flows. This is due to the observed destabilisation of the base film by generation of additional periodic small amplitude interfacial waves (examined more closely in Chapter 6). This is in precise agreement with results of Furukawa et al. [61] and Matsuyama et al. [114]. In their experiments for upwards annular flows with soluble surfactant they also found the roughness of the base film to increase, which subsequently increases interfacial friction force driving the base film faster. The obtained velocities of the small amplitude waves were shown to increase for surfactant-laden flows, which, in both cases, supports the reason not only for the presently increased normalised film roughness ($\sigma_h/\langle h \rangle$) at $Re_G \leq 20 \times 10^3$, but also for the marked film thinning for the surfactant-laden flows shown earlier in Fig. 5.6. Experimental work by Setyawan et al. [147] investigated the effect of soluble surfactant on the interfacial wave velocities in horizontal flows. Similarly to the results of Furukawa et al. [61] and Matsuyama et al. [114], their findings also reveal that the wave velocities increase for surfactant-laden flows (relative to the surfactant-free case) at superficial liquid velocities similar to those used in the present work. Moreover, their results agree with the current findings on the reduction of frequency of large waves for surfactant-laden flows, particularly at lower range of Re_L and higher values of Re_G (discussed in the Chapter 6). They also found that the difference in the film velocity between clean and surfactant cases increases with increasing liquid Reynolds number. This partly justifies the observed increasing difference in the mean film thickness $\langle h \rangle$ with Re_L for the falling films (Fig. 5.5) as well as gas sheared films (Fig. 5.6) between the flows in the absence and presence of DAF surfactant.

The observed reduction in height of large waves and additional film thinning for surfactant-laden flows may also occur due to an increase in liquid entrainment in the form of droplets of various sizes into the gas core. Numerous well-known experimental works (e.g., Hanratty and Hershman [72], Hewitt and Hall-Taylor [73], van Rossum [172]) were among the first ones to have qualitatively demonstrated that the peaks of large amplitude waves are sheared-off from the wave crests by the parallel turbulent gas flow. It was proposed that the drag force acting on the wave tops deforms the interface against the restraining force of the liquid surface tension. In the presence of surfactant (or reduced surface tension for the same fluid viscosity) this phenomenon is likely to be enhanced. An additional mechanism by which liquid entrainment occurs is through instabilities induced by the gas stream that creates small amplitude (ripple) waves that travel over the large amplitude (disturbance/roll) waves until these get disrupted and broken-up. The mechanism for this event was clearly demonstrated and explained by

Woodmansee and Hanratty [177]. Primarily, liquid entrainment was shown to occur due to imbalance between the pressure variations in the air flowing over wavelets and the stabilising forces of gravity and surface tension, which is known as Kelvin-Helmholtz (K-H) instability. It was shown that for K-H instability to occur a critical gas velocity needs to be reached which reduces when the surface tension is lowered, which again, may reason the observed variation in $\sigma_{\mathrm{h}}/\langle h \rangle$ (see Fig. 5.9). This instability grows as both Re_{L} and Re_{G} increases (with latter having a greater effect) inducing the amplitude and the frequency of large and small waves (seen from the flow regime transitions discussed earlier). More recently, this was confirmed by Alekseenko et al. [5, 6, 7] using optical diagnostic techniques, and Pham et al. [129] using high-speed imaging.

Interestingly, a potentially higher rate of liquid entrainment occurring due to the shearing-off the crests of the large waves by the turbulent gas stream may also lead to additional energy dissipation, and thus, reduction in its wave velocity, which supports the observations of the aforementioned studies by Furukawa et al. [61] and Setyawan et al. [147]. Moreover, these large waves are formed and grow in size and velocity through coalescence with other waves, but since it is predicted that the development length increases for surfactant-laden flows (see discussion in Chapter 6), a lower frequency of large waves would be expected, which is in agreement with findings of the present study. This indicates that the coalescence events are more infrequent for surfactant-laden flows than in the surfactant-free flows, despite the recorded higher frequency of waves with smaller amplitudes in the former case. In fact, it was shown by Alekseenko et al. [6] that the absence of coalescence of waves results in deceleration and reduction in amplitude of large waves. Moreover, small amplitude waves were shown to carry the highest amount of energy in the shape of the liquid film interface [186], hence, the recorded thinner films (with DAF surfactant) that potentially are flowing at a higher velocity relative to the clean films.

Further increase in the gas Reynolds number ($\geq 30 \times 10^3$) for surfactant-laden flows substantially decreases $\sigma_{\mathrm{h}}/\langle h \rangle$, which is due to the observed formation of 'foamy' crests of large waves and overall increase in gas entrainment close to and beneath the film surface (further details in Chapter 7). This agrees with qualitative observations by Nimwegen et al. [171] who showed that such foams result in suppression of large interfacial waves as well as reduction in the liquid entrainment in the form of large droplets. In addition, the presence of foam (or high fraction of entrained gas in the form of bubbles) above the annular liquid film increases the interfacial friction which potentially leads to faster flow of the foam, subsequently increasing the velocity of the underlying liquid film, which supports the observed film thinning shown in Fig. 5.6 [171].
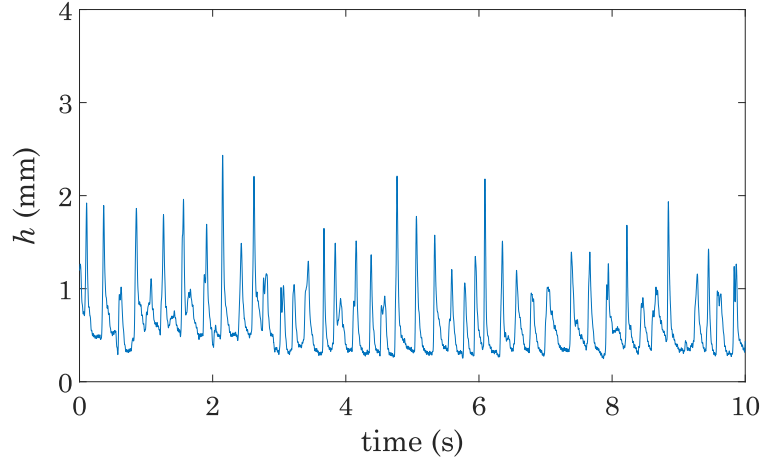
(a) $Re_L = 750$ and $Re_G = 20 \times 10^3$
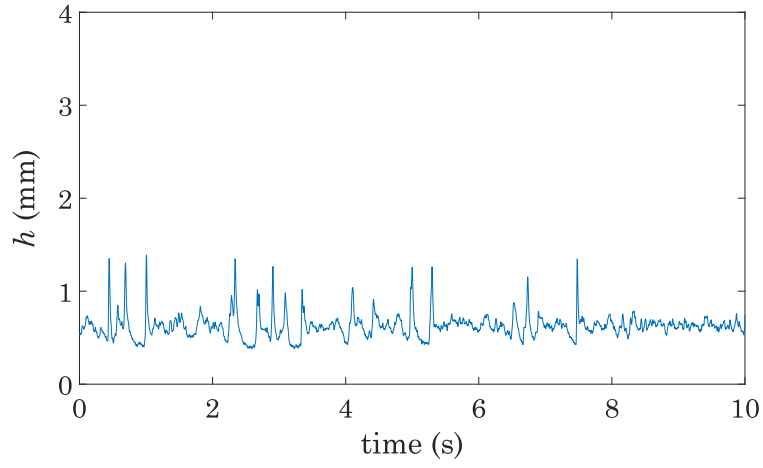
(b) $Re_L = 875$ and $Re_G = 20 \times 10^3$
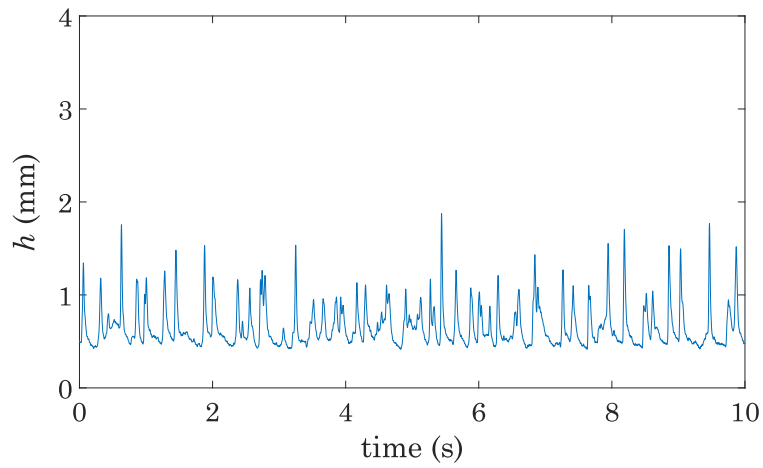
(c) $Re_L = 1000$ and $Re_G = 20 \times 10^3$

Figure 5.10: Time-traces obtained with the capacitance probe for annular flows in the presence of DAF surfactant.
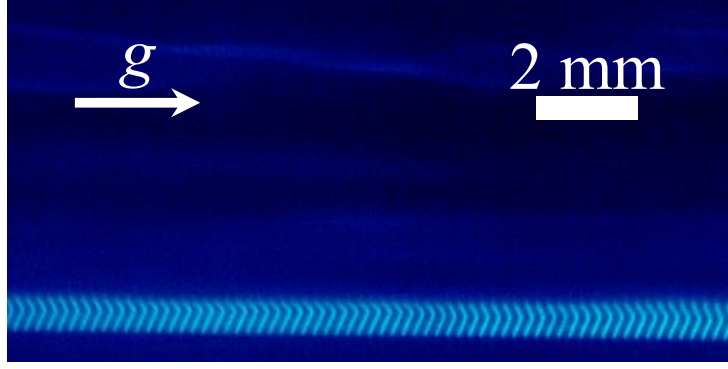
(a) Thin film with long wavelength.
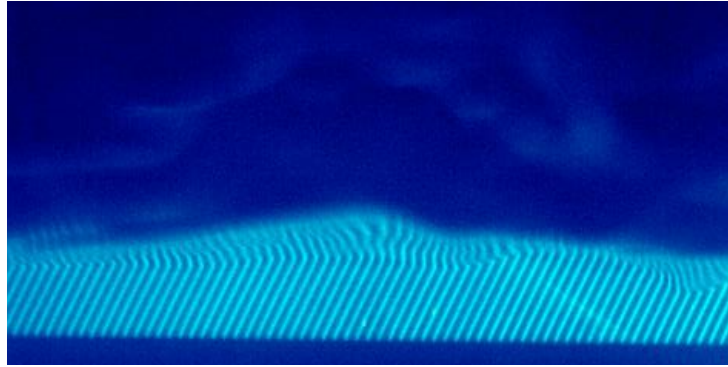
(b) Thick film with interfacial disturbances in the form of waves with short wavelength.

Figure 5.11: Instantaneous S-PLIF images of flow at $Re_L = 875$ and $Re_G = 20 \times 10^3$ showing a typical example of thin annular film flow dynamics in the presence of DAF surfactant.

An interesting change in dynamics is observed for the flow conditions at $Re_L = 875$ and $Re_G = 20 \times 10^3$ (Fig. 5.9(b)) in the presence of DAF surfactant, seen as a sudden reduction in the relative film roughness by as much as $\sim 45\%$ measured using S-PLIF method. This is also confirmed using CP method where a reduction by $\sim 58\%$ was recorded (see Fig. 5.9(d)). Smoother films in the presence of surfactant are also recorded at lower gas shear rates (i.e., Re_G ranging from 0 to 10×10^3) at the same Re_L (= 875). Taking a closer look at the details for this particular flow condition ($Re_L = 875$ and $Re_G = 20 \times 10^3$), a reduction of the film interfacial activity as well as relative wave amplitudes are clearly observed from the film time-traces obtained with CP method (see Fig. 5.10) and from the instantaneous S-PLIF images (see Fig. 5.11). As shown in Fig. 5.10, an enhancement in the stability of the film flow upon increase in Re_L from 750 to 875 is attained, which showed a marked reduction in the highest spatially-averaged film thickness by ≈ 1.05 mm (or $\approx 43\%$), yet the relative mean film thickness ($\langle h \rangle / R$) increases with the trend (as discussed earlier) due to an observed thickening of the base film. The observed reduction in film roughness at these flow conditions may be explained by the stabilisation of the film due to potential Marangoni stresses (discussed in Chapter 6) and reduced surface tension which can suppress the formation of primary and secondary waves close to the inlet having a

subsequent effect further downstream. As was shown by Alekseenko et al. [6], these waves are potentially key influencers of interfacial flow instability and formation of disturbance waves, which are predominantly absent as recorded using two independent measurement methods. The reduction in the wave frequency (see Chapter 6) has naturally resulted in increase of number of waves with long wavelengths, and hence, thickening of the bulk film, which is in good agreement with experimental results of Rivera et al. [136] and Thwaites et al. [164]. In the latter work, similar trends were observed for flows in the presence of drag-reducing agent, which stabilised the film by delaying the disturbance wave transition to higher Reynolds numbers, increasing base film thickness, and decreasing interfacial wave frequency. Such dynamics can also be potentially associated with the transition of flow regime from 'dual-wave' to 'thick ripple' due to presence of mutual characteristics e.g., waves with long wavelengths (common for 'dual-wave') and rare gas entrainment in the form of small bubbles (common for 'thick ripple'). This is evident also from direct qualitative observations using instantaneous S-PLIF images (see Fig. 5.11). Thin base films (Fig. 5.11(a)) are observed to be relatively quiescent, with the presence of large interfacial disturbances (see Fig. 5.11(b)), where the spatial film thickness is at least twice the value of the measured mean film thickness. In addition, small entrained bubbles in the bulk are also observed. The recorded stability reverses upon further increase of Re_L from 875 to 1000 (see Fig. 5.10(c)), where the flow dynamics start to acquire characteristics typical of a 'thick ripple' flow regime.

The work by Ishii and Grolmes [80] proposed a correlation to predict the wave roughness σ_w (comparable to the present work's roughness σ_h), which can be estimated by assuming that the motion of the wave crest with respect to the liquid film can be expressed by a shear flow model. To elaborate, it is an approximation for the case of wave formation in vertical annular flow, given that gravitational forces are neglected due to the calculation of the wave height in the radial direction. On the basis of this, the correlation can be expressed as

$$\sigma_\mathrm{w} = \sqrt{2}C_\mathrm{w}\frac{\mu_\mathrm{L}}{(\rho_\mathrm{L}\tau_\mathrm{int}f_\mathrm{L})^{0.5}} \tag{5.5}$$

where τ_int is the interfacial shear stress, and C_w is a factor that takes into account the effect of the surface tension on the circulation/dissipation flow in the wave, which was defined by Ishii and Grolmes [80] as

$$C_\mathrm{w} = 0.028N_\mu^{-0.8} \quad \text{for} \quad N_\mu \leq 1/15$$
$$C_\mathrm{w} = 0.25 \quad \text{for} \quad N_\mu > 1/15 \tag{5.6}$$

where N_μ is the viscosity number, which compares the viscous force induced by an internal flow

to the surface tension force, expressed as

$$N_\mu = \frac{\mu_L}{\left(\rho_L \sigma \sqrt{\frac{\sigma}{g \Delta \rho}}\right)^{0.5}} \tag{5.7}$$

where $\Delta \rho$ is the density difference between gas and liquid (i.e., air and water). The parameter f_L defined in Eq. 5.5 is the interfacial liquid friction factor defined as

$$\sqrt{f_L} = K Re_L^{m_h} \tag{5.8}$$

where K and m_h are given by

$$
\begin{aligned}
K = 1.962, \quad m_h = -1/3 \quad &\text{for} \quad 100 < Re_L < 1000 \\
K = 0.735, \quad m_h = -0.19 \quad &\text{for} \quad 1000 \leq Re_L
\end{aligned}
\tag{5.9}
$$

The τ_{int} in Eq. 5.5 is calculated similarly to Eq. 5.2, except for interfacial gas friction factor f_G, expressed as

$$f_G = 0.079 Re_L^{-0.25} \left[1 + 24 \left(\frac{\rho_L}{\rho_G}\right)^{1/3} \frac{\langle h \rangle}{D} \right] \tag{5.10}$$

Using correlation shown in Eq. 5.5, the predicted values of the wave roughness σ_w are compared with the experimental film roughness data (σ_h/R) of the present study. A comparison between σ_w/R and σ_h/R (for both surfactant-free and surfactant-laden flows) is shown in Fig. 5.12 from which it can be seen that the predicted values follow a decreasing trend with Re_G in agreement with both cases (absence/presence of DAF), while Re_L displays a variable trend for both cases. To expand on this, a fairly good agreement is observed for the surfactant-free flows at $Re_G = 10 \times 10^3$ and all Re_L values with differences spanning between $\sim 4\%$ and $\sim 20\%$, and $\sim 3\%$ and $\sim 40\%$ in comparison for data acquired using S-PLIF and CP methods, respectively. For the same flow conditions in the presence of surfactant, the differences are found to be higher i.e., varying from $\sim 5\%$ to $\sim 50\%$ for the S-PLIF case, and from $\sim 8\%$ to $\sim 60\%$ for the CP case. While a gradual increasing trend with Re_L is observed for the predicted values for surfactant-free flows (in agreement with experimental data), nearly constant values are predicted for the surfactant-laden flows, albeit surface tension is considered in Eq. 5.5. A similar effect as for the predicted h/R values (Fig. 5.7) is observed when increasing Re_G above 10×10^3 i.e., a steep decrease followed by a gradual to nearly no reduction in the film roughness. This change appears to be better agreement for the surfactant-laden flows than for the surfactant-free flows.

Interestingly, for the former case the film roughness appears to reach a plateau with increasing Re_G (i.e., $= 40 \times 10^3$), particularly at the lower range of Re_L values (≤ 875), which, as explained earlier, may occur due to higher gas entrainment and formation of a foam above the bulk film.

(a) S-PLIF (clean case)

(b) S-PLIF (surfactant case)

(c) Capacitance probe (clean case)

(d) Capacitance probe (surfactant case)
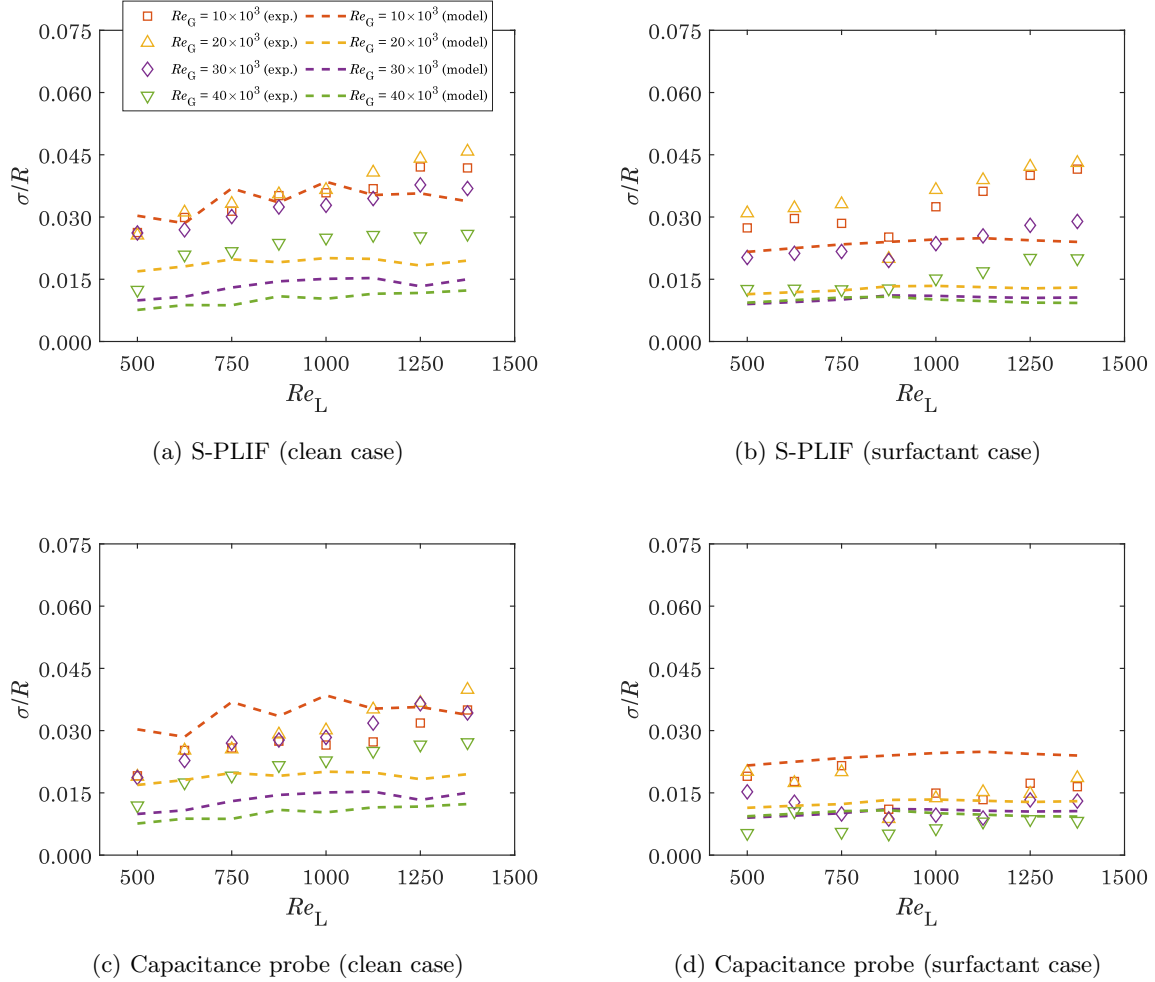
Figure 5.12: Results of film roughness normalised to internal pipe radius R obtained from the present experiments (hollow shapes) and correlation using Equations 5.5–5.10 (dashed lines) displayed as a function of the liquid Reynolds number.

5.4   Concluding remarks

Downwards annular film flows in the absence and presence of water soluble fluorescent surfactant were studied using two measurement methods simultaneously, i.e., S-PLIF and capacitance probe. The study was conducted for a wide-range of flow conditions, spanning from falling films to highly gas-sheared films. In order to overcome the limitations of PLIF method identified by Charogiannis et al. [32], for the first time the interface is tracked accurately with a newly developed S-PLIF method for gas-sheared films. Four different flow regimes were identified,

namely 'dual-wave', 'thick ripple', 'disturbance wave' and 'regular wave', which are in good agreement with the earlier findings of Zadrazil et al. [186]. Using this, flow regime pattern maps were constructed for surfactant-free and surfactant-laden flows, where in the latter case this is done for the first time in literature. It was found that in the presence of DAF surfactant the flow regime has shifted for two flow conditions both of which are gas sheared films. The change in the film flow characteristics in terms of interfacial wave activity and increased gas entrainment was identified using both measurement methods. In agreement with literature, surfactant-laden flows have been found to be strongly affected by the high gas shear rates due to reduced cohesion forces, which results in greater agitation between air and water, and thus, higher gas entrainment and potentially liquid entrainment rates [3, 81, 170].

Film thickness measurements for all flow conditions in the presence/absence of surfactant were also performed. The obtained results for the surfactant-free falling films are found to be in good agreement with literature. The acquired data of spatially-averaged film thickness measurements for surfactant-laden flows were also found to be in good agreement with the results for similar experimental investigations carried out by several works (e.g., [26, 136]). For both surfactant-free and surfactant-laden flows the relative film thickness was found to increase with Re_L and decrease with Re_G, in agreement with quasi-linear trends observed by Zadrazil et al. [186]. Interestingly, for nearly all flow conditions the mean film thickness was found to decrease in the presence of fluorescent DAF surfactant (relative to the clean case), which was also observed earlier by Rivera et al. [136]. This may be a result of higher rates of liquid entrainment in the form of droplets that can mainly occur due to the K-H instability. The critical value for this instability to occur is reduced when the surface tension is lowered [5, 129]. This also agrees with the observed changes in the film roughness of surfactant-laden flows where it was found to increase for nearly all liquid Reynolds numbers and for gas Reynolds numbers up to 20×10^3. As a result of increased 'waviness' it may lead to higher energy in the shape of the interface which subsequently increase its velocity [61, 186]. Setting gas Reynolds number values to 30×10^3 or 40×10^3 revealed that it has a greater effect on the film thinning for the surfactant-laden flows than for the flows in the absence of surfactant. It may occur due to higher gas entrainment rates which lead to formation of foam at the crests of large waves subsequently reducing their peak amplitudes, but increasing the thickness of the base film [170].

The obtained experimental results for the film thickness $\langle h \rangle / R$ and film roughness σ_h / R are compared with the predictions estimated using correlations developed by Ishii and Grolmes [80]. It is found that the correlation follows an increasing linear trend with Re_L, and a decreasing effect

with Re_G in agreement with experimental data. Correlation is found to overpredict film thickness at low gas shear rate, i.e., $Re_\mathrm{G} = 10 \times 10^3$, and underpredict at subsequently higher Re_G values indicating a stronger effect exerted by the gas stream on the film relative to experimental data. Generally, data is agreement within $\sim 50\%$ difference for the surfactant-free flows, and within $\sim 35\%$ for surfactant-laden flows. Similarly, the predicted values for the film roughness follow a decreasing trend with Re_G in agreement with the experimental results. A gradual increasing trend with Re_L is observed for the predicted values for surfactant-free flows (in agreement with experimental data), but nearly constant values are predicted for the surfactant-laden flows, which agrees with the data only at the highest gas shear rate ($Re_\mathrm{G} = 40 \times 10^3$) and $Re_\mathrm{L} \leq 875$.

Chapter 6

The effect of surfactant on interfacial waves of annular films

Contents

Annular films are characterised by complex interfacial wave behaviour, which, depending on the flow conditions, may often lead to numerous other multi-phase flow phenomena further reducing controllability of the flow [80, 175]. Gaining an understanding of the interfacial flow behaviour from a quantitative perspective requires information on the flow characteristics not only of the film thickness (as discussed in the previous chapter), but also of the interfacial wave activity which were shown to be the primary reason for gas and liquid entrainment [11, 186]. Furthermore, various surface active substances, i.e., surfactant, may also substantially alter the flow behaviour either promoting or impeding the observed phenomena [170]. These characteristics may have significant implications on the actual system operation and fluid process. To overcome these difficulties, it is feasible to acquire quantitative information of the annular film flows using non-intrusive methods i.e., optical or capacitance techniques, which can assist in construction of e.g., predictive tools, and validation of numerical models.

In this chapter, measurements of downwards annular air-water flows (with and without DAF surfactant) are performed using S-PLIF and CP methods simultaneously to study the behaviour

of the base films and interfacial waves for a range of flow conditions shown in Table 3.2. For the first time, these types of measurements are performed on both the falling films and gas-sheared films in the presence of water-soluble fluorescent surfactant, demonstrating the capability of DAF surfactant to be utilised in other relevant applications. The height of the base film, amplitude of large waves and their corresponding frequencies, probability density functions of the film thickness distributions, and the time-scales of interfacial waves are investigated and statistical data is presented for surfactant-free and surfactant-laden flows. The effect of the surfactant on the annular flow is identified from a qualitative and quantitative perspective. Findings in this chapter are closely linked with the observations made in Chapter 5, particularly on the changes in the mean film thickness and behaviour of the film for surfactant-laden flows. Certain correlations were also used to estimate flow characteristics for the present experiments.

6.1 Statistics of large waves and base film flows

Annular films can be characterised based on the activity of various interfacial disturbances in the form of waves. The amplitude of these waves can vary substantially, ranging from very small values (e.g., typically termed as 'ripple' waves whose standard deviation of film thickness is 0.3 of the mean film thickness in the base film region and 0.2 in the large wave region), to very large values (e.g., 'disturbance' or 'roll' waves whose amplitude is at least several times higher than the mean film thickness) [7, 186]. The residual liquid film that flows between the large waves is often termed as 'base' film [35]. Due to the complex nature of interfacial waves, it is often very difficult to distinguish, with high certainty, between a wide range of small amplitude waves present at the base film and the varying thickness of the base film itself. For this reason, the base film thickness and the amplitude of large waves are defined as $h_{\text{base}} \leq 2 \times \langle h \rangle$ and $h_{\text{wave}} = h > 2 \times \langle h \rangle$, respectively. The factor of 2 was selected after careful consideration of the data, and according to previous experimental studies [186].

The measurements of the normalised base film thickness, $\langle h_{\text{base}} \rangle / R$, are shown in Fig. 6.1. With increasing Re_{L} for surfactant-free flows (Figs. 6.1(a) and (c)), the $\langle h_{\text{base}} \rangle / R$ values fluctuate within a fixed range particularly for the falling films and gas sheared films at $Re_{\text{G}} \leq 20 \times 10^3$, while for $Re_{\text{G}} \geq 30 \times 10^3$ values remain nearly unchanged. This fluctuation is observed to be greater for data measured using CP method (Fig. 6.1(c)) than for the S-PLIF method (Fig. 6.1(a)). This may be due to the inherent spatial-averaging effects present in the CP method, meaning that the amplitude of smaller waves present in the 'dual-wave' and 'thick

ripple' regimes (see Fig. 5.1) are smoothed, and thus, recorded as the base film (also evident from marginally thinner $\langle h \rangle / R$ values shown earlier in Fig. 5.6). In addition, occasional appearance of large waves, which is characteristic for these flow regimes, may also influence the observed higher $\langle h_{\text{base}} \rangle / R$ values. As the gas Reynolds number increases, the thickness of the base film decreases, observed using both methods, and in agreement with literature [136, 186]. As a result of strong shear force exerted by the gas stream on the film substantially reduces the height and limits the maximum attainable thickness by the base film and interfacial waves, potentially leading to liquid entrainment events.
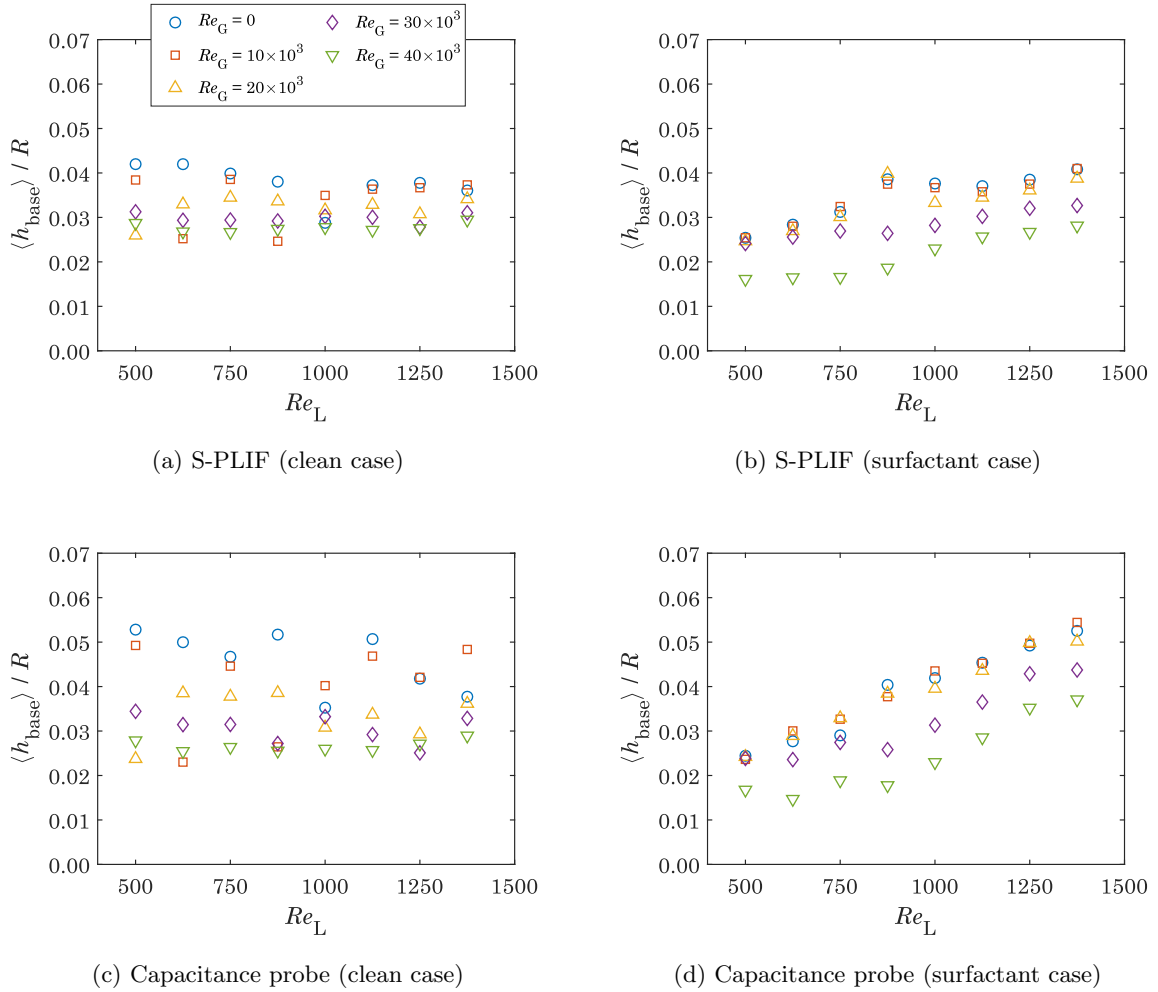
Figure 6.1: Measurements of the base film thickness, defined as $h_{\text{base}} \leq 2 \times \langle h \rangle$, displayed as a function of the liquid Reynolds number.

In the case of surfactant-laden flows (Fig. 6.1(b) and (d)), the normalised base film thickness is observed to increase with Re_{L}, and a decrease with Re_{G}, in agreement with Rivera et al. [136]. When Re_{G} is increased from 0 to 20×10^3 for all Re_{L} values, it appears to have very little effect on the base film thickness, similarly to $\langle h \rangle / R$ (see Fig. 5.6 in Chapter 5). A noticeable reduction is observed once Re_{G} increases to a value of 30×10^3, and especially to 40×10^3, having a bigger

difference between the recorded values of $\langle h_{\text{base}} \rangle / R$ at these two highest gas flow rates. This shows that the gas shearing effect is more pronounced in the presence of surfactant than for the flows without it, a directly visible result of which is the increased entrainment indicating a higher agitation of the two phases (see Chapter 7). Contrarily to the clean case, the $\langle h_{\text{base}} \rangle / R$ values recorded by the CP and S-PLIF methods are observed to be very similar at flow conditions corresponding to 'dual-wave' and 'thick ripple' flow regimes. The difference appears to increase once the film flow reaches 'disturbance wave' and 'regular wave' regimes where the measured $\langle h_{\text{base}} \rangle / R$ values are observed to be higher for CP method than those recorded using the S-PLIF method, likely due to the aforementioned limitation inherent in the former case.

Comparing the $\langle h_{\text{base}} \rangle / R$ values obtained using S-PLIF method between surfactant-free and surfactant-laden flows, the widest difference appears to occur at nearly all Re_{L} values that are ≤ 1000 for the falling films and gas-sheared films. This is not surprising since the base film thickness increases with Re_{L} to a level where both methods are capable of distinguishing waves and base film at the set threshold. Yet, some difference is still observed when comparing values obtained using the CP method, which may also be additionally influenced, as previously discussed, by the thickening of the base film and reduction in the height of the waves for flows in the presence of DAF surfactant. Whilst the $\langle h_{\text{base}} \rangle / R$ values remain relatively unchanged for surfactant-free flows with increasing Re_{L} for Re_{G} at 30×10^3 and 40×10^3, an increasing trend in $\langle h_{\text{base}} \rangle / R$ is observed for surfactant-laden flows. As discussed in Chapter 5, this may be a result of the reduction of amplitude of large waves, and thickening of the base films with a greater effect than for the surfactant-free flows (both points are discussed further below), which was also observed in other studies [114, 136].

Since the thickness of the base film is found to be mostly affected by the gas flow rate in a decreasing manner, it can be predicted that the Re_{G} is an inverse function of the base film thickness h_{base}. This agrees with the work of Schubring [143] in which a correlation that approximates base film thickness is expressed as

$$h_{\text{base}} = 4.8 D Re_{\text{G}}^{-0.6} \qquad (6.1)$$

The predicted values for the flow conditions of the present study (Table 3.2) are shown in Figure 6.2. The experimental data is in good agreement with the approximated values, particularly for the surfactant-free flows, which demonstrates that Re_{L} has nearly no effect on h_{base}. On the other hand, the correlation would need to be adjusted accordingly in order to

account for increasing base film thickness in the case of surfactant-laden flows.

(a) S-PLIF (clean case)

(b) S-PLIF (surfactant case)

(c) Capacitance probe (clean case)

(d) Capacitance probe (surfactant case)
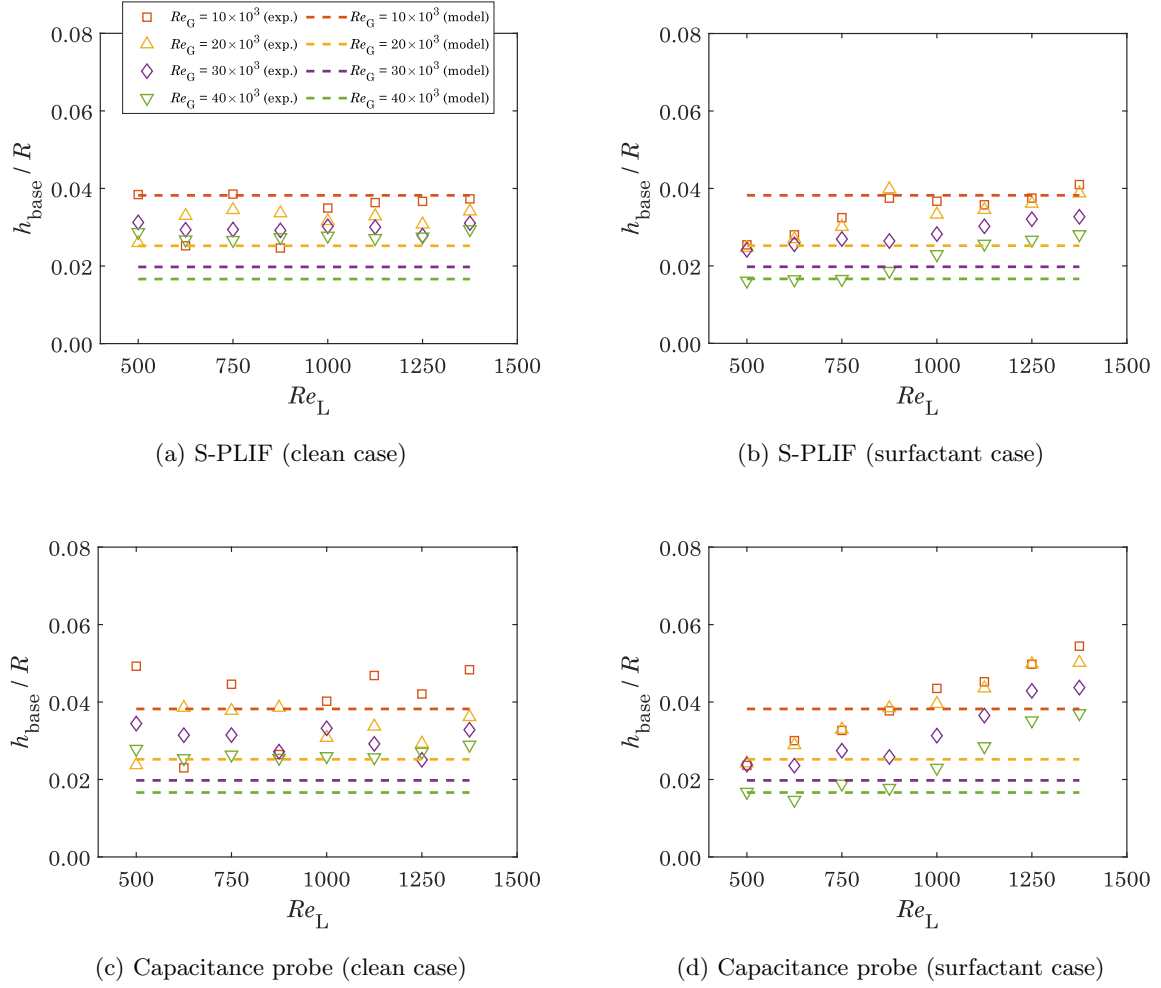
Figure 6.2: Results of base film thickness normalised to internal pipe radius R obtained from the present experiments (hollow shapes) and correlation using Equation 6.1 (dashed lines) displayed as a function of the liquid Reynolds number.

As per measurements of the base film thickness, very similar trends are also observed for measurements of amplitudes of large waves (see Fig. 6.3). As expected of increasing Re_{L}, the mean thickness of large waves, $\langle h_{\mathrm{waves}}\rangle/R$, also increases, which is particularly visible when Re_{L} exceeds a value of 1000 when $Re_{\mathrm{G}} \leq 20 \times 10^3$ for the surfactant-free flows, and all Re_{G} values for the surfactant-laden flows. In both cases, this corresponds to a developed 'thick ripple' regime followed by a 'disturbance wave' regime ($Re_{\mathrm{G}} < 30 \times 10^3$) both of which are characterised by an increase in large wave frequency and amplitude (see Fig. 5.1 in Chapter 5). It is evident from both Fig. 6.1 and Fig. 6.3 that with increasing Re_{L} for the surfactant-laden flows the growth of the base film thickness is more pronounced than the amplitude of large waves. In the case of surfactant-free flows, the growth of the amplitude of large waves appears to be marginally bigger than the base film, indicating on the potential dampening effect by the surfactant [170].

105

The observed amplitudes of large wave are also significantly lower for the surfactant-laden flows at the highest gas shear rate ($Re_G = 40 \times 10^3$), indicating a film thinning effect in the presence of surfactant which may occur due enhanced liquid entrainment rates, especially at the crests and bulk of the large waves.

(a) S-PLIF (clean case) (b) S-PLIF (surfactant case)

(c) Capacitance probe (clean case) (d) Capacitance probe (surfactant case)
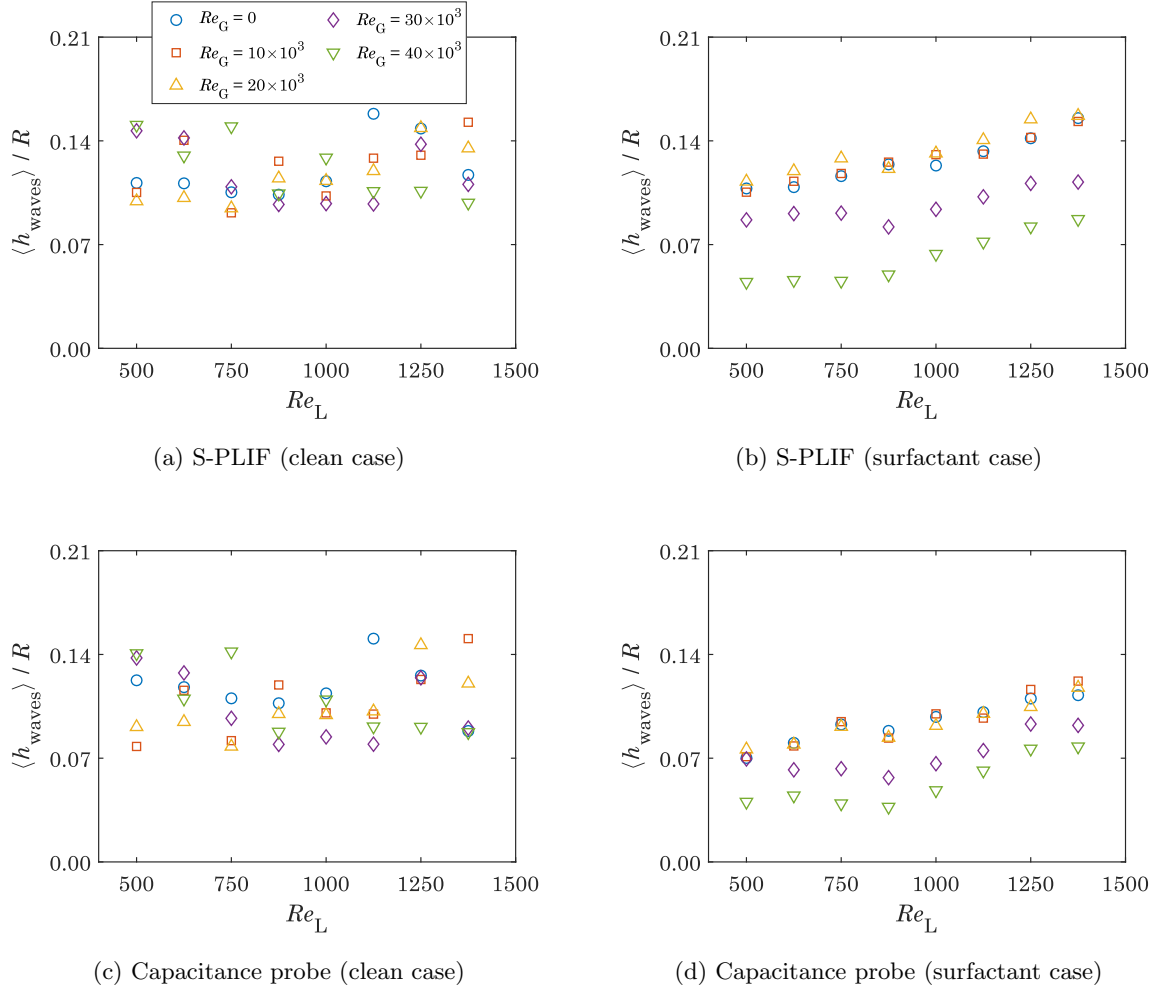
Figure 6.3: Measurements of the amplitude of large waves, defined as $h_{\text{wave}} = h > 2 \times \langle h \rangle$, displayed as a function of the liquid Reynolds number.

A correlation model that predicts amplitude of the waves, h_{waves} was proposed in the experimental study of Han et al. [70] on vertical annular flows, which can is expressed as

$$h_{\text{waves}} = 4000 D Re_G^{-1.12} \tag{6.2}$$

From Figure 6.4 it becomes evident that the predicted values are in agreement with the experimental data, particularly on the reducing effect of increasing Re_G on the wave amplitude. This is in agreement with the work by Han et al. [70] which showed than by doubling the gas mass

flux the wave amplitude decreases by as much as $\sim 43\%$. From Fig. 6.4 the approximated h_{waves} for low Re_{G} ($= 10 \times 10^3$) is well-overpredicted in all cases by $\sim 100\%$, indicating its validity only for higher gas flow rates. The correlation shows a much better agreement once Re_{G} is increased to 20×10^3. Although, the present correlation does not consider surface tension effects, the predicted values are in better agreement with the present experimental results for surfactant-laden flows than for the surfactant-free flows. The maximum difference is found to be $\sim 45\%$ for the former case, while the maximum difference doubles in the latter case (i.e., $\sim 90\%$). As discussed previously, the predicted values also indicate that with increasing Re_{G} the maximum attainable wave amplitude is decreasing leading to high gas-shear forces exerted on the film, and thus, high fractions of liquid and gas entrainment.

(a) S-PLIF (clean case) (b) S-PLIF (surfactant case)

(c) Capacitance probe (clean case) (d) Capacitance probe (surfactant case)
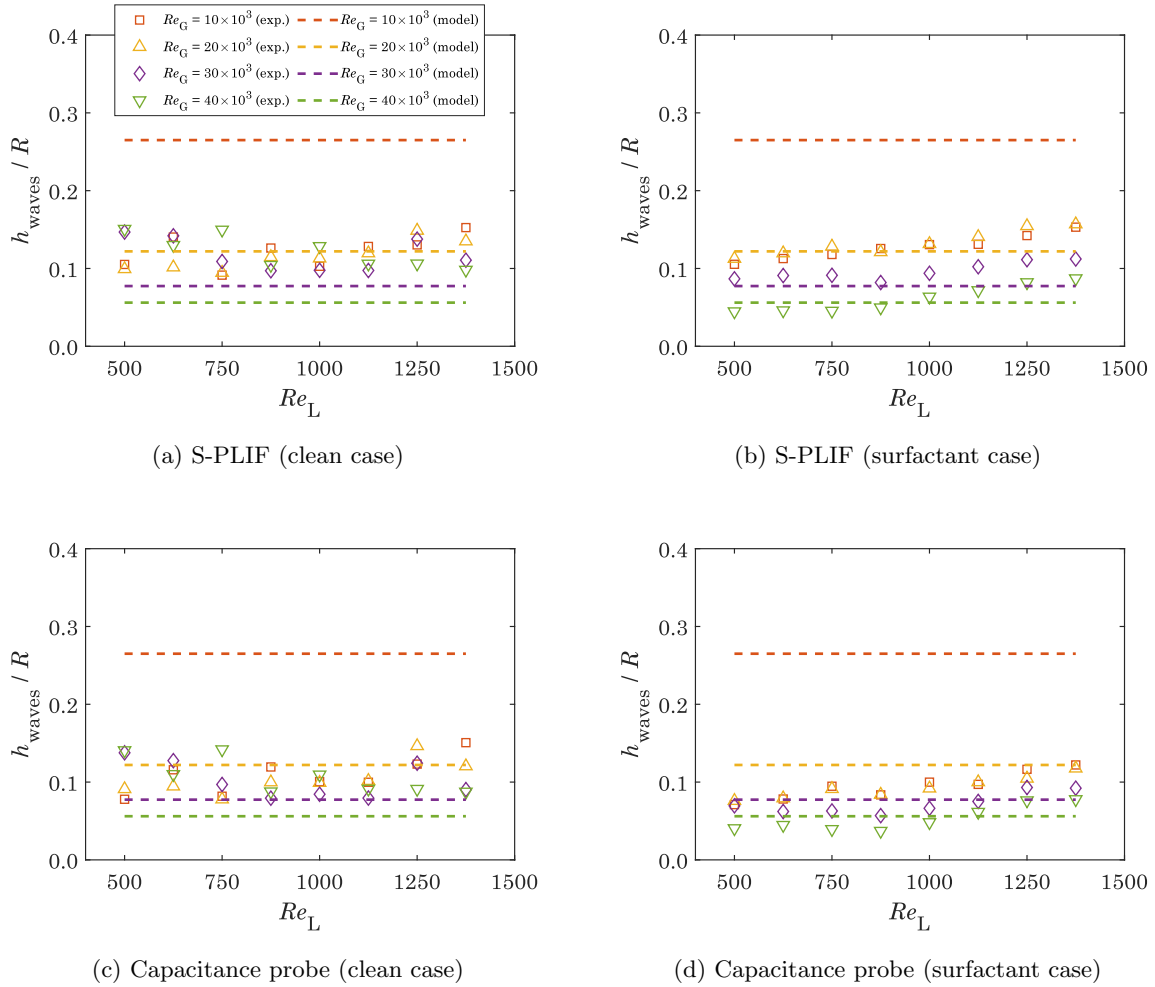
Figure 6.4: Results of wave amplitude normalised by the internal pipe radius R obtained from the present experiments (hollow shapes) and correlation using Equation 6.2 (dashed lines) displayed as a function of the liquid Reynolds number.

The acquired data on the frequency of the large waves, f_{waves}, defined as the number of samples with $h > 2\times$ over the total, reveals several interesting observations (see Fig. 6.5).

Firstly, it is evident that both in the surfactant-free and surfactant-laden flows the effect of increasing liquid Reynolds number is insignificant. Nevertheless, the frequency of large waves was qualitatively observed to increase with Re_L, especially noticeable in the 'disturbance wave' regime, it is evident that the frequency of waves with amplitude below the set threshold ($h \leq 2\times$) also increases in a quasi-linear manner. The effect of Re_G is not clear for both surfactant-free and surfactant-laden flows.

An increase in f_{waves} is observed for the surfactant-free falling film flows at $Re_L \leq 750$ using S-PLIF method. This may be associated with the relatively quiescent films that are in 'dual-wave' flow regime. Under these flow conditions the presence of waves with long wavelengths and intermittent waves with larger amplitudes are qualitatively observed from instanteneous S-PLIF images (see Fig. 5.1(b)) and CP time-traces (see Fig. 5.1(f)). Other noticeable differences in f_{waves} are found for gas sheared flows when $Re_G \geq 30 \times 10^3$. Here, the frequency of large wave decreases in agreement with the work of Rivera et al. [136]. Interestingly, numerous works (e.g., Pham et al. [129], Zadrazil et al. [186], Zhang et al. [189]) have experimentally demonstrated that energy dissipation of large amplitude waves can occur due to various mechanisms (promoted by high gas shear) that lead to disintegration of the interfacial waves e.g., 'wave undercut', 'bubble burst' and 'liquid impingement', which are enhanced for surfactant-laden flows.

A steep decrease in f_{waves} is recorded for the surfactant case using CP method for all Re_G values and $Re_L \geq 875$. This agrees-well with the observed reductions in the measurements of normalised film roughness (σ_h/R and $\sigma_h/\langle h \rangle$, see Fig. 5.8 and Fig. 5.9, respectively) for the same flow conditions. Since a reduction in the amplitude of large waves was not observed (see Fig. 6.3), this may be a result of an increased number of interfacial waves with smaller amplitude. As discussed in Chapter 5, large amplitude waves are formed and grow in size and velocity through coalescence with other waves which depends on the development length [6, 8]. Since the present data for surfactant case suggests that there is a higher number of smaller waves and/or lower number of large waves (with amplitude satisfying $h_{wave} = h > 2 \times \langle h \rangle$), it is feasible that DAF surfactant reduces the coalescence events, and thus, increases the development length. Very similar reduction in f_{waves} is also observed in the S-PLIF case at $Re_L = 875$ for $Re_G \leq 20 \times 10^3$, which follows a gradual increase to its initial values with Re_L. In addition, f_{waves} data acquired using CP method in the strongly gas-sheared films suggests that the interface is saturated with waves whose height are below the set threshold. Nevertheless, as it was explained in Chapter 3 using joint probability distributions (see Fig. 3.10) the comparison of f_{waves} between S-PLIF and CP methods does not exhibit a clear trend, and thus, the measurements may differ. This

may be further promoted by the substantial increase gas entrainment qualitatively observed at the highest gas flow rate, which results in waves with lower amplitudes and smoother films.

(a) S-PLIF (clean case)

(b) S-PLIF (surfactant case)

(c) Capacitance probe (clean case)

(d) Capacitance probe (surfactant case)
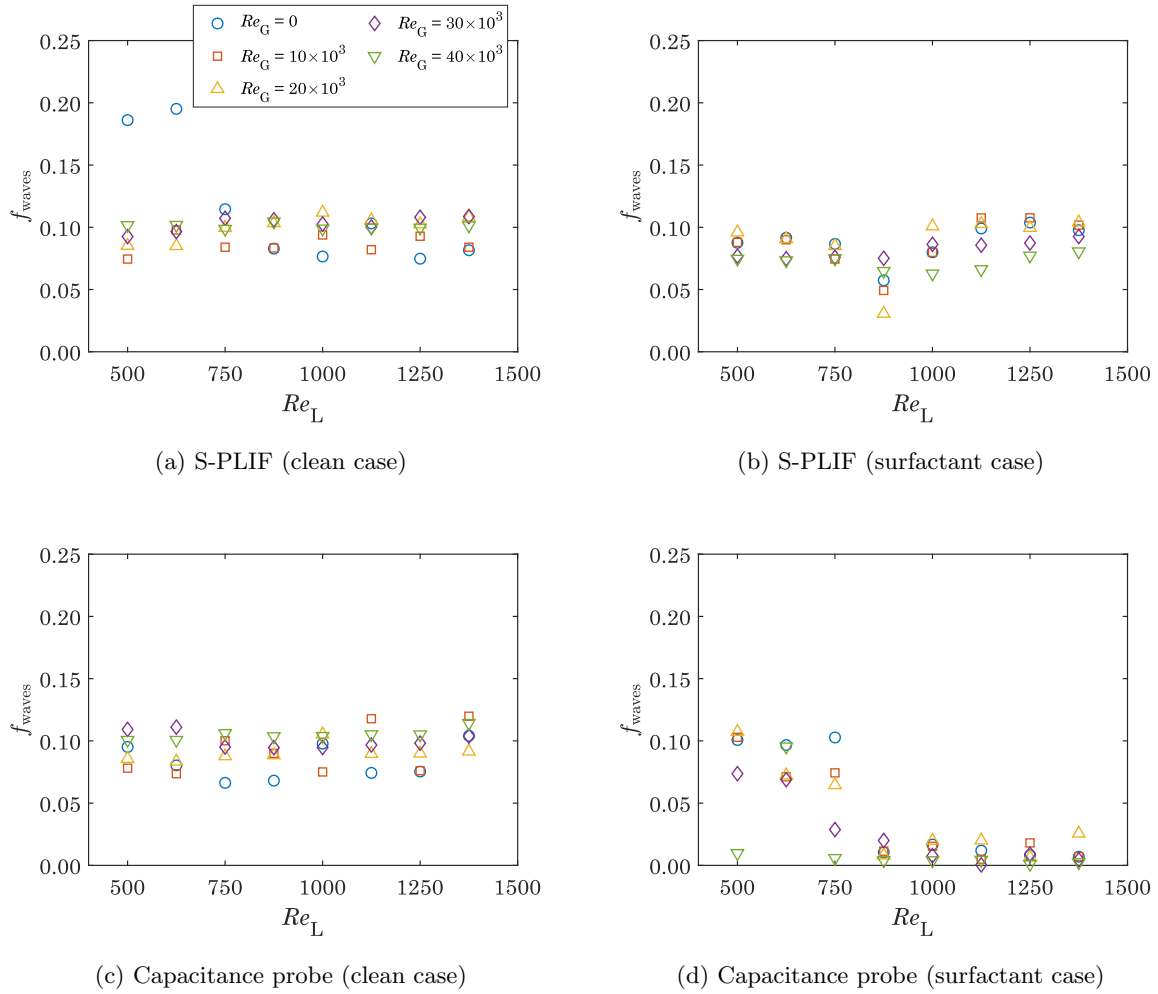
Figure 6.5: Measurements of frequency of the waves, defined as the number of samples with $h > 2\times$ over the total, displayed as a function of the liquid Reynolds number.

6.2 Distribution of film thickness

The quantities discussed in the previous section are primarily based on the first and second moments of the film thickness, which inherently carry certain limitations in their ability to illustrate the whole range of properties of a distribution. Rather than showing higher moments (i.e., skewness and kurtosis) in a similar fashion, the probability density functions (PDFs) of the film thickness distribution, obtained both from the CP and the S-PLIF methods are investigated instead. The fitted log-normal PDFs produced from the measurements in falling films are shown in Fig. 6.6, while for the gas-sheared films are shown in Figs. 6.7-6.8. Both measurement methods

exhibit a dominant peak at low film thickness (attributed to the base film), which decreases with Re_L and increases with Re_G. To elaborate, the 'tails' of the distributions include values up to 2.5 mm when $Re_G = 0$, and gradually decreases up to ≈ 2 mm with Re_G. The density of these 'tails' increases with Re_L, indicating stronger wave activity, and decreases with Re_G. The effect of the gas shear at different fixed liquid flow rates is also well-described by the PDFs plotted as a function of Re_G (see Appendix B). The trend in the data for the surfactant-laden flows obtained using CP method somewhat differs from these observations and is discussed further below.

For all flow conditions in the presence of DAF surfactant higher dominant peaks towards thinner films and a reduction in the 'tails' of the distribution are obtained, supporting observations of film thinning discussed previously (see Fig. 5.5 and Fig. 5.6). This is also evident from the earlier intersection and denser stacking of the distributions towards thinner films for flows with surfactant starting from lower liquid Reynolds number ($Re_L \geq 875$), while for the surfactant-free flows it is observed to initially occur at $Re_L \geq 1125$. Distributions obtained for surfactant case using CP method (Fig. 6.6(d)) are somewhat different from those observed using the S-PLIF method. While the peaks gradually reduce and the 'tails' increase for $Re_L \leq 750$ at $Re_G = 0$, a dominant peak appears with very short 'tail' at $Re_L = 875$ and $Re_G = 0$ (similar to the observed reduction in $\sigma_h/\langle h \rangle$ discussed in Chapter 5). Increasing Re_L further when $Re_G = 0$, marginally reduces the peaks of the distributions and shifts them towards thicker films, also with relatively short 'tails'. For the gas-sheared films (Figs. 6.7, 6.8), an increase in the peaks of the distributions towards thinner films are observed for Re_L values between 625 and 1000 at $Re_G = 20 \times 10^3$, and Re_L values between 625 and 1125 at $Re_G = 30 \times 10^3$. In the former case, distributions gradually shift towards thicker films with Re_L as the flow regimes change from 'dual-wave' to 'thick ripple' and 'disturbance wave'. In the latter case, the shift of the distributions is not as pronounced due to high gas-shearing effects, particularly for $Re_L \leq 1125$ where all flow conditions correspond to 'regular wave' regime (in agreement with data obtained using S-PLIF method). Such change in the film thickness can be ascribed to smoother films and explains earlier observations made on the reduction of frequency of large wave (Fig. 6.5) and normalised film roughness (Fig. 5.8 and Fig. 5.9).
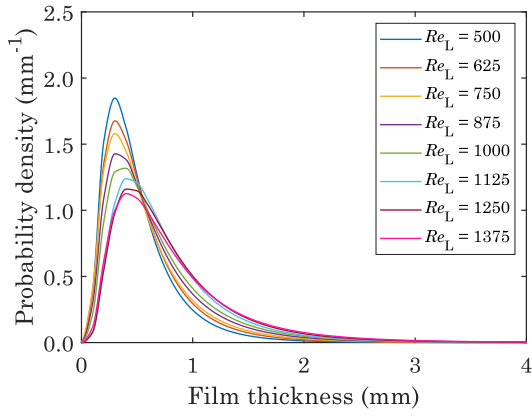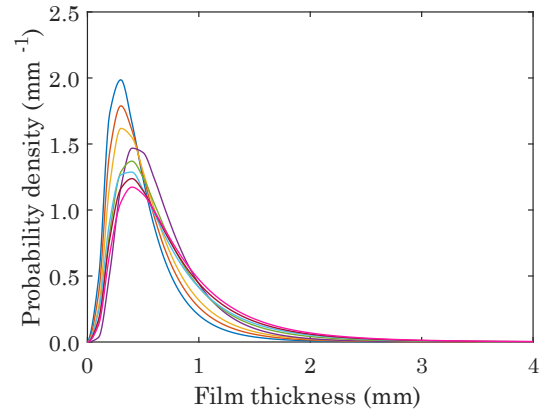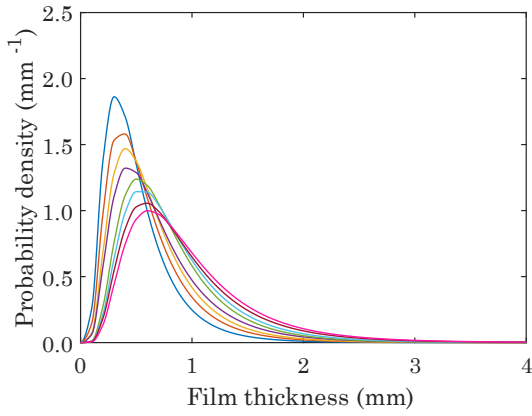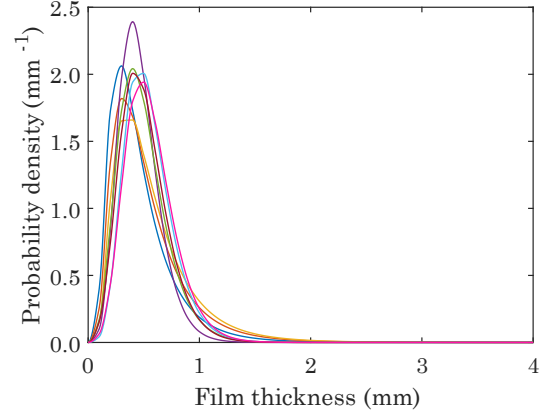
Figure 6.6: Log-normal probability density functions of the film thickness measurements for gas sheared annular flows of Table 3.2, for $Re_L \in [0; 1375]$ and $Re_G = 0$.
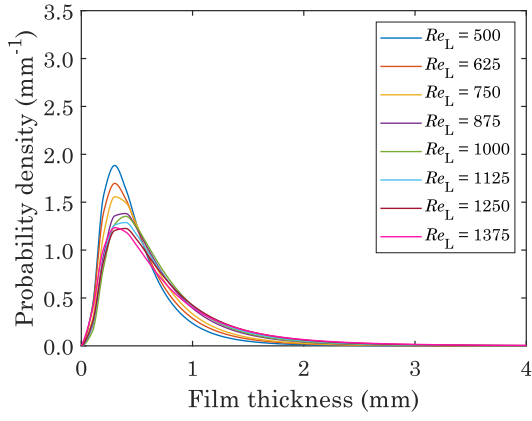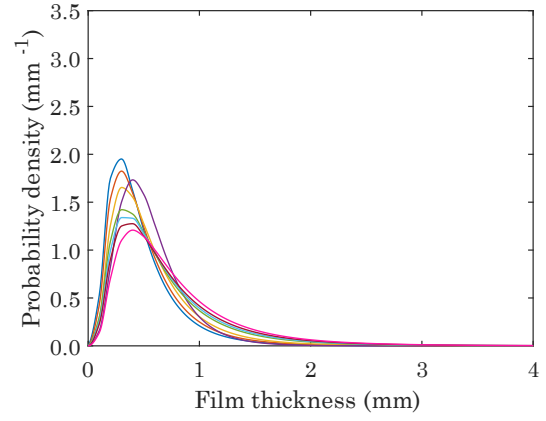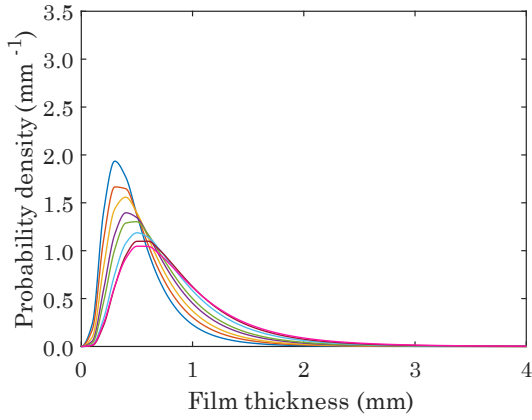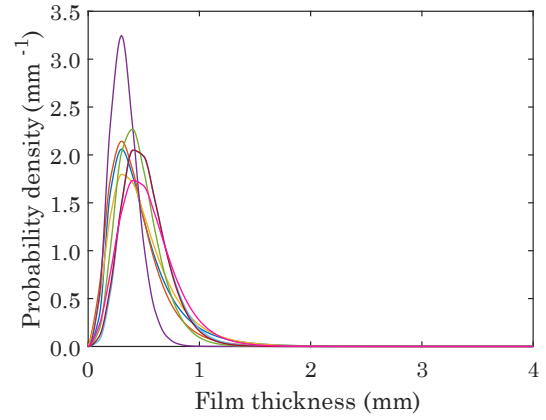
Figure 6.7: Log-normal probability density functions of the film thickness measurements for gas sheared annular flows of Table 3.2, for $Re_L \in [0; 1375]$ and $Re_G = 20 \times 10^3$.
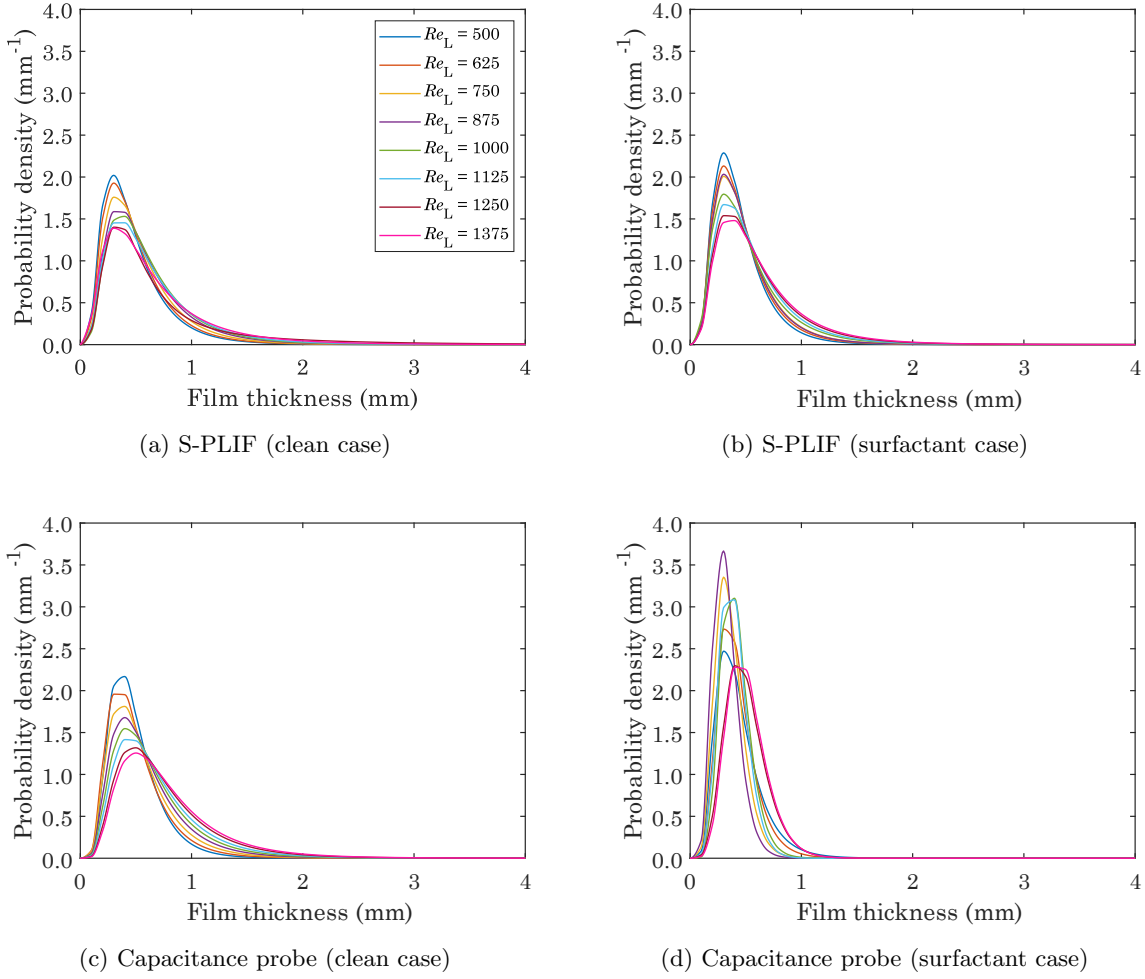
Figure 6.8: Log-normal probability density functions of the film thickness measurements for gas sheared annular flows of Table 3.2, for $Re_\mathrm{L} \in [0; 1375]$ and $Re_\mathrm{G} = 30 \times 10^3$.

6.3   Interfacial wave activity

A highly temporally-resolved signal (recorded at 10 kHz) from the capacitance probe provides a reliable representation of the film thickness time-trace of each flow condition of Table 3.2, which is, in turn, used to calculate the corresponding integral time-scale, τ_i. The method followed here is similar to the one typically employed in turbulence measurements (e.g., see refs. [132, 167]), i.e., integrating the auto-correlation (auto-covariance) function of the time-trace of the velocity components. Figure 6.9(a) shows the effect of Re_L on the auto-correlation functions for the surfactant-free falling film cases, i.e., $Re_\mathrm{G} = 0$. The auto-correlation coefficient ($\mathcal{A}$) exhibits a global minimum peak, which is shifted to shorter time delays (τ_d) and decreases in absolute value with an increase in Re_L. The effect of Re_L on the behaviour of the auto-correlation functions is observed for all investigated values of Re_G, however, some deviations can still be identified, especially in the transitions between the flow regimes. The inset of Fig. 6.9(a) shows a typical film

thickness auto-correlation function for the whole available domain. It is found that the functions have a non-periodic behaviour and decay to zero within a sufficiently large temporal domain - similarly to the auto-correlation functions encountered in homogeneous isotropic turbulence measurements. There is still some evidence of periodicity shown in the inset of Fig. 6.9(a), albeit small, and may be attributed to the dominant frequency of the spectrum. Similar characteristics were observed in the auto-correlation functions for higher liquid Reynolds numbers of free-falling films by Karapantsios et al. [86].

The auto-correlation functions need to be integrated to obtain the τ_i of each flow condition. Several methods were proposed for the selection of the temporal domain for the integration, see for example the work by O'Neill et al. [125] who evaluate four different methods. By analysing the temporal behaviour of the film thickness auto-correlation functions and according to available literature (e.g., [90, 132, 167]), a commonly employed method is followed in the present work for non-periodic auto-correlation functions. The functions are integrated until their first zero-crossing, which, as the inset of Fig. 6.9(a) shows, corresponds to the maximum value of the integrated auto-correlation function. The resulting integral time-scales, $\tau_i = \int \mathcal{A} d\tau_d$, are shown in Fig. 6.9(b) and (c) for the surfactant-free and surfactant-laden flows, respectively. The values vary from approximately 9 ms to 29 ms for the surfactant-free flows, and from 10 ms to 28 ms for the surfactant-laden flows for the range of flow conditions investigated herein (see Table 3.2). In general, τ_i is found to decrease with an increase in the Re_G, suggesting the presence of higher frequency waves and in agreement with the film thickness PDFs (see Appendix B for additional data). The effect of Re_L on τ_i is not as pronounced, a behaviour which indicates that the dominant frequency of the waves does not significantly alter with an increase in the liquid flow rate, despite the change in the wave amplitude, which was shown in Figs. 6.6-6.8. Interestingly, the effect of Re_L on τ_i is more pronounced for the falling films and low Re_G ($\leq 20 \times 10^3$) flow conditions. For high Re_G, the integral time-scales appear to depend primarily on the strength of the gas shear, particularly when the flow is in 'regular wave' regime, in agreement with the study of Alekseenko et al. [7, 6] which showed that three-dimensional waves grow with increasing gas superficial velocity. This is clearly evident from the film thickness time-traces that were shown earlier in Fig. 5.1.

Comparing the τ_i values obtained for surfactant-free with surfactant-laden flows, it is evident that for almost all Re_L and $Re_G \leq 20 \times 10^3$ flow conditions the integral time-scales decrease in the presence of DAF surfactant by as much as 12%. This suggests that the frequency of waves increases, most probably those with small amplitude, which agrees with the observations
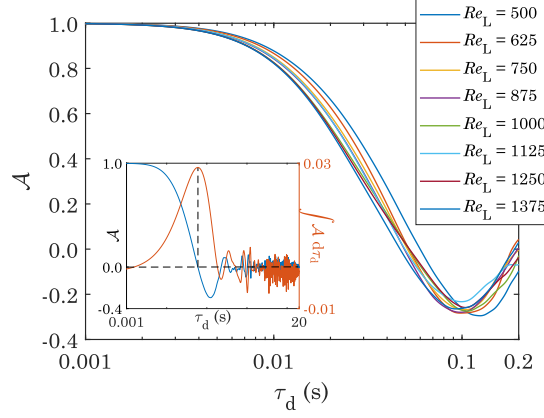
(a) Auto-correlation function
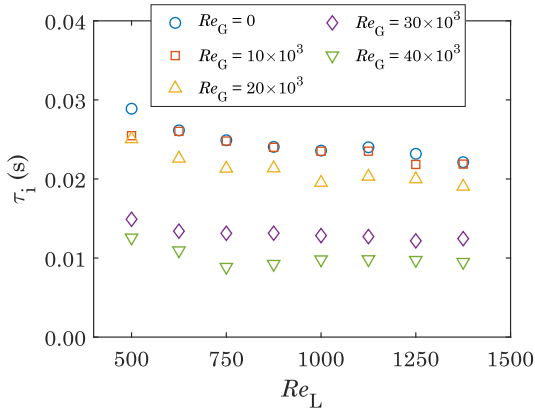
(b) Integral time-scale (clean case)
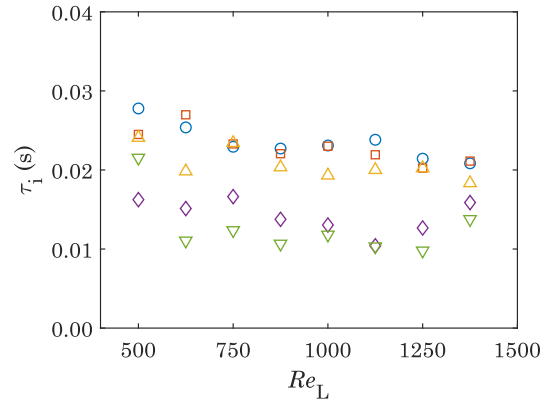
(c) Integral time-scale (surfactant case)

Figure 6.9: Auto-correlation results obtained from the time-traces of the capacitance probe. (a) Auto-correlation coefficient versus the time delay for the surfactant-free falling films, i.e., $Re_G = 0$. The inset shows the auto-correlation function for $\tau_d \in [0; 20]$ s and its respective integrated function. The arrows point to the zero-crossing value in $\mathcal{A}$ and the selected τ_i; (b) Integral time-scales of all flow conditions in the absence of surfactant; (c) Integral time-scales of all flow conditions in the presence of surfactant.

made from the film roughness (see Fig. 5.9), film thickness PDFs (see Fig. 6.6 and Fig. 6.7), and frequencies of large waves (see Fig. 6.5). Moreover, this is directly linked to the change in the flow regimes with evident variation (increase) in the activity of interfacial waves (see Fig. 5.1) [114, 136]. Higher frequency of small waves relative to the large waves suggests that these small waves carry the highest amount of energy in the shape of the liquid film interface [186]. Thus, the overall spectral energy contents of the interfacial signature signals are affected more significantly by the smaller frequent waves. In addition, higher frequencies of smaller waves also suggest that the development length may increase for the surfactant-laden flows, since the overall frequency of interfacial waves typically decreases with downstream length, which was proposed to occur due to coalescence of waves and development of coherent wave structures [69, 190].

Interestingly, it was reported earlier that some fraction of smaller amplitude waves (with amplitudes higher than of the ripple waves) may also travel at higher velocity than the large waves due to the presence of surfactant [61, 114, 147]. If this is the case, the faster moving waves may undergo partial coalescence with slower moving waves and partly result in droplet entrainment occurring in a similar manner as the fast-ripples [177] (see also Chapter 2 on this type of entrainment mechanism). In fact, it was experimentally demonstrated that the small amplitude waves are one of the primary causes of liquid entrainment into the gas core [6, 7, 177]. Both observations justifies thinning of the annular films for surfactant-laden flows (see Fig. 5.6).

Increasing gas shear rate to $Re_G \geq 30 \times 10^3$ led to increase in τ_i for surfactant-laden flows in comparison to surfactant-free flows. This well-explains results of the present study on the reduction of the film roughness (Fig. 5.9) and the changes observed in the film thickness PDFs. In fact, this agrees with qualitative observations by Nimwegen et al. [171] who showed that due to the presence of soluble surfactant in liquid annular films that are highly gas-sheared results in increased gas entrainment and formation of foams (high fraction of bubbles near the liquid surface) that suppress large and small interfacial waves. As a result of this, it may also lead to a reduction in the liquid entrainment. On the other hand, the presence of foam and high bubble entrainment close to and above the annular liquid film increases the interfacial friction due to high gas-shear rate, which, potentially, leads to faster flow of the foam, and thus, increases the velocity of the underlying liquid film [171].

An effect of Re_L and Re_G on the wave celerity (without considering surface tension effects) can be calculated using an equation that was devised by Marmottant and Villermaux [109] from their theoretical study on co-axial jets, which configuration is very similar to that of annular flow. It was demonstrated that a shear instability governs the large waves on the jet. The linear shear instability analysis outputs a following equation

$$u_w = \frac{\sqrt{\rho_G}u_{s,G} + \sqrt{\rho_L}u_{s,L}}{\sqrt{\rho_G} + \sqrt{\rho_L}} \tag{6.3}$$

where u_w is the wave celerity. An important assumption for validity of this equation is $u_{s,G} \gg u_{s,L}$. A very similar equation was proposed earlier by Pearce [13], which shows a linear relationship between u_w and $u_{s,G}$. Applying Eq. 6.3 for the flow conditions used in the present study, apart from $Re_G = 0$ (see Table 3.2), the same linear behaviour is observed from Fig. 6.10. The wave celerity increases with Re_L and Re_G, but with a greater extent in the latter case, in agreement with Belt et al. [18].
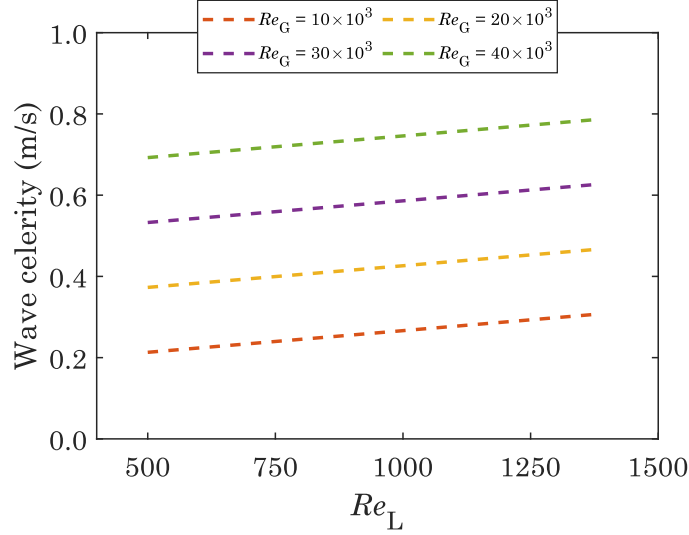
Figure 6.10: Predicted values for interfacial wave celerity using Eq. 6.3 for the given gas-sheared film flows.

The gas shear rate is an important factor which not only influences the wave velocities and gas entrainment (discussed in Chapter 7), but also the liquid entrainment. Since it was not feasible to acquire velocity profiles in the liquid film and quantitative data on liquid entrainment due to optical constraints, a critical gas velocity for the onset of liquid entrainment (also called the 'entrainment inception velocity') can be estimated from the Kutateladze number criterion ($Ku > 3.1$) [20]:

$$Ku^2 = \frac{\rho_G u_{iv}^2}{\sqrt{\sigma g \rho_L}} \geq 9.61 \tag{6.4}$$

Rearranging for the entrainment inception velocity u_{iv} leads to

$$u_{iv} \geq \sqrt{\frac{9.61\sqrt{\sigma g \rho_L}}{\rho_G}} \tag{6.5}$$

Thus, the inception velocities for surfactant-free and surfactant-laden flows are found to be $\approx 14.7 \text{ m s}^{-1}$ and $\approx 12.7 \text{ m s}^{-1}$, respectively. Referring to the flow conditions used in the present work (Table 3.2), for surfactant-free flows it is predicted that the entrainment of liquid is likely to occur when $Re_G > 30 \times 10^3$ as it appears to be a transitional point due to marginal difference between $u_{s,G}$ at $Re_G = 30 \times 10^3$ (14.4 m s^{-1}) and u_{iv}. Hence, some liquid entrainment may also occur. For the surfactant-laden flows, the predicted u_{iv} decreases relative to the clean case due to the lower surface tension caused by DAF surfactant, which, most likely, leads to higher liquid entrainment since the gas superficial velocities for $Re_G \geq 30 \times 10^3$ are higher than the predicted entrainment inception velocity. It is important to note, however, that surfactant concentration gradients also induce gradients of surface tension, and therefore Marangoni stresses, which could

potentially influence the interfacial dynamics as we will discuss below.

A qualitative example of liquid entrainment events that are found to occur in the present experimental set-up is shown in Figure 6.11, which corresponds to surfactant-free flows at $Re_\mathrm{L} = 1250$ and $Re_\mathrm{G} = 40 \times 10^3$. It appears that the wave disintegrates via 'rolling' mechanism explained earlier by Hewitt and Hall-Taylor [73], which occurs at high gas flow rate as in the present case. This leads to evident entrainment of droplets that vary in size between ~ 0.2 mm and ~ 0.8 mm, and a ligament with a length of ~ 10 mm and thickness of ~ 0.7 mm. Similar events were identified by Zadrazil et al. [186] using the PLIF method.

The observed dampening or a slower growth of interfacial wave amplitudes may lead to a delay of the natural growth of hydrodynamic instabilities, and, as mentioned earlier, shift the formation of large amplitudes waves to further downstream distances [102]. It is vital to understand whether this occurs only due to the reduction in the surface tension or also because of the dynamic surface tension. To elaborate, in the former case, it may be that the waves develop in the same manner as for a pure liquid with physical properties modified by the surfactant [26]. In the latter case, when concentration gradients exist, the Marangoni flows are directed radially along an interface from areas of high surfactant concentration (low surface tension) to areas of low surfactant concentration (high surface tension). This phenomena can have a noticeable effect in situations when surface tension is dominant. For instance, it is capable of suppressing interfacial waves in the free-surface turbulent flows [149].

In order to understand the effect of the surfactant on the wave, two competing time-scales, namely Marangoni flow in the liquid film, τ_M, and wave flow, τ_f, need to be defined and compared; these are associated with the balance between: (1) gravitational and viscous stresses; and (2) Marangoni and viscous stresses. The first scales as $\rho g = \mu \dfrac{\mathrm{d}^2 u}{\mathrm{d}y^2} \sim \mu \dfrac{u_{flow}}{h^2}$, and the second as $\dfrac{\Delta \sigma}{\lambda} = \mu \dfrac{\mathrm{d}u}{\mathrm{d}y} \sim \mu \dfrac{u_{film}}{h}$, where u_{flow} and u_{film} are the characteristic velocities of the wave and the liquid film, i.e., $u_{flow} \sim \dfrac{\lambda}{\tau_f}$ and $u_{film} \sim \dfrac{\lambda}{\tau_M}$, respectively. Thus, the balance of (1) and (2) gives $\tau_f = \dfrac{\mu \lambda}{g h^2 \rho}$ and $\tau_M = \dfrac{\mu \lambda^2}{h \Delta \sigma}$, respectively [33]. In the experiments of surfactant-laden flows, water was seeded with DAF surfactant at a concentration of 0.114 mM, which results in the difference in surface tension between the clean and surfactant-contaminated surfaces as $\Delta \sigma = 0.072 - 0.041 = 0.031$ N m^{-1}. The time-scales are compared for two types of waves, small (ripple) waves and large (disturbance) waves, with corresponding wavelengths $\lambda = 0.001$ m and $\lambda = 0.1$ m, respectively [35]. The corresponding heights of disturbance and ripple waves $h = 0.002$ m and $h = 0.0004$ m, respectively, where the former h value is taken from the
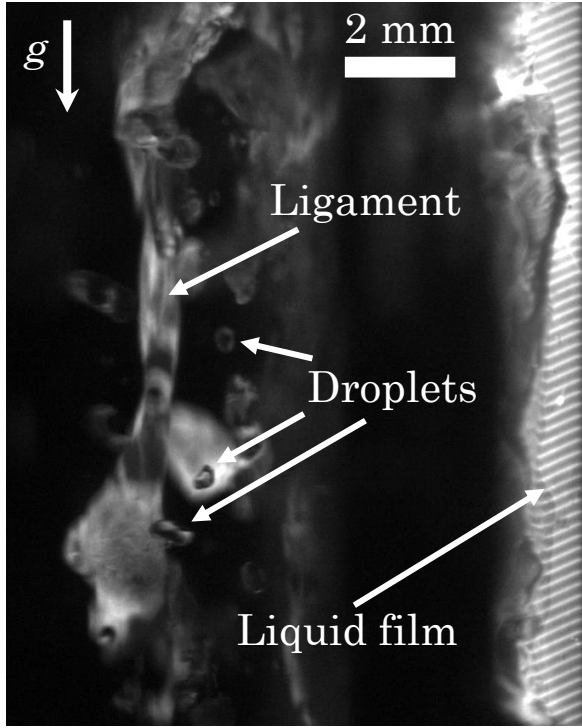
(a) Instantaneous image of liquid entrainment
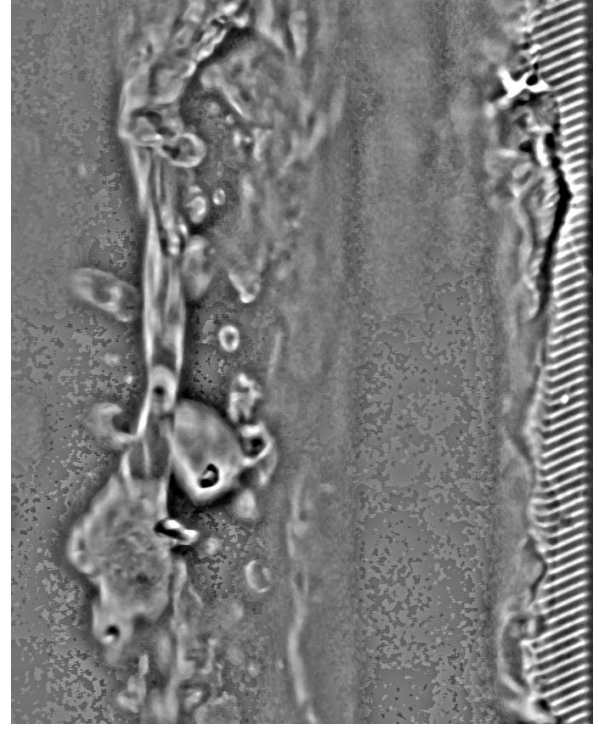
(b) Grayscale image of (a)
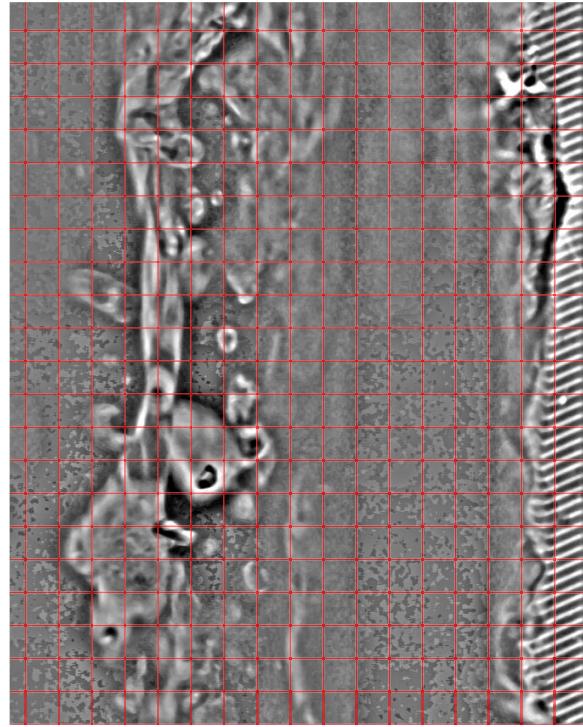
(c) Grayscale image of (a) with raster overlay

Figure 6.11: Instantaneous image of surfactant-free flow at $Re_{\mathrm{L}} = 1250$ and $Re_{\mathrm{G}} = 40 \times 10^3$ manifesting liquid entrainment into the gas core. (a) Spatially corrected and calibrated instantaneous image showing film thickness on the right, and a breakdown of a wave by a 'rolling' mechanism (left side) leading to liquid entrainment events in the form of droplets and a ligament; (b) Conversion of (a) into grayscale image; (c) Applied raster overlay onto image (b) with one square with a size equal to 0.6 mm.

experimentally measured mean amplitude of large waves (Fig. 6.3), while the latter h value is taken from the experimental measurements of Schubring et al. [144]. For these experimental parameter values, τ_f for large waves is of order 10^{-3} s, while τ_M is 10^{-1} s, which suggests that Marangoni flow does not have a significant effect. For ripple waves, τ_f is also found to be in the order of 10^{-3} s, but τ_M is 10^{-4} s, which indicates that Marangoni flow plays a key role in the dynamics of ripple waves. In view of this, the effect of Marangoni flow decreases with increasing wave amplitude for the given flow conditions, which was observed from the measured flow characteristic analysed in the present and previous chapters.

As discussed in Chapters 3 and 4, surfactant can diffuse in the bulk of liquid phase and along the gas-liquid interface. The former and latter terms are denoted here as D_{b} and D_{s}, respectively. In Chapter 4, D_{b} was found to be $= 5.6 \times 10^{-10}$ m^2/s, while D_{s} is taken as 7.7×10^{-9} m^2/s (valid for similar types of surfactants [48, 84, 108]). Diffusion time-scales can be evaluated on the basis of given wave amplitude and its wavelength, i.e., $D_{\mathrm{b}} \sim \dfrac{h^2}{\tau_b}$ and $D_{\mathrm{s}} \sim \dfrac{\lambda^2}{\tau_s}$, where τ_b and τ_s are the time-scales for bulk diffusion and surface diffusion, respectively. Thus, using corresponding λ and h values for large and small waves (see above), τ_b is found to be in the order of 10^3 s for large waves, while for the small waves it is 10^1 s. This shows not only that the bulk diffusion in large waves is slower by two order of magnitude than in the small waves, but also that the surfactant transport by bulk diffusion is also much slower than both Marangoni and interfacial wave flows. The time-scales for surface diffusion in large and small waves are estimated to be in the order of 10^6 s and 10^2 s, respectively, which shows an even weaker effect by the surfactant through surface diffusion relative to Marangoni flow, especially for large amplitude waves. All of the above findings are in agreement with the work of Bobylev et al. [26] who experimentally studied the effect of soluble surfactants on wave evolution on falling films. Even though a surfactant with different physico-chemical properties and substantially lower liquid Reynolds numbers were used in Bobylev et al. [26] study relative to the present work, the group also observed a reduction in the amplitude of waves and thickening of the base film, which is in good agreement with the present work discussed earlier in this chapter. Moreover, they also observed a decrease in the velocity of large interfacial waves which also agrees with earlier propositions made on the basis of film statistics.

6.4   Concluding remarks

In this chapter, an experimental characterisation of the interfacial waves and films of downwards air-water annular flows in the presence and absence of water-soluble fluorescent surfactant is conducted. This was done using two non-intrusive methods, namely S-PLIF and CP, on a wide range of flow conditions that allowed to attain more understanding not only on the behaviour of annular films with and without the gas-shear (often met in various industrial processes), but also on the effect of soluble surfactant on the complex interfacial activity. The provision of such quantitative data can be used for development and validation of predictive tools, from correlations to three-dimensional direct numerical simulations.

It was found that the base film thickness marginally increases with liquid Reynolds number for surfactant-laden flows, and decreases as the gas-shear rate increases for both clean and surfactant cases. While a difference in the base film thickness is observed with every step-change in Re_G for surfactant-free flows, the gas shear appears to play a role only when $Re_G \geq 30 \times 10^3$ for the surfactant-laden flows. The presence of DAF surfactant was observed to have a reducing effect on the base film thickness for flows at $Re_L \leq 1000$ and all Re_G values, and even at higher liquid Reynolds number i.e., once the 'disturbance wave' regime is reached. This is in agreement with predicted values using correlation which shows that the base film thickness decreases with increasing Re_G. The effect of Re_L appears to play nearly no role in thickening of the base film for the surfactant-free flows. On the other hand, it appears to marginally increase for flows in the presence of DAF surfactant, for which a correlation does not account for, and hence, a small disagreement is found.

A slightly different trend was observed for the measurements of amplitude of large waves, where it is found to increase with Re_L. This becomes particularly evident when disturbance waves are found more frequent and larger at the 'thick ripple' and 'disturbance wave' regimes, which was characterised qualitatively in Chapter 5. Interestingly, it is observed that for the surfactant-laden flows the growth of base film thickness is more pronounced than the amplitude of the large waves, whilst the difference is marginal for surfactant-free flows. Moreover, it is observed that at the high gas-shear rates (i.e., $Re_G = 40 \times 10^3$) the amplitudes of large waves are significantly lower in the presence of surfactant relative to the flows without it. This can be caused by the formation of a foam above the film and increased gas entrainment for surfactant-laden flows, which is discussed in the following chapter. A good agreement is found with correlation for all flows at $Re_G \geq 20 \times 10^3$ that predicts the amplitude of large waves. It

agrees with the present observations on a strong reducing effect of Re_G on maximum attainable wave amplitude. Similarly to the correlation used to approximate base film thickness, the reduction in surface tension is not considered, hence, small deviation from the experimental results.

The effect of Re_L was found to be minimal on the frequency of large waves, while Re_G has not showed any specific trend, suggesting that additional waves of smaller amplitude may be forming in a quasi-linear manner with large waves. An apparent difference in frequency of large waves between the surfactant-free and surfactant-laden flows is found for gas-sheared flows at $Re_G \geq 30 \times 10^3$, where it is observed to decrease in agreement with literature. Some differences between the data acquired for surfactant-laden flows using S-PLIF and CP methods are in agreement with the results presented in the Chapters 3 and 5, which can be caused by the increase in gas entrainment as well as spatial-averaging effects that are inherent in the CP technique, thus, limiting its use for certain flow conditions.

The properties of mean film thickness distribution was investigated using probability density functions. The presence of a dominant peak at low film thickness was identified, which decreases with Re_L and increases with Re_G. The 'tails' of the distributions are found to extend up to 2.5 mm when $Re_G = 0$, and reduce up to ≈ 2 mm with Re_G. The density of these 'tails' increases with Re_L, indicating stronger wave activity, and decreases with Re_G. These observations are also in good agreement with literature. Higher dominant peaks towards thinner films and a reduction in the 'tails' of the distribution are measured for all flow conditions of surfactant-laden flows, in agreement with observations on film thinning for flows with DAF surfactant.

Auto-correlating the time-traces of the CP provided an insight into the integral time-scales of the flows, which spanned a range from approximately 10 ms to 30 ms for both surfactant-free and surfactant-laden flows. The shorter time-scales were measured at the highest gas-shear rates, which can be attributed to the enhanced turbulent gas shear causing stronger wave activity. This finding confirms the regime characterisation, where the 'regular wave' regime, encountered at high Re_G, displays an increased number of waves (shorter wavelengths and increased frequency). For surfactant-laden flows it was found that the time-scales decrease for almost all Re_L values and at $Re_G \leq 20 \times 10^3$ flow conditions, suggesting an increase in the frequency of small amplitude interfacial waves. This agrees not only with the current observations on film thickness PDFs, but also with literature. This seems a reasonable justification for the observed film thinning for flows with DAF surfactant, since an increase in the frequency of waves may carry a higher

amount of energy in the shape of the liquid film interface, which is typically affected most significantly by the smaller frequent waves as it was shown in the study by Zadrazil et al. [186]. Subsequently, this may be a primary reason for increased gas and liquid entrainment observed widely in literature.

Using a derived equation by Marmottant and Villermaux [109], wave celerity was calculated for each flow condition at $Re_{\mathrm{G}} \geq 10 \times 10^3$. A linear relationship was found between the wave celerity and superficial gas velocity, where the former increases with Re_{L} and Re_{G}. In addition, using the Kutateladze number criterion, an entrainment inception velocity was also calculated taking into consideration surface tension effects. For the surfactant-free flows it is predicted that mainly liquid entrainment will occur only at $Re_{\mathrm{G}} > 30 \times 10^3$ with some probable minor entrainment at $Re_{\mathrm{G}} \approx 30 \times 10^3$. The inception velocity is found to decrease for the surfactant-laden flows, which results in probable occurrence of liquid entrainment at lower gas shear rates, and higher liquid entrainment rates at the same gas flow rate e.g., $Re_{\mathrm{G}} \approx 30 \times 10^3$.

The effect of DAF surfactant on large and small amplitude waves was also evaluated in terms of the Marangoni flow. A comparison between two competing time-scales associated with the wave flow and Marangoni flow in the liquid film revealed that surfactant plays a key role in the dynamics of ripple waves, but not of large amplitude waves e.g., disturbance waves. This suggests that the effect of Marangoni flow decreases with increasing wave amplitude for the given flow conditions, in agreement with literature on similar experimental works. The estimated time-scales for surfactant diffusion in the bulk and along the surface did not indicate that diffusion will have any significant effect on the interfacial waves.

Chapter 7

Gas entrainment characteristics in annular films

Contents

Gas-liquid annular flows are commonly characterised not only by their bulk film and interfacial behaviour (as described in the last two chapters), but also by the occurrence of gas and liquid entrainment events via various mechanisms. These are typically caused by gas-induced interfacial disturbances that grow with increasing gas and liquid Reynolds numbers, where the former was shown to have a more significant influence on promotion of mechanisms responsible for primary and secondary entrainment [170]. A high gas stream typically leads to a significant increase in turbulent mixing and expansion of interfacial area, resulting in high rates of heat and mass transfer which is beneficial for many processes. Some of the key entrainment mechanisms were experimentally evidenced by Zadrazil et al. [186] who showed the presence of events such as 'wave undercut', 'bubble burst', and 'liquid impingement' using the PLIF method. Specifically, gas entrainment (in the form of bubbles) into the liquid film, may occur, for instance, due to turbulent wavy motions or gas injection [92]. Even though a vast amount of studies were performed with focus on liquid entrainment (e.g., see refs. [11, 21, 80]), limited interest in the literature is found in gas entrainment particularly for downwards flows in vertical orientation (e.g., see ref. [186] for study on surfactant-free annular flows), and especially for surfactant-laden flows.

125

Studies of flows in horizontal orientation have attracted more attention (e.g., see refs. [71, 138]), amongst which, work by Vasques et al. [174] considered the effect of surface tension by addition of butanol at different concentrations. To the best of our knowledge, no work was found to study gas entrainment for downwards annular flows in the presence of water-soluble surfactant.

In this chapter, details of the entrainment characteristics of air bubbles in the water film are presented. The study investigates the distributions of the bubble size and the bubble location relative to the gas-liquid interface (entrainment depth). The measurements of size and entrainment depth are performed on the S-PLIF images for the flow conditions where a sufficient number of bubbles is present in the film, and thus, statistically meaningful results can be obtained. For this, it is found that the number of bubbles measured in each case (300 bubbles or more) results in a standard deviation of less than 5%.

7.1 Bubble size distribution

The area and perimeter of the bubbles are measured on the spatially-corrected and calibrated S-PLIF images, and an equivalent bubble size, d_{eq}, is calculated assuming ellipsoidal shapes. It is important to note that d_{eq} is not equal to an equivalent bubble diameter as the laser sheet can 'slice' the bubbles at any depth (detailed discussions on this effect and potential ways to correct for it are offered by Morgan et al. [117]). Figure 7.1 shows the normalised probability distributions of the sizes of the bubbles entrained in the liquid film. The sizes are distributed in bins of fixed length to 0.1 mm.

The effect of Re_G for flows at $Re_L = 1125$ is shown in Fig. 7.1(a) and (b). The lower range of Re_G ($\leq 20 \times 10^3$) for the surfactant-free flows is shown to produce $\sim 85\%$ bubbles within the size distribution of 0.1-0.7 mm. Larger bubbles are found for flows at $Re_G = 10 \times 10^3$, while $Re_G = 20 \times 10^3$ generates bubbles with a more uniform size distribution. Increasing Re_G to $\geq 30 \times 10^3$ results in a substantial shift of the distribution towards smaller sizes. Approximately 50% of the bubbles measured have a size between 0.1-0.3 mm for $Re_G = 30 \times 10^3$, while for $Re_G = 40 \times 10^3$ it is $\sim 70\%$ for the same range of sizes. In comparison with the lower gas shear rate (e.g., $Re_G = 20 \times 10^3$), only about 20% of the bubbles have that size. Moreover, bubbles that are $d_{eq} < 1.0$ are found more frequently for the two highest gas shear rates. The enhanced turbulent wave-activity induced at increased Re_G results in the generation of smaller bubbles, a behaviour which is also clearly highlighted in the inset of Fig. 7.1(a).
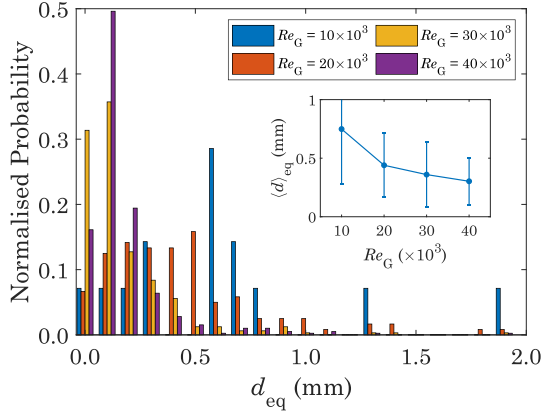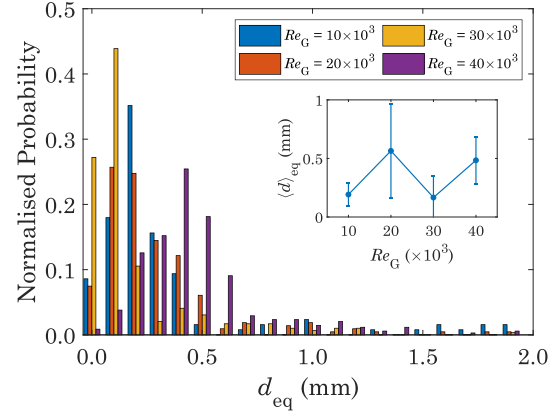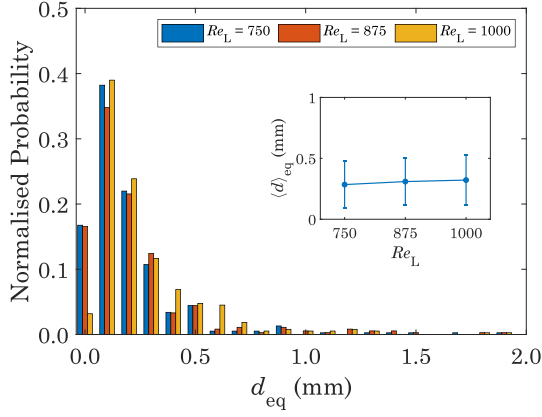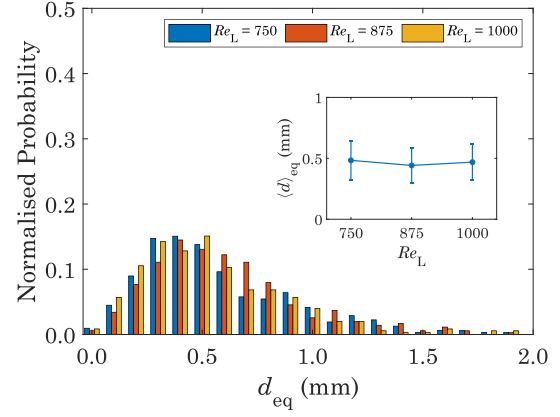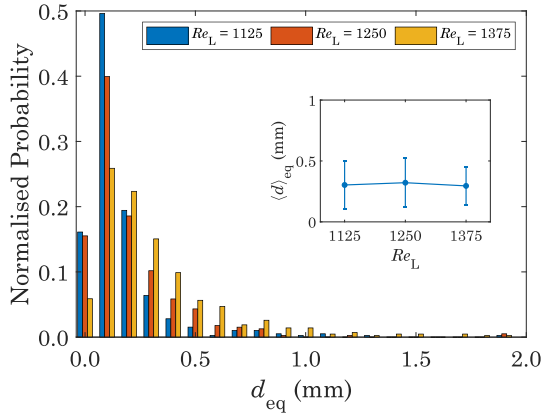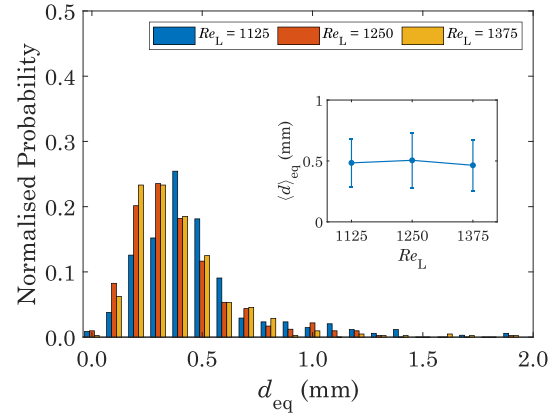
Figure 7.1: Normalised probability distributions of the sizes of the bubbles entrained in the bulk of liquid film. (a) Effect of Re_{G} for surfactant-free flows at $Re_{\mathrm{L}} = 1125$; (b) Effect of Re_{G} for surfactant-laden flows at $Re_{\mathrm{L}} = 1125$; (c) Effect of low Re_{L} for surfactant-free flows at $Re_{\mathrm{G}} = 40 \times 10^3$; (d) Effect of low Re_{L} for surfactant-laden flows at $Re_{\mathrm{G}} = 40 \times 10^3$; (e) Effect of high Re_{L} for surfactant-free flows at $Re_{\mathrm{G}} = 40 \times 10^3$; (f) Effect of high Re_{L} for surfactant-laden flows at $Re_{\mathrm{G}} = 40 \times 10^3$. The symbols in the insets show the time-averaged equivalent bubble sizes measured, while the corresponding 'error' bars show the associated standard deviations.

The bubble size distributions are found to slightly change for the surfactant-laden flows as a function of Re_G (see Fig. 7.1(b)). Evident reduction in the bubble sizes is observed for flows at $Re_G \leq 20 \times 10^3$ where $\sim 90\%$ of the bubbles have sizes $d_{eq} < 0.4$ mm. A significant reduction in the mean bubble size and the standard deviation is measured for low gas shear ($Re_G = 10 \times 10^3$) shown in the insets of Fig. 7.1(a) and (b), while for $Re_G = 20 \times 10^3$ the values are fairly similar. The distribution for $Re_G = 30 \times 10^3$ is not significantly altered for flows in the presence of DAF surfactant, except for the reduction in the mean bubble size. However, for $Re_G = 40 \times 10^3$, the distribution is observed to shift towards larger sizes where $\sim 80\%$ of the bubbles are distributed in the range of 0.2-0.6 mm. The mean bubble size appears to increase by approximately a factor of two.

Figures 7.1(c)–(f) illustrate the effect of Re_L for flows at the highest gas-shear rate ($Re_G = 40 \times 10^3$). Firstly, it is observed that increasing Re_L appears to have an inverse effect to increasing gas shear rate. For the surfactant-free flows (Figs. 7.1(c) and (e)), the distributions at $Re_L < 1250$ exhibit a prominent peak (quasi-mono-disperse) at low bubble sizes, i.e., $\approx 90\%$ $d_{eq} \approx 0.1$-0.3 mm. The probabilities for each interval of d_{eq} appear to be fairly similar. As the Re_L increases to 1375 the distribution flattens, expanding the range of bubble sizes with $\approx 25\%$ of $d_{eq} \geq 0.4$ mm. Such shift in the bubble size distributions with Re_L is comparable to the shift observed in the film thickness PDFs (see Fig. 6.8). From the insets of Figs. 7.1(c) and (e), it is evident that despite the change in the distributions, the mean bubble size, $\langle d_{eq} \rangle$, and the standard deviation remains quasi-constant. On the other hand, a distinct effect of DAF surfactant on the distributions is observed for surfactant-laden flows (see Fig. 7.1(d) and (f)). In the lower range of Re_L (≤ 1000) the bubble sizes are well-distributed with about 85% of d_{eq} ranging from ≈ 0.2 mm to ≈ 0.9 mm, and with very similar probabilities for each interval of d_{eq}. In the higher range of Re_L (≥ 1125), the distribution is found to narrow with $d_{eq} \approx 0.1$-0.6 mm, where about 87% of bubble sizes are found to be distributed within this range. More bubbles with $d_{eq} \geq 1.0$ mm are expected to be found in the lower range of Re_L (≤ 1000) relative to higher Re_L values.

Interestingly, very few bubbles with $d_{eq} < 0.1$ mm are found for surfactant-laden flows relative to the clean case. This may be due to a higher stability of bubbles attributed to the repulsive disjoining pressure due to the steric and hydration forces [140]. On the other hand, due to relatively thinner films at $Re_L < 1000$ for surfactant-laden flows, the entrained bubbles move in a smaller volume which may lead to a more frequent coalescence, despite a delay in coalescence due to Marangoni flows [107]. This shift in the distribution may also be directly

related to the observed increase in the height of large waves ($\langle h_{\text{waves}}\rangle/R$) at $ReL \geq 1000$ (see Fig. 6.3), which may lead to more liquid entrainment in the form of droplets and ligaments promoted by high gas-shear rate and interfacial disturbances, that subsequently undergo re-deposition onto the liquid film causing entrapment of small bubbles relative to the events such as 'ligament break-up' that lead to formation of larger bubbles [180, 186].

Similarly to surfactant-free flows, marginal differences in the mean bubble size and the standard deviation are found with increasing Re_{L} (see insets of Fig. 7.1(d) and (f)). That said, the difference in these two dimensions is evident when comparing the data of surfactant-free with surfactant-laden flows, for the latter case showing higher values i.e., formation of larger bubbles. The dynamics of these bubbles within the film can have a significant contribution towards increased liquid entrainment [92]. For instance, when an entrained bubble rises towards the surface of the film, a thin liquid film forms at the top of the bubble. As the liquid is drained from the bubble film to a critical point, it ruptures in several places ejecting fine droplets into the gas phase. Even larger liquid droplets can be generated on the bursting of bubbles by the motion of the surrounding liquid phase that fills the crater formed by the bubble. At the centre of such craters liquid filaments can rise and disintegrate into larger droplets. The observed presence of larger bubbles for surfactant-laden flows may potentially further promote these liquid entrainment events.

7.2   Bubble entrainment depth

The depth of entrainment of the bubbles in the liquid film is defined as the distance of the bubble centre from the local annular film height, l_{ib}, and is normalised with the local annular film thickness, h, resulting in values that span the range from zero to unity, where zero and unity translate to a bubble located at the gas-liquid interface of annular film and the pipe wall, respectively. To the best of our knowledge, this measurement has not been presented before in the available literature for such flows. As shown in Fig. 7.2, the locations of the bubbles encountered in the film, form a PDF, which is Gaussian-like for the flow conditions investigated (in the absence and presence of DAF surfactant), which means that the bubbles have the highest probability to be located close to the middle of the film, i.e., equal distance between the wall and the gas-liquid interface. As gravity does not play a significant role in the cross-stream motion of the bubbles due to the vertical arrangement of the flow and its inertia, the location of the bubbles is primarily dominated by shear forces. The highest shear gradients, present close to the

solid and gas-liquid boundary, generate lift forces that can lead the bubbles to the film centre. These shear-induced migration effects have also been encountered in a more canonical system of wall-bounded linear shear flow [158].

(a) Surfactant-free flows at $Re_L = 1125$

(b) Surfactant-laden flows at $Re_L = 1125$

(c) Surfactant-free flows at $Re_G = 40 \times 10^3$

(d) Surfactant-laden flows at $Re_G = 40 \times 10^3$
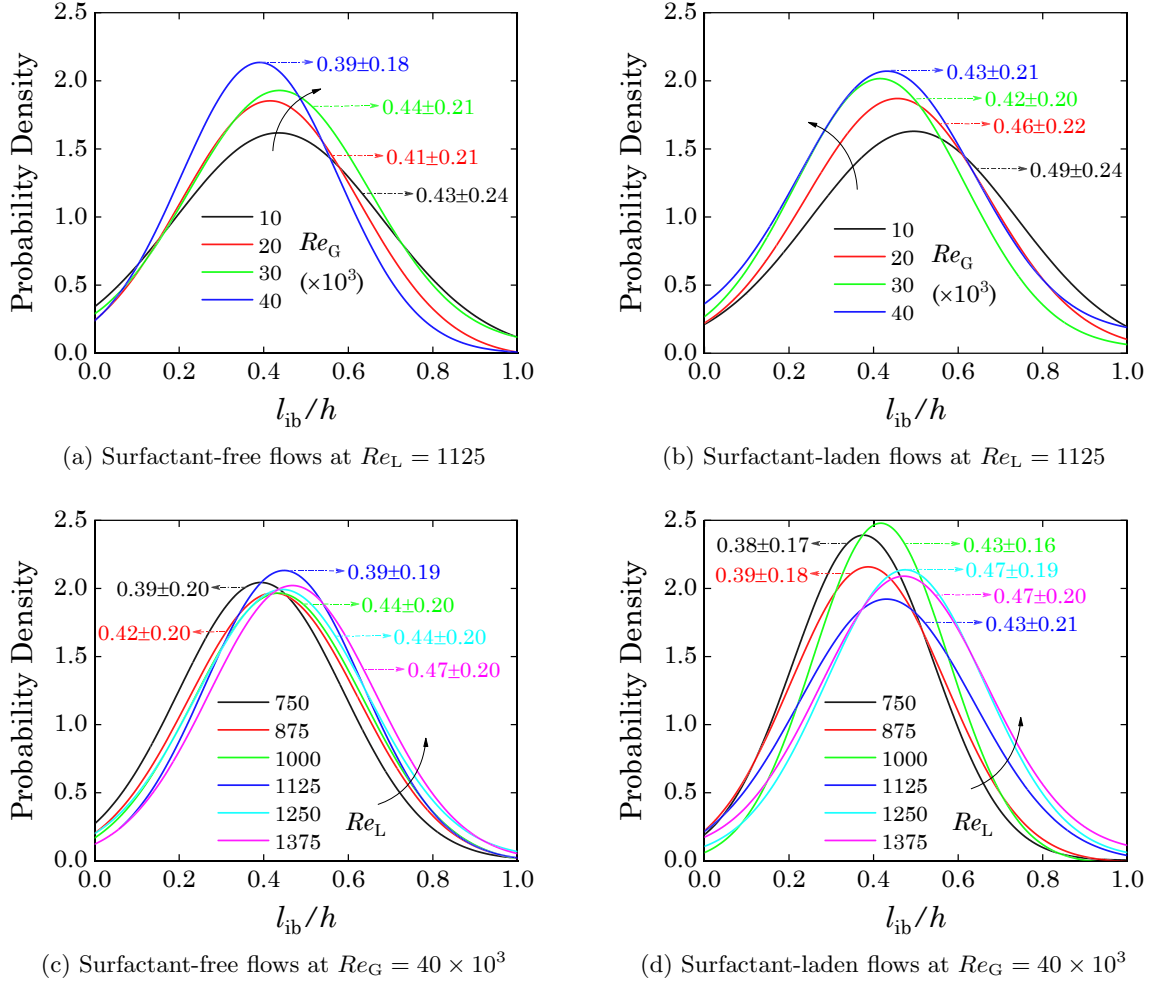
Figure 7.2: Probability density functions of the relative depth of entrainment of bubbles in the liquid film (i.e., ratio of the distance of a bubble from the film's free surface to the bubble centre). (a) Effect of Re_L for $Re_G = 40 \times 10^3$ in surfactant-free flows; (b) Effect of Re_L for $Re_G = 40 \times 10^3$ in surfactant-laden flows; (c) Effect of Re_G for $Re_L = 1125$ in surfactant-free flows; (d) Effect of Re_G for $Re_L = 1125$ in surfactant-laden flows. The arrows show the spatially mean values ($\langle l_{ib}/h \rangle$) of that specific flow condition, while the corresponding '$\pm$' bounds equate to one standard deviation.

The effect of the gas-shear on the bubble entrainment depth is shown in Fig. 7.2(a) and (b). Most importantly, it was found that by increasing the gas-shear rate from $Re_G = 10 \times 10^3$ to $Re_G = 40 \times 10^3$, the probability to find bubble close to the centre of the film increases for surfactant-free and surfactant-laden flows. As a result of increasing Re_G, the spatially-averaged values of the relative entrainment depth, $\langle l_{ib}/h \rangle$, are found to increase by $\sim 10\%$ and $\sim 13\%$ for surfactant-free and surfactant-laden flows, respectively, where in the latter case bubbles are found to be located marginally closer to the centre of the film by 5%-12%. As discussed

130

previously, increasing superficial gas velocity should in parallel also increase superficial velocity of the liquid film. As a result of this, bubbles show a tendency to move away from the pipe wall towards the centre, which is particularly visible when comparing distributions for $Re_{\mathrm{G}} = 10 \times 10^3$ with $Re_{\mathrm{G}} = 40 \times 10^3$.

The effect of Re_{L} on the bubble entrainment depth is also investigated. Figure 7.2(c) and (d) shows that an increase of Re_{L} from 750 to 1375 signifies a gradual shift of the peak of the relative entrainment depth PDFs towards the solid wall, an inverse effect to Re_{G}. The values of $\langle l_{\mathrm{ib}}/h \rangle$ appears to increase by $\sim 16\%$ and $\sim 20\%$ for surfactant-free and surfactant-laden flows, respectively. For $Re_{\mathrm{L}} \leq 1125$ there is a higher probability for bubbles to be found nearer to the gas-liquid film interface for surfactant-laden flows. This may be a result of higher liquid entrainment caused by more frequent bursting of bubble mechanism described by Ishii and Grolmes [80]. Thus, a wider distribution of liquid droplets, including those with fine sizes, may be formed [23, 24]. Consequently, this may increase relative humidity within the gas core, which, as a result, may decrease surface tension air-water annular films [133]. This marginally reverses for $Re_{\mathrm{L}} \geq 1250$ where bubbles are located closer to the centre with some fraction closer to the wall as well. The presence of DAF surfactant does not meaningfully alter $\langle l_{\mathrm{ib}}/h \rangle$, but appears to reduce the standard deviation by as much as $\sim 26\%$.

For a complete picture, it is worth to qualitatively assess the difference in the extent of gas entrainment between surfactant-free and surfactant-laden flows, particularly at the wave front and beneath the large waves. To date, no such examination was done in the literature for downwards annular flows, and especially with high-quality instantaneous images as those acquired in the present work using S-PLIF method. Typical flow and entrainment events of large waves are shown in Figure 7.3 and Figure 7.4 for surfactant-free and surfactant-laden flows, respectively, all corresponding to 'regular wave' regime. Similar behaviour of the wave fronts is observed in both cases (Fig. 7.3(a) and Fig. 7.4(a)), where small bubbles are found to be entrained in the base of the film, and substantially larger bubbles are entrained in the trailing edge of the large waves. The latter case may be one of the main liquid entrainment mechanisms that occurs through bubble bursting as well as subsequent entrainment of smaller sized bubbles. Looking beneath the large waves, evidently different gas entrainment in terms of bubble sizes, concentration and the relative depth is observed between the clean and surfactant cases (Fig. 7.3(b) and Fig. 7.4(b), respectively). Typically, bubbles with larger cord lengths are found to be formed under the waves in surfactant-laden flows. Moreover, bubbles are found to have a propensity to assemble close to the peaks of large waves, likely to occur by the 'rolling'

(a) $Re_L = 1125$, $Re_G = 30 \times 10^3$ (b) $Re_L = 1125$, $Re_G = 30 \times 10^3$ (c) $Re_L = 1125$, $Re_G = 30 \times 10^3$

(d) $Re_L = 1250$, $Re_G = 40 \times 10^3$ (e) $Re_L = 1250$, $Re_G = 40 \times 10^3$

Figure 7.3: Instantaneous S-PLIF images of surfactant-free flows at two different flow conditions at which gas and liquid entrainment events occur. (a) Wave front with a large bubble; (b) Gas entrainment under large wave; (c) Gas and liquid entrainment; (d) Gas entrainment under large wave; (e) Gas entrainment under large wave.
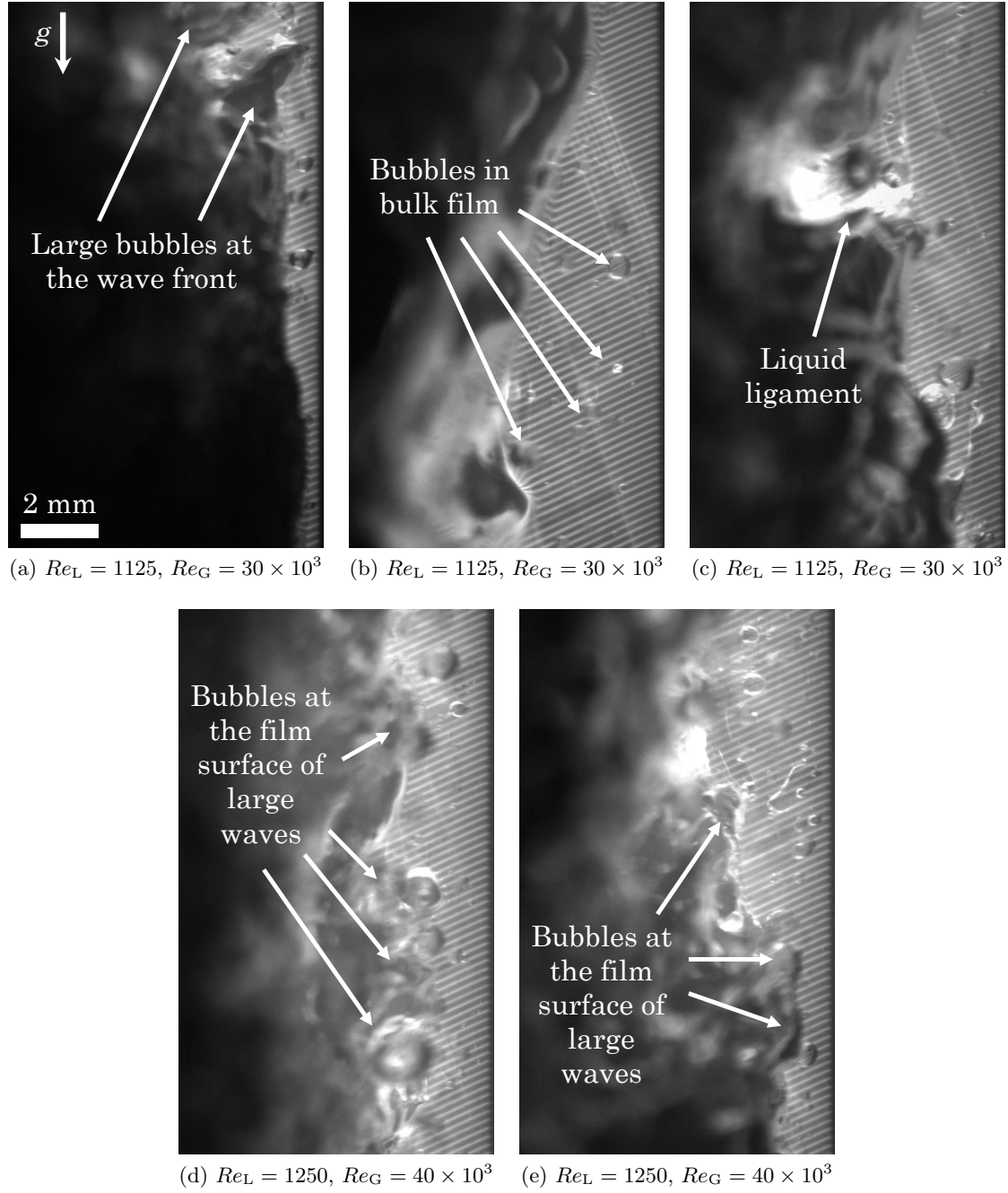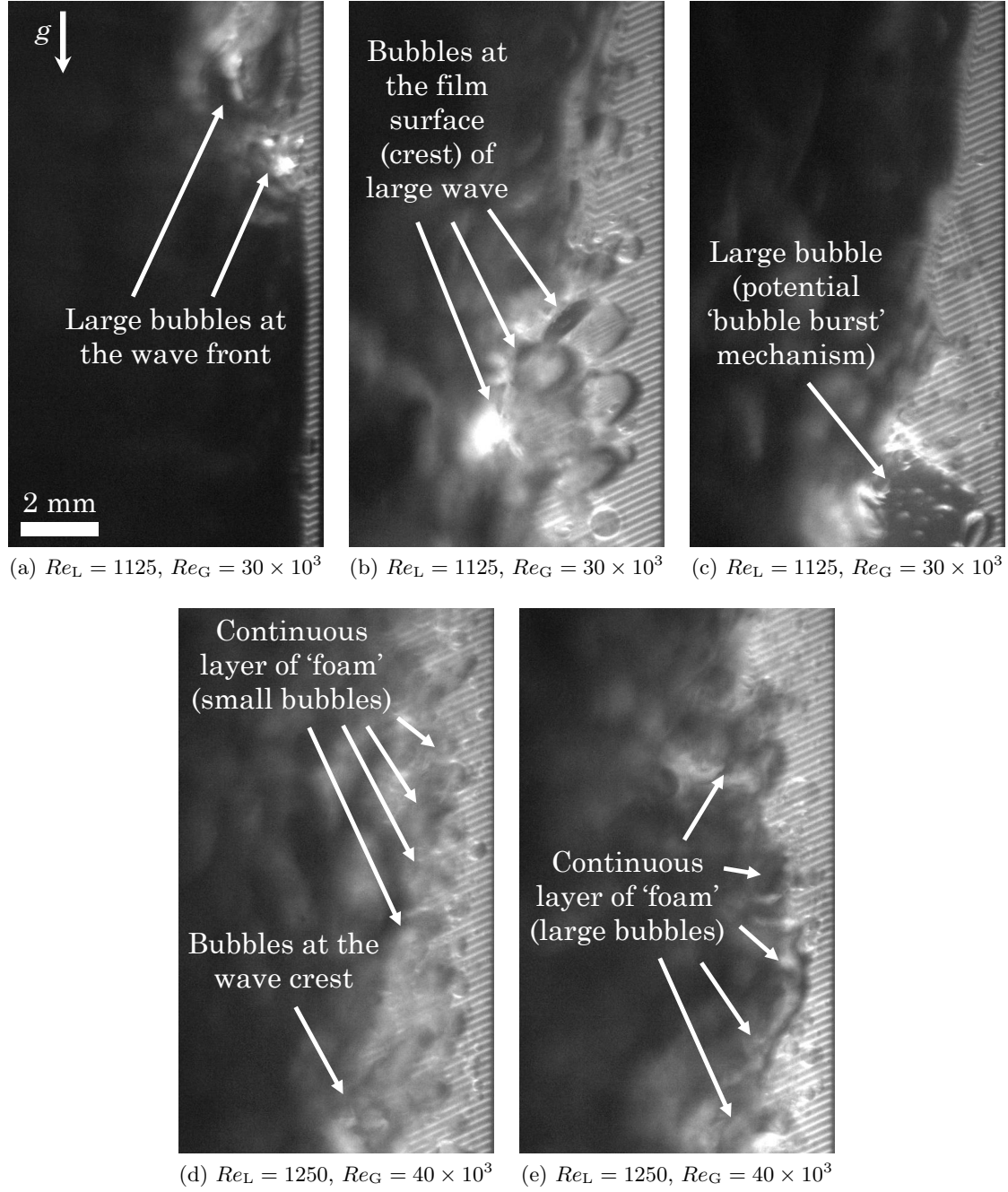
Figure 7.4: Instantaneous S-PLIF images of surfactant-laden flows at two different flow conditions at which gas and liquid entrainment events occur. (a) Wave front with a large bubble; (b) Gas entrainment under large wave; (c) Entrainment of large bubble containing multiple small bubbles; (d) Gas entrainment above and beneath a large wave; (e) Gas entrainment above and beneath a large wave.

mechanism [73]. This agrees with the observations made in Chapter 6 on reduction of wave amplitude for flows with DAF surfactant. These type of 'foamy' crests were also observed by Nimwegen et al [170] using high speed imaging for surfactant-laden upwards annular flows. Possible event of bubble burst can be seen in Fig. 7.3(c), where a ligament appears to be forming, likely to be redeposited by the strong gas shear, and thus, entrapping additional gas into the film bulk. Very similar observation is captured for surfactant-laden flows shown in Fig. 7.4(c), where an unbursted bubble appears in the wave forming a similar curvature in contact with the liquid film to that observed in Fig. 7.3(c).

To elaborate further on the differences in the entrainment events, instantaneous images of typical large wave flows at a higher liquid and gas mass fluxes are shown in Fig. 7.3(d)–(e) and Fig. 7.4(d)–(e) for surfactant-free and surfactant-laden flows, respectively. The largest concentration of bubbles is most frequently found under the large waves, in agreement with Hann et al. [71]. For flows with DAF surfactant this concentration is observed to be higher. It may be the key reason for formation of a foam-like structure close to and above the liquid surface of large waves – expected result of surfactant-laden flows [170, 171]. Due to this, flattening of large waves is observed, in agreement with quantitative results presented in Chapters 5 and 6.

7.3 Concluding remarks

Examination of bubble size distribution as a function of gas Reynolds number has revealed several interesting observations. For surfactant-free flows at $Re_\mathrm{L} = 1125$ and $Re_\mathrm{G} \leq 20 \times 10^3$ about 85% of bubbles are produced within the size range of 0.1-0.7 mm. Higher gas shear rates $(Re_\mathrm{G} \geq 30 \times 10^3)$ result in the formation of smaller bubbles where $\sim 50\%$ are in the size range of 0.1-0.3 mm at $Re_\mathrm{G} = 30 \times 10^3$ and this fraction increases to $\sim 70\%$ when $Re_\mathrm{G} = 40 \times 10^3$. This observation may be a result of enhanced turbulent wave activity that is promoted with increasing Re_G. For surfactant-laden flows, approximately 90% of bubbles have sizes less than 0.4 mm when $Re_\mathrm{G} \leq 20 \times 10^3$. While bubble sizes are not meaningfully altered when Re_G is set to 30×10^3 relative to the clean case, the size distribution is observed to shift towards larger sizes at $Re_\mathrm{G} = 40 \times 10^3$. At these flow conditions, $\sim 80\%$ of bubbles are distributed in the range of 0.2-0.6 mm.

Increasing Re_L was shown to have an inverse effect to increasing gas shear rate. For the surfactant-free flows at $Re_\mathrm{L} < 1250$ and $Re_\mathrm{G} = 40 \times 10^3$ about 90% of bubbles are within size

distribution of 0.1-0.3 mm. Increasing Re_L to 1375 results in the formation of $\sim 25\%$ bubbles with sizes ≥ 0.4 mm. A shift in the distribution was observed for surfactant-laden flows, where $\sim 85\%$ of bubbles have sizes between 0.2 mm and 0.9 mm at $Re_L \leq 1000$. Increasing Re_L above 1125, the narrowing of the distribution to a size range of 0.1-0.6 mm with $\sim 87\%$ of bubbles being found within it. Generally, the mean bubble size is found to increase for surfactant-laden flows for all Re_L values.

In terms of bubble entrainment depth relative to the air-water interface, a Gaussian-like distribution is found for all flow conditions investigated for both surfactant-free and surfactant-laden cases i.e., highest probability of entrainment depth is around the middle of the film. Such an observation is likely to be a direct result of shear-induced migration effects found in such flows. The probability of finding bubbles around the centre of the film also increases with Re_G for clean and DAF cases. On the other hand, an inverse effect is observed when increasing Re_L i.e., bubbles are prone to moving towards the pipe wall.

Qualitative assessment of gas entrainment has shown that areas of highest bubble concentration are typically found beneath the large waves, in agreement with the literature. Interestingly, for flows with DAF surfactant, a higher proportion of bubbles of larger sizes are found to be located closer to the liquid film surface with clearly visible thinning of the film and amplitude of the waves. Foam-like structures close to the interface are visible which were also reported earlier in the literature for similar experiments. This is found to agree with the results discussed in the previous two chapters.

Chapter 8

Conclusions and future outlooks

Contents

The work presented in this thesis in relation to co-current downwards air-water annular flows in the absence and presence of water-soluble fluorescent surfactant over a wide-range of flow conditions revealed the complex hydrodynamic behaviour of the film and interfacial flows. For the first time in the literature, the application of an in-house developed optical method, namely S-PLIF, was applied for gas-liquid annular flows that provided detailed qualitative and quantitative evidence on the effect of surfactant on these flows. The S-PLIF method was complemented with measurements using a capacitance probe that provided even deeper insight into the interfacial flows. The commercially acquired fluorescent surfactant that was employed in the present study was further treated using an in-house developed method to transform it from insoluble to soluble state in sustainable solvents such as water. To date, no such water-soluble fluorescent surfactants were reported in literature. A detailed characterisation of this fluorescent surfactant was also performed. In addition, recommendations for future work are included that would further advance our understanding not only the development and behaviour of annular flows, but also permit us to elucidate the mechanisms associated with effect of surfactants on complex interfacial flows.

8.1 Conclusions

In the present study, a novel method developed in-house to treat commercially available insoluble fluorescent surfactant 5-dodecanoylaminofluorescein (DAF) to convert it to a water-soluble fluorescent surfactant that can find its applicability in a wide-range of applications related to fluid mechanics and interface science, particularly where surface tension plays a key role e.g., capillary and thin film flows. One of the primary advantages of this development is the ability to track surfactant concentration by the DAF molecule's fluorescence signal, which was demonstrated in the present work using a widely-employed Nd:YAG laser. DAF molecule was experimentally characterised in detail to unveil its optical properties (i.e., light absorption and emission spectra, self-quenching concentration), molecular stability under basic conditions (i.e., due to potential hydrolysis reaction), surfactant properties (i.e., surface pressure-area isotherm, dynamic and equilibrium surface tension data, CMC, diffusivity constant, adsorption constant, desorption constant, and maximum packing concentration).

To demonstrate not only the applicability of the DAF fluorescent surfactant in fluid mechanics applications, but also to understand the effect of soluble surfactant on complex multiphase flows, a detailed study of downwards annular film flows in the absence and presence of DAF surfactant was conducted. A novel adaptation of planar laser-induced fluorescence (PLIF), which in the present work is referred to as structured PLIF (S-PLIF), was successfully applied not only in the study of the falling films confirming previous experimental results for surfactant-free flows, but also, for the first time, its application in the study of gas-sheared annular flows. This methodology permits to probe film characteristics not only from a quantitative perspective by detecting gas-liquid interface with a greater accuracy than other traditional methods such as PLIF and capacitance probe (typical measurement tools used in multiphase flows studies), but also maintaining access to qualitative assessment, i.e., gas and liquid entrainment statistics and phenomenology. Comparing S-PLIF with the PLIF method, it was generally found that the error in the film thickness measurements present due to refraction or total internal reflection of the light at the interface of a circumferentially non-uniform film is substantially reduced when using the S-PLIF method owing to developments of both measurement and advanced image processing techniques (outlined in Chapter 3). In addition, also for the first time, simultaneous measurements of S-PLIF and capacitance probe (CP) were conducted in the present work. Assembling a bespoke capacitance probe enabled to conduct temporally resolved film thickness measurements with high temporal resolution along the circumferential perimeter of the pipe. Comparison of time-averaged film thicknesses over a wide range of flow conditions showed a good agreement

with S-PLIF and results obtained from the available literature, where deviations are found to be below $\sim 20\%$. The application of S-PLIF method in the present experimental campaign displays its versatility towards applications for a wide range of different pipe diameters, shapes, and orientations.

Using the obtained qualitative and quantitative data from S-PLIF and CP methods, firstly, the adequacy of the chosen flow conditions (shown in Table 3.2) was confirmed by identifying four different annular flow regimes, namely 'dual-wave', 'thick ripple', 'disturbance wave' and 'regular wave', in agreement with literature. The film characteristics (i.e., film thickness, roughness, interfacial wave activity, gas entrainment) corresponding to each flow regime were found to differ sufficiently enough to construct flow pattern maps for the chosen set of flow conditions. Close assessment of these data revealed that the flow regimes are affected by the presence of surfactant in annular flows, which were not explored in literature to date. The characteristic differences were primarily found to be in interfacial wave activity and higher gas entrainment rates for flows with DAF surfactant. These findings agree with literature works that also observed a strong change in the behaviour of surfactant-laden flows under influence of high gas-shear due to reduced cohesion forces.

Detailed quantitative measurements of the aforementioned film characteristics using S-PLIF and CP methods allowed to improve our understanding of air-water annular flows in pipe in the presence of surfactant. Firstly, the obtained results for the surfactant-free falling films were compared with literature and good agreement was found, which verified the methodology used herein. Following that, a comparison between flow characteristics of surfactant-free and surfactant-laden flows in the absence and presence of gas-shear, led to several new findings. For instance, a reduction in film thickness for surfactant-laden flows at nearly all flow conditions was observed relative to the results for surfactant-free flows of the present study and literature. The same observations were established for gas-sheared films, which was found to agree with literature works on similar experimental studies (e.g., upwards co-current annular flows). It is proposed that this may be caused by a higher rate of liquid entrainment events which are related to higher and/or earlier occurrence of Kelvin-Helmholtz instability due reduced surface tension. In fact, this agrees with the observed higher interfacial instabilities in terms of film roughness. Moreover, quantitative and qualitative results showed not only the smoothing of the interfacial films due to DAF surfactant, but also a change in gas entrainment characteristics, which is proposed to be the primary reason for observed changes at high gas mass fluxes. Using correlations developed by Ishii and Grolmes [80], a fairly good agreement is found between the

predicted and experimental values. The film thickness was found to be within $\sim 50\%$ difference for the surfactant-free flows, and within $\sim 35\%$ for surfactant-laden flows. This reveals the inadequacy of current correlations found in literature, which do not account for surface tension effects.

Findings from the present study may permit in the design and optimisation of relevant industrial processes especially those where the control of heat and/or mass transfer plays a key role. This is evident from the results that revealed not only on the aforesaid film thinning effect by the surfactant, which may increase mass transfer by potentially higher film velocity, but also change in the characteristics of interfacial waves and entrainment events. Surfactant was found to generally lead to thickening of the base film, reduction in the amplitude of large waves, and increase in the frequency of small waves, which subsequently may alter the surface area in a desirable manner. Furthermore, potentially higher liquid entrainment, and recorded increase in gas entrainment, change in entrained bubble size distribution and bubble entrainment depth for surfactant-laden flows may also significantly modify the operation efficiency and controlability of pertinent unit operations such as thin-film reactors or bubble column reactors. All in all, the presented novel experimental methods and results of the current work may have positive implications for industrially relevant processes and future technological advancements due to a wide scope of applicability, which are elaborated in the following section.

8.2 Future outlooks

The results of the present work allowed us to identify a number of important fundamentals that would require further study and development associated not only with the annular film flows, but also with a wide-range of other multiphase flows. The scope of these are outlined in this section. Evident results from the present work on the study of downwards air-water annular flows have provided strong indication that water-soluble surfactants can considerably change the flow patterns and interfacial wave dynamics. In order to elucidate the mechanisms for these changes, the following studies should be carried out:

- The effect of the surface tension on the wave dynamics (e.g., development and velocity) by varying the surfactant bulk concentration between zero/low values and values equal to several CMCs. It is known that variation either in bulk concentration or surfactant physico-chemical properties may stabilise or destabilise downwards flowing films [26]. In

Chapter 5 it was proposed that surfactant may substantially alter the velocities of the waves. Thus, acquiring a distribution of wave velocity/celerity as a function of wave amplitude may explain the reported herein observations.

- Variation of surfactant bulk concentration will also have an influence on the development of waves starting from the inlet point. To understand how the evolution of interfacial waves are affected by this, it is necessary to perform S-PLIF measurements across the whole flow development length. This could be performed not only at fixed locations along the pipe, but also with a moving frame-of-reference [8].

- Design a simultaneous application of S-PLIF and PIV to closely evaluate velocity profiles within the liquid film. This would allow to establish not only the flow profiles for surfactant-free and surfactant-laden flows, which could explain the observed differences in the film thickness for the same mass fluxes, but also the effect of surfactant on various flow properties such wave celerity, shear stresses close to the gas-liquid and liquid-wall interfaces, turbulent characteristics (e.g., recirculation zones), liquid and gas entrainment events.

- The applied correlations in the present study that were drawn from literature, were found to be either overpredicted or underpredicted relative to the experimental results. Majority of the chosen models do not take into account the potential effects of surfactant on film dynamics (e.g., change in the 'waviness', thickness of the waves and base films, or frequency of different types of waves) as well as liquid and gas entrainment. To advance the predictive tools, a parametric study (more extensive than performed in the present work) is required. Acquisition of the data also as a function of surfactant bulk concentration (as per above points) would provide more accurate correlations.

- The developed method herein to treat insoluble DAF surfactant with basic solution in order to make it soluble in sustainable solvents such as water, offers an opportunity to measure, for the first time, the surfactant concentration in the film bulk as well as at the air-liquid interface applicable for many relevant industrial applications. This can be potentially performed using a structured light variation of two-colour laser-induced fluorescence. This method typically uses the emission of two different tracer dyes, where the intensity ratio contains the desired information. Both tracers must fluoresce at different wavelengths to separate them with appropriate optical filters on two different cameras. Preliminary results of most potential candidate dyes that would combine under these conditions with DAF surfactant is Sulforhodamine B (SR), which is a naturally water-soluble (non-surfactant)

141

dye. The in-house measured absorption/emission spectra is presented in Appendix D. The feasibility of this combination is further demonstrated by the fluorescence intensity measurements for a mixture of DAF and SR solution which are also included in Appendix D. Successfully tracking surfactant concentration would allow to understand the mechanism of interface rigidification at low gas flow rates i.e., how surfactant-induced Marangoni stresses heal interfacial deformations, leading to wave amplitude reduction. Additionally, measuring concentration fields would provide answers to mechanisms of interface destabilisation at high liquid flow rates i.e., if inertial contributions to the flow are sufficiently large, surfactant can collect preferentially in the wave trough so that Marangoni stresses will drive the flow from the troughs towards the wave crests leading to further destabilisation.

- Ability to measure surfactant concentration provides opportunities to study fluid mechanics not only on a large-scale, but also at a small-scale e.g., droplet impact, tip-streaming, as well as at a macro and micro scales e.g., adsorption of surfactant in capillaries of porous rocks, flow in micro-channels for semiconductor applications.

- The statistics of gas entrainment presented in Chapter 7 was performed by identifying bubble sizes and location in the bulk film manually. In order to make this process more reliable and systematic (as the present method carries human errors and is time-demanding), a machine learning for image segmentation could be used. To elaborate, this type of image processing would require to extract various features from the image(s) using different filters (e.g., Gaussian, Mean, Sobel, Hessian, etc.) with different parameters and sizes of the selected filter areas around the pixels within the uploaded image (2D Kernels). The outputted results would then be merged into a single feature vector for every pixel, and the resulting analysis model would generate a segmented image(s). An applied example of this image processing technique to the current annular flows is shown in Appendix C. Preliminary results on the determining bubble sizes and the entrainment depth appear to be promising. Further adjustments and training of such module would be beneficial for quantitative data analysis. This could be also potentially applied for wider application e.g., analysis of liquid entrainment.

- Further characterisation of physico-chemical properties DAF surfactant would expand its use in other applications. One of such characterisations could be focused on DAF foaming properties, and applied in the large-scale experiments relevant to industrial-based processes such as the carry-over problems in oil and gas separators [148].

Bibliography

[1] Critical micelle concentration (CMC) and surfactant concentration, Feb 2021. [Online; accessed 18. Feb. 2021].

[2] OCA Optical contact angle goniometers and drop shape analysis systems - DataPhysics Instruments, Feb 2021. [Online; accessed 18. Feb. 2021].

[3] M. B. Alamu and B. J. Azzopardi. Wave and drop periodicity in transient annular flow. *Nucl. Eng. Des.*, 241(12):5079–5092, Dec 2011.

[4] S. Alekseenko, V. Antipin, A. Cherdantsev, S. Kharlamov, and D. Markovich. Two-wave structure of liquid film and wave interrelation in annular gas-liquid flow with and without entrainment. *Phys. Fluids*, 21(6):061701, Jun 2009.

[5] S. V. Alekseenko, V. A. Antipin, A. V. Cherdantsev, S. M. Kharlamov, and D. M. Markovich. Investigation of Waves Interaction in Annular Gas–Liquid Flow Using High-Speed Fluorescent Visualization Technique. *Microgravity Sci. Technol.*, 20(3):271–275, Sep 2008.

[6] S. V. Alekseenko, A. V. Cherdantsev, M. V. Cherdantsev, S. V. Isaenkov, and D. M. Markovich. Study of formation and development of disturbance waves in annular gas–liquid flow. *Int. J. Multiphase Flow*, 77:65–75, Dec 2015.

[7] S. V. Alekseenko, A. V. Cherdantsev, O. M. Heinz, S. M. Kharlamov, and D. M. Markovich. Analysis of spatial and temporal evolution of disturbance waves and ripples in annular gas–liquid flow. *Int. J. Multiphase Flow*, 67:122–134, Dec 2014.

[8] J. S. An, A. V. Cherdantsev, I. Zadrazil, and C. N. Markides. Study of disturbance wave development in downwards annular flows with a moving frame-of-reference brightness-based laser-induced fluorescence method. *Exp. Fluids*, 61(7):169–6, Jul 2020.

[9] P. Andreussi, E. Pitton, P. Ciandri, D. Picciaia, A. Vignali, M. Margarone, and A. Scozzari. Measurement of liquid film distribution in near-horizontal pipes with an array of wire probes. *Flow Measurement and Instrumentation*, 47:71–82, 2016.

[10] M. Aytouna, D. Bartolo, G. Wegdam, D. Bonn, and S. Rafaï. Impact dynamics of surfactant laden drops: dynamic surface tension effects. *Experiments in fluids*, 48(1):49–57, 2010.

[11] B. Azzopardi. Drops in annular two-phase flow. *International Journal of Multiphase Flow*, 23(7):1–53, 1997.

[12] B. J. Azzopardi. Drop sizes in annular two-phase flow. *Exp. Fluids*, 3(1):53–59, Jan 1985.

[13] B. J. Azzopardi. Disturbance wave frequencies, velocities and spacing in vertical annular two-phase flow. *Nucl. Eng. Des.*, 92(2):121–133, Apr 1986.

[14] B. J. Azzopardi. *Gas-liquid Flows.* Begell House, 2006.

[15] B. J. Azzopardi and P. B. Whalley. Artificial waves in annular two-phase flow. *Harry Diamond Laboratories (Technical Report) HDL-TR*, pages 1–8, 1980.

[16] D. Barnea, O. Shoham, and Y. Taitel. Flow pattern transition for downward inclined two phase flow; horizontal to vertical. *Chemical Engineering Science*, 37(5):735–740, 1982.

[17] J. K. Beattie, A. M. Djerdjev, A. Gray-Weale, N. Kallay, J. Lützenkirchen, T. Preočanin, and A. Selmani. ph and the surface tension of water. *Journal of Colloid and Interface Science*, 422:54–57, 2014.

[18] R. Belt, J. Van't Westende, H. Prasser, and L. Portela. Time and spatially resolved measurements of interfacial waves in vertical annular flow. *International Journal of Multiphase Flow*, 36(7):570–587, 2010.

[19] F. Benjamin, B. William, and Farish. XLIV. Of the stilling of waves by means of oil. Extracted from sundry letters between Benjamin Franklin, LL. D. F. R. S. William Brownrigg, M. D. F. R. S. and the Reverend Mr. Farish. *Philos. Trans. R. Soc. Lond.*, 64:445–460, Dec 1774.

[20] C. Berna, A. Escrivá, J. L. Muñoz-Cobo, and L. E. Herranz. Review of droplet entrainment in annular flow: Interfacial waves and onset of entrainment. *Prog. Nucl. Energy*, 74:14–43, Jul 2014.

[21] C. Berna, A. Escrivá, J. L. Muñoz-Cobo, and L. E. Herranz. Review of droplet entrainment in annular flow: Characterization of the entrained droplets. *Prog. Nucl. Energy*, 79:64–86, Mar 2015.

[22] J. D. Berry, M. J. Neeson, R. R. Dagastine, D. Y. Chan, and R. F. Tabor. Measurement of surface and interfacial tension using pendant drop tensiometry. *Journal of Colloid and Interface Science*, 454:226–237, 2015.

[23] D. C. Blanchard. Bursting of Bubbles at an Air–Water Interface. *Nature*, 173(4413):1048, May 1954.

[24] D. C. Blanchard. The ejection of drops from the sea and their enrichment with bacteria and other materials: A review. *Estuaries*, 12(3):127–137, Sep 1989.

[25] G. Bleys and P. Joos. Adsorption kinetics of bolaform surfactants at the air/water interface. *The Journal of Physical Chemistry*, 89(6):1027–1032, 1985.

[26] A. Bobylev, V. Guzanov, A. Kvon, and S. Kharlamov. Influence of soluble surfactant on wave evolution on falling liquid films. In *Journal of Physics: Conference Series*, volume 1382, page 012073. IOP Publishing, 2019.

[27] H. Bouyahiaoui, A. Azzi, A. Zeghloul, A. H. Hasan, A. Al-Sarkhi, and M. Parsi. Vertical upward and downward churn flow: Similarities and differences. *J. Nat. Gas Sci. Eng.*, 73:103080, Jan 2020.

[28] N. Brauner, D. Moalem Maron, and I. Toovey. Characterization of the interfacial velocity in wavy thin films flow. *Int. Commun. Heat Mass Transfer*, 14(3):293–302, May 1987.

[29] R. Brown, A. Bennet, and H. Slebocka-Tilk. Recent perspectives concerning the mechanism of h3o+- and hydroxide-promoted amide hydrolysis. *Accounts of chemical research*, 25(11):481–488, 1992.

[30] A. Casandra, M.-C. Chung, B. A. Noskov, and S.-Y. Lin. Adsorption kinetics of sodium dodecyl sulfate on perturbed air-water interfaces. *Colloids Surf., A*, 518:241–248, Apr 2017.

[31] C.-H. Chang and E. I. Franses. Adsorption dynamics of surfactants at the air/water interface: a critical review of mathematical models, data, and mechanisms. *Colloids Surf., A*, 100:1–45, Jul 1995.

145

[32] A. Charogiannis, J. S. An, V. Voulgaropoulos, and C. N. Markides. Structured planar laser-induced fluorescence (S-PLIF) for the accurate identification of interfaces in multiphase flows. *International Journal of Multiphase Flow*, 2019.

[33] Z. Che and O. K. Matar. Impact of Droplets on Liquid Films in the Presence of Surfactant. *Langmuir*, 33(43):12140–12148, Oct 2017.

[34] C. V.-H. Chen, Y. Liu, H. A. Stone, and R. K. Prud'homme. Visualization of surfactant dynamics to and along oil–water interfaces using solvatochromic fluorescent surfactants. *Langmuir*, 34(36):10512–10522, 2018.

[35] A. V. Cherdantsev. Overview of physical models of liquid entrainment in annular gas-liquid flow. *AIP Conf. Proc.*, 1939(1):020006, Mar 2018.

[36] A. V. Cherdantsev, J. S. An, A. Charogiannis, and C. N. Markides. Cross-validation of PLIF and BBLIF towards the detailed study of gas-sheared liquid films in downward annular flows. In *19th International Symposium on the Application of Laser and Imaging Techniques to Fluid Mechanics*, 2018.

[37] A. V. Cherdantsev, J. S. An, A. Charogiannis, and C. N. Markides. Simultaneous application of two laser-induced fluorescence approaches for film thickness measurements in annular gas-liquid flows. *International Journal of Multiphase Flow*, 119:237–258, 2019.

[38] A. V. Cherdantsev, D. B. Hann, and B. J. Azzopardi. Study of gas-sheared liquid film in horizontal rectangular duct using high-speed LIF technique: Three-dimensional wavy structure and its relation to liquid entrainment. *Int. J. Multiphase Flow*, 67:52–64, Dec 2014.

[39] K. Chu and A. Dukler. Statistical characteristics of thin, wavy films: Part ii. studies of the substrate and its wave structure. *AIChE Journal*, 20(4):695–706, 1974.

[40] K. J. Chu and A. E. Dukler. Statistical characteristics of thin, wavy films III. Structure of the large waves and their resistance to gas flow. *AIChE J.*, 21(3):583–593, May 1975.

[41] R. V. Craster and O. K. Matar. Dynamics and stability of thin liquid films. *Rev. Mod. Phys.*, 81(3):1131–1198, Aug 2009.

[42] F. D. Curbelo, V. C. Santanna, E. L. B. Neto, T. V. Dutra Jr, T. N. C. Dantas, A. A. D. Neto, and A. I. Garnica. Adsorption of nonionic surfactants in sandstones. *Colloids and Surfaces A: Physicochemical and Engineering Aspects*, 293(1-3):1–4, 2007.

[43] A. Czajka, G. Hazell, and J. Eastoe. Surfactants at the Design Limit. *Langmuir*, 31(30):8205–8217, Aug 2015.

[44] B. Dabir, M. R. Riazi, and H. R. Davoudirad. Modelling of falling film reactors. *Chem. Eng. Sci.*, 51(11):2553–2558, Jun 1996.

[45] J. Davies and R. Vose. On the damping of capillary waves by surface films. *Proceedings of the Royal Society of London. Series A. Mathematical and Physical Sciences*, 286(1405):218–234, 1965.

[46] K. De Kerpel, B. Ameel, S. De Schampheleire, C. T'Joen, H. Canière, and M. De Paepe. Calibration of a capacitive void fraction sensor for small diameter tubes based on capacitive signal features. *Applied Thermal Engineering*, 63(1):77–83, 2014.

[47] K. De Kerpel, B. Ameel, C. T'Joen, H. Canière, and M. De Paepe. Flow regime based calibration of a capacitive void fraction sensor for small diameter tubes. *International Journal of Refrigeration*, 36(2):390–401, 2013.

[48] R. Dimova, K. Danov, B. Pouligny, and I. B. Ivanov. Drag of a Solid Particle Trapped in a Thin Film or at an Interface: Influence of Surface Viscosity and Elasticity. *J. Colloid Interface Sci.*, 226(1):35–43, Jun 2000.

[49] T. Dong, W. H. Weheliye, and P. Angeli. Laser induced fluorescence studies on the distribution of surfactants during drop/interface coalescence. *Physics of Fluids*, 31(1):012106, 2019.

[50] G. G. Dotchi Exerowa. *Foam Films and Foams:Fundamentals and Applications*. Taylor & Francis, Andover, England, UK, Aug 2018.

[51] M. J. Doughty. ph dependent spectral properties of sodium fluorescein ophthalmic solutions revisited. *Ophthalmic and Physiological Optics*, 30(2):167–174, 2010.

[52] J. G. Drobny. *Technology of fluoropolymers*. CRC Press, 2008.

[53] A. K. Dutta and C. Salesse. A spectroscopic and epifluorescence microscopic study of (hexadecanoylamino) fluorescein aggregates at the air- water interface and in langmuir-blodgett films. *Langmuir*, 13(20):5401–5408, 1997.

[54] J. Eastoe and J. S. Dalton. Dynamic surface tension and adsorption mechanisms of surfactants at the air–water interface. *Adv. Colloid Interface Sci.*, 85(2):103–144, Mar 2000.

[55] D. A. Edwards, H. Brenner, and D. T. Wasan. *Interfacial Transport Processes and Rheology*. Butterworth-Heinemann, Oxford, England, UK, 1991.

[56] V. Fainerman and R. Miller. Adsorption kinetics of short-chain alcohols at the water/air interface: Diffusion-controlled adsorption under the conditions of a nonequilibrium surface layer. *Journal of Colloid and Interface Science*, 178(1):168–175, 1996.

[57] D. W. Fallest, A. M. Lichtenberger, C. J. Fox, and K. E. Daniels. Fluorescent visualization of a spreading surfactant. *New Journal of Physics*, 12(7):073029, 2010.

[58] H. Fan, E. W. Leve, C. Scullin, J. Gabaldon, D. Tallant, S. Bunge, T. Boyle, M. C. Wilson, and C. J. Brinker. Surfactant-assisted synthesis of water-soluble and biocompatible semiconductor quantum dot micelles. *Nano letters*, 5(4):645–648, 2005.

[59] W. Fan, A. V. Cherdantsev, and H. Anglart. Experimental and numerical study of formation and development of disturbance waves in annular gas-liquid flow. *Energy*, 207:118309, Sep 2020.

[60] D. P. Fernandez, Y. Mulev, A. Goodwin, and J. L. Sengers. A database for the static dielectric constant of water and steam. *Journal of Physical and Chemical Reference Data*, 24(1):33–70, 1995.

[61] T. Furukawa, F. Matsuyama, and M. Sadatomi. Effects of Reduced Surface Tension on Liquid Film Structure in Vertical Upward Gas-Liquid Annular Flows. *JPES*, 4(1):1–11, 2010.

[62] G. Gaines. *Insoluble Monolayers at Liquid-gas Interfaces*. Interscience monographs on chemistry, physical chemistry section. Interscience Publishers, 1966.

[63] F. Gallou, N. A. Isley, A. Ganic, U. Onken, and M. Parmentier. Surfactant technology applied toward an active pharmaceutical ingredient: more than a simple green chemistry advance. *Green Chemistry*, 18(1):14–19, 2016.

[64] A. Georgantaki, M. Vlachogiannis, and V. Bontozoglou. Measurements of the stabilisation of liquid film flow by the soluble surfactant sodium dodecyl sulfate (sds). *International Journal of Multiphase Flow*, 86:28–34, 2016.

[65] B. Guo. *Well Productivity Handbook*. Gulf Professional Publishing, 2019.

[66] H. Gutiérrez, L. Echevarria, and M. Caetano. Phase transitions in langmuir monolayer of long chain attached fluorescein studied by second harmonic generation technique. *Colloids and Surfaces A: Physicochemical and Engineering Aspects*, 348(1-3):64–69, 2009.

[67] T. Häber, M. Gebretsadik, H. Bockhorn, and N. Zarzalis. The effect of total reflection in plif imaging of annular thin films. *International Journal of Multiphase Flow*, 76:64–72, 2015.

[68] N. Hall Taylor, G. F. Hewitt, and P. M. C. Lacey. The motion and frequency of large disturbance waves in annular two-phase flow of air-water mixtures. *Chem. Eng. Sci.*, 18(8):537–552, Aug 1963.

[69] N. S. Hall Taylor and R. M. Nedderman. The coalescence of disturbance waves in annular two phase flow. *Chem. Eng. Sci.*, 23(6):551–564, Aug 1968.

[70] H. Han, Z. Zhu, and K. Gabriel. A study on the effect of gas flow rate on the wave characteristics in two-phase gas–liquid annular flow. *Nucl. Eng. Des.*, 236(24):2580–2588, Dec 2006.

[71] D. B. Hann, A. V. Cherdantsev, and B. J. Azzopardi. Study of bubbles entrapped into a gas-sheared liquid film. *International Journal of Multiphase Flow*, 108:181–201, 2018.

[72] T. J. Hanratty and A. Hershman. Initiation of roll waves. *AIChE J.*, 7(3):488–497, Sep 1961.

[73] G. F. Hewitt and N. S. Hall-Taylor. *Annular Two-Phase Flow*. Pergamon, Oxford, England, UK, 1970.

[74] G. F. Hewitt and P. B. Whalley. Advanced optical instrumentation methods. *Int. J. Multiphase Flow*, 6(1):139–156, Feb 1980.

[75] K. Holmberg. Surfactant-templated nanomaterials synthesis. *Journal of Colloid and Interface Science*, 274(2):355–364, 2004.

[76] T. Hu, Q. Fu, and L. Yang. Falling film with insoluble surfactants: effects of surface elasticity and surface viscosities. *Journal of Fluid Mechanics*, 889, 2020.

[77] R. Ibarra, I. Zadrazil, O. K. Matar, and C. N. Markides. Dynamics of liquid–liquid flows in horizontal pipes using simultaneous two–line planar laser–induced fluorescence and particle velocimetry. *International Journal of Multiphase Flow*, 101:47–63, 2018.

[78] M. Iijima, M. Kobayakawa, M. Yamazaki, Y. Ohta, and H. Kamiya. Anionic surfactant with hydrophobic and hydrophilic chains for nanoparticle dispersion and shape memory polymer nanocomposites. *Journal of the American Chemical Society*, 131(45):16342–16343, 2009.

[79] S. V. Isaenkov, A. V. Cherdantsev, I. S. Vozhakov, M. V. Cherdantsev, D. G. Arkhipov, and D. M. Markovich. Study of primary instability of thick liquid films under strong gas shear. *Int. J. Multiphase Flow*, 111:62–81, Feb 2019.

[80] M. Ishii and M. A. Grolmes. Inception criteria for droplet entrainment in two-phase concurrent film flow. *AIChE J.*, 21(2):308–318, Mar 1975.

[81] P. W. James, G. F. Hewitt, and P. B. Whalley. Droplet motion in two-phase flow, 1980. [Online; accessed 6. Nov. 2020].

[82] D. M. Jepson, B. J. Azzopardi, and P. B. Whalley. The effect of gas properties on drops in annular flow. *Int. J. Multiphase Flow*, 15(3):327–339, May 1989.

[83] D. Kandel and E. Kaxiras. Surfactant mediated crystal growth of semiconductors. *Physical review letters*, 75(14):2742, 1995.

[84] S. I. Karakashev and A. V. Nguyen. Effect of sodium dodecyl sulphate and dodecanol mixtures on foam film drainage: Examining influence of surface rheology and intermolecular forces. *Colloids Surf., A*, 293(1):229–240, Feb 2007.

[85] T. Karapantsios and A. Karabelas. Longitudinal characteristics of wavy falling films. *International Journal of Multiphase Flow*, 21(1):119–127, 1995.

[86] T. Karapantsios, S. Paras, and A. Karabelas. Statistical characteristics of free falling films at high reynolds numbers. *International Journal of Multiphase Flow*, 15(1):1–21, 1989.

[87] G. Karapetsas and V. Bontozoglou. The primary instability of falling lms in the presence of soluble surfactants. *J. Fluid Mech*, 729:123–150, 2016.

[88] G. Karapetsas, R. V. Craster, and O. K. Matar. On surfactant-enhanced spreading and superspreading of liquid drops on solid surfaces. *Journal of fluid mechanics*, 670:5, 2011.

[89] A. Katsiavria and V. Bontozoglou. Stability of liquid film flow laden with the soluble surfactant sodium dodecyl sulphate: predictions versus experimental data. *Journal of Fluid Mechanics*, 894, 2020.

[90] G. G. Katul and M. B. Parlange. Analysis of land surface heat fluxes using the orthonormal wavelet approach. *Water Resources Research*, 31(11):2743–2749, 1995.

[91] S. J. Kline, W. C. Reynolds, F. A. Schraub, and P. W. Runstadler. The structure of turbulent boundary layers. *J. Fluid Mech.*, 30(4):741–773, Dec 1967.

[92] F. Knelman, N. Dombrowski, and D. M. Newitt. Mechanism of the Bursting of Bubbles. *Nature*, 173(4397):261, Feb 1954.

[93] R. C. Knox, D. A. Sabatini, J. H. Harwell, R. E. Brown, C. C. West, F. Blaha, and C. Griffin. Surfactant remediation field demonstration using a vertical circulation well. *Groundwater*, 35(6):948–953, 1997.

[94] N. Kovalchuk, O. Matar, R. Craster, R. Miller, and V. Starov. The effect of adsorption kinetics on the rate of surfactant-enhanced spreading. *Soft Matter*, 12(4):1009–1013, 2016.

[95] I. Kralova and J. Sjöblom. Surfactants used in food industry: a review. *Journal of Dispersion Science and Technology*, 30(9):1363–1383, 2009.

[96] J. Lea, Jr. and L. Rowlan. *Gas Well Deliquification*. Gulf Professional Publishing, Feb 2019.

[97] S. Lecompte, J. S. An, A. Charogiannis, M. De Paepe, and C. N. Markides. Simultaneous capacitive probe and planar laser-induced fluorescence measurements in downwards gas-liquid annular flow. In *9th World Conference on Experimental Heat Transfer, Fluid Mechanics and Thermodynamics*, 2017.

[98] K. Y. C. Lee. Collapse mechanisms of langmuir monolayers. *Annu. Rev. Phys. Chem.*, 59:771–791, 2008.

[99] Y.-C. Liao, H. J. Subramani, E. I. Franses, and O. A. Basaran. Effects of soluble surfactants on the deformation and breakup of stretching liquid bridges. *Langmuir*, 20(23):9926–9930, 2004.

[100] S.-Y. Lin, T.-L. Lu, and W.-B. Hwang. Adsorption kinetics of decanol at the air-water interface. *Langmuir*, 11(2):555–562, 1995.

[101] S.-Y. Lin, K. McKeigue, and C. Maldarelli. Diffusion-controlled surfactant adsorption studied by pendant drop digitization. *AIChE Journal*, 36(12):1785–1795, 1990.

[102] J. S. Lioumbas, C. Kolimenos, and S. V. Paras. Liquid layer characteristics in gas–liquid flow in slightly inclined pipes: Effect of non-ionic surfactant additives. *Chem. Eng. Sci.*, 64(24):5162–5172, Dec 2009.

[103] L. Liu, O. K. Matar, and G. F. Hewitt. Laser-induced fluorescence (LIF) studies of liquid–liquid flows. Part II: Flow pattern transitions at low liquid velocities in downwards flow. *Chem. Eng. Sci.*, 61(12):4022–4026, Jun 2006.

[104] M. Liu, M. Jia, H. Pan, L. Li, M. Chang, H. Ren, F. Argoul, S. Zhang, and J. Xu. Instrument response standard in time-resolved fluorescence spectroscopy at visible wavelength: quenched fluorescein sodium. *Applied spectroscopy*, 68(5):577–583, 2014.

[105] M. A. Lopez-Quintela. Synthesis of nanomaterials in microemulsions: formation mechanisms and growth control. *Current Opinion in Colloid & Interface Science*, 8(2):137–144, 2003.

[106] M. Lotya, P. J. King, U. Khan, S. De, and J. N. Coleman. High-concentration, surfactant-stabilized graphene dispersions. *ACS nano*, 4(6):3155–3162, 2010.

[107] J. Lu, C. M. Corvalan, Y. M. J. Chew, and J.-Y. Huang. Coalescence of small bubbles with surfactants. *Chem. Eng. Sci.*, 196:493–500, Mar 2019.

[108] E. D. Manev and A. V. Nguyen. Effects of surfactant adsorption and surface forces on thinning and rupture of foam liquid films. *Int. J. Miner. Process.*, 77(1):1–45, Sep 2005.

[109] P. Marmottant and E. Villermaux. On spray formation. *J. Fluid Mech.*, 498:73–111, Jan 2004.

[110] C. Martin, B. Azzopardi, et al. Waves in vertical annular flow. *Physicochemical Hydrodynamics*, 6(12):257–265, 1985.

[111] M. M. Martin and L. Lindqvist. The ph dependence of fluorescein fluorescence. *Journal of Luminescence*, 10(6):381–390, 1975.

[112] O. Matar, S. Kumar, and R. Craster. Nonlinear parametrically excited surface waves in surfactant-covered thin liquid films. *Journal of Fluid Mechanics*, 520:243, 2004.

[113] R. Mathie, H. Nakamura, and C. N. Markides. Heat transfer augmentation in unsteady conjugate thermal systems – Part II: Applications. *Int. J. Heat Mass Transfer*, 56(1):819–833, Jan 2013.

[114] F. Matsuyama, A. Kawahara, M. Sadatomi, K. Nakashima, and Y. Johno. Effects of surface tension on liquid film behavior and interfacial shear stress in upward annular flows in a vertical pipe. *Journal of Mechanical Engineering and Automation*, 7(5):164–171, 2017.

[115] J. W. Miles. Surface-wave damping in closed basins. *Proceedings of the Royal Society of London. Series A. Mathematical and Physical Sciences*, 297(1451):459–475, 1967.

[116] J. M. Mollerup and M. P. Breil. Modeling the permittivity of electrolyte solutions. *AIChE J.*, 61(9):2854–2860, Sep 2015.

[117] R. G. Morgan, C. N. Markides, C. P. Hale, and G. F. Hewitt. Horizontal liquid–liquid flow characteristics at low superficial velocities using laser-induced fluorescence. *International journal of multiphase flow*, 43:101–117, 2012.

[118] I. Mudawwar and M. El-Masri. Momentum and heat transfer across freely-falling turbulent liquid films. *International Journal of Multiphase Flow*, 12(5):771–790, 1986.

[119] S. Mukherjee, P. Das, and R. Sen. Towards commercial production of microbial surfactants. *TRENDS in Biotechnology*, 24(11):509–515, 2006.

[120] C. N. Mulligan, R. Yong, and B. Gibbs. Surfactant-enhanced remediation of contaminated soil: a review. *Engineering geology*, 60(1-4):371–380, 2001.

[121] C. Munkholm, D. R. Parkinson, and D. R. Walt. Intramolecular fluorescence self-quenching of fluoresceinamine. *Journal of the American Chemical Society*, 112(7):2608–2612, 1990.

[122] V. E. Nakoryakov, B. G. Pokusaev, and S. V. Alekseenko. Stationary two-dimensional rolling waves on a vertical film of fluid. *Journal of Engineering Physics*, 30(5):517–521, May 1976.

[123] W. Nusselt. Die oberflachenkondensation des wasserdamphes. *Zeitschrift des Vereines Deutscher Ingenieure*, 60:541, 1916.

[124] C. O'Connor. Acidic and basic amide hydrolysis. *Quarterly Reviews, Chemical Society*, 24(4):553–564, 1970.

[125] P. L. O'Neill, D. Nicolaides, D. Honnery, J. Soria, et al. Autocorrelation functions and the determination of integral length with reference to experimental and numerical data. In *15th Australasian fluid mechanics conference*, volume 1, pages 1–4. Univ. of Sydney Sydney, NSW, Australia, 2004.

[126] J. Orbulescu, S. V. Mello, Q. Huo, G. Sui, P. Kele, and R. M. Leblanc. Reexamination of the monolayer properties of a fluorescein amphiphile in langmuir and langmuir- schaefer films. *Langmuir*, 17(5):1525–1528, 2001.

[127] H. W. Ott. *Electromagnetic compatibility engineering*. John Wiley & Sons, 2011.

[128] R. Pan, J. Green, and C. Maldarelli. Theory and experiment on the measurement of kinetic rate constants for surfactant exchange at an air/water interface. *Journal of Colloid and Interface Science*, 205(2):213–230, 1998.

[129] S. H. Pham, Z. Kawara, T. Yokomine, and T. Kunugi. Detailed observations of wavy interface behaviors of annular two-phase flow on rod bundle geometry. *Int. J. Multiphase Flow*, 59:135–144, Feb 2014.

[130] A. Pinazo, C.-H. Chang, and E. Franses. Dynamic surface tension behavior of aqueous solutions of n-dodecyl-n, n dimethyl aminobetaine chlorohydrate. *Colloid and Polymer Science*, 272(4):447–455, 1994.

[131] A. Pockels. On the Relative Contamination of the Water-Surface by Equal Quantities of Different Substances. *Nature*, 46(1192):418–419, Sep 1892.

[132] S. B. Pope. Turbulent flows, 2001.

[133] E. Portuguez, A. Alzina, P. Michaud, M. Oudjedi, and A. Smith. Evolution of a Water Pendant Droplet: Effect of Temperature and Relative Humidity. *Natural Science*, 09:1, 2017.

[134] C. N. R. Rao, A. Govindaraj, F. L. Deepak, N. Gunari, and M. Nath. Surfactant-assisted synthesis of semiconductor nanotubes and nanowires. *Applied Physics Letters*, 78(13):1853–1855, 2001.

[135] N. Reinike and D. Mewes. Multielectrode capacitance sensors for the visualization of transient two-phase flows. *Experimental Thermal and Fluid Science*, 15:253–266, 1997.

[136] Y. Rivera, J.-L. Muñoz-Cobo, J.-L. Cuadros, C. Berna, and A. Escrivá. Experimental study of the effects produced by the changes of the liquid and gas superficial velocities and the surface tension on the interfacial waves and the film thickness in annular concurrent upward vertical flows. *Exp. Therm. Fluid Sci.*, 120:110224, Jan 2021.

[137] J. N. Robert Sjoback and M. Kubista. Absorption and fluorescence properties of fluorescein. *Spectrochimica Acta Part A*, 51(995):L7–L2l, 1995.

[138] D. J. Rodrıguez and T. A. Shedd. Entrainment of gas in the liquid film of horizontal, annular, two-phase flow. *Int. J. Multiphase Flow*, 30(6):565–583, Jun 2004.

[139] M. J. Rosen and J. T. Kunjappu. *Surfactants and Interfacial Phenomena.* Jan 2012.

[140] S. Samanta and P. Ghosh. Coalescence of bubbles and stability of foams in aqueous solutions of Tween surfactants. *Chem. Eng. Res. Des.*, 89(11):2344–2355, Nov 2011.

[141] J. R. Sander, D.-K. Bučar, R. F. Henry, G. G. Zhang, and L. R. MacGillivray. Pharmaceutical nano-cocrystals: sonochemical synthesis by solvent selection and use of a surfactant. *Angewandte Chemie International Edition*, 49(40):7284–7288, 2010.

[142] L. M. Sayre. Metal ion catalysis of amide hydrolysis. *Journal of the American Chemical Society*, 108(7):1632–1635, 1986.

[143] D. Schubring. *Behavior interrelationships in annular flow.* PhD thesis, 2009.

[144] D. Schubring, A. C. Ashwood, T. A. Shedd, and E. T. Hurlburt. Planar laser-induced fluorescence (PLIF) measurements of liquid film thickness in annular flow. Part I: Methods and data. *Int. J. Multiphase Flow*, 36(10):815–824, Oct 2010.

[145] D. Schubring and T. A. Shedd. A model for pressure loss, film thickness, and entrained fraction for gas–liquid annular flow. *Int. J. Heat Fluid Flow*, 32(3):730–739, Jun 2011.

[146] A. Sciacchitano, D. R. Neal, B. L. Smith, S. O. Warner, P. P. Vlachos, B. Wieneke, and F. Scarano. Collaborative framework for piv uncertainty quantification: comparative assessment of methods. *Measurement Science and Technology*, 26(7):074004, 2015.

[147] A. Setyawan, Indarto, and Deendarlianto. The effect of the fluid properties on the wave velocity and wave frequency of gas–liquid annular two-phase flow in a horizontal pipe. *Exp. Therm. Fluid Sci.*, 71:25–41, Feb 2016.

[148] Habib. I. Shaban. A study of foaming and carry-over problems in oil and gas separators. *Gas Sep. Purif.*, 9(2):81–86, Jun 1995.

[149] L. Shen, D. K. P. Yue, and G. S. Triantafyllou. Effect of surfactants on free-surface turbulent flows. *J. Fluid Mech.*, 506:79–115, May 2004.

[150] A. V. Shenoy. A review on drag reduction with special reference to micellar systems. *Colloid Polym. Sci.*, 262(4):319–337, Apr 1984.

[151] B. A. Smith, L. A. Soderblom, R. Beebe, J. Boyce, G. Briggs, M. Carr, S. A. Collins, A. F. Cook, G. E. Danielson, M. E. Davies, G. E. Hunt, A. Ingersoll, T. V. Johnson, H. Masursky, J. Mccauley, D. Morrison, T. Owen, C. Sagan, E. M. Shoemaker, R. Strom, V. E. Suomi, and J. Veverka. The Galilean Satellites and Jupiter: Voyager 2 Imaging Science Results. *Science*, 206(4421):927–950, Nov 1979.

[152] A. D. Smith McWilliams, S. Ergülen, M. M. Ogle, C. A. de los Reyes, M. Pasquali, and A. A. Martí. Fluorescent surfactants from common dyes–rhodamine b and eosin y. *Pure and Applied Chemistry*, 92(2):265–274, 2020.

[153] G. Soligo, A. Roccon, and A. Soldati. Breakage, coalescence and size distribution of surfactant-laden droplets in turbulent flow. *J. Fluid Mech.*, 881:244–282, Dec 2019.

[154] P. Somasundaran and L. Zhang. Adsorption of surfactants on minerals for wettability control in improved oil recovery processes. *Journal of Petroleum Science and Engineering*, 52(1-4):198–212, 2006.

[155] S. L. Strickland, M. Shearer, and K. E. Daniels. Spatiotemporal measurement of surfactant distribution on gravity–capillary waves. *Journal of Fluid Mechanics*, 777:523–543, 2015.

[156] R. Subramanyam and C. Maldarelli. Fluorescence evidence that a phase transition causes the induction time in the reduction in dynamic tension during surfactant adsorption to a clean air/water interface and a kinetic–diffusive transport model for the phase-induced induction. *Journal of Colloid and Interface Science*, 253(2):377–392, 2002.

[157] H. Takahama and S. Kato. Longitudinal flow characteristics of vertically falling liquid films without concurrent gas flow. *International Journal of Multiphase Flow*, 6(3):203–215, 1980.

[158] F. Takemura, J. Magnaudet, and P. Dimitrakopoulos. Migration and deformation of bubbles rising in a wall-bounded shear flow at finite reynolds number. *Journal of fluid mechanics*, 634:463–486, 2009.

[159] F. I. Talens-Alesson. The modelling of falling film chemical reactors. *Chem. Eng. Sci.*, 54(12):1871–1881, Jun 1999.

[160] K. C. Taylor and H. A. Nasr-El-Din. Water-soluble hydrophobically associating polymers for improved oil recovery: A literature review. *Journal of Petroleum Science and Engineering*, 19(3-4):265–280, 1998.

[161] A. D. S. Telles. *Liquid film characteristics in vertical two-phase flow*. PhD thesis, University of Houston, 1969.

[162] A. S. Telles and A. E. Dukler. Statistical Characteristics of Thin, Vertical, Wavy, Liquid Films. *Ind. Eng. Chem. Fundam.*, 9(3):412–421, Aug 1970.

[163] Y. Thomas. III. An essay on the cohesion of fluids. *Philos. Trans. R. Soc. Lond.*, 95:65–87, Dec 1805.

[164] G. R. Thwaites, N. N. Kulov, and R. M. Nedderman. Liquid film properties in two-phase annular flow. *Chem. Eng. Sci.*, 31(6):481–486, Jan 1976.

[165] M. Tomassone, A. Couzis, C. Maldarelli, J. Banavar, and J. Koplik. Phase transitions of soluble surfactants at a liquid- vapor interface. *Langmuir*, 17(20):6037–6040, 2001.

[166] T. Tran, H. de Maleprade, C. Sun, and D. Lohse. Air entrainment during impact of droplets on liquid surfaces. *Journal of Fluid Mechanics*, 726, 2013.

[167] D. J. Tritton. *Physical fluid dynamics*. Springer Science & Business Media, 2012.

[168] K. Usui. Vertically Downward Two-Phase Flow, (II). *J. Nucl. Sci. Technol.*, 26(11):1013–1022, Nov 1989.

[169] M. Van den Tempel and R. Van de Riet. Damping of waves by surface-active materials. *The Journal of Chemical Physics*, 42(8):2769–2777, 1965.

[170] A. T. van Nimwegen, L. M. Portela, and R. A. W. M. Henkes. The effect of surfactants on air–water annular and churn flow in vertical pipes. Part 1: Morphology of the air–water interface. *Int. J. Multiphase Flow*, 71:133–145, May 2015.

[171] A. T. van Nimwegen, L. M. Portela, and R. A. W. M. Henkes. The Effect of Surfactants on Vertical Air/Water Flow for Prevention of Liquid Loading. *SPE J.*, 21(02):488–500, Apr 2016.

[172] J. J. van Rossum. Experimental investigation of horizontal liquid films: Wave formation, atomization, film thickness. *Chem. Eng. Sci.*, 11(1):35–52, Aug 1959.

[173] N. Vargaftik, B. Volkov, and L. Voljak. International tables of the surface tension of water. *Journal of Physical and Chemical Reference Data*, 12(3):817–820, 1983.

[174] J. Vasques, A. Ibrahim, D. Hann, K. Simmons, and M. Walsh. The Effect of Surface Tension on Bubble Generation in Gas-Sheared Liquid Films. *American Society of Mechanical Engineers Digital Collection*, Nov 2019.

[175] D. Webb and G. Hewitt. Downwards co-current annular flow. *International Journal of Multiphase Flow*, 2(1):35–49, 1975.

[176] N. S. Wilkes, B. J. Azzopardi, and C. P. Thompson. Wave coalescence and entrainment in vertical annular two-phase flow. *Int. J. Multiphase Flow*, 9(4):383–398, Aug 1983.

[177] D. E. Woodmansee and T. J. Hanratty. Mechanism for the removal of droplets from a liquid surface by a parallel air flow. *Chem. Eng. Sci.*, 24(2):299–307, Feb 1969.

[178] S. G. Woolfrey, G. M. Banzon, and M. J. Groves. The effect of sodium chloride on the dynamic surface tension of sodium dodecyl sulfate solutions. *J. Colloid Interface Sci.*, 112(2):583–587, Aug 1986.

[179] S. F. Wright, I. Zadrazil, and C. N. Markides. A review of solid–fluid selection options for optical-based measurements in single-phase liquid, two-phase liquid–liquid and multiphase solid–liquid flows. *Experiments in Fluids*, 58(9):108, 2017.

[180] Z. Xie, G. F. Hewitt, D. Pavlidis, P. Salinas, C. C. Pain, and O. K. Matar. Numerical study of three-dimensional droplet impact on a flowing liquid film in annular two-phase flow. *Chem. Eng. Sci.*, 166:303–312, Jul 2017.

[181] Z. Xu and L. Xu. Fluorescent probes for the selective detection of chemical species inside mitochondria. *Chemical Communications*, 52(6):1094–1119, 2016.

[182] T. Xue, Z. Li, C. Li, and B. Wu. Measurement of thickness of annular liquid films based on distortion correction of laser-induced fluorescence imaging. *Review of Scientific Instruments*, 90(3):033103, 2019.

[183] T. Xue, L. Yang, P. Ge, and L. Qu. Error analysis and liquid film thickness measurement in gas–liquid annular flow. *Optik*, 126(20):2674–2678, 2015.

[184] S. X. Yang and W. Q. Yang. A portable stray-immune capacitance meter. *Review of Scientific Instruments*, 73:1958–1961, 2001.

[185] I. Zadrazil and C. N. Markides. An experimental characterization of liquid films in downwards co-current gas–liquid annular flow by particle image and tracking velocimetry. *International Journal of Multiphase Flow*, 67:42–53, 2014.

[186] I. Zadrazil, O. K. Matar, and C. N. Markides. An experimental characterization of downwards gas–liquid annular flow by laser-induced fluorescence: flow regimes and film statistics. *International Journal of Multiphase Flow*, 60:87–102, 2014.

[187] M. Zanfir, A. Gavriilidis, Ch. Wille, and V. Hessel. Carbon Dioxide Absorption in a Falling Film Microstructured Reactor: Experiments and Modeling. *Ind. Eng. Chem. Res.*, 44(6):1742–1751, Mar 2005.

[188] X.-F. Zhang, J. Zhang, and L. Liu. Fluorescence properties of twenty fluorescein derivatives: lifetime, quantum yield, absorption and emission spectra. *Journal of fluorescence*, 24(3):819–826, 2014.

[189] Z. Zhang, Z. Wang, H. Liu, Y. Gao, H. Li, and B. Sun. Experimental study on bubble and droplet entrainment in vertical churn and annular flows and their relationship. *Chem. Eng. Sci.*, 206:387–400, Oct 2019.

[190] Y. Zhao, C. N. Markides, O. K. Matar, and G. F. Hewitt. Disturbance wave development in two-phase gas–liquid upwards vertical annular flow. *International Journal of Multiphase Flow*, 55:111–129, 2013.

Appendix A

Statistical convergence tests
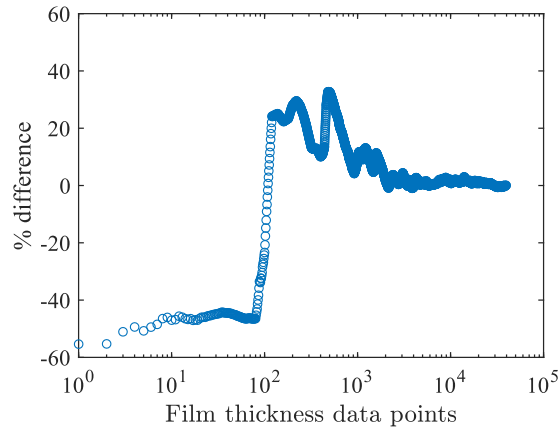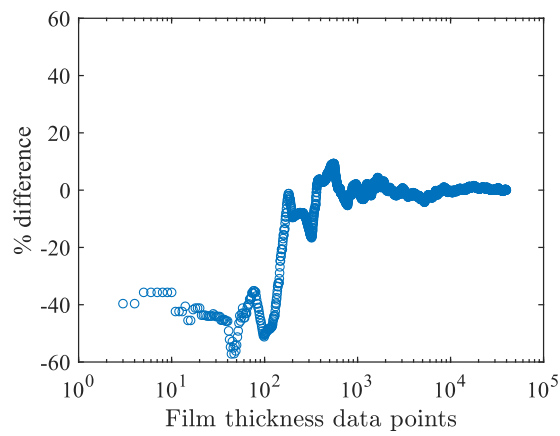
Figure A.1: Typical convergence of standard error towards $> 1\%$ in image analysis using S-PLIF method. The process involves a random selection of 20 film thickness data points per image pair from 2000 images per flow condition. (a) Surfactant-free flow at $Re_{\mathrm{L}} = 1000$ and $Re_{\mathrm{G}} = 0$; (b) Surfactant-free flow at $Re_{\mathrm{L}} = 1000$ and $Re_{\mathrm{G}} = 40 \times 10^3$.

Appendix B

Probability density functions of the film thickness distribution: effect of gas shear rate
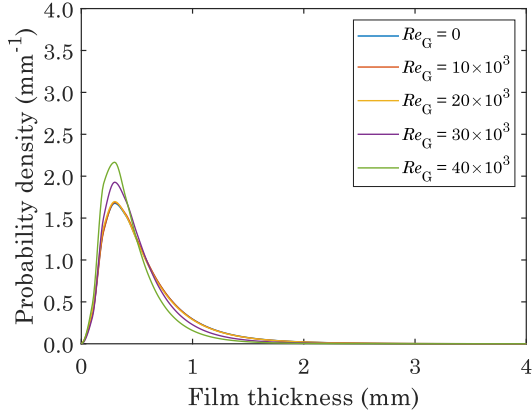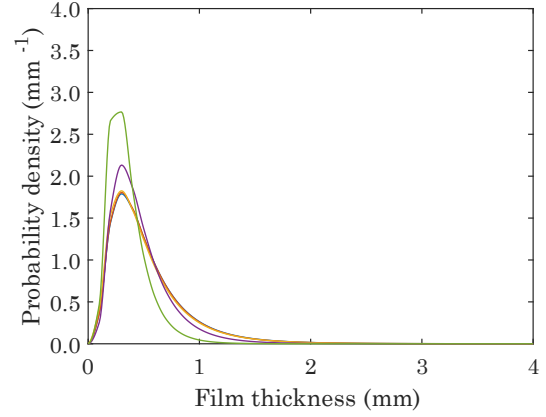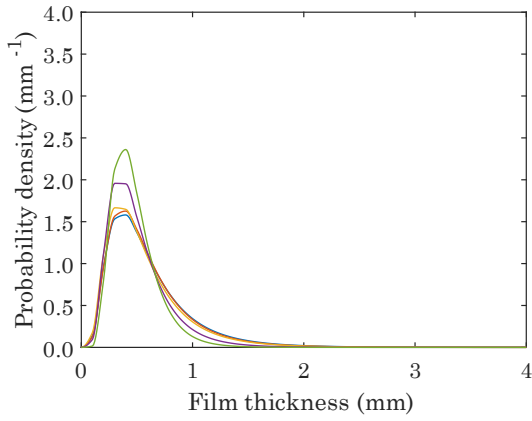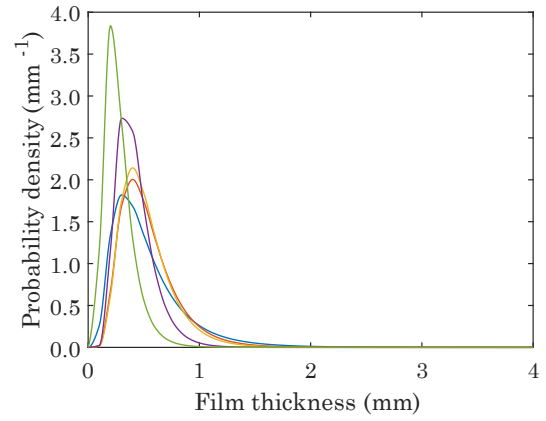
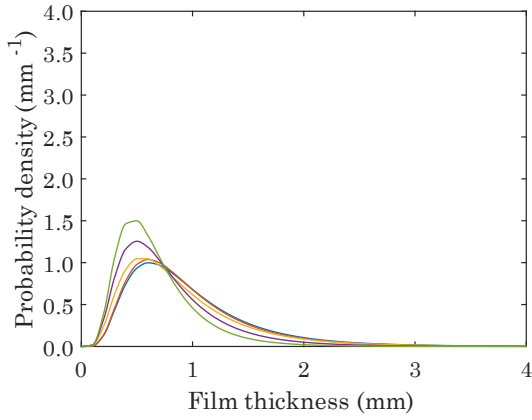Figure B.1: Log-normal probability density functions of the film thickness measurements for gas sheared annular flows of Table 3.2, for $Re_\mathrm{G} \in \left[0; 40 \times 10^3\right]$ and $Re_\mathrm{L} = 625$. Dry-out regions encountered in the high Re_G cases were ignored.
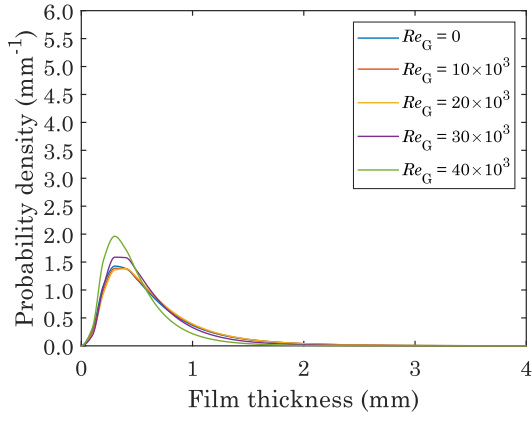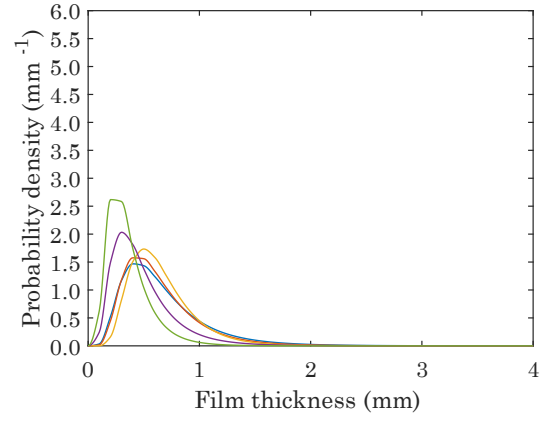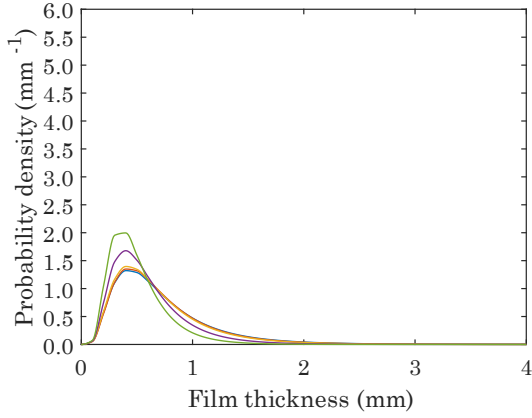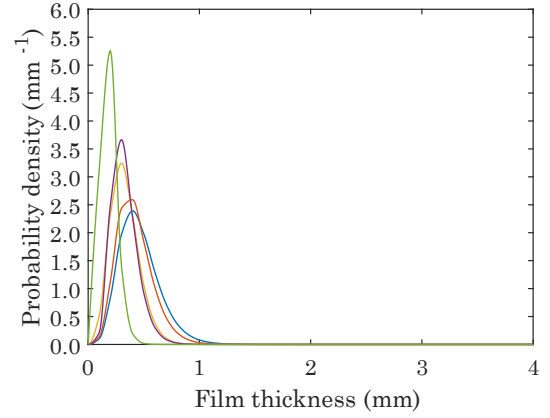
Figure B.2: Log-normal probability density functions of the film thickness measurements for gas sheared annular flows of Table 3.2, for $Re_G \in \left[0; 40 \times 10^3\right]$ and $Re_L = 875$.
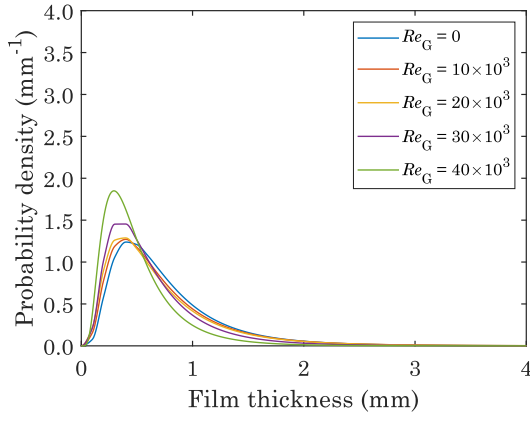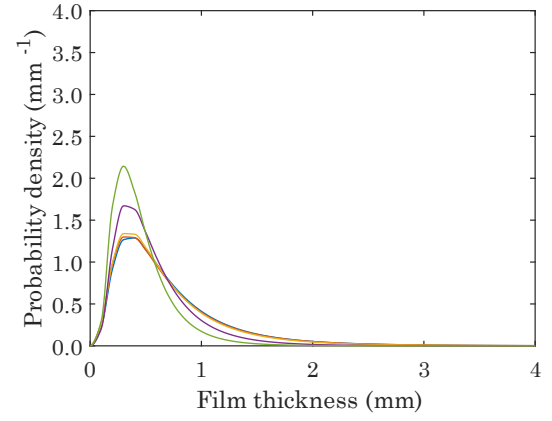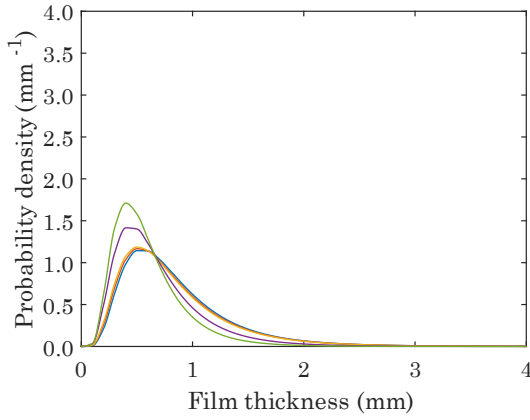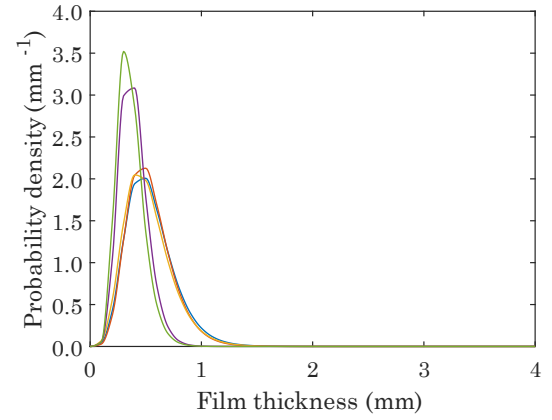
Figure B.3: Log-normal probability density functions of the film thickness measurements for gas sheared annular flows of Table 3.2, for $Re_{\mathrm{G}} \in \left[0; 40 \times 10^3\right]$ and $Re_{\mathrm{L}} = 1125$.
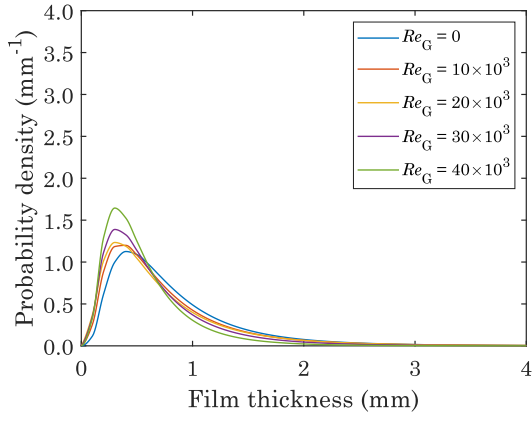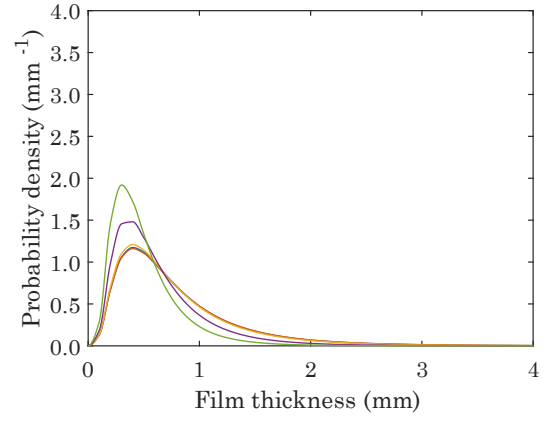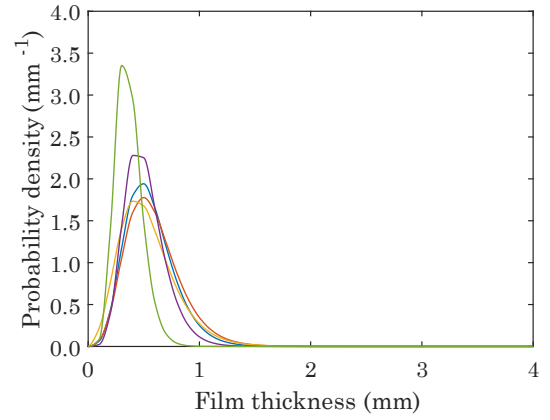
Figure B.4: Log-normal probability density functions of the film thickness measurements for gas sheared annular flows of Table 3.2, for $Re_\mathrm{G} \in \left[0; 40 \times 10^3\right]$ and $Re_\mathrm{L} = 1375$.

Appendix C

Machine learning-based image segmentation for gas entrainment statistics
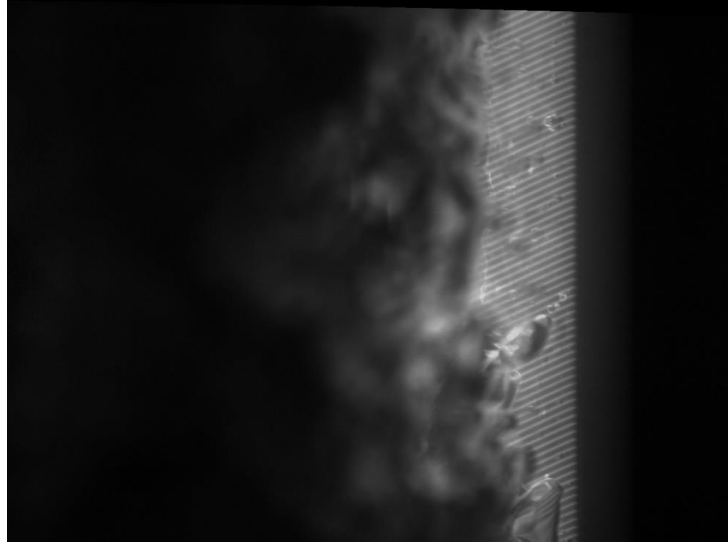
(a) Uploaded raw image
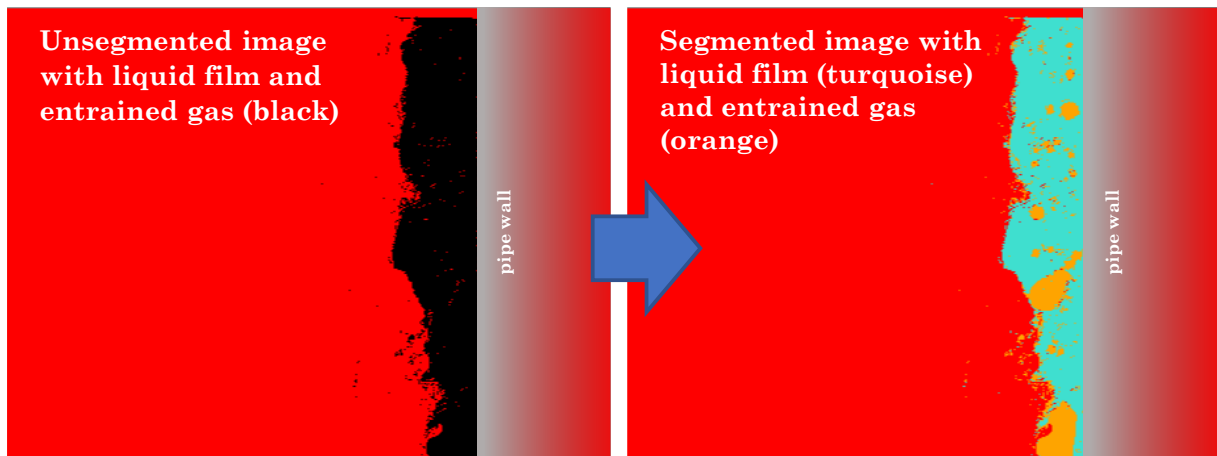
(b) Sample result of image segmentation

Figure C.1: Example of applying machine learning-based image segmentation to one of the instantaneous S-PLIF images of the annular flow. (a) Uploaded raw image to the training module; (b) Resultant image segmentation based on the selected features – liquid film and entrained air bubbles (left: film and entrained bubbles (black); right: film (blue-green) and entrained bubbles (orange)).

Appendix D

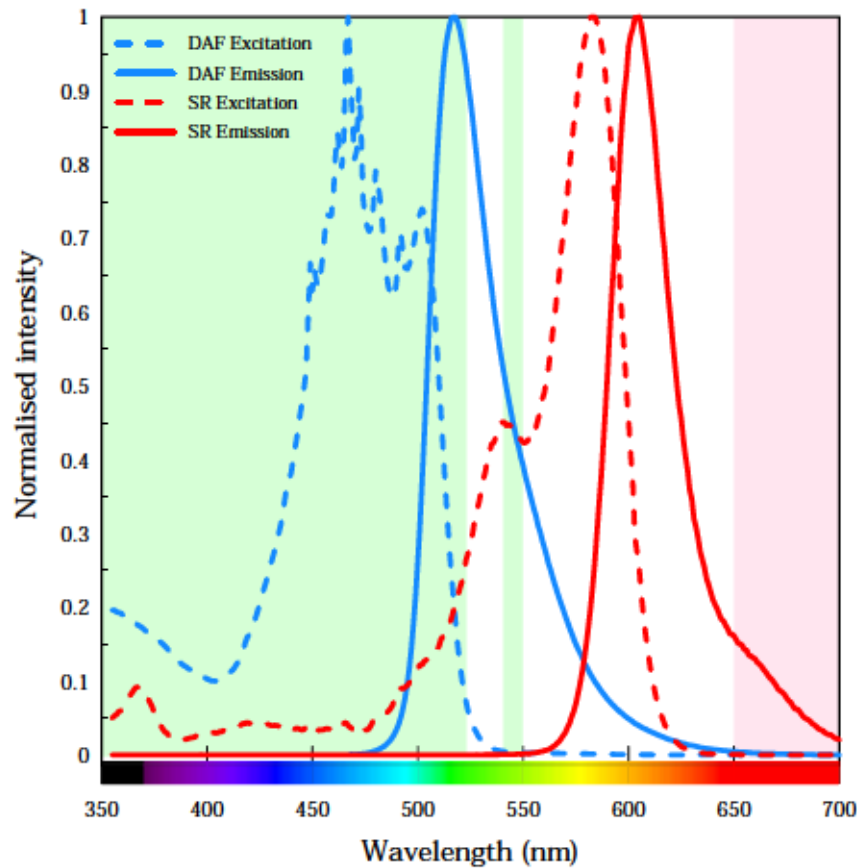# Optical properties of DAF and SR dyes for two-colour LIF application

Figure D.1: Excitation (dashed lines) and emission spectra (solid lines) of DAF surfactant (blue) and SR dye (red). Green coloured area represents recorded light wavelength with one camera equipped with short-pass 550 nm and notch 532 nm (FWHM 17 nm) filters, whilst red coloured area – second camera equipped with a long-pass 650 nm filter.
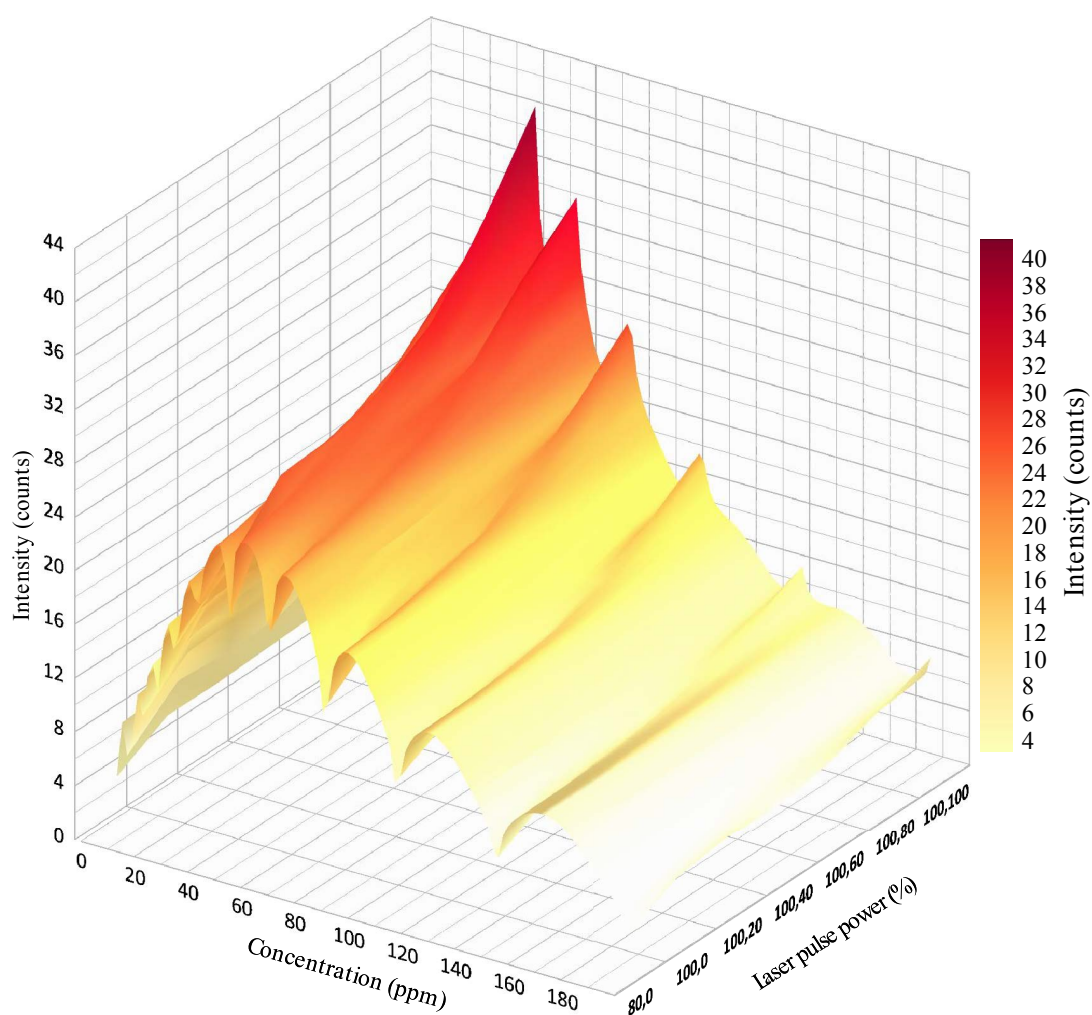
Figure D.2: Recorded fluorescence intensity of DAF surfactant as a function of concentration (4 ppm to 195 ppm) and laser power (at a fixed SR concentration of 1.5 ppm) using camera equipped with short-pass 550 nm and notch 532 nm (FWHM 17 nm) filters.
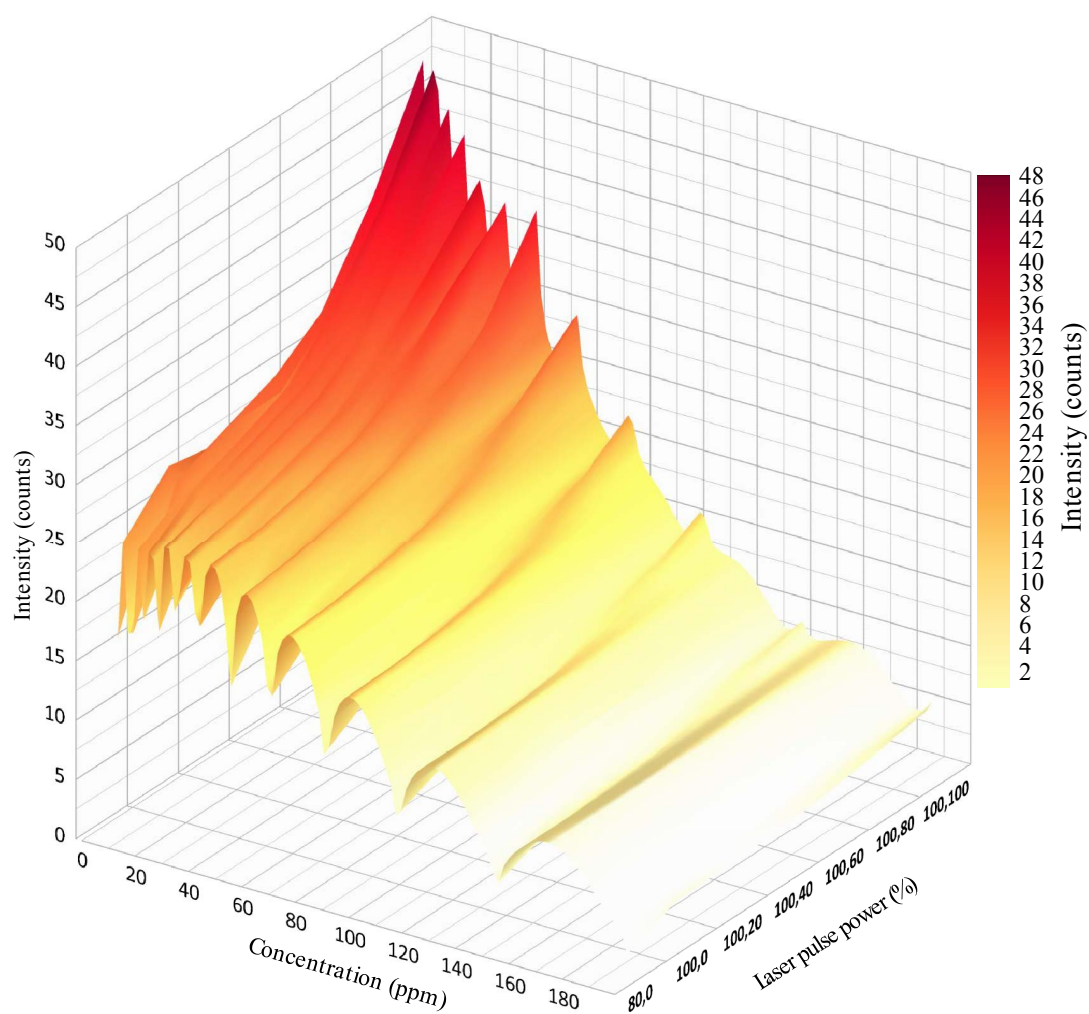
Figure D.3: Recorded fluorescence intensity of SR dye (1.5 ppm) as a function of DAF concentration (4 ppm to 195 ppm) and laser power using camera equipped with a long-pass 650 nm filter.